9th International Conference on Vortex Flow Mechanics

ICVFM 2021

11-13 October 2021, Virtual Conference,
University of Patras, Greece

Proceedings

9th International Conference on Vortex Flow Mechanics ICVFM 2021

11-13 October 2021, Virtual Conference,
University of Patras, Greece

Vortices play a dominant role in fluid dynamics. Besides their fascinating shape and structure, they are important in many physical phenomena and technological applications and may require special tools for their analysis and experimental or numerical study. Mastering vortex dynamics and modeling is relevant for both fundamental and applied sciences. Understanding vortex dynamics is key to solve multiscale problems in turbulence, to predict unsteady loadings on engineering devices, to forecast the weather, etc.

The scope of the series of the International Conferences on Vortex Flow Mechanics is to provide a platform for scientists and engineers to present state-of-the art research and discuss recent developments in the field of vortex physics, modeling, and applications. This series of successful meetings commenced in Kobe in 1999 and continued in Istanbul (2001), Yokohama (2005), Daejeon (2008), San Leucio (2010), Nagoya (2014), Rostock (2016), and Xi'an (2018).

The 9th International Conference on Vortex Flow Mechanics, originally planned to take place in 2020, in Patras, Greece, has suffered the difficulties of the COVID-19 pandemic. Postponed to October 2021, due to ongoing COVID-19 concerns, the conference is organized by the University of Patras as a virtual conference held entirely online from 11th to 13th October 2021.

The conference covers but is not limited to the following topics:

- Turbulent flow
- Multiphase flow
- Reacting flow
- Free-shear flow
- Stratified flow
- Bio-fluid mechanics
- Computation fluid mechanics
- Flow measurements
- Flow control
- Turbomachinery
- Aero-acoustics
- Aerodynamic design optimization
- Flow-induced vibration
- Microfluidics
- Scientific visualization methods
- Vortex dynamics in ship hydromechanics

9th International Conference on Vortex Flow Mechanics ICVFM 2021

11-13 October 2021, Virtual Conference,
University of Patras, Greece

Organizing Committee

Chair
Prof. Thrassos Panidis, University of Patras, Greece
Vice-Chair
Prof. Xiande Fang, Nanjing University of Aeronautics and Astronautics, China
Members
Prof. Yannis Kallinderis, University of Patras, Greece
Prof. Dionyssios Margaris, University of Patras, Greece
Prof. Spyros Voutsinas, National Technical University of Athens, Greece
Prof. Kyros Yakinthos, Aristotle University of Thessaloniki, Greece
Secretary
Dr. Alexandros Romeos, University of Patras, Greece

Executive Committee

Prof. Hikaru Aono, Tokyo University of Science, Japan
Prof. Keh-Chin Chang, Cheng Kung University, Taiwan China
Prof. Bin Chen, Xi'an Jiaotong University, China
Prof. Galina Dynnikova, Moscow State University, Russia
Prof. John Ekaterinaris, Embry-Riddle Aeronautical University, FL USA
Prof. Masaki Fuchiwaki, Kyushu Institute of Technology, Japan
Prof. Hitoshi Ishikawa, Tokyo University of Science, Japan
Prof. Kyoji Kamemoto, Yokohama National University, Japan
Prof. Nikolai Kornev, University of Rostock, Germany
Prof. Petros Koumoutsakos, ETH Zurich, Switzerland
Prof. Jiun-Jih Miau, National Cheng Kung University, Taiwan China
Prof. Iraj Mortazavi, Institute Polytechnique de Bordeaux, France
Prof. Andrew Pollard, Queen's University, Kingston, ON Canada
Prof. Alexei Setukha, Moscow State University, Russia
Prof. Tomomi Uchiyama, Nagoya University, Japan
Prof. Gregoire Winckelmans, Université Catholique de Louvain, Belgium
Prof. Xiaogang Yang, The University of Nottingham, UK
Prof. Yoshifumi Yokoi, National Defense Academy of Japan, Japan

ICVFM 2021

9th International Conference on Vortex Flow Mechanics

11-13 October 2021, Virtual Conference, University of Patras, Greece

Programme

[Reference time zone is that in Patras, Greece (EEST, GMT+3)]

1st Day	**Monday, October 11th, 2021**	
11:00-11:20	Welcome	
	SESSION 1 Chair Prof. Nikolai Kornev	
11:20-12:00 *(S1.K1)*	Keynote Presentation Vortex induced vibrations in aerodynamics *Spyros Voutsinas*	Keynote p. 3
12:00-12:20 *(S1.1)*	Sinusoidally heaving airfoil on an elastic hinge *Yaroslav Dynnikov, Galina Dynnikova, Sergey Guvernyuk and Tatyana Malakhova*	Article p. 4
12:20-12:40 *(S1.2)*	Resonant vortex-wake forces on circular cylinders *Efstathios Konstantinidis*	Abstract p. 11
12:40-13:00 *(S1.3)*	A Computer Aided Optimizing Design for Drone Rotors *Daichi Yoshidome and Norihiko Watanabe*	Article p. 12
13:00-13:20 *(S1.4)*	On the Vortex Method for Modeling a Separated Flow of an Inviscid Fluid *Alexey Setukha*	Abstract p. 22
13:20-13:40	Break	
	SESSION 2 Chair Prof. Thrassos Panidis	
13:40-14:00 *(S2.1)*	Calculation of pressure, force, and moment in meshless vortex methods *Galina Dynnikova*	Article p. 23
14:00-14:20 *(S2.2)*	Interpolating Vortex Particle Methods using Splines Wavelets *Matthias Kirchhart*	Abstract p. 36
14:20-14:40 *(S2.3)*	Effect of Froude number on the motion of a sphere launched vertically upward in water *Kotaro Takamure and Tomomi Uchiyama*	Abstract p. 37
14:40-15:00 *(S2.4)*	Analytical Description of the Vortex Ring Induced by a Ring Plume *Maria Stefanidou, Aristeidis Bloutsos, George Horsch, Athanassios Dimas and Panayotis Yannopoulos*	Abstract p. 38
15:00-15:20 *(S2.5)*	Flow visualization of transitional channel flow with polymer additive *Sattaya Yimprasert, Per Henrik Alfresdsson and Masaharu Matsubara*	Article p. 39
15:20-15:40 *(S2.6)*	Micropolar Theory on Turbulence Modulation *George Sofiadis, Evangelos Karvelas and Ioannis Sarris*	Abstract p. 46
15:40-16:00	Break	
	SESSION 3 Chair Prof. Spyros Voutsinas	
16:00-16:40 *(S3.K1)*	Keynote Presentation Vortices interacting with smart materials and structures: the case of energy harvesting *Oleg Goushcha/Yannis Andreopoulos*	Keynote p. 47

2nd Day	**Tuesday, October 12th, 2021**	
	SESSION 4 Chair Prof. Bin Chen	
11:00-11:40 *(S4.K1)*	Keynote Presentation Empirical Predictive Method for Two-Phase Flow Condensation Heat Transfer in Plain Channels *Xiande Fang*	Keynote p. 49
11:40-12:20 *(S4.K2)*	Keynote Presentation Flow and Control of Some Jets and Separated Flows *Toshihiko Shakouchi*	Keynote p. 76
12:20-12:40	Break	
	SESSION 5 Chair Prof. Alexei Setukha	
12:40-13:00 *(S5.1)*	Experimental study on the heat transfer characteristics and frequency control of flashing spray cooling under varying operating conditions *Shangming Wang, Zhifu Zhou and Bin Chen*	Abstract p. 77
13:00-13:20 *(S5.2)*	Influence of the inlet local annular swirling zone on an axisymmetric turbulent jet *Yevhenii Shkvar, Shiju E, Dmytro Redchyts and Svitlana Moiseienko*	Article p. 78
13:20-13:40 *(S5.3)*	Experimental Study on Coaxial Swirling Jets *Andreas Naxakis, Alexandros Romeos, Athanasios Giannadakis and Thrassos Panidis*	Article p. 86
13:40-14:00 *(S5.4)*	Patient-Specific Diastolic Vortex Flow Patterns in the Left Ventricle *Dimitrios Zantzas, Vasileios Gkoutzamanis, Vasiliki Kantartzi, Vasileios Saxpeckidis and Anestis Kalfas*	Abstract p. 95
14:00-14:20	Break	
	SESSION 6 Chair Dr. Alexandros Romeos	
14:20-14:40 *(S6.1)*	Hot-wire measurement of asymptotic characteristics of lobed jet flow *Ren Fukui, Mamoru Takahashi, Koichi Tsujimoto, Toshitake Ando, Tishihiko Shakouchi and Ryuichi Momiyama*	Article p. 96
14:40-15:00 *(S6.2)*	Vortex Structure Produced by a Sweeping Jet in a Cross Flow *Masaki Fuchiwaki, Eisei Kobayashi and Surya Raghu*	Abstract p. 101
15:00-15:20 *(S6.3)*	Supersonic Under-Expanded Reattached Jet with Vortex Region *Tetsuji Ohmura, Toshihiko Shakouchi, Ryota Matsui and Koichi Tsujimoto*	Abstract p. 102
15:20-15:40 *(S6.4)*	Fundamental Study on Design Methodology of a Solar Car Considering Aerodynamic and Power Generation Performance *Arata Muto, Ichiro Uto, Kota Fukuda, Kouhei Sagawa and Hideki Kimura*	Article p. 103
15:40-16:00 *(S6.5)*	Study on Drag Reduction of Superstructure of Ships and Improvement of Fuel Consumption *Kodai Fukushima, Kota Fukuda, Takao Kashiwagi, Takashi Danno, Koeki Onishi and Koyu Kimura*	Article p. 111

3rd Day	**Wednesday, October 13th, 2021**	
	SESSION 7 Chair Prof. Tomomi Uchiyama	
11:00-11:40 *(S7.K1)*	Keynote Presentation Mitigating Aircraft Wake Vortex Risks During Final Approach via Plate Lines *Frank Holzäpfel*	Keynote p. 122
11:40-12:00 *(S7.1)*	Comparison of Synthetic Inflow Generation Methods for Atmospheric Boundary Layer Flows *Henry Plischka, Johann Turnow and Nikolai Kornev*	Article p. 124
12:00-12:20 *(S7.2)*	Identification and Analysis of vortical structures over an airliner's wing-fuselage junction *Stylianos Adamidis and Nicholas C. Markatos*	Abstract p. 138
12:20-12:40 *(S7.3)*	Vortex Dynamics Effects on the Development of a Confined Wake and a Channel Flow in a Rectangular Duct Under Identical Inlet Flow Conditions *Ioannis Kalogirou*	Abstract p. 139
12:40-13:00 *(S7.4)*	The Numerical Simulation of the Vortex Shedding Flow from Two Circular Cylinders of the Parallel Arrangement in the Lock-in State in the Different Mode *Yoshifumi Yokoi*	Article p. 140
13:00-13:20	Break	
	SESSION 8 Chair Prof. Xiande Fang	
13:20-13:40 *(S8.1)*	Turbulent channel flow past a wall-mounted cuboid *Ariane Neale Ramos Vieira, Hendrik Kuhlmann, Johann Waringer, Carina Zittra, Jan Martini, Simon Vitecek and Stephan Handschuh*	Abstract p. 149
13:40-14:00 *(S8.2)*	Numerical Investigation of a Backward Facing Step Flow Controlled by a Synthetic Jet *Dionysia Voultsou, Alexandros Romeos, Alexandros Kalarakis and Athanasios Giannadakis*	Abstract p. 150
14:00-14:20 *(S8.3)*	An experimental study on the wake of a sphere having a uniaxial through-hole *Hayato Kato, Kotaro Takamure and Tomomi Uchiyama*	Abstract p. 151
14:20-14:40 *(S8.4)*	Vortical systems, generated by Darrieus and Savonius Rotors *Dmytro Redchyts, Svitlana Moiseienko, Yevhenii Shkvar and Shiju E*	Article p. 152
14:40-15:00 *(S8.5)*	The assessment of the impact of turbulence generated by wind turbines planned for construction in close proximity of high voltage power transmission lines on the wind farm location problems *Waldemar Kamrat*	Article p. 158
15:00-15:20 *(S8.6)*	Vortical flows in the wake of bluff bodies and their role in flame anchoring. *Georgios Paterakis, Konstantinos Souflas, Evangelos Panagiotis Mitsopoulos, Eleni Manouskou and Panagiotis Koutmos*	Abstract p. 168
15:20-15:40	Closing remarks	

9th International Conference on Vortex Flow Mechanics

ICVFM 2021

11-13 October 2021, Virtual Conference,
University of Patras, Greece

Proceedings

Keynote Lecture

Spyros Voutsinas
Professor
School of Mechanical Engineering
National Technical University of Athens, Greece

Faculty member of the School of Mechanical Engineering at NTUA since 1991. He received his PhD from NTUA on Unsteady Aerodynamics and carried on his career working on Aerodynamics and related topics such as Aeroelasticity and Aeroacoustics. In terms of applications his focus was on Wind Turbines and Helicopters. He has been active in numerous EU-funded projects on these topics, in four of them as coordinator.

Lecture title:
Vortex induced vibrations in aerodynamics

In aerodynamics external flows are often dominated by vorticity which is linked to the vortex structures that are formed in the wake of solid bodies. Such structures induce velocity and therefore pressure variations both back to the body where-from they are released, and to any other body on which they impinge. If in addition the solid body (or configuration) is flexible, then it is quite frequent that flow-structure interaction will lead to vibrations which under certain conditions means at least degradation of the structure or even failure.

From a practical stand point, vortex induced vibrations (VIV) are critical in many applications; e.g. helicopter rotors, wind turbines, risers, nucleal cooling etc. Also, from a theoretical/numerical point of view the topic is quite challenging due to the strong non-linear character of the interaction between the flow and the structure. While there have been important experimental works in this respect, the focus will be on the theoretical/numerical aspect of the topic. In particular, hybrid Eulerian-Lagrangian numerical solvers will be presented together with results from two cases. The method combines conventional CFD (of the finite volume type) close to the boundaries with an underlying “flow carpet” of moving particles. The specific method was first introduced as a “vortex method” but then extended to also treat compressible flows.

In terms of results, the first set, concerns the interaction of two elastically mounted cylinders in close tandem arrangement that are excited by the same flow but oscillate independently. Depending on the external conditions, different wake patterns are formed that lead to different kind of vibrations; a point that will be discussed. The second concerns the aeroelastic behaviour of a helicopter that has its blades flexible. In this respect predictions will be compared to test data taken on a scaled BO105 helicopter in the DNW tunnel.

Article S1.1

Sinusoidally heaving airfoil on an elastic hinge

Yaroslav Dynnikov[1*], Galina Dynnikova[1] , Sergey Guvernyuk[1], Tatyana Malakhova[1]

[1]*Lomonosov Moscow State University, Institue of Mechanics, Moscow, Russia*
** Corresponding Author: yaroslav.dynnikov@gmail.com*

ABSTRACT

The aerodynamics of a sinusoidally heaving airfoil on an elastic hinge is considered. The case of a lite airfoil relative to its added mass is numerically investigated. The fluid-structure interaction problem is solved in a complete conjugate formulation. Calculations are performed using the fully Lagrangian method of viscous vortex domains (VVD). A continuous medium and a moving rigid body are described as a general dynamical system without splitting into dynamic and hydrodynamic components. The mechanism of a thrust performance is investigated based on the added mass force analysis.

KEYWORDS: Flapping airfoil, Fluid-structure interaction, Viscous vortex domains method

1. INTRODUCTION

In independent studies in 1909 and 1912, Knoller [1] and Betz [2], respectively, were the first to notice that a sinusoidally heaving symmetrical wing creates thrust and lift. In work [3], The Knoller–Betz effect was investigated experimentally and reproduced numerically for a two-dimensional inviscid flow around the heaving airfoil using the discrete vortices method. Currently, there is a large number of works in which two- and three-dimensional inviscid and viscous flapping-wing aerodynamics is investigated [4]-[6]. The review [6] contains links to about three hundred works that studied a foil performing a combination of plunging and pitching oscillations numerically and experimentally. In most of the studies, the deterministic motion of a rigid airfoil in a fluid flow is considered. In works [7]-[10], the influence of elasticity on thrust and lift is studied numerically and experimentally. In these works, the reason for the production of thrust and lift is explained by the structure of vortex wakes. Hydrodynamic forces are closely related to the vorticity generation. However, the formation of vortices should be considered rather not as a cause, but as a consequence of the applied force. To numerically study the effect of elasticity on the production of thrust and lift, it is necessary to solve the coupled problem of fluid-structure interaction. In this work, it is solved by the mesh-free vortex method of Viscous Vortex Domains (VVD). The mechanism underlying the production of propulsive force is explained on the basis of the extraction and analysis of the added mass force.

2. FORMULATION OF THE PROBLEM AND METHOD OF SOLVING

We consider a two dimensional flow of a viscous incompressible fluid around the symmetrical airfoil which is formed by a circular arc forming a leading edge and two straight lines tangent to it (see Figure 1). The ratio of the arc radius R to the length L is $R/L = 0.078$. The airfoil is mounted on an elastic hinge, the axis of which is in the center of the arc. The hinge performs translational oscillation along the Y axis according to the law $y(t) = h\sin(2\pi ft)$. At the initial time (t = 0), the flow is irrotational. Fluid flow is described by the Navier–Stokes equations which is written for the vorticity ω in the form

$$\frac{\partial \omega}{\partial t} = \nabla(\mathbf{u}\omega), \quad \mathbf{u} = \mathbf{V} + \mathbf{V}_d, \quad \mathbf{V}_d = -\nu\frac{\nabla\omega}{\omega}, \qquad \boldsymbol{\omega} = \omega\mathbf{e}_z = \nabla\times\mathbf{V}, \tag{1}$$

where $\mathbf{V}$ is fluid velocity, $\mathbf{V}_d$ is so called diffusion velocity [11]. The no-slip condition is imposed on the airfoil surface.

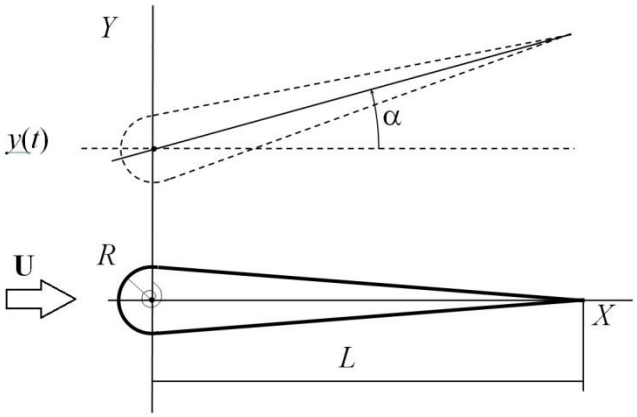

Fig. 1 The scheme of the airfoil movement

The angle α obeys the equation

$$I\ddot{\alpha} = M^{\text{hinge}} + M^{\text{inertia}} + M^{\text{hydro}}.$$

Here I is an inertia moment $I = \rho\int_s (\mathbf{r}-\mathbf{r}_0)^2\, ds$, ρ is the airfoil density, $\mathbf{r}_0$ is the hinge axis coordinate. M^{hinge} is a torque created by the hinge

$$M^{\text{hinge}} = -k\alpha,$$

where k is the hinge stiffness. M^{inertia} is

$$\mathbf{M}^{\text{inertia}} = M^{\text{inertia}}\mathbf{e}_z = (\mathbf{r}_0 - \mathbf{r}_m)\times\ddot{\mathbf{r}}_0 m,$$

where m, $\mathbf{r}_m$ are the airfoil mass and center of mass respectively.
M^{hydro} is a hydrodynamic force moment expressed via the vortex flux $\boldsymbol{\sigma}^{\text{new}} = \mathbf{n}\cdot\mathbf{V}_d\omega$ [12]

$$\mathbf{M}^{\text{hydro}} = M^{\text{hydro}}\mathbf{e}_z = \frac{\rho_f}{2}\oint_C (\mathbf{r}-\mathbf{r}_0)^2\,\boldsymbol{\sigma}_{new}\,\mathrm{d}l$$
$$+2\dot{\alpha}I_f - \ddot{\mathbf{r}}_0\times(\mathbf{r}_m-\mathbf{r}_0)m_f + \mathbf{M}_w,$$

where ρ_f, m_f, I_f are density, mass and moment of inertia of the displaced fluid respectively, M_w is moment of friction.

Numerical simulation was carried out using the Vvflow CFD software (https://github.com/vvflow/vvflow/) which is based on the Viscous Vortex Domains method (VVD) [12], [13]. The method VVD is an improved kind of the diffusion velocity method [11]. The vortex region of the flow is represented by the set of vortex particles (small domains) that move relative fluid at diffusion velocity. New vortex particles are generated at the body surfaces at each time step. The values of the new particles circulation must provide the no-slip boundary conditions. These conditions are written as linear equations relative to these values. This system of equations is supplemented by equations of body dynamics, which are linear to acceleration and the new particle's circulation. Thus, all unknown quantities are calculated simultaneously without splitting the step into hydrodynamic and dynamic parts.

3. NUMERICAL RESULTS

The calculations were performed in dimensionless parameters: $\bar{h} = h/L$, $\bar{t} = tU/L$, $\bar{\mathbf{u}} = \mathbf{u}/U$, $\mathrm{Sh} = fL/U$, $\mathrm{Re} = UL/\nu$, $\bar{\rho} = \rho/\rho_f$, $\bar{\mathbf{F}} = \mathbf{F}/(\rho_f U^2 L^2)$, $\bar{\mathbf{M}} = \mathbf{M}/(\rho_f U^2 L^3)$, $\bar{k} = k/(\rho_f U L^4)$, $\bar{m} = m/(\rho L^3)$.

Figure 2 shows the vortex wakes obtained at $\mathrm{Re} = 200,\ \ \bar{h} = 0.5,\ \ \mathrm{Sh} = 0.75$ for different values of $\bar{k}$. The wakes are asymmetric, that is similar to the experimental and numerical results obtained in [3], [4], [14] for rigid flapping airfoils. The violation of symmetry is explained in our recent work [15] by the fact that a reverse vortex street that is formed behind the flapping airfoil is unstable to bending disturbances when oscillations are intensive enough.

The wake deflection can be either up or down. It depends on the initial conditions, but not only. It was experimentally observed in [3] that wakes can switch randomly indicating that a relatively small disturbance may be sufficient to initiate the change. The bifurcation behavior of the wake was observed in [16] when frequency changed slow.

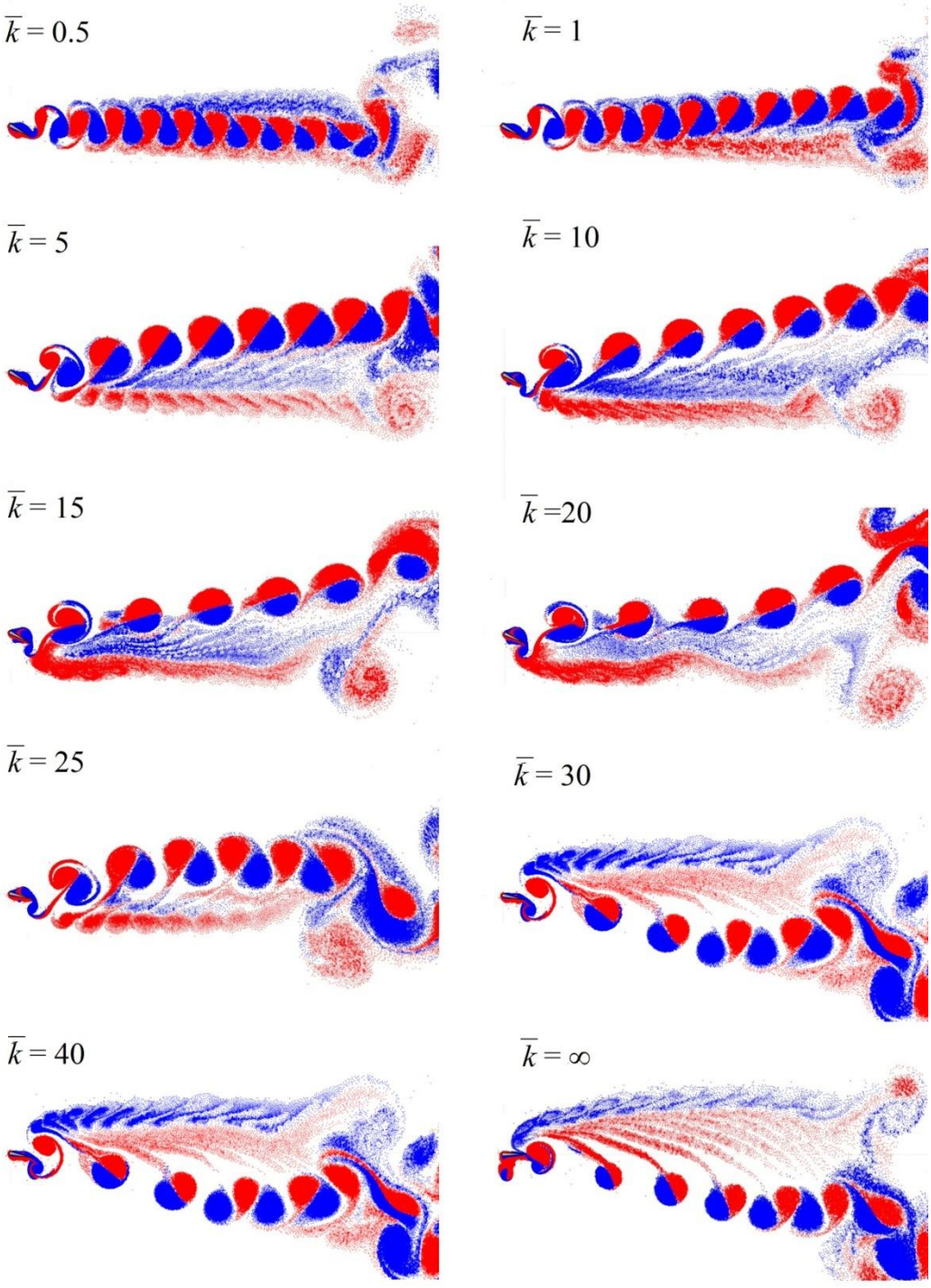

Fig. 2. The vortex wakes at $\mathrm{Re} = 200,\ \ \bar{h} = 0.5,\ \ \mathrm{Sh} = 0.75$ for different values of $\bar{k}$.

Figure 3 shows the drag force dependencies on the hinge stiffness at $\bar{h}$ = 0.5, Re = 200, $\bar{\rho}=1$, and different Sh. Negative drag force is a thrust. It can be seen that for a fixed frequency, there is a value of $\bar{k}$ at which the thrust is maximum.

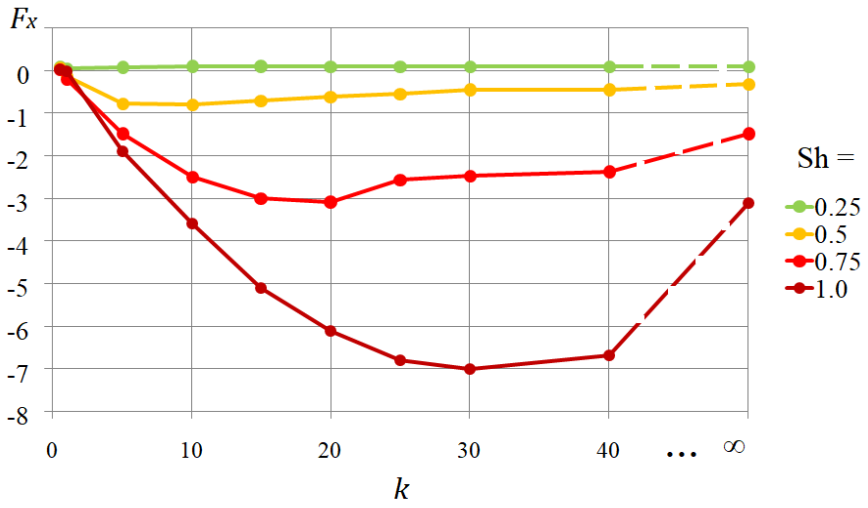

Fig. 3. Drag force dependencies on the hinge stiffness at $\bar{h}$ = 0.5, Re = 200, ρ = ρ_f.

To explain the mechanism underlying the creation of thrust, it is shown in Figure 4 the hydrodynamic force vectors obtained in the calculations and the direction of the chord of the profile at different points of the trajectory in the coordinate system associated with a stationary fluid at infinity at Re = 500, $\bar{h}$ = 0.5, Sh = 0.5.

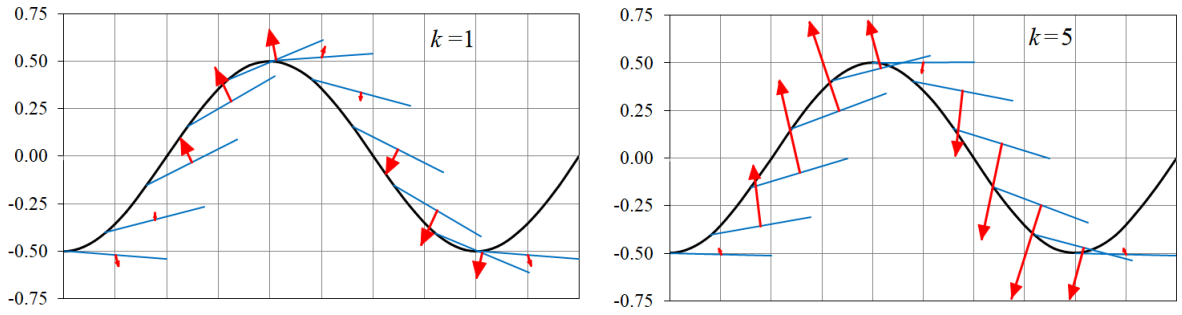

Fig. 4 Trajectory of the axis (black line), the chord direction (blue lines show dimensionless vector *OL* on a scale 1:2), and the dimensionless hydrodynamic force (red vectors are depicted on a scale of 1:10) at Re = 500, $\bar{h}$ = 0.5, Sh = 0.5.

One can see that the hydrodynamic force direction is close to the downwind normal to the chord. This is because the profile is thin. Since the profile is also deflected to the downwind side, the horizontal projection of the hydrodynamic force in all positions, except for cases where it is very small, is negative, i.e. generates thrust. The greatest contribution to thrust occurs when the airfoil moves from the trajectory's extreme points to the trajectory's midline. This is due to the influence of the force of the added masses. In work [17], it is shown that the hydrodynamic force acting on a body moving with acceleration is equal to the sum of two forces $\mathbf{F}^{\text{hydro}}=\mathbf{F}^{\text{ad}}+\mathbf{F}^{\text{st}}$. The force $\mathbf{F}^{\text{ad}}$ is equal to the added mass force acting on the body when moving with the same acceleration in an ideal potential flow. Force $\mathbf{F}^{st}$ is equal to the force acting on the body when it moves without acceleration with the same velocity distribution in space.

In the case of a thin airfoil, the direction of both forces is close to the perpendicular to the chord (see Appendix A). When moving from the top point to the midline, the force $\mathbf{F}^{ad}$ is pointing upward, since the acceleration is directed downward, and the force $\mathbf{F}^{st}$ is pointing upward too. Therefore, the modules of the forces are added up. When moving from the middle line upwards, the forces $\mathbf{F}^{ad}$ and $\mathbf{F}^{st}$ are directed in the opposite. On the middle line, the force of the added mass is close to zero, due to the absence of translational acceleration and the smallness of the angular acceleration. When moving to the top point, the added mass force increases, decreasing the total hydrodynamic force.

Comparing Figures 4a) and 4b), it can be seen that with an increase in the stiffness of the hinge, the amplitude of the angle change decreases, and the modulus of the hydrodynamic force increases. A decrease in the angle leads to a decrease in the force projection on the X-axis, and an increase in the force to an increase in thrust. These two oppositely directed processes are the reason for the existence of the optimal value of the hinge stiffness.

Unlike horizontal force, vertical force changes sign over a period. It is positive when the profile goes down and negative when it rises. If, when moving up and down, the forces change in a symmetrical manner then the mean lift is zero. When symmetry is broken, a positive or negative average lift arises.

Table 1 shows the values of the vertical component of the hydrodynamic force, averaged over the period preceding the moment corresponding to the vortex patterns in Figure. 2. As mentioned above, the direction of the averaged vertical component of the force depends on the deflection of the vortex wake.

Table 1

$\bar{k}\cdot$	0.5	1	5	10	15	20	25	30	40	∞
$\bar{F}_y^{\text{hydro}}$	-001	-0.03	0.31	0.70	0.69	0.64	0.49	-1.70	-1.35	-4.7

It seems surprising that the force F_y^{hydro} is directed to the same side as the deflection of the vortex street. But this phenomenon was also noted in work [3], where it was explained by the fact that the average value of the velocity circulation around the airfoil is negative (clockwise) when the vortex street is deflected upward. Consequently, the average value of Zhukovsky's lift is positive. This result was obtained in the framework of the ideal fluid model.

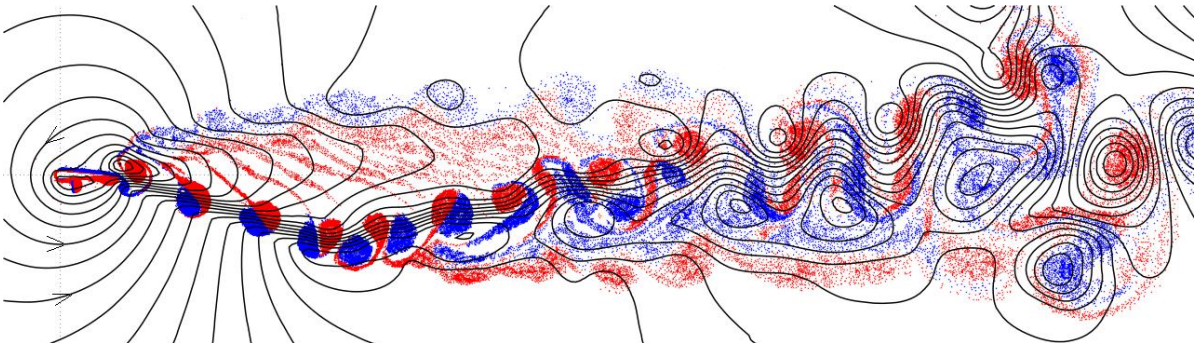

Fig. 5 The streamlines of the averaged velocity field $\mathbf{u}' = \langle\mathbf{u}\rangle - \mathbf{U}_\infty$.

In Figure 5 it is shown the streamlines of the averaged velocity field $\mathbf{u}' = \langle\mathbf{u}\rangle - \mathbf{U}_\infty$ of an asymmetric vortex street obtained in present work for the case of a flow around an airfoil performing deterministic angular oscillations with amplitude $\alpha_0 = 10°$, frequency Sh = 1.8 at Re = 1000.

Averaging is performed over one oscillation period. The figure shows that the velocity circulation around the airfoil is positive (counterclockwise). In this case, the vortex street is deflected downward, i.e. in the same direction in which the vertical component of the force is directed. Thus, the conclusion of work [3] is confirmed.

4. CONCLUSIONS

The flow-structure interaction problem is solved for a symmetrical airfoil performing translational heaving and passive pitching on an elastic hinge when the airfoil mass is much less than its added mass. The solution method is monolithic, based on the mesh-free method of viscous vortex domains. The role of the added mass force in the generation of the propulsive force is shown. The physical mechanism underlying the thrust and lift is revealed. The influence of the hinge stiffness on the thrust is explained.

ACKNOWLEDGMENT

The authors wish to acknowledge supports from the Lomonosov Moscow State University, Russian Federation.

APPENDIX A: Added mass force

The added mass force is expressed via the added mass tensor. In the case of two-dimensional flows it is

$$\begin{pmatrix} F_x^{ad} \\ F_y^{ad} \\ M^{ad} \end{pmatrix} = -\mathbf{\Lambda} \begin{pmatrix} \ddot{x} \\ \ddot{y} \\ \ddot{\alpha} \end{pmatrix} = - \begin{pmatrix} \lambda_{xx} & \lambda_{xy} & \lambda_{x\alpha} \\ \lambda_{yx} & \lambda_{yy} & \lambda_{y\alpha} \\ \lambda_{\alpha x} & \lambda_{\alpha y} & \lambda_{\alpha\alpha} \end{pmatrix} \begin{pmatrix} \ddot{x} \\ \ddot{y} \\ \ddot{\alpha} \end{pmatrix}, \tag{A1}$$

In the coordinate system shown in Figure 1, the matrix Λ can be expressed via matrix Λ', which is calculated in the coordinate system attached to the body

$$\mathbf{\Lambda} = \begin{pmatrix} \cos\alpha & -\sin\alpha & 0 \\ \sin\alpha & \cos\alpha & 0 \\ 0 & 0 & 1 \end{pmatrix} \cdot \begin{pmatrix} \lambda_{x'x'} & \lambda_{x'y'} & \lambda_{x'\alpha} \\ \lambda_{y'x'} & \lambda_{y'y'} & \lambda_{y'\alpha} \\ \lambda_{\alpha x'} & \lambda_{\alpha y'} & \lambda_{\alpha\alpha} \end{pmatrix} \cdot \begin{pmatrix} \cos\alpha & \sin\alpha & 0 \\ -\sin\alpha & \cos\alpha & 0 \\ 0 & 0 & 1 \end{pmatrix}. \tag{A2}$$

For the considered airfoil, the dimensionless coefficients of the matrix Λ' are

$$\lambda_{x'x'} = 0.017,\ \lambda_{y'y'} = 0.96,\ \lambda_{\alpha\alpha} = 0.16,$$
$$\lambda_{x'y'} = \lambda_{y'x'} = \lambda_{x'\alpha} = \lambda_{\alpha x'} = 0,\ \lambda_{y'\alpha} = \lambda_{\alpha y'} = 0.43.$$

Substituting these values into (A2) and (A1) we obtain

$$\begin{aligned} F_x^{ad} &= 0.943\ddot{y}\cos\alpha\sin\alpha + 0.43\ddot{\alpha}\sin\alpha \\ F_y^{ad} &= -\left(0.017 + 0.943\cos^2\alpha\right)\ddot{y} - 0.43\ddot{\alpha}\cos\alpha \\ M^{ad} &= 0.43\ddot{y}\cos\alpha + 0.16\ddot{\alpha} \end{aligned}$$

If we neglect the value 0.017 in comparison with $0.943\cos^2\alpha$, we get

$$F_x^{ad} = F\sin\alpha$$
$$F_y^{ad} \approx -F\cos\alpha$$
$$F = 0.943\ddot{y}\cos\alpha + 0.43\ddot{\alpha}$$

From here, it can be seen that the direction of the vector $\mathbf{F}^{ad}$ is close to the perpendicular to the chord.

REFERENCE

[1] Knoller R., Die Gesetze des Luftwiderstandes, Flug- und Motortechnik (Wien) 1909, **3**(21): 1–7.
[2] Betz A., Ein Beitrag zur Erklarung des Segel uges, Zeitschrift fur Flugtechnik und Motorluftschiffahrt, 1912, **3**(1): 269–272.
[3] Jones K.D., Dohring C.M., and Platzer M. F. Experimental and Computational Investigation of the Knoller–Betz Effect. AIAA Journal 1998, 36(7).
[4] Platzer M.F. and Jones K.D. Flapping-wing aerodynamics: progress and challenges. AIAA Journal 2008, 46(9).
[5] Xiao Q.; Zhu Q. A review on flow energy harvesters based on flapping foils. J. Fluids Struct. 2014, 46, 174–191
[6] Wu X., Zhang X, Tian X, Li X., Lu W. A review on fluid dynamics of flapping foils. Ocean Engineering, 2020, **195** 106712. https://doi.org/10.1016/j.oceaneng.2019.106712.
[7] Brousseau P.; Benaouicha M.; Guillou S. Dynamics of a Free Heaving and Prescribed Pitching Hydrofoil in a Turbulent Flow, with a Fluid-Structure Interaction Approach. In Proceedings of the ASME 2018 Pressure Vessels and Piping Conference, Prague, Czech Republic, 15–19 July 2018: p. 9.
[8] Marais C., Thiria B., Wesfreid J. E., Godoy-Diana R.. Stabilizing effect of flexibility in the wake of a flapping foil. Journal of Fluid Mechanics, 2012, **710**, 659–669.
[9] Zeyghami S., Zhong Q., Liu G., and Dong H. Passive Pitching of a Flapping Wing in Turning Flight. AIAA Journal 57(1): 1-9. DOI:10.2514/1.J056622
[10] Brousseau, P.; Benaouicha, M.; Guillou, S. Hydrodynamic Efficiency Analysis of a Flexible Hydrofoil Oscillating in a Moderate Reynolds Number Fluid Flow. Energies, 2021, 14, 4370. https:// doi.org/10.3390/en14144370
[11] Ogami Y., Akamatsu T., Viscous flow simulation using the discrete vortex method – the diffusion velocity method. Computers & Fluids. 1991, 19, (¾), 433–441. DOI: https://doi.org/10.1016/0045-7930(91)90068-S
[12] Andronov P.R., Grigorenko D.A., Guvernyuk S.V., Dynnikova G.Ya. Numerical simulation of plate autorotation in a viscous fluid flow. Fluid Dynamics. 2007, 42, (5), 719–731. DOI: 10.1134/S0015462807050055
[13] Andronov P. R., Dynnikov Y. A., Dynnikova G. Y., Guvernyuk S. V. Flow-induced oscillations of circular cylinder in a narrow channel. Aerospace Science and Technology. 2019, 93, 105348: 1–5. **DOI:** 10.1016/j.ast.2019.105348
[14] Godoy-Diana R., Aider J. L., Wesfreid J. E.. Transitions in the wake of a flapping foil. Phys. Rev. E 2008, **77**, 016308.
[15] Dynnikova G. Y., Dynnikov Y. A., Guvernyuk S. V., Malakhova T. V. Stability of a reverse Karman vortex street. Physics of Fluids. 2021, **33**(2), 024102–1–024102–10. **DOI:** 10.1063/5.0035575
[16] Cleaver, D., Wang, Z., & Gursul, I. (2012). Bifurcating flows of plunging aerofoils at high Strouhal numbers. Journal of Fluid Mechanics, 708, 349-376. doi:10.1017/jfm.2012.314
[17] Dynnikova G. Y. Added mass in a model of a viscous incompressible fluid, Doklady Physics. 2019, **64**(10): 397-400. **DOI:** 10.1134/S1028335819100045

Resonant vortex-wake forces on circular cylinders

Efstathios Konstantinidis[1*]

[1]*University of Western Macedonia, Department of Mechanical Engineering, Bakola & Sialvera, 50132, Kozani, Greece*
** Corresponding Author:ekonstantinidis@uowm.gr*

The fluid loading on bluff bodies depends strongly on the wake being at a resonant state, which may occur when the flow is excited by some external disturbance, or when the body undergoes flow-induced vibration. Modeling and prediction of the flow-induced forces on bluff bodies still poses a major challenge because different physical mechanisms are not fully accounted for. In this study, we attempt to shed light into these mechanisms by looking into the elemental- volume contributions of the vorticity to the integrated forces on a circular cylinder using the decomposition by Chang [1], which has its origin in the work of Quartapelle and Napolitano [2].

In this study, we consider a fixed body in a time-dependent free stream, a case that provides a generalized framework to uncover the elemental force contributions in resonant wakes. Flow data were produced by two-dimensional simulations using an in-house finite-volume code on an orthogonal curvilinear mesh [3]. The freestream velocity far upstream oscillates harmonically as $U(t) = U_0 + \Delta U \cos(\omega t)$ at a maximum Reynolds number of 180 based on the instantaneous velocity. The problem is described by two dimensionless parameters, i.e. the frequency and velocity ratios

$$\omega_r = \frac{\omega}{4\pi f_{v0}} \qquad \varepsilon_r = \frac{\Delta U}{U_0} \tag{1}$$

where f_{v0} is the frequency of vortex shedding in steady flow of the same average Reynolds number.

Assuming a potential velocity field $\boldsymbol{u} = \nabla\Phi$ the contribution of vorticity within the fluid to the force acting on the body can be expressed as

$$-\frac{\rho}{U}\int_{V_f} \boldsymbol{u} \otimes \boldsymbol{\omega} \cdot \nabla\Phi \; \mathrm{d}V \tag{2}$$

where $\boldsymbol{\omega}$ is the vorticity vector and the integral is computed over the entire fluid domain. The integrant quantity represents the elemental-volume force. In two dimensions, we can calculate the elemental-volume forces in the drag and lift directions, δ_{Dv} and δ_{Lv} respectively such that the integrated vortex-drag force is given by

$$F_{Dv} = \rho\int_{V_f} \delta_{Dv} \; \mathrm{d}V \tag{3}$$

and the integrated vortex-lift force is given by

$$F_{Lv} = \rho\int_{V_f} \delta_{Lv} \; \mathrm{d}V \tag{4}$$

It should be noted that the fluid forces also include contributions from inviscid inertia and skin friction (for details see [1]).

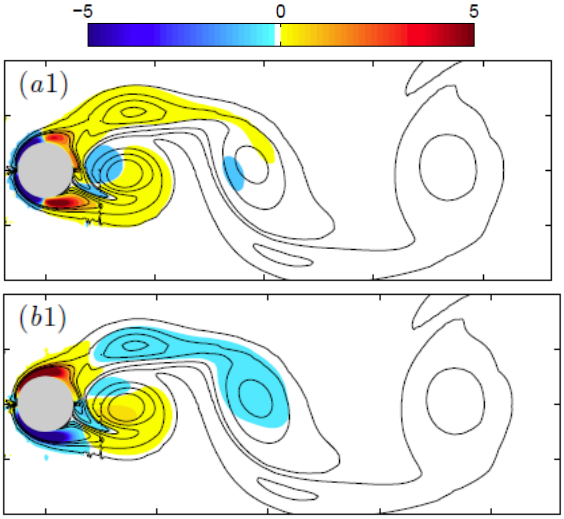

Fig. 1: Contour lines of planar vorticity juxtaposed with elemental-volume force distributions of ($a1$) drag δ_{Dv} and ($b1$) lift δ_{Lv}. Values are normalized with $\frac{1}{2}\rho U_0^2 d$. Run $(\omega_r, \varepsilon_r) = (0.669, 0.333)$.

Fig. 1 shows the instantaneous distributions of δ_{Dv} and δ_{Lv} in the resonant wake at relatively high amplitude. It can be seen that high δ_{Dv} and δ_{Lv} values appear in the region of attached flow around the surface whereas the contribution of wake vortices decreases rapidly with the distance from the body. By analyzing several snapshots over the entire cycle of vortex shedding, we see the variation of elemental force contributions from different flow regions and can explain the origin of double peaks in the time history of the lift force. There is one component that scales with $\sim U(t)$ and another one whose phase is determined by the timing of vortex shedding. Furthermore, the present results gives credence to the in-line force (drag) model proposed recently in [4].

References

[1] Chang, C. C. Potential flow and forces for incompressible viscous flow. Proceedings of the Royal Society of London. Series A: Mathematical and Physical Sciences, 1992, 437: 517-525.

[2] Quartapelle, L., Napolitano, M. Force and moment in incompressible flows. AIAA Journal 1983, 21: 911-913.

[3] Konstantinidis, E., Bouris, D., Vortex synchronization in the cylinder wake due to harmonic and non-harmonic perturbations. Journal of Fluid Mechanics, 2016, 804:248-277.

[4] Konstantinidis, E., Dorogi, D., Baranyi, L. Resonance in vortex-induced in-line vibration at low Reynolds numbers. Journal of Fluid Mechanics, 2021, 907: A34.

Article S1.3

A Computer Aided Optimizing Design for Drone Rotors

Daichi Yoshidome[1*], Norihiko Watanabe[1]

[1]Sojo University, Ikeda 4-22-1, Kumamoto City, 860-0082, Japan
** Corresponding Author: nwatanabe@mec.sojo-u.ac.jp*

ABSTRACT

In recent years, Multirotor UAVs (drones) have been expected to play an active role in various fields, However, the design method of drones for flexibly respond to various requirement would be necessary for more widely applications. One of such design methods is a combination of numerical optimization and computational fluid dynamics (CFD). A rotor shape that can be silent while maintaining as high a lift as possible using CFD and numerical optimization with lift and noise as objective functions, assuming that the drone will be applied to a residential environment. Additionally, discussions will be performed for the cause of the different tendency in the noise value between the analytical and experimental values, which was found in the verification experiments for two optimal solutions obtained by the optimization. As a result, it was found that the evaluation method of using the volume of the isosurface of the sound pressure level (SPL) as the noise level in the analysis did not select a suitable SPL because the evaluation tendency was different depending on the selected SPL. Also, Also, the relationship between the design parameters and the objective function was discussed from the CFD results of the optimal solution . Then, it was confirmed that there is a relationship between the angle of attack at the middle-section and the angle of attack at the outer cross-section of the wing. The noise distribution at the wing tip was reduced when former angle becomes large, and later angle becomes small.

KEYWORDS: Drones, CFD, CAD, Numerical optimization, Aerodynamical noise.

1. INTRODUCTION

Recently, drones have been used in a variety of fields, especially in industrial applications and disaster relief. However, if the application of drones expands further in the future, it will be necessary to design drones in consideration of various factors depending on the environment, and the design cost is expected to increase. Therefore, it is thought that a flexible and efficient design method will be required for the rotor design of drones in the future.

One effective method is a design method that combines CFD and numerical optimization technology, which have been used in a variety of fields in recent years. In the past, there has been an example of an optimal design of a rotor shape for a drone using CFD and optimization methods that considered both power and flight performance by using the torque coefficient and thrust coefficient as objective functions[1].

Present study shows a design way for a rotor shape that is quiet while maintaining as high lift as possible by using CFD and numerical optimization with lift and noise as objective functions, assuming that the drone will be applied to a residential environment. The verification experiments are also conducted for two of the optimal solutions obtained by optimization, and the results are discussed. Furthermore, the CFD results of the two optimal solutions are used to discuss the relationship between the design parameters and the objective function based on fluid phenomena.

2. METHODOLOGY

2.1 PRESENT DESIGN PROCEDURE

Fig. 1 shows the workflow of the optimal design. At first, the rotor to be designed is analyzed to determine the design parameters that are highly related to the objective functions and their ranges. Next, sampling is performed to select the samples to be studied for optimization, and CFD analysis is performed on the sampling models. A response surface representing the relationship between the design parameters and the objective function was created from the results of the analysis. Finally, multi-objective optimization will be performed to design the optimal rotor shape from the response surface.

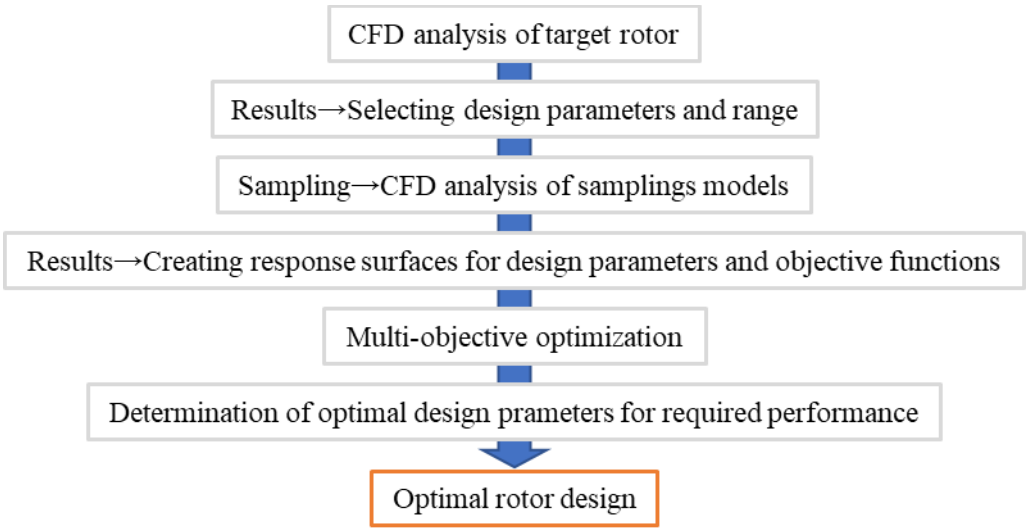

Fig. 1 Workflow of the optimal design

2.2 ROTOR MODEL TO BE DESIGNED

A hobby drone HS110D (Holy Stone Enterprise Co., Ltd.) was adopted as a design model. The root cross-section, middle cross-section, and outer cross-section of this rotor were measured using calipers and micrometers, and the wing cross-section shape was reconstructed based on the Joukowski wing to create a reference 3D model. Fig. 2 shows the appearance of the drone and the schematic rotor shape.

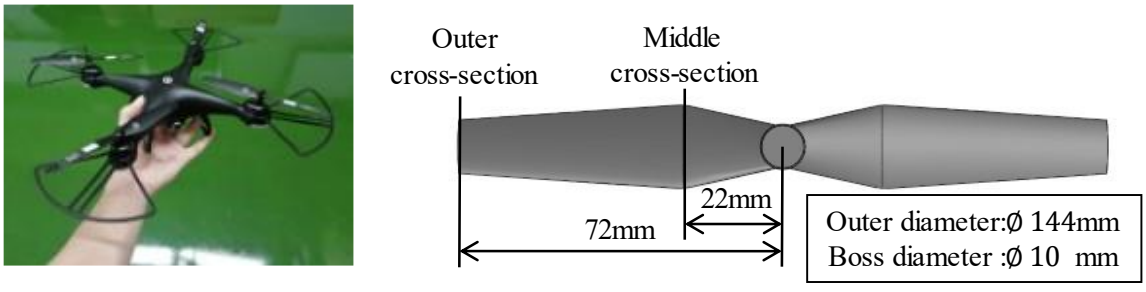

Fig. 2 Drone exterior and Schematic rotor shape

2.3 NUMERICAL ANALYSIS

CFD analysis was performed using commercial thermo-fluid analysis software SCRYU/Tetra Version 14 (Software Cradle Co., Ltd.). This software uses the finite volume method with an unstructured grid. The fluid was assumed to be uncompressed air, and the basic equation is the Navier-Stokes equation. The analysis model assumes that the target drone is hovering at 1250mm above the ground, and the analysis space is divided into four sections at the center of the drone because the drone shape is symmetrical. The rotation of the rotor wing was completely simulated by the sliding mesh technique.

The major analysis conditions are shown in Table 1. Figure 3-A and 3-B show the stationary and rotating part of the computational domain. Figure 3-C shows boundary conditions and rotating area position. and Fig. 3-D shows the computational mesh for the entire region and around the wing section.

Table 1 Analysis conditions

Flow	Turbulence flow
Turbulence model	RANS SST k-ω
Analysis method	Initial steady analysis 1000 cycle Unsteady analysis 8640 cycle (Calculation after steady analysis)
Time size	4.529×10^{-6}s (Equivalent to 3 rotations)
Rotational speed	4600rpm
Element number	≈13 million
Node number	≈3 million

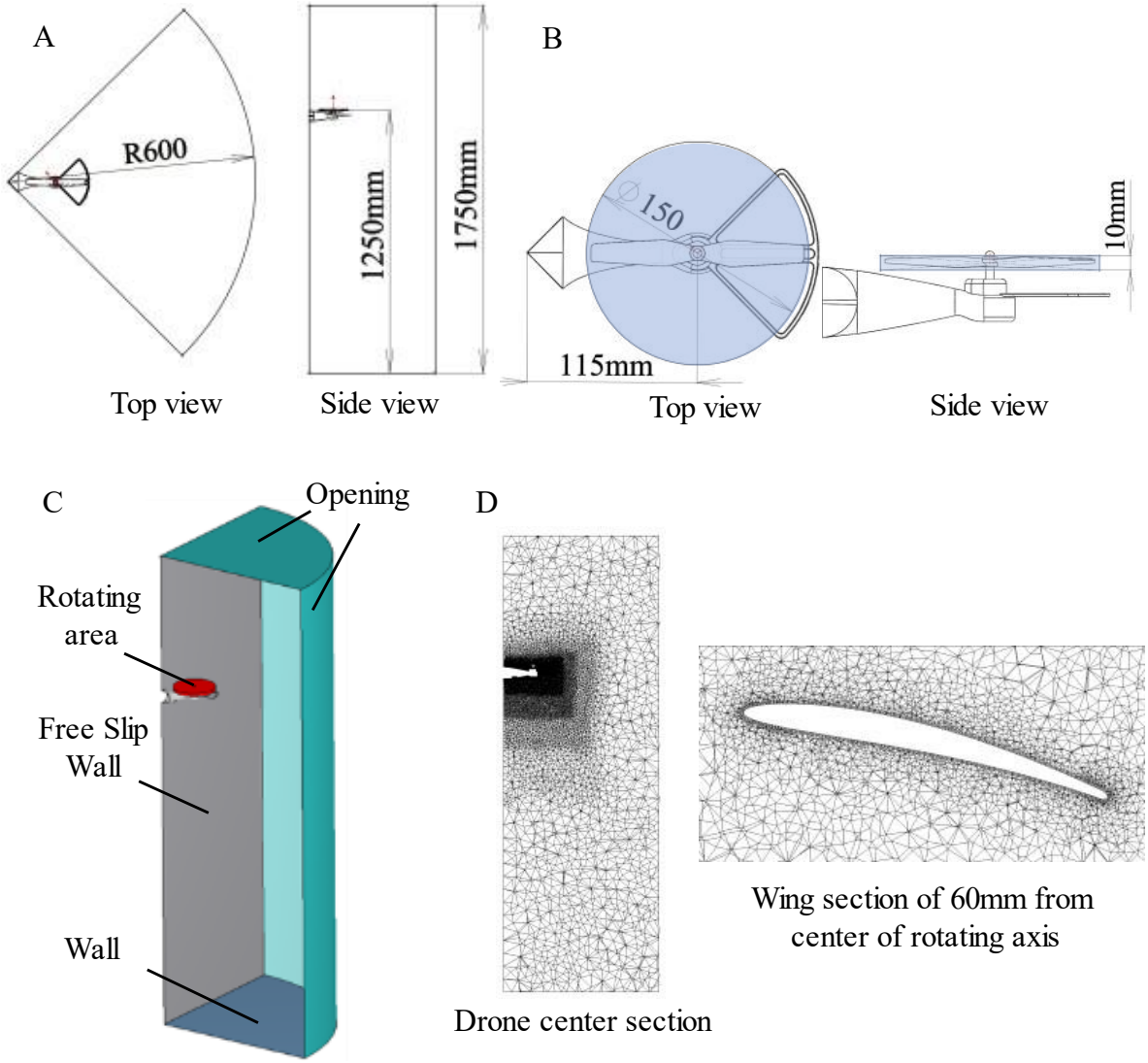

Fig. 3 A: Computational domain of the static area. B: Computational domain of the rotating area. C: Boundary conditions and rotating area position. D: Computational mesh system

2.4 NOISE LEVEL EVALUATION

The Proudman model [2] to evaluate the aerodynamic noise, which can calculate the SPL of the source using the turbulent energy and the turbulent loss rate. The Proudman model is defined as

$$SPL = 10\,log\left(\frac{\alpha\rho\varepsilon Ms^5}{P_{ref}}\right)\ [\mathrm{dB}], \quad \text{where } Ms = \frac{\sqrt{2k}}{c} \tag{1}$$

where ρ is the air density, ε is the turbulent dissipation rate, k is the turbulent energy, c is the sound velocity, α is the model coefficient, and P_{ref} is the reference sound pressure of 10^{-12} [Pa]. The model coefficient α is chosen as 0.1 based on the work of Sarkar et al [3]. One of the features of this model is that the SPL can be evaluated directly from the turbulence analysis results by CFD. Fig. 4-A shows an example of the CFD results. Velocity distribution near the rotor and the sound pressure level distribution can be seem.

The Proudman model calculates the SPL generated from an local observation point. Thus, it is difficult to calculate the total SPL including the propagation from the surroundings of an any observation point. So the volumetric amount of space above a specific SPL was used as the index of the noise level to compare experimental observation.

Since the SPL in a residential area is about 40 dB, the regions of this and higher SPL can be considered as the noisy space.

The volume of spaces with SPLs higher than 40 dB is chosen as an index of the noise magnitude of the system, by shown in Fig.4-B. This index will be called as the noise level, in the present study.

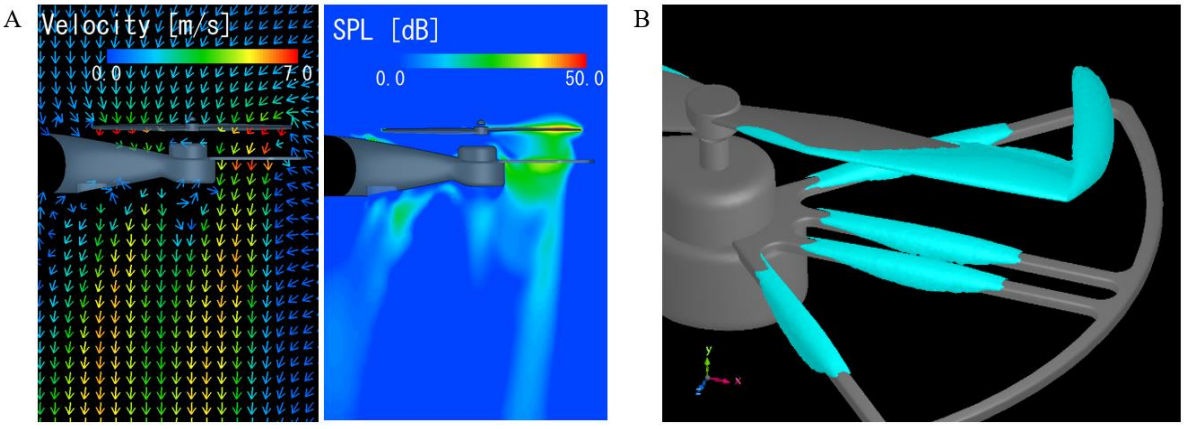

Fig. 4 A: Velocity vectors and SPL distributions on the center section of drone. B: Volumetric regions on the SPL over 40 dB

2.5 NUMARICAL OPTIMIZATION

The numerical optimization was performed using a commercial multi-objective optimization software EOopti (Software Cradle Co., Ltd.), which uses the following methods in each of the optimization calculation processes

Sampling: Latin Hypercube Sampling [4]
Response surface method: Kriging method [5]
Optimal solution calculation: Multi-objective genetic algorithm (MOGA) [6]

The eight design parameters were considered in advance. These parameters were evaluated for selection based on three points: high contribution to the objective function, low noise increase for lift increase, and high noise decrease for lift decrease. As a result, three parameters were selected: the angle of attack at the middle cross-section (mid angle), the camber of the wing at the middle cross-section (mid camber), and the angle of attack of the wing at the outer cross-section (out angle). Camber is a measure of the

curvature of the wing shape and is one of the two variables that define a Joukowski wing and is a dimensionless number. The design parameters ranged from 5 to 25 degrees for the mid angle, 0.00 to 0.35 for the mid camber, and 0 to 15 degrees for the out angle. These ranges were set in consideration of the wing stall and other factors. Fig. 5 shows a schematic illustration of the design parameters.
The sampling number was set to 50 to ensure sufficient accuracy in optimization. Objective function of present optimization was set to lift and noise level, and it was a multi-objective optimization problem to search for the condition that maximizes lift and minimizes noise level.

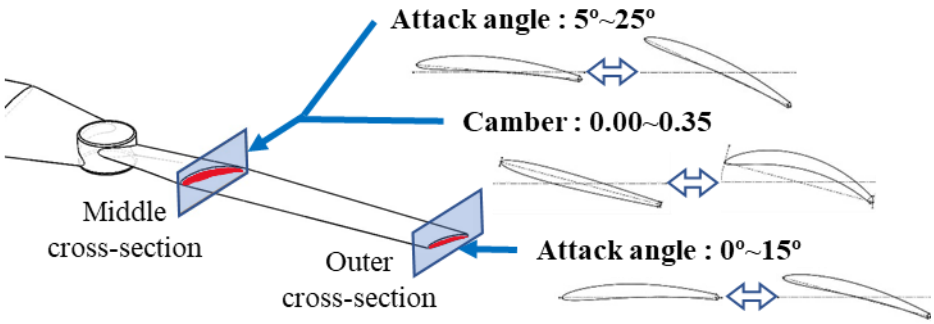

Fig. 5 Design parameters

2.6 NOISE AND LIFT MEASUREMENT

The rotors were made with a 3D printer for each of the optimal solutions A and B, which will be described later, and lift and noise measurement experiments were conducted.
On the other hand, the weight was added to the drone, and the lift was measured with the weight until the rotation speed during hovering reached 5400 rpm, which is the rotation speed with low lift value. A laser tachometer (DT2236B) was used to measure the rotation speed.
In the noise measurement, the drone was hovered at 1250mm above the ground and the sound level meter (CENTER 322) was placed at 1000mm horizontally from the drone in order to measure the noise of the drone in a similar condition of CFD analysis. The measurement was carried out for 30 seconds with a weight added and the rotation speed set at 5,400 rpm as in the lift force measurement, and the average value was used as the noise value. Fig. 6 shows a position of sound level meter and drone during noise measurement.

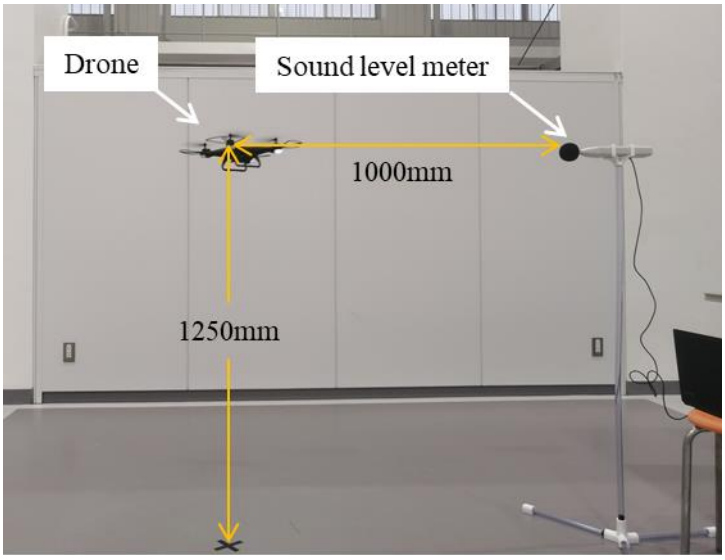

Fig. 6 Position of noise meter and drone

3. RESULTS AND DISCUSSIONS

3.1 COMPARISON OF EXPERIMENTAL RESULTS AND CFD ANALYSIS

Fig. 6 shows the optimal solution distribution diagram obtained by the optimization. The horizontal and vertical axis are the lift and noise level respectively. The dot points on the figure are the 1024 candidate optimal solutions obtained as result of multi-objective optimization. When the color changes from red to green to blue, the solution becomes more optimal for the objective and the set of blue points indicates the Pareto front.

The solution A which has small lift and low noise level, and the solution B which has medium lift and medium noise level, were selected to verify the optimization result, as shown in Fig. 6.

Previous study [7] suggested that the optimization in the low noise part of the optimization distribution may not have been done well, because a large difference in the noise value of solution A was observed by comparing the value on the optimal solution distribution with the CFD analysis. To obtain the confirmation, CFD analysis and experimental measurements of lift and noise were conducted and compared.

Fig. 7 shows the experimental and analytical results of solutions A and B. The left graph is the lift, and the right one is the noise level. Experimental result of the noise shows the observed sound pressure level, and the analysis result shows the noise level which was determined on previous section.

It could be seen that an inverse trend between the experimental and analytical values for noise level. This result seems to be suggested one of difficulty of optimization on the low-noise part.

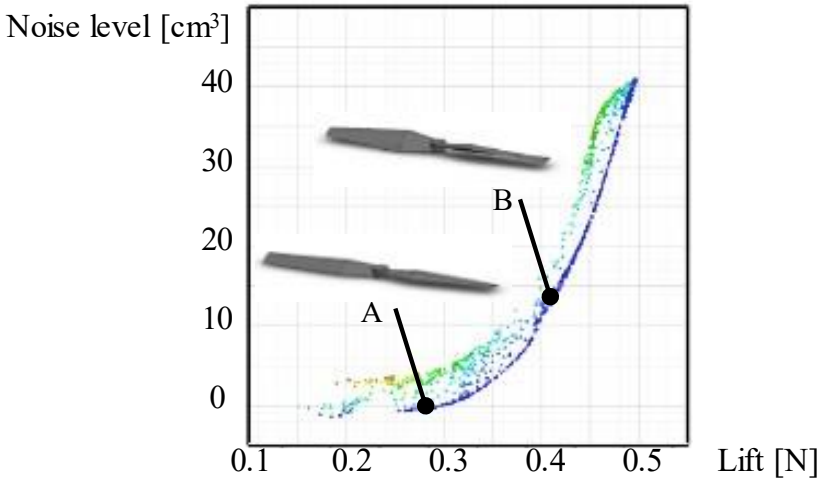

Fig. 6 Optimal solution distribution

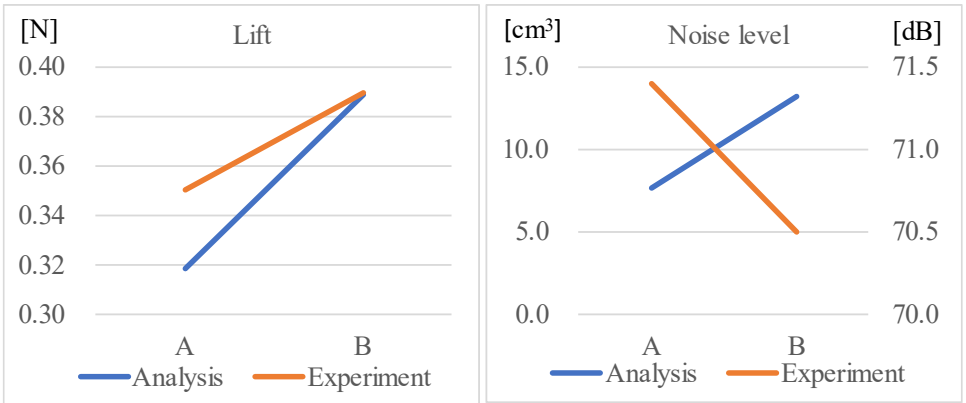

Fig. 7 Comparison of experimental and analytical values (Left: Lift, Right: Noise level)

To investigate the cause of the difference between the experimental and analytical trends in noise level, the SPL of the noise evaluation by the volumetric amount of the isosurface of SPL was varied to investigate the change in noise evaluation.
The sum total of solution A and solution B is set to 100%, and they are compared in proportion to each other, to match the indexes for the evaluated values from the analysis and the experimental values.
It can be seen in Fig. 8 that the tendency of the noise levels changes with each SPL, and the tendency is similar to the experimental values after 55 dB. This suggests that the noise source from the rotor was measured to be 55 dB or higher in this experimental environment. Therefore, the selection of a suitable SPL is considered necessary for the noise evaluation by the amount of SPL volume, and this fact can be considered as one of the reasons for the difference of tendency.

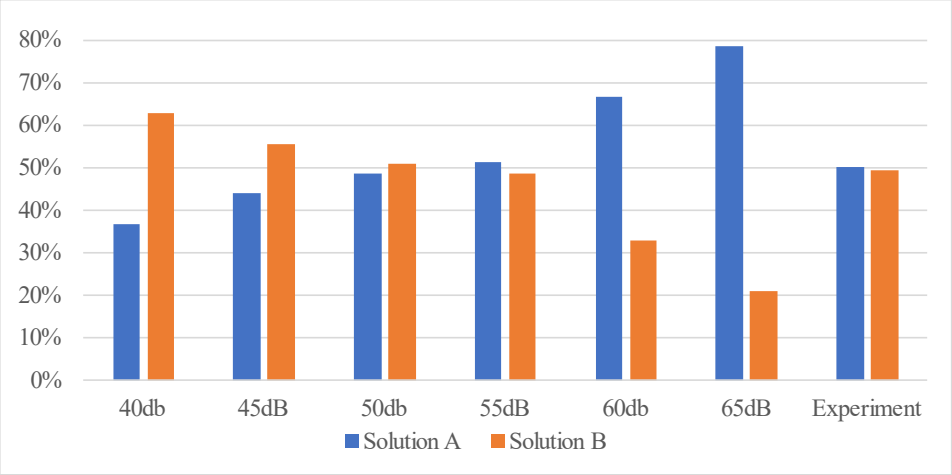

Fig. 8 Trends in noise evaluation with changes in evaluation SPL

3.2 RELATIONSHIP BETWEEN NOISE LEVEL AND DESIGN PARAMETERS

The solution B has a higher lift value of 0.04 N and a lower noise value of 0.9 dB than solution A, on the Table 2. Therefore, solution B is the best solution for the objective than solution A. This will be discussed using CFD analysis in terms of the relationship between noise and the design parameters. The noise evaluation in the CFD analysis was based on the volume of the isosurfaces with an SPL of 55 dB, which was most similar to the experimental trend
Figure 9 shows the noise distributions of solutions A and B. Comparing the noise distributions from Fig. 9, there is a change in the distribution at the wing tip and rotor guard, and the noise level at the wing tip is reduced in Solution B. This result exhibits the reduction in noise distribution at the wing tip is one of the factors that made Solution B optimal for the objective. The relationship between the noise at the blade tip and the design parameters is discussed in the following subsections.

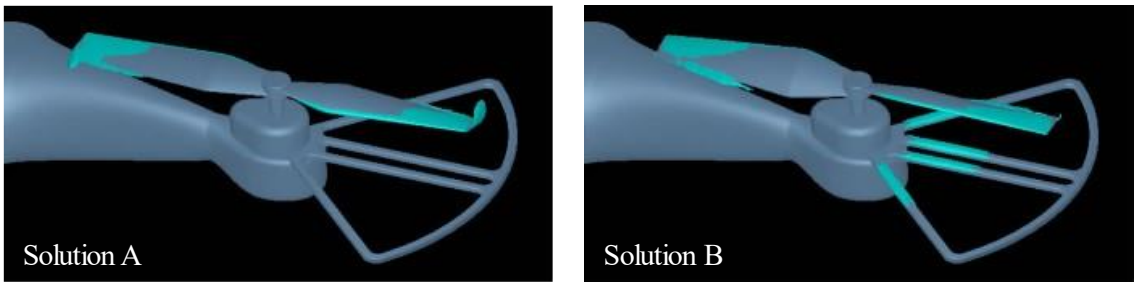

Fig. 9 Noise distributions around rotor

3.2.1 Noise distribution at wing tip.

The CFD analysis results are discussed in detail to clarify the cause of the noise distribution at the wing tip. Fig. 10 exhibits the pressure distribution at 3 mm intervals on the wing tip of solution A. The white translucent isosurface is the vorticity distribution with a vorticity of 7500 s^{-1}. There is a correlation between the pressure distribution and the isosurface distribution of vorticity, and the generation of wing tip vortex could be captured in the CFD analysis.

Figure 11 shows the vorticity and velocity distributions at 3 mm intervals at the wing tip of solution A. The translucent white isosurface of each is the noise distribution at 55 dB. Comparing the vorticity and velocity distributions in Fig. 11, the shape of the vorticity distribution is not very close to the isosurface distribution of the noise, while the isosurface distribution of the velocity distribution is close to the isosurface distribution of the noise. These results suggests that the noise is caused particular strongly by the flow component of the wing tip vortex.

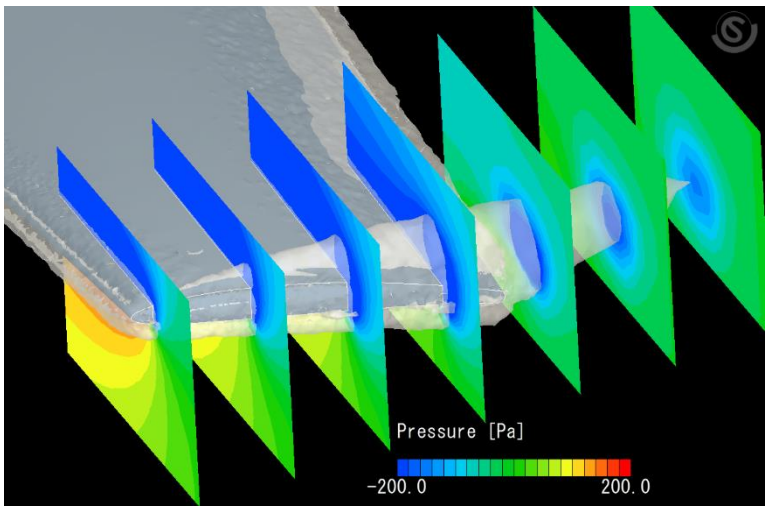

Fig. 10 Pressure distribution at 3 mm intervals on the wing tip and vorticity distribution

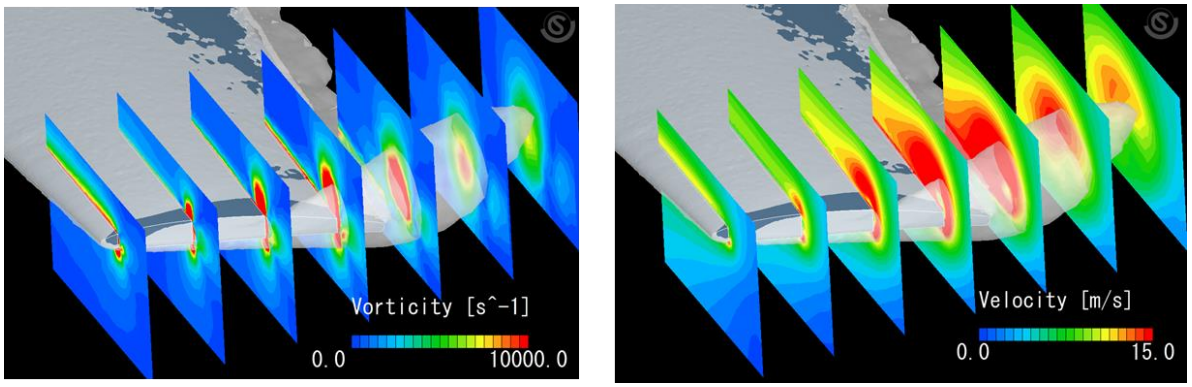

Fig. 11 Distribution of 3 mm intervals at wing tip and 55 dB noise distribution (Left: Vorticity Right: Velocity)

On the other hand, the velocity distribution, and its vectors at 3 mm intervals in solution A is shown in Fig.12. The white translucent surface is the noise distribution at 55 dB. Figure 12 shows that the noise distribution is proportional to the velocity distribution from the under of the wing to the wing tip side. This suggests that the noise at the wing tip is strongly caused by the velocity of the wing tip vortex, especially from the under of the wing to the wing tip side.

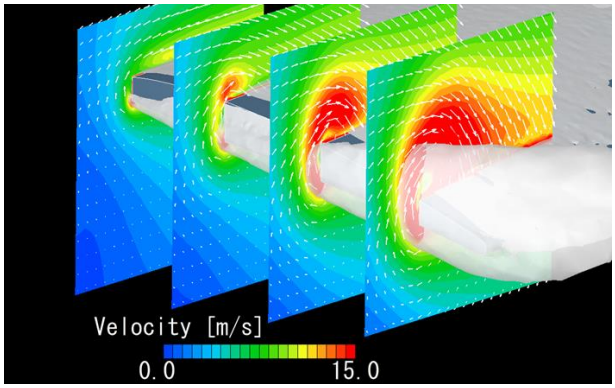

Fig. 12 Velocity and these vectors at 3 mm intervals on the wing tip and 55 dB noise distribution

3.2.2 Relationship between noise distribution at wing tip and design parameters.

Table 2 shows the design parameters for solution A and solution B. Comparing the respective design parameters, the mid angle and the out angle changed significantly, and these two design parameters are responsible for the change in noise at the wing tip. That is also for the velocity distribution from the under of the wing to the wing tip side.

Table 2 Design parameters for each rotor

	mid camber [-]	mid angle [deg]	out angle [deg]
A	0.35	5.6	14.9
B	0.35	25.0	4.0

Figure 13 and 14 show the velocity and pressure distributions on the rotor center section for solutions A and B. Comparing Figure 13 and 14, it can be seen that the distributions of both solutions almost coincide with the part of the velocity of 15 m/s and the pressure of -200 Pa at the wing tip. The negative pressure distribution on the upper surface of the wing is distributed up to the under of the wing tip, and the velocity increases from the under of the wing to the wing tip side. The velocity increasing is considered as a cause of noise generation at the wing tip.

Table 2 also shows that solution A has a smaller mid angle and a larger outer angle than solution B. Therefore, solution A has a wing shape that gradually increases in angle of attack toward the wing tip. This wing shape has the pressure distribution shown in Fig. 14, the negative pressure distribution on the upper surface of the wing is biased to the wing tip, and the negative pressure area is distributed to the under of the wing. As a result, noise distribution is considered to have occurred at the wing tip in solution A. On the other hand, wing shape of solution B has the opposite tendency to that of solution A, the negative pressure distribution on the upper surface of the wing was closer to the center of the wing, and the negative pressure distribution was not distributed to the under part of the wing, so the noise distribution might be suppressed.

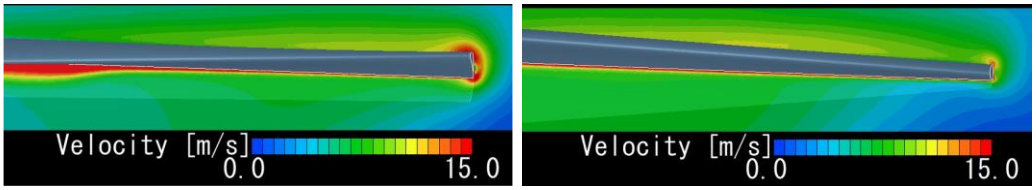

Fig. 13 Velocity distribution on the center section of the rotor (Left: Solution A. Right: Solution B)

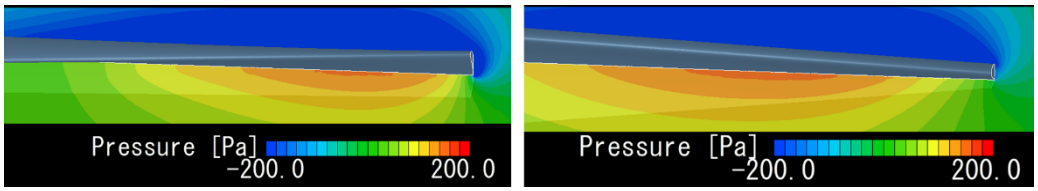

Fig. 14 Pressure distribution on the center section of the rotor (Left: Solution A. Right: Solution B)

The wing shape of the noise reduction through optimization was discussed, and it was confirmed that it was caused by the wing tip vortex, which is generally considered as the source of energy loss of the wing.

4. CONCLUSION

Present paper mentioned about an optimizing design for rotor shape by using CFD and numerical optimization to make the drone quieter. A validation experiment of the optimization was performed and discussed on the relationship between the objective function and the design parameters from the CFD analysis results through comparisons with experimental results. Concluding remarks are itemized as follows.

(1) Selecting a suitable SPL according to the actual environment is necessary to evaluate the volumetric amount of space above a specific SPL as the index of the noise level noise in CFD analysis.
(2) Clearly correlation between the angle of attack at the middle-section and the angle of attack at the outer cross-section of the wing existed on noise generation. The noise distribution at the wing tip was reduced when former angle becomes large, and later angle becomes small.

A present optimal design might be expected as one of the effectively realized design methods through the series of discussions. As the future work, the optimization will be performed and verified in noise evaluation with suitable SPL, and in addition, optimization for more objective functions and design parameters will be performed to further enhance the usefulness of the optimal design.

REFERENCE

[1] Lee H.M. et al., "Aerodynamic Design Optimization of UAV Rotor Blades using a Genetic Algorithm", Journal of computational fluids engineering 19-3, (2014), pp.29-36.
[2] Proudman, I., "The generation of noise by isotropic turbulence", Proceedings of the Royal Society of London, A214, (1952), pp. 119-132.
[3] Sarkar, S. and Hussaini, M.Y., "Computation of the Sound Generated by Isotropic Turbulence", ICASE Report No.93-74, (1993).
[4] McKay M.D. et al., "A Comparison of Three Methods for Selecting Values of Input Variables in the Analysis of Output from a Computer Code", Technometrics Vol. 21, No. 2, (1979), pp.239-245.
[5] Krige, D.G., "A statistical approach to some mine valuations and allied problems at the Witwatersrand", Master's thesis of the University of Witwatersrand, (1951).
[6] Holland J.H., "Adaptation in Natural and Artificial Systems", University of Michigan Press/MIT Press, (1975).
[7] Yoshidome, D. and Watanabe, N., "A Computer Aided Optimizing Design for Drone Rotors", Proceedings of Annual Meeting, Japan Society of Fluid Mechanics, No.103, (2020). [in Japanese]

On the Vortex Method for Modeling a Separated Flow of an Inviscid Fluid

Alexey Setukha

Research Computer Centre, Lomonosov Moscow State University, Leninskie Gory, 1, building 4, Moscow, 119234
setuhaav@rambler.ru

A Lagrangian mathematical model of the separated flow of an inviscid incompressible fluid around body with the generation of vorticity on the entire surface of the body is constructed. In this model, an inviscid fluid is treated as the limiting case of a viscous fluid with the Reynolds number tending to infinity.

Consider a flow with constant free-stream velocity $\mathbf{w}_\infty$ and pressure p_∞. Assume that the boundary of the body is a smooth closed surface Σ. The mathematical model is based on the continuity equation and the vorticity transport equation in a viscous fluid:

$$\operatorname{div}\mathbf{w}=0,\quad \frac{\partial\boldsymbol{\omega}}{\partial t}+\operatorname{curl}\left[\boldsymbol{\omega}\times\mathbf{w}\right]=\frac{1}{\mathrm{Re}}\Delta\boldsymbol{\omega}, \tag{1}$$

where $\mathbf{w}=\mathbf{w}(x,t)$ - is the flow velocity, $\boldsymbol{\omega}=curl\,\mathbf{w}$ - the vorticity, t is time; x denotes points of space.

Using the relations

$$\Delta\boldsymbol{\omega}=-\operatorname{curl}\operatorname{curl}\boldsymbol{\omega}=-\operatorname{curl}\left[\frac{\boldsymbol{\omega}\times[\operatorname{curl}\boldsymbol{\omega}\times\boldsymbol{\omega}]}{\boldsymbol{\omega}^2}+\frac{\boldsymbol{\omega}(\operatorname{curl}\boldsymbol{\omega},\boldsymbol{\omega})}{\boldsymbol{\omega}^2}\right],$$

we can rewrite equation (1) in the following form:

$$\frac{\partial\boldsymbol{\omega}}{\partial t}+\operatorname{curl}\left[\boldsymbol{\omega}\times\mathbf{u}\right]=\frac{1}{\mathrm{Re}}curl\,\frac{\boldsymbol{\omega}(\operatorname{curl}\boldsymbol{\omega},\boldsymbol{\omega})}{\boldsymbol{\omega}^2}, \tag{2}$$

$$\mathbf{u}=\mathbf{w}+\mathbf{w}',\quad \mathbf{w}'=\frac{1}{\mathrm{Re}}\frac{\operatorname{curl}\boldsymbol{\omega}\times\boldsymbol{\omega}}{\boldsymbol{\omega}^2}.$$

The vector field $\mathbf{w}'$ is known as the diffusion velocity. The velocity $\mathbf{u}$ is called the vorticity transport velocity.

Next, we use boundary layer approximation, according to which viscosity plays an important role only in a thin layer on the body surface, while, outside this layer, the viscosity has no effect. This follows from the theory and the boundary layer that the vorticity in the boundary layer is orthogonal to its curl. Therefore, we hypothesize that for large values of the Reynolds number, the right-hand side of equation (2) is negligible (see [1]).

Based on equation (2) with a zero right-hand side, the transition to the Lagrangian description of the flow is carried out. We will consider the laws of motion of particles $x(\xi,t)$, which move with a velocity $\mathbf{u}$, where $\xi=(z,\tau)$ is the Lagrangian coordinate of a particle that was born at a point $z\in\Sigma$ at a moment in time $\tau\ge 0$. We assume that all vorticity is concentrated only in such particles. It is proved that it is possible to introduce the Lagrangian vorticity density $\boldsymbol{\psi}(\xi,\tau)$ so that the fluid velocity is represented as:

$$\mathbf{w}(x,t)=\mathbf{w}_\infty+\int_0^t d\tau\int_{z\in\Sigma_\omega(\tau,t)}\boldsymbol{\psi}(\xi,t)\times\mathbf{V}(x-x(\xi,t))d\sigma_z,$$

$$\mathbf{V}(x)=x\left(4\pi\right)^{-1}|x|^{-3}.$$

For a pair of functions $x(\xi,t)$ and $\boldsymbol{\psi}(\xi,\tau)$, a complete system of equations is constructed

$$\frac{\partial x(\xi,t)}{dt}=\mathbf{u}(x(\xi,t),t), \tag{3}$$

$$\frac{\partial\boldsymbol{\psi}(\xi,t)}{\partial t}=\left(\boldsymbol{\psi}\nabla\right)\mathbf{u} \tag{4}$$

$$x(\xi,\tau)=z,\quad \boldsymbol{\psi}(\xi,\tau)=\boldsymbol{\gamma}(z,\tau)$$

where $\boldsymbol{\gamma}$ denotes the vorticity flux density on the body surface Σ:

$$\boldsymbol{\gamma}(z,\tau)=\boldsymbol{\omega}(z,\tau)\left(\mathbf{u}(z,\tau)\mathbf{n}(z)\right),\quad \tau\in[0,T],\ z\in\Sigma,$$

the function $\boldsymbol{\gamma}(z,\tau)$ is a solution of the equation

$$-\frac{1}{2}\mathbf{n}(x)\times\boldsymbol{\gamma}(x,t)+\int_\Sigma\boldsymbol{\gamma}(z,t)\times\mathbf{V}(x-z)d\sigma_z=\mathbf{f}(x,t),\quad x\in\Sigma,$$

$$\mathbf{f}(x,t)=-\lim_{\Delta t\to 0}\int_0^{t-\Delta t}d\tau\int_\Sigma\frac{\boldsymbol{\psi}(\xi_z,t')\times\mathbf{V}(x-x(\xi_z,t'))\big|_{t'=t-\Delta t}^{t}}{\Delta t}d\sigma_z$$

Given mathematical model can be used as a theoretical basis for refining and developing some classes of vortex numerical methods. Own version of the numerical scheme based on the discretization of the written equations was built, under the hypothesis is accepted that after its formation, each vortex particle immediately leaves the viscous boundary layer. Therefore, the viscosity initiated the formation of a vortex particle, and its motion occurs in accordance with equations (3)-(4), in which we neglect the diffusion velocity and assume that $\mathbf{u}=\mathbf{w}$.

The method is tested on examples of a number of classical problems of separated flow around bodies.

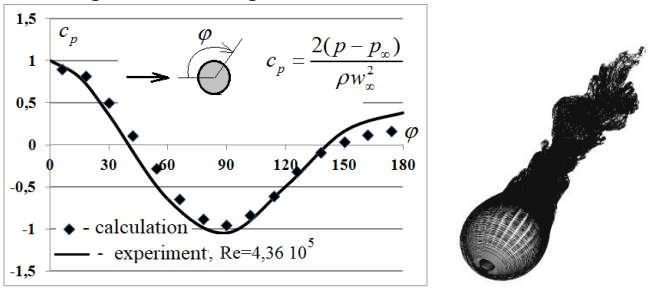

Fig. 1: Distribution of the pressure coefficient over the surface of a sphere in a separate flow (left) and the instantaneous shape of vortex structures (right).

References

[1] Setukha A.V. Lagrangian Description of Three-Dimensional Viscous Flows at Large Reynolds Numbers. Computational Mathematics and Mathematical Physics, 2020, 60(2): 302–326.

Article S2.1

Calculation of pressure, force, and moment in meshless vortex methods

Galina Dynnikova
[1]*Lomonosov Moscow State University, Institute of Mechanics,*
Michurinsky pr. 1, 119192, Moscow, Russia
dun@imec.msu.ru

ABSTRACT

When simulating incompressible fluid flows by vortex methods, pressure is excluded from the equations. For calculating the pressure field or forces acting on bodies, it is necessary to use formulas that express these values in terms of the vorticity and velocity distributions. There are various forms of such expressions in literature. Not all of them are easy to use in vortex meshless methods. Additionally, they are written in continuous form and need an adjustment for use in numerical schemes. In this work, the existing and some new expressions of pressure, force, and moment are presented in the form adapted for use in numerical meshless vortex methods for simulation of two- and three-dimensional flows under the general boundary conditions (slip, partial slip, no-slip).

KEYWORDS: Aerodynamic nonstationary loads, Meshless vortex methods, Viscous incompressible fluid, Partial slip.

1. INTRODUCTION

Vortex meshless methods are used to simulate flows of an ideal and viscous incompressible fluid described by the Euler or Navier-Stokes equations, from which the pressure is excluded by the application of the curl. To calculate the pressure field, if necessary, formulas are required expressing the pressure in terms of the velocity and vorticity fields. In the case of stationary and nonstationary potential flows, the Bernoulli and Cauchy-Lagrange integrals are applied. A generalization of these formulas for vortex unsteady flows of an ideal fluid and some special cases of viscous fluid flows are contained in the works [1-3]. In [4, 5], the general integral expressions of pressure for unsteady flows of viscous fluid were obtained. The expression [4] is not explicit, since it contains the pressure under the integral over the surface, while the one obtained in the work [5] is explicit. The following expression for Bernoulli function $B = \frac{p}{\rho} + \frac{u^2}{2} + H$ is obtained in [5] for viscous fluid

$$B(\mathbf{R}) - \int_{\tau} \mathbf{u}\cdot(\boldsymbol{\omega}\times\mathbf{K})\,d\tau - \int_{s} \mathbf{u}_s\cdot(\boldsymbol{\gamma}\times\mathbf{K})\,ds + \dot{\varphi} + \frac{\partial\varphi_q}{\partial t} - \nu\oint_{s}\mathbf{K}\cdot(\mathbf{n}\times\boldsymbol{\omega})\,ds = C$$

$$\mathbf{K}(\mathbf{R},\mathbf{r}) = \frac{1}{2(\kappa-1)\pi}\frac{\mathbf{R}-\mathbf{r}}{|\mathbf{R}-\mathbf{r}|^{\kappa}}, \quad \mathbf{r}\in\tau, \quad \boldsymbol{\gamma} = \mathbf{n}\times(\mathbf{u}-\mathbf{u}_s), \quad C = \begin{cases} B_{\infty}, & \text{infinite space} \\ C(t), & \text{bounded region} \end{cases} \tag{1}$$

where p, ρ, $\mathbf{u}$, $\boldsymbol{\omega}$, ν, H are pressure, density, velocity, vorticity, kinematic viscosity, and potential of mass force respectively; $\mathbf{u}_s$ is the surface velocity, τ is all regions containing vorticity including the body region if it rotates; s is entire flow boundaries; n is normal directed from the surface into fluid; $\dot{\varphi}$ is potential of the vorticity generated at the time unit; φ_q is potential of the sources if they are used in the flow or body regions; κ is the space dimension.

By integrating pressure it is possible to calculate aerodynamic loads, but it is easier to apply formulas expressing loads in terms of the velocity and vorticity fields directly.

A large number of works are devoted to the study of the dependence of aerodynamic forces on the velocity field and its derivatives. The classical theorem of N.E. Zhukovsky about the lifting force in steady flows of an ideal fluid is well-known. Generalizations of Zhukovsky's theorem for unsteady separated flows of an ideal fluid were developed in [6-10].

In works [11-14], the aerodynamic force expressions are derived using the law of conservation of hydrodynamic momentum in infinite space. The formulas obtained contains the time derivative of a volume integral (first moment of vorticity), that requires computational costs and the accuracy of the flow simulation in the far field. Besides, it does not provide calculating the forces for each body if there are several in the flow.

The formulas obtained in [15-22] are based on the use of auxiliary harmonic functions which correspond to potential flow. Using this approach, the method of the forces decomposition in the case of many bodies was proposed in [22]. The formulas contain the volume integrals also. In the case of many bodies moving arbitrarily, the auxiliary functions have to be calculated at every time step.

In works [23-28], the theory of boundary vorticity flux is developed. In [26], for the derivation of the force expression, the law of momentum conservation was applied to the region between the body surface and the external control surface, after that the outer surface was moved close to the surface of the body. As a result, the force expression via the vortex structures on the surface was obtained. This expression contains the surface integrals only, and as it is shown in [27], can be used for calculating forces exerted on a body under boundary partial-slip condition. The expression contains an acceleration of the fluid at the body surface. In the case of no-slip boundary condition, the fluid acceleration coincides with the body surface acceleration, but when slipping, the calculation of the fluid acceleration is difficult, especially at arbitrary body movements.

In [29] the similar expressions of force and moment exerted on a body in a viscous flow via the flux of vorticity generated on its surface were derived directly from vector calculus identities and Navier-Stokes equations for a solid body under the no-slip boundary conditions.

In work [30], a generalized formula for the aerodynamic force in an incompressible fluid is obtained, which does not contain volume integrals and is valid both for the no-slip conditions and for partial or complete slip. The pressure force expression obtained in [30] has the following form

$$\frac{\mathbf{F}_p}{\rho}=\frac{1}{\kappa-1}\left(\oint\limits_{S_b}\left(\boldsymbol{\sigma}_{new}+\dot{\boldsymbol{\gamma}}-\boldsymbol{\Omega}\times\boldsymbol{\gamma}-\mathbf{u}'\left(\mathbf{n}\cdot\boldsymbol{\omega}\right)\right)\times\mathbf{r}\,\mathrm{d}s+\int\limits_{L}\boldsymbol{\sigma}_{\Gamma}\times\mathbf{r}dl+2V_b\dot{\boldsymbol{\Omega}}\times\mathbf{r}_m\right)$$
$$+\oint\limits_{S_b}\mathbf{n}\frac{u'^2}{2}\mathrm{d}s+V_b\ddot{\mathbf{r}}_m, \qquad (2)$$
$$\boldsymbol{\sigma}_{new}=\nu\mathbf{n}\times\left(\nabla\times\boldsymbol{\omega}\right)\Big|_{S_b},\quad \boldsymbol{\sigma}_{\Gamma}=\mathbf{e}_L\frac{u'^2_{+}-u'^2_{-}}{2}.$$

Here V_b and r_m are the body volume and its center mass respectively.

In contrast to [26], the relative velocity of the fluid on the surface and the rate of its change are presented explicitly, which makes the formula convenient for use in meshless vortex methods. In addition, the formula provides for possible velocity discontinuity that can occur in an ideal fluid (for example, on a sharp edge). Thereby the formula (2) is applicable for both viscous and ideal fluid, while formula from [26] is inapplicable for ideal flows with tangential velocity discontinuity.

The work structure is the following. In section 2, an expression of the aerodynamic moment is derived for general boundary conditions (slip, partial slip, no-slip). In section 3, the physical meaning of expressions of force and moment is explained. In section 4, the formulas are presented in a discrete form adapted for application in the vortex methods.

2. EXPRESSION OF THE AERODYNAMIC MOMENT EXERTING ON A RIGID BODY UNDER GENERAL BOUNDARY CONDITIONS (SLIP, PARTIAL SLIP, NO-SLIP)

The pressure moment $\mathbf{M}_p$ around a point $\mathbf{r}_0$ is

$$\mathbf{M}_p = -\oint_{S_b} (\mathbf{r}-\mathbf{r}_0)\times \mathbf{n} p \, \mathrm{d}s .$$

In [29], the following identity is proved

$$\oint_{S_b} (\mathbf{r}-\mathbf{r}_0)\times \mathbf{n} p \, \mathrm{d}s = \frac{1}{2}\oint_{S_b} (\mathbf{r}-\mathbf{r}_0)^2 (\mathbf{n}\times\nabla p)\mathrm{d}s .$$

Expressing the pressure gradient from the Navies-Stokes equations, we obtain

$$\frac{\mathbf{M}_p}{\rho} = \frac{\nu}{2}\oint_{S_b} (\mathbf{r}-\mathbf{r}_0)^2 \left(\mathbf{n}\times(\nabla\times\boldsymbol{\omega})\right)\mathrm{d}s + \frac{1}{2}\oint_{S_b} (\mathbf{r}-\mathbf{r}_0)^2 \left(\mathbf{n}\times\left(\frac{\partial \mathbf{u}}{\partial t} + (\mathbf{u}\cdot\nabla)\mathbf{u}\right)\right)\mathrm{d}s . \tag{3}$$

In [29], it was shown, that $\nu\mathbf{n}\times(\nabla\times\boldsymbol{\omega}) = \boldsymbol{\sigma}^{new}$ is the vortex flux from the surface.

Using the notation, $\mathbf{u}' = \mathbf{u} - \mathbf{u}_s$ we rewrite the expression $\mathbf{n}\times\left(\partial\mathbf{u}/\partial t + (\mathbf{u}\cdot\nabla)\mathbf{u}\right)$ as follows:

$$\begin{aligned}
&\mathbf{n}\times\left(\frac{\partial \mathbf{u}}{\partial t} + (\mathbf{u}\cdot\nabla)\mathbf{u}\right) = \mathbf{n}\times\left(\frac{\partial(\mathbf{u}_s+\mathbf{u}')}{\partial t} + ((\mathbf{u}_s+\mathbf{u}')\cdot\nabla)(\mathbf{u}_s+\mathbf{u}')\right) = \\
&= \mathbf{n}\times\left(\frac{\partial \mathbf{u}_s}{\partial t} + (\mathbf{u}_s\cdot\nabla)\mathbf{u}_s\right) + \mathbf{n}\times\left(\frac{\partial \mathbf{u}'}{\partial t} + (\mathbf{u}_s\cdot\nabla)\mathbf{u}' + (\mathbf{u}'\cdot\nabla)\mathbf{u}_s + (\mathbf{u}'\cdot\nabla)\mathbf{u}'\right) = \\
&== \mathbf{n}\times\dot{\mathbf{u}}_s + \mathbf{n}\times\dot{\mathbf{u}}' + \mathbf{n}\times\left((\mathbf{u}'\cdot\nabla)\mathbf{u}_s + (\mathbf{u}'\cdot\nabla)\mathbf{u}'\right).
\end{aligned} \tag{4}$$

We denote $\dot{\mathbf{f}} = \left(\frac{\partial}{\partial t} + \mathbf{u}_s\cdot\nabla\right)\mathbf{f}$ for any variable $\mathbf{f}$.

The velocity and acceleration of the rigid body points can be expressed via the translational velocity **U** of the selected point $\boldsymbol{r}_0$ and the angular velocity $\boldsymbol{\Omega}$

$$\begin{aligned}
&\mathbf{u}_s = \mathbf{U} + \boldsymbol{\Omega}\times(\mathbf{r}-\mathbf{r}_0) \\
&\dot{\mathbf{u}}_s = \dot{\mathbf{U}} + \dot{\boldsymbol{\Omega}}\times(\mathbf{r}-\mathbf{r}_0) + \boldsymbol{\Omega}\times\left(\boldsymbol{\Omega}\times(\mathbf{r}-\mathbf{r}_0)\right)
\end{aligned} \tag{5}$$

Applying this to (4) we obtain

$$\begin{aligned}
&\mathbf{n}\times\left(\frac{\partial \mathbf{u}}{\partial t} + (\mathbf{u}\cdot\nabla)\mathbf{u}\right) = \\
&= \mathbf{n}\times\dot{\mathbf{u}}_s + \dot{\boldsymbol{\gamma}} - (\boldsymbol{\Omega}\times\mathbf{n})\times\mathbf{u}' + \mathbf{n}\times\left(\boldsymbol{\Omega}\times\mathbf{u}' + (\mathbf{u}'\cdot\nabla)\mathbf{u}'\right) = \\
&= \mathbf{n}\times\dot{\mathbf{u}}_s + \dot{\boldsymbol{\gamma}} - \mathbf{n}(\boldsymbol{\Omega}\cdot\mathbf{u}') - \mathbf{u}'(\boldsymbol{\Omega}\cdot\mathbf{n}) + \mathbf{n}\times\left(\nabla\frac{\mathbf{u}'^2}{2} - \mathbf{u}'\times(\nabla\times\mathbf{u}')\right) = \\
&= \mathbf{n}\times\dot{\mathbf{u}}_s + \dot{\boldsymbol{\gamma}} + \mathbf{n}\times\nabla\frac{\mathbf{u}'^2}{2} - \boldsymbol{\Omega}\times\boldsymbol{\gamma} - \mathbf{u}'(\mathbf{n}\cdot\boldsymbol{\omega}).
\end{aligned} \tag{6}$$

Here we used the equalities $\dot{\mathbf{n}} = \boldsymbol{\Omega}\times\mathbf{n}$, $(\mathbf{u}'\cdot\nabla)\mathbf{u}_s = \boldsymbol{\Omega}\times\mathbf{u}'$, $\mathbf{n}\cdot\mathbf{u}' = 0$, $\nabla\times\mathbf{u}' = \boldsymbol{\omega} - 2\boldsymbol{\Omega}$

Substituting (6) into (3) we can write

$$\frac{\mathbf{M}_p}{\rho}=\frac{1}{2}\oint_{S_b}\left(\mathbf{r}-\mathbf{r}_0\right)^2\left(\boldsymbol{\sigma}^{new}+\dot{\boldsymbol{\gamma}}-\boldsymbol{\Omega}\times\boldsymbol{\gamma}-\mathbf{u}'\left(\mathbf{n}\cdot\boldsymbol{\omega}\right)\right)\mathrm{d}s+\frac{1}{2}\oint_{S_b}\left(\mathbf{r}-\mathbf{r}_0\right)^2\left(\mathbf{n}\times\dot{\mathbf{u}}_s\right)\mathrm{d}s+$$
$$+\frac{1}{2}\oint_{S_b}\left(\mathbf{r}-\mathbf{r}_0\right)^2\left(\mathbf{n}\times\nabla\frac{\mathbf{u}'^2}{2}\right)\mathrm{d}s \tag{7}$$

The second integral on the right side (7) we transform using the Stokes theorem

$$\frac{1}{2}\oint_{S_b}\left(\mathbf{r}-\mathbf{r}_0\right)^2\left(\mathbf{n}\times\dot{\mathbf{u}}_s\right)\mathrm{d}s=\frac{1}{2}\int_{\tau_b}\left(\mathbf{r}-\mathbf{r}_0\right)^2\left(\nabla\times\dot{\mathbf{u}}_s\right)d\tau+\frac{1}{2}\int_{\tau_b}\left(\nabla\left(\mathbf{r}-\mathbf{r}_0\right)^2\right)\times\dot{\mathbf{u}}_s d\tau=$$
$$=\dot{\boldsymbol{\Omega}}\int_{\tau_b}\left(\mathbf{r}-\mathbf{r}_0\right)^2 d\tau+\int_{\tau_b}\left(\mathbf{r}-\mathbf{r}_0\right)\times\dot{\mathbf{u}}_s d\tau \tag{8}$$

The second integral on the right side (8) is the change rate of the moment of momentum of the virtual internal flow in the body region.
The third integral on the right side (7) is transformed as follows:

$$\frac{1}{2}\oint_{S_b}\left(\mathbf{r}-\mathbf{r}_0\right)^2\left(\mathbf{n}\times\nabla\frac{\mathbf{u}'^2}{2}\right)\mathrm{d}s=\frac{1}{2}\oint_{S_b}\left(\mathbf{n}\times\nabla\right)\left(\left(\mathbf{r}-\mathbf{r}_0\right)^2\frac{\mathbf{u}'^2}{2}\right)\mathrm{d}s-\oint_{S_b}\left(\mathbf{n}\frac{\mathbf{u}'^2}{2}\times\left(\mathbf{r}-\mathbf{r}_0\right)\right)\mathrm{d}s \tag{9}$$

For transformation of the first integral on the right side (7) we use the formula of vector calculus [31], which is valid for an arbitrary continuous differentiable function *f* on the surface *s* bounded by the contour *L*:

$$\int_s\left(\mathbf{n}\times\nabla\right)f\,\mathrm{d}s=\oint_L f d\mathbf{r}.$$

The closed surface on which the function *f* is piece-wise smooth can be composed of parts whose boundaries include discontinuity lines. Hence

$$\oint_S\left(\mathbf{n}\times\nabla\right)f\,\mathrm{d}s=\int_L\mathbf{e}_L\left(f_+-f_-\right)dl.$$

Here $\mathbf{e}_L=d\mathbf{r}/dl$ is a tangent unit vector to the line *L*, f_+, f_- are the values of the function on the left and right sides of the vector $\mathbf{e}_L$, respectively.

Employing this equality we rewrite (9) in the form

$$\frac{1}{2}\oint_{S_b}\left(\mathbf{r}-\mathbf{r}_0\right)^2\left(\mathbf{n}\times\nabla\frac{\mathbf{u}'^2}{2}\right)\mathrm{d}s=\frac{1}{2}\int_L\mathbf{e}_L\left(\mathbf{r}-\mathbf{r}_0\right)^2\frac{\mathbf{u}'^2_+-\mathbf{u}'^2_-}{2}dl+\oint_{S_b}\left(\left(\mathbf{r}-\mathbf{r}_0\right)\times\mathbf{n}\frac{\mathbf{u}'^2}{2}\right)\mathrm{d}s \tag{10}$$

Substituting (10) in (7) we obtain the final expression of the pressure force

$$\frac{\mathbf{M}_p}{\rho}=\frac{1}{2}\oint_{S_b}\left(\mathbf{r}-\mathbf{r}_0\right)^2\boldsymbol{\sigma}_\Sigma\,\mathrm{d}s+\frac{1}{2}\oint_{S_b}\left(\mathbf{r}-\mathbf{r}_0\right)^2\left(\mathbf{n}\times\dot{\mathbf{u}}_s\right)\mathrm{d}s+$$
$$+\frac{1}{2}\int_L\mathbf{e}_L\left(\mathbf{r}-\mathbf{r}_0\right)^2\frac{\mathbf{u}'^2_+-\mathbf{u}'^2_-}{2}dl+\oint_{S_b}\left(\left(\mathbf{r}-\mathbf{r}_0\right)\times\mathbf{n}\frac{\mathbf{u}'^2}{2}\right)\mathrm{d}s \tag{11}$$
$$\boldsymbol{\sigma}_\Sigma=\boldsymbol{\sigma}^{new}+\dot{\boldsymbol{\gamma}}-\boldsymbol{\Omega}\times\boldsymbol{\gamma}-\mathbf{u}'\left(\mathbf{n}\cdot\boldsymbol{\omega}\right)$$

The expression seems complicated, but it has a simple physical meaning and can be easily

used to simulate vortex flows.

The full aerodynamic moment is a sum of the pressure and friction force moments.

$$\mathbf{M} = \mathbf{M}_p + \mathbf{M}_w$$

The moment of the friction force is

$$\mathbf{M}_w = \oint_{S_b} (\mathbf{r} - \mathbf{r}_0) \times \boldsymbol{\eta} \, \mathrm{d}s, \tag{12}$$

where $\boldsymbol{\eta}$ is the shear stress. In an incompressible Newtonian fluid it can be represented as follow [29]

$$\boldsymbol{\eta} = \nu\rho\big(2(\mathbf{n}\times\nabla)\times\mathbf{u} - \mathbf{n}\times\boldsymbol{\omega}\big). \tag{13}$$

Substituting this in (12) we obtain the expression of the friction moment exerted on a rigid body in a Newtonian incompressible fluid (See Appendix A).

$$\mathbf{M}_w = -\nu\rho\left(4\boldsymbol{\Omega}V_b + 2\oint_{S_b}\boldsymbol{\gamma}\,\mathrm{d}s + \oint_{S_b}(\mathbf{r}-\mathbf{r}_0)\times(\mathbf{n}\times\boldsymbol{\omega})\,\mathrm{d}s\right) \tag{14}$$

3. THE EXPRESSIONS OF FORCE AND MOMENT IN TERMS OF VORTEX METHODS.

In vortex simulation of flows, researchers deal with a set of discrete vortex elements with intensity $\boldsymbol{\Gamma}_i^{\text{free}}$. The vorticity field $\boldsymbol{\omega}$ is a superposition of the fields of the vortex elements

$$\boldsymbol{\omega}(\mathbf{r},t) = \sum_{i=1}^{N}\boldsymbol{\omega}_i(\mathbf{r},t) = \sum_{i=1}^{N}\boldsymbol{\Gamma}_i^{\text{free}}\zeta_i(\mathbf{r},\mathbf{r}_i,\mathbf{e}_\Gamma),$$

where $\zeta_i(\mathbf{r},\mathbf{r}_i)$ is the normalized distribution of i-th element, depending on the vortex model, $\mathbf{e}_\Gamma$ is the unit vector $\mathbf{e}_\Gamma = \boldsymbol{\Gamma}_i^{\text{free}} \big/ \left|\boldsymbol{\Gamma}_i^{\text{free}}\right|$. In the case of a two-dimensional flow, the circulation of the element $\boldsymbol{\Gamma}_i^{\text{free}}$ and $\mathbf{e}_\Gamma$ are constant.

The velocity field $\mathbf{u}$ is expressed by the Biot-Savart formula via vorticity and the velocity $\mathbf{u}(\mathbf{r}_s)$ at the bodies surfaces

$$\begin{gathered}\mathbf{u}(\mathbf{r}) = \int_{\tau_f}\boldsymbol{\omega}(\xi)\times\mathbf{K}(\mathbf{r},\xi)\,d\tau + \int_s\big(\mathbf{n}\times\mathbf{u}(\xi_s)\big)\times\mathbf{K}(\mathbf{r},\xi_s)\,ds + \int_s\big(\mathbf{n}\cdot\mathbf{u}(\xi_s)\big)\mathbf{K}(\mathbf{r},\xi_s)\,ds + \mathbf{u}_\infty \\ \xi\in\tau_f, \quad \xi_s\in s, \quad \mathbf{K}(\mathbf{r},\xi) = \frac{\mathbf{r}-\xi}{2(\kappa-1)\pi|\mathbf{r}-\xi|^\kappa},\end{gathered} \tag{15}$$

where τ_f and s are the flow region and its entire boundary respectively, $\mathbf{n}$ is a normal directed from the surface into the fluid, $\mathbf{u}_\infty$ is the velocity at infinity if the region is infinite, κ is the dimension of space.

In the case of a slip or partial slip boundary conditions, the velocity $\mathbf{u}(\xi_s)$ does not equal the surface velocity $\mathbf{u}_s$ but their normal components are the same. The vector $\boldsymbol{\gamma}^{\text{att}} = \mathbf{n}\times(\mathbf{u}(\xi_s) - \mathbf{u}_s)$ is called the attached vorticity. In vortex methods, the attached vorticity is simulated by a set of vortex elements that move with the surface velocity, and their circulations $\boldsymbol{\Gamma}_j^{att}$ change over time. In addition, at each time step, new free vortex elements with circulations $\boldsymbol{\Gamma}_j^{\text{new}}$ arise. They arise due to the vortex flux $\boldsymbol{\sigma}^{new}$ generated by the surface. The new vortex elements simulate a

thin layer near the surface with vortex intensity $\boldsymbol{\gamma}^{\text{new}} = \boldsymbol{\sigma}^{\text{new}}\Delta t$. Equation (15) takes the form

$$\alpha\mathbf{u}(\mathbf{r}) = \sum_{i=1}^{N}\int_{\tau_f}\boldsymbol{\omega}_i(\xi)\times\mathbf{K}(\mathbf{r},\xi)d\tau + \int_s\left(\boldsymbol{\gamma}^{\text{new}}+\boldsymbol{\gamma}^{\text{att}}\right)\times\mathbf{K}(\mathbf{r},\xi_s)ds +$$
$$+\int_s(\mathbf{n}\times\mathbf{u}_s)\times\mathbf{K}(\mathbf{r},\xi_s)ds + \int_s(\mathbf{n}\cdot\mathbf{u}_s)\mathbf{K}(\mathbf{r},\xi_s)ds + \mathbf{u}_\infty$$
$$\alpha = \begin{cases} 1, & \mathbf{r}\in\tau_f \\ 1/2, & \mathbf{r}\in S \end{cases}$$

In order to find the unknown function $\boldsymbol{\gamma} = \boldsymbol{\gamma}^{\text{new}} + \boldsymbol{\gamma}^{\text{att}}$, in vortex meshless methods, a system of linear equations is solved, based on the equality of the normal components of the velocities [32] $\mathbf{n}\cdot\mathbf{u}(\mathbf{r}_s) = \mathbf{n}\cdot\mathbf{u}_s$ or the equality of the tangent components [33], [34] $\mathbf{n}\times\mathbf{u}(\mathbf{r}_s) = \mathbf{n}\times\mathbf{u}_s + \boldsymbol{\gamma}$.

The expressions of force and moment contain the term $\boldsymbol{\sigma}_\Sigma = \boldsymbol{\sigma}^{new} + \dot{\boldsymbol{\gamma}} - \boldsymbol{\Omega}\times\boldsymbol{\gamma} - \mathbf{u}'(\mathbf{n}\cdot\boldsymbol{\omega})$. In work [29], it is shown that $\boldsymbol{\sigma}^{\text{new}} = \nu\mathbf{n}\times(\nabla\times\boldsymbol{\omega})\big|_{S_b}$ is a vortex flux from the surface. This means that an additional vortex with intensity $\boldsymbol{\sigma}^{\text{new}}\Delta t\Delta s$ sheds into the afluid during a time Δt from a surface area Δs. Two subsequent terms are $\dot{\boldsymbol{\gamma}} - \boldsymbol{\Omega}\times\boldsymbol{\gamma} = \left(\boldsymbol{\gamma}(t,\xi) - \boldsymbol{\gamma}(t-\Delta t,\xi) - \boldsymbol{\Omega}\times\boldsymbol{\gamma}\Delta t\right)/\Delta t$ where ξ is the point attached to the surface. Vector $\tilde{\boldsymbol{\gamma}} = \boldsymbol{\gamma}(t-\Delta t,\xi) + \boldsymbol{\Omega}\times\boldsymbol{\gamma}\Delta t$ is a result of rotation of the vector $\boldsymbol{\gamma}(t-\Delta t,\xi)$ with the surface. The last term $\mathbf{u}'(\mathbf{n}\cdot\boldsymbol{\omega})$ arises when some free vortex lines end on the surface. They are continued by lines of attached vorticity or vortices modeling the body. If $\mathbf{u}'$ is not equal to zero, the ends of the free lines are displaced relative to the surface, "drawing" the vortex lines with the intensity. Hence $\boldsymbol{\sigma}_\Sigma\Delta t$ is the added vorticity compared to that obtained by moving the vortices in the previous step. In work [30], it is shown, that expression $\left(\mathbf{u}'^{\,2}_{+} - \mathbf{u}'^{\,2}_{-}\right)/2$ is the vorticity shedding into the flow at the separation line (for example, on sharp edges). Also in work [30], it is shown that the expression $\frac{\rho u'^2}{2}$ can be written in the following form

$$\mathbf{n}\frac{\rho u'^2}{2} = (\mathbf{u}_f - \mathbf{u}_s)\times\boldsymbol{\gamma}, \tag{16}$$

where $\boldsymbol{u}_f$ is the velocity of the free vortex layer $\mathbf{u}_f = (\mathbf{u}+\mathbf{u}_s)/2$. Expression (16) is similar to the Zhukovskiy's lifting force.

$$\mathbf{F}_p = \mathbf{F}^{\text{new}} + \mathbf{F}^{\text{Zhuk}} + \mathbf{F}^{\text{in}},$$
$$\mathbf{M}_p = \mathbf{M}^{\text{new}} + \mathbf{M}^{\text{Zhuk}} + \mathbf{M}^{\text{in}}$$
$$\mathbf{F}^{\text{new}} = \frac{\rho}{\kappa-1}\left(\oint_{S_b}\boldsymbol{\sigma}_\Sigma\times\mathbf{r}\,ds + \int_L\boldsymbol{\sigma}_\Gamma\times\mathbf{r}dl + 2V_b\dot{\boldsymbol{\Omega}}\times\mathbf{r}_m\right),$$
$$\mathbf{F}^{\text{Zhuk}} = \rho\oint_{S_b}\mathbf{n}\frac{u'^2}{2}ds, \quad \mathbf{F}^{\text{in}} = m_f\ddot{\mathbf{r}}_m,$$
$$\mathbf{M}^{\text{new}} = \frac{\rho}{2}\left(\oint_{S_b}(\mathbf{r}-\mathbf{r}_0)^2\boldsymbol{\sigma}_\Sigma\,ds + \int_L(\mathbf{r}-\mathbf{r}_0)^2\sigma_\Gamma dl + 2\dot{\boldsymbol{\Omega}}\int_{\tau_b}(\mathbf{r}-\mathbf{r}_0)^2 d\tau\right),$$
$$\mathbf{M}^{\text{Zhuk}} = \rho\oint_{S_b}(\mathbf{r}-\mathbf{r}_0)\times\mathbf{n}\frac{\mathbf{u}'^2}{2}ds, \quad \mathbf{M}^{\text{in}} = \rho\int_{\tau_b}(\mathbf{r}-\mathbf{r}_0)\times\dot{\mathbf{u}}_s d\tau$$

The terms $\mathbf{F}^{\text{new}}, \mathbf{M}^{\text{new}}$ are related to the change in the hydrodynamic and rotational impulses caused by the generation of additional vorticity. The terms $\mathbf{F}^{\text{Zhuk}}, \mathbf{M}^{\text{Zhuk}}$ are the forces arising when the velocity of the vortices movement do not coincide with the free velocity. The terms $\mathbf{F}^{\text{in}}, \mathbf{M}^{\text{in}}$ are the change rate of the momentum and the moment of momentum of the virtual flow in the body region. In two-dimensional case $\mathbf{M}^{\text{in}}$ is

$$\frac{\mathbf{M}^{\text{in}}}{\rho} = \int_{\tau_b} (\mathbf{r}-\mathbf{r}_0)\times\left(\dot{\mathbf{U}} + \dot{\boldsymbol{\Omega}}\times(\mathbf{r}-\mathbf{r}_0) + \boldsymbol{\Omega}\times(\boldsymbol{\Omega}\times(\mathbf{r}-\mathbf{r}_0))\right)\mathrm{d}\tau =$$
$$= V_b(\mathbf{r}_m-\mathbf{r}_0)\times\dot{\mathbf{U}} + \dot{\boldsymbol{\Omega}} I_0$$

In three-dimensional flow, in the case of constant direction of the axis passing through the point $\mathbf{r}_0$, $\mathbf{M}^{\text{in}}$ equals to

$$\mathbf{M}^{\text{in}} = (\mathbf{r}_m-\mathbf{r}_0)\times\dot{\mathbf{U}}V_b + \dot{\boldsymbol{\Omega}} I_0 - \dot{\Omega}\mathbf{I}_1 - \Omega^2\mathbf{e}\times\mathbf{I}_1$$
$$I_0\int_{\tau_b}(\mathbf{r}-\mathbf{r}_0)^2\,d\tau, \quad \mathbf{I}_1 = \int_{\tau_b}(\mathbf{r}-\mathbf{r}_0)\left(\mathbf{e}\cdot(\mathbf{r}-\mathbf{r}_0)\right)d\tau$$

4. THE EXPRESSION OF PRESSURE IN TERMS OF VORTEX METHODS.

Expression from the integrals in (1) can be written as

$$\mathbf{u}\cdot(\boldsymbol{\omega}\times\mathbf{K})\,d\tau = \mathbf{u}\cdot\mathbf{v}(\mathbf{R},\mathbf{r},\boldsymbol{\omega}\,d\tau)$$
$$\mathbf{u}_s\cdot(\boldsymbol{\gamma}\times\mathbf{K})\,ds = \mathbf{u}_s\cdot\mathbf{v}(\mathbf{R},\mathbf{r},\boldsymbol{\gamma}\,ds)$$

were $\mathbf{v}(\mathbf{R},\mathbf{r},\mathbf{g})$ is velocity induced at point **R** by point vortex element located at the point **r**.

The term $\dot{\varphi}$ is the potential of the «new vorticity» arised per unit time. In the case of two-dimensional flows, the total circulation of new vortices is zero. They are concentrated on the surface or inside the body area. This set can be represented as a set of vortex dipoles with a continuous potential outside the body. The potential of a pair of vortices of opposite sign Γ and $-\Gamma$ is equal to the angle α between the vectors connecting the observation point with the vortex points (see Figure1)

$$\varphi(\mathbf{R}) = \frac{\Gamma\alpha}{2\pi} = \frac{\Gamma}{2\pi}\operatorname{atan2}\left((\mathbf{R}-\mathbf{r}_1)\cdot(\mathbf{R}-\mathbf{r}_2), \mathbf{e}_z\cdot((\mathbf{R}-\mathbf{r}_2)\times(\mathbf{R}-\mathbf{r}_1))\right)$$

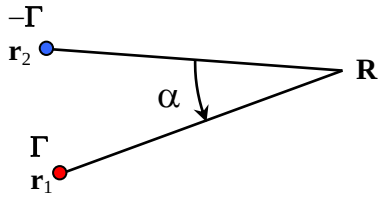

Fig. 1 The schema of the angle α calculation

In the case of three-dimensional flows, the set of new vorticity consists of closed vortex lines. The potential of a closed vortex line at point **R** is $\varphi = \Gamma\Theta/4\pi$ where Θ is the solid angle of observation from this point. In the case of a triangle contour, it is [35]

$$\Theta = 2\operatorname{atan2}\left(abc + (\mathbf{a}\cdot\mathbf{b})c + (\mathbf{b}\cdot\mathbf{c})a + (\mathbf{c}\cdot\mathbf{a})b, \mathbf{a}\cdot(\mathbf{b}\times\mathbf{c})\right)$$

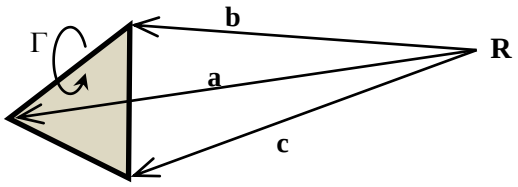

Fig. 2 The schema of the solid angle Θ calculation

If the sources are used for modeling the flow, then the terms $\partial\varphi_q/\partial t$ have to be calculated too

$$\frac{\partial\varphi_q(R)}{\partial t}=\sum_i\left(-\frac{1}{2(\kappa-1)\pi|\mathbf{R}-\mathbf{r}_i|^{\kappa-1}}\frac{dq_i}{dt}+q_i\mathbf{K}\cdot\mathbf{u}_{q_i}\right),$$

where $q_i,\mathbf{u}_{q_i}$ are intensity and velocity of i-th source respectively.

5. SOME EXAMPLES OF NUMERICAL SCHEMES

Two-dimensional flow.

Translational movement of a rigid body.

In this case, three kinds of vortex elements exist under the partial slip boundary conditions: free vortices, new vortices arised during the current time step, and the attached vortices (see Figure 3a). In the particular case, under the no-slip condition, the attached vorticity is equal to zero. When solving a system of equations satisfying the no-flow conditions, the values of Γ_k^{att} and Γ_k^{new} are found as the sum $\Gamma_k^{\text{att}}+\Gamma_k^{\text{new}}$. After that, they are separated in accordance with the slip model. In the particular case, under the slip condition, the new free vorticity is equal to zero, except for those where flow separation occurs.

To calculate pressure, force, and moment, the following formulas apply

$$B(\mathbf{R})-\sum_{i=1}^{N^{\text{free}}}\mathbf{u}_i\cdot\mathbf{v}_i(\mathbf{R},\mathbf{r}_i,\Gamma_i^{\text{free}})-\mathbf{U}\cdot\sum_{k=1}^{N_k}\mathbf{v}_k(\mathbf{R},\mathbf{r}_k,\Gamma_k^{att})+\sum_{k=1}^{N_k}\frac{G_k\alpha(\mathbf{R},\mathbf{r}_k,\mathbf{r}_{k+1})}{2\pi\Delta t}-$$

$$-\nu\sum_{k=1}^{N_k}\mathbf{K}(\mathbf{R},\mathbf{r}_{k+1/2})\cdot(\mathbf{n}_k\times\boldsymbol{\omega})l_k=B_\infty,$$

$$G_1=\Gamma_1^{\text{new}}-\Gamma_1^{\text{del}}+\Delta\Gamma_1^{\text{att}},$$

$$G_k=\Gamma_k^{\text{new}}-\Gamma_k^{\text{del}}+\Delta\Gamma_k^{\text{att}}+G_{k-1},\quad k=2,3,...,N_k,$$

$$\mathbf{r}_{N_k+1}=\mathbf{r}_1,\quad \mathbf{r}_{k+1/2}=(\mathbf{r}_k+\mathbf{r}_{k+1})/2,\quad l_k=|\mathbf{r}_{k+1}-\mathbf{r}_k|$$

$$\Delta\Gamma_k^{\text{att}}=\Gamma_k^{\text{att}}(t)-\Gamma_k^{\text{att}}(t-\Delta t)$$

$$\frac{\mathbf{F}_p}{\rho}=\frac{1}{\Delta t}\sum_{k=1}^{N_k}\left(\Gamma_k^{\text{new}}-\Gamma_k^{\text{del}}+\Delta\Gamma_k^{\text{att}}\right)\times\mathbf{r}_k+\sum_{k=1}^{N_k}\mathbf{n}_k\frac{\left\langle\Gamma_{k+1/2}^{\text{att}}(t-\Delta t)\right\rangle^2}{2l_k}+V_b\dot{\mathbf{U}},$$

$$\frac{M_p}{\rho}=\frac{1}{2\Delta t}\sum_{k=1}^{N_k}\left(\Gamma_k^{\text{new}}-\Gamma_k^{\text{del}}+\Delta\Gamma_k^{\text{att}}\right)(\mathbf{r}_k-\mathbf{r}_0)^2+\sum_{k=1}^{N_k}(\mathbf{r}_{k+1/2}-\mathbf{r}_0)\times\mathbf{n}_k\frac{\left\langle\Gamma_{k+1/2}^{\text{att}}(t-\Delta t)\right\rangle^2}{2l_k}+$$

$$+(\mathbf{r}_m-\mathbf{r}_0)\times V_b\dot{\mathbf{U}}$$

$$\left\langle\Gamma_{k+1/2}^{\text{att}}\right\rangle=\left(\Gamma_k^{\text{att}}+\Gamma_{k+1}^{\text{att}}\right)/2$$

Here Γ_k^{del} is the circulation of the old vortex elements if they were removed when crossing the surface of the body near k-th point during the current time step.

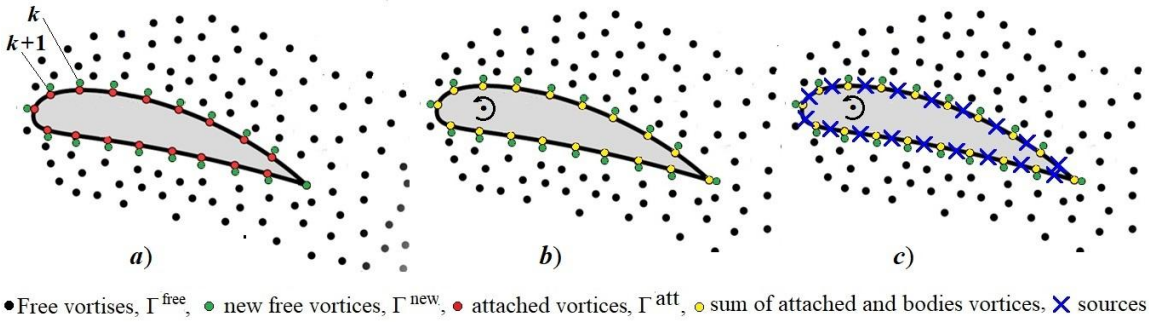

Fig. 3 Some kinds of the two-dimensional vortex models: *a*) translational motion; *b*) and *c*) – rotational motion

Rotational motion of a rigid body.

If the body rotates, vorticity is contained in its area. It can be distributed in volume or on the surface. This does not affect the external flow field if the no-flow condition is satisfied. In addition, sources can be used to simulate the flow in the body region. If the sources are not used, and the vortices modeling the body are located on the surface (Figure 3b), then the solution of the system of equations is the sum $\Gamma_k^b + \Gamma_k^{\text{att}} + \Gamma_k^{\text{new}}$, where $\mathbf{\Gamma}_k^b = \mathbf{n} \times (\mathbf{u}_s - \mathbf{u}_{s-}) l_k$. These quantities are proportional to Ω, and do not depend on the distribution of vorticity outside the body region; therefore, it is sufficient to calculate them once for the potential flow using the equalities

$$\left(\mathbf{n} \times \left(\mathbf{u}_{s+} - \mathbf{u}_{s-}\right)\right) \cdot \mathbf{e}_z = \frac{\Gamma_k^{\text{att}} + \Gamma_k^b}{l_k}$$

$$\left(\mathbf{n} \times \left(\mathbf{u}_{s+} + \mathbf{u}_{s-}\right)\right) \cdot \mathbf{e}_z = \frac{\Gamma_k^{\text{att}} - \Gamma_k^b}{l_k}$$

$$\mathbf{u}_{s+} + \mathbf{u}_{s-} = 2\mathbf{u}(\mathbf{r}_k)$$

from which it follows

$$\Gamma_k^b = \frac{\Gamma_k^{\text{att}} + \Gamma_k^b}{2} - \frac{\mathbf{n} \times 2\mathbf{u}(\mathbf{r}_k) \cdot \mathbf{e}_z}{2} l_k.$$

Here $\mathbf{u}(\mathbf{r}_k)$ is the velocity at point $\mathbf{r}_k$, calculated by the Biot-Savart formula.

The expressions for the pressure, force, and moment, in this case, have the form:

$$B(\mathbf{R}) - \sum_{i=1}^{N^{\text{free}}} \mathbf{u}_i \cdot \mathbf{v}_i(\mathbf{R}, \mathbf{r}_i, \Gamma_i^{\text{free}}) - \sum_{k=1}^{N_k} \mathbf{u}_s \cdot \mathbf{v}_k(\mathbf{R}, \mathbf{r}_k, \Gamma_k^{\Sigma}) + \sum_{k=1}^{N_k} \frac{G_k \alpha(\mathbf{R}, \mathbf{r}_k, \mathbf{r}_{k+1})}{2\pi \Delta t} -$$

$$-\nu \sum_{k=1}^{N_k} \mathbf{K}(\mathbf{R}, \mathbf{r}_{k+1/2}) \cdot (\mathbf{n}_k \times \boldsymbol{\omega}) l_k = B_\infty,$$

$$\Gamma_k^{\Sigma} = \Gamma_k^{\text{att}} + \Gamma_k^{\text{b}}$$

$$G_1 = \Gamma_1^{\text{new}} - \Gamma_1^{\text{del}} + \Delta\Gamma_1^{\Sigma},$$

$$G_k = \Gamma_k^{\text{new}} - \Gamma_k^{\text{del}} + \Delta\Gamma_k^{\Sigma} + G_{k-1}, \quad k = 2, 3, ..., N_k,$$

$$\Delta\Gamma_k^{\Sigma} = \Gamma_k^{\Sigma}(t) - \Gamma_k^{\Sigma}(t - \Delta t),$$

$$\frac{\mathbf{F}_p}{\rho}=\frac{1}{\Delta t}\sum_{k=1}^{N_k}\left(\Gamma_k^{\text{new}}-\Gamma_k^{\text{del}}+\Delta\Gamma_k^{\text{att}}\right)\times\mathbf{r}_k+\sum_{k=1}^{N_k}\mathbf{n}_k\frac{\left\langle\Gamma_{k+1/2}^{\text{att}}(t-\Delta t)\right\rangle^2}{2l_k}+2V_b\dot{\boldsymbol{\Omega}}\times\mathbf{r}_m+V_b\dot{\mathbf{U}},$$

$$\frac{M_p}{\rho}=\frac{1}{2\Delta t}\sum_{k=1}^{N_k}\left(\Gamma_k^{\text{new}}-\Gamma_k^{\text{del}}+\Delta\Gamma_k^{\text{att}}\right)\left(\mathbf{r}_k-\mathbf{r}_0\right)^2+\sum_{k=1}^{N_k}\left(\mathbf{r}_{k+1/2}-\mathbf{r}_0\right)\times\mathbf{n}_k\frac{\left\langle\Gamma_{k+1/2}^{\text{att}}(t-\Delta t)\right\rangle^2}{2l_k}+$$
$$+2\dot{\boldsymbol{\Omega}}I_0+V_b\left(\mathbf{r}_m-\mathbf{r}_0\right)\times\dot{\mathbf{U}}.$$

Three-dimensional flow.

Some kinds of the three-dimensional vortex models are shown in Figure 4 for different boundary conditions. Red and green lines show attached and new free vorticity respectively

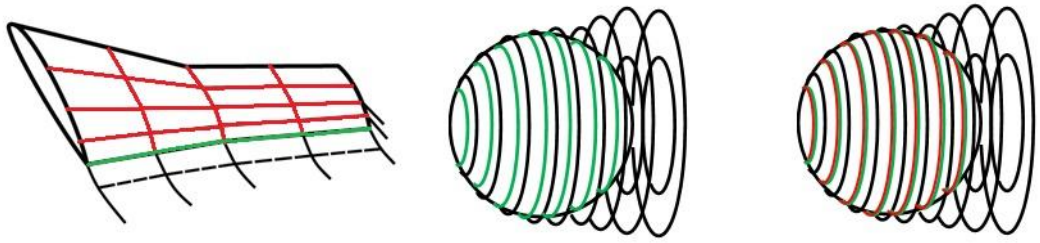

Figure 4. Some kinds of the three-dimensional vortex models; red and green lines show attached and new free vorticity respectively; *a*) ideal flow;
b) no-slip boundary condition *c*) partial slip boundary condition.

In three-dimensional flows in the case of slip and partial slip, situations are possible when part of the vortex line belongs to the attached vorticity and the other part to the free one. An example of this is tip vortices on an airplane wing. When modeling such flows, the solenoidal part of the attached vorticity and the vortices that simulate the continuation of free vortices should be considered separately. If this part in the simulation moves with the surface velocity, then it enters the expressions for the loads as attached vorticity, but its increment due to the displacement of the attachment point relative to the surface (the dashed red segment in Figure 4) is not included in the set $\left(\Delta\boldsymbol{\Gamma}_k^{att}+\Delta\boldsymbol{\Gamma}_k^{b}+\boldsymbol{\Gamma}_k^{\text{new}}\right)$, which is always solenoidal.

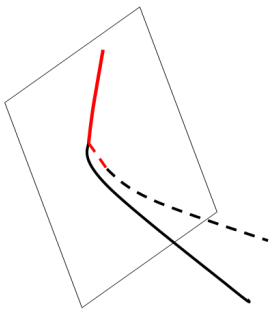

Fig. 5. The movement of a vortex line consisting of an attached and a free part. The red lines show the attached part. The dashed line represents the line after moving.

In the case of the body movement with the constant translational and angular velocities, the expressions of pressure, force and moment have the form

$$B(\mathbf{R}) - \sum_{i=1}^{N^{\text{free}}} \mathbf{u}_i(\mathbf{r}_i)\cdot\mathbf{v}_i(\mathbf{R},\mathbf{r}_i,\boldsymbol{\Gamma}_i^{\text{free}}) - \sum_{k=1}^{N_k} \mathbf{u}_s(\mathbf{r}_k)\cdot\mathbf{v}_k(\mathbf{R},\mathbf{r}_k,\boldsymbol{\Gamma}_k^{\text{att}} + \boldsymbol{\Gamma}_k^{\text{b}}) +$$

$$+\sum_{j=1}^{N_j} \frac{\left(\Delta\Gamma_j^{\text{att}} + \Gamma_j^{\text{new}}\right)\Theta_j(\mathbf{R})}{4\pi\Delta t} - \nu\sum_{j=1}^{N_j} \mathbf{K}\left(\mathbf{R},\mathbf{r}_j\right)\cdot\left(\mathbf{n}_j\times\boldsymbol{\omega}\right)s_j = B_\infty,$$

$$\frac{\mathbf{F}_p}{\rho} = \frac{1}{2\Delta t}\sum_{k=1}^{N_k}\left(\boldsymbol{\Gamma}_k^{\text{new}} + \Delta\boldsymbol{\Gamma}_k^{\text{att}}\right)\times\mathbf{r}_k + \sum_{j=1}^{N_j}\mathbf{n}_j\frac{\left\langle\Gamma_j^{\text{att}}(t-\Delta t)\right\rangle^2}{2s_k},$$

$$\frac{\mathbf{M}_p}{\rho} = \frac{1}{2\Delta t}\sum_{k=1}^{N_k}\left(\boldsymbol{\Gamma}_k^{\text{new}} + \Delta\boldsymbol{\Gamma}_k^{\text{att}}\right)\left(\mathbf{r}_k-\mathbf{r}_0\right)^2 + \sum_{j=1}^{N_j}\left(\mathbf{r}_j-\mathbf{r}_0\right)\times\mathbf{n}_j\frac{\left\langle\Gamma_j^{\text{att}}(t-\Delta t)\right\rangle^2}{2s_k} -$$

$$-\boldsymbol{\Omega}\times\int_{\tau_b}\left(\mathbf{r}-\mathbf{r}_0\right)\left(\boldsymbol{\Omega}\cdot\left(\mathbf{r}-\mathbf{r}_0\right)\right)d\tau.$$

Summation over *i* and *k* is performed over free and attached segments, respectively. Summation over *j* is performed over closed contours with area s_j. These expressions are written in the assumption of a small length of vortex segments. Otherwise, integration should be performed along the segments.

5. CONCLUSIONS

A new expression is derived for the moment of aerodynamic forces acting on a rigid body in a viscous incompressible fluid under general boundary conditions (slip, partial slip, no-slip). Aerodynamic loads are expressed in terms of the vortex flux from the surface, the rate of change of the attached vorticity, and the vector product of the attached vorticity by the difference between the forced and free velocities. This confirms that the origin of the aerodynamic loads is the generation of vorticity and the forced motion of the attached vorticity The generalized Cauchy-Lagrange formula for calculating the pressure field in viscous flow and the expressions for the force and moment are adapted to application in the vortex meshless methods. Some examples of the numeric schemes are presented.

ACKNOWLEDGMENT

The authors wish to acknowledge supports from the Lomonosov Moscow State University, Russian Federation.

APPENDIX A: Proof of equation (14)

Substituting (13) into (12), we obtain

$$\mathbf{M}_w = 2\nu\rho\oint_{S_b}\left(\mathbf{r}-\mathbf{r}_0\right)\times\left(\left(\mathbf{n}\times\nabla\right)\times\mathbf{u}\right)\mathrm{d}s - \nu\rho\oint_{S_b}\left(\mathbf{r}-\mathbf{r}_0\right)\times\left(\mathbf{n}\times\boldsymbol{\omega}\right)\mathrm{d}s. \tag{A1}$$

We write the first integral as follows:

$$\oint_{S_b}\left(\mathbf{r}-\mathbf{r}_0\right)\times\left(\left(\mathbf{n}\times\nabla\right)\times\mathbf{u}\right)\mathrm{d}s = -\oint_{S_b}\left(\left(\mathbf{n}\times\nabla\right)\times\mathbf{u}\right)\times\left(\mathbf{r}-\mathbf{r}_0\right)\mathrm{d}s - \oint_{S_b}\left(\mathbf{u}\times\left(\mathbf{n}\times\nabla\right)\right)\times\left(\mathbf{r}-\mathbf{r}_0\right)\mathrm{d}s \tag{A2}$$

Here the operator $\mathbf{n}\times\nabla$ acts on all factors to the right of it. In the case under consideration, the function **u** is continuous since the friction stress occurs in a viscous fluid. Let us show that the first integral on the right-hand side of (A2) is equal to zero if the function **u** is continuous. This follows from the identity [31]

$$\oint_{S_b}\mathbf{n}\times\nabla f\,\mathrm{d}s = 0.$$

which is valid for any scalar function f continuous on the surface S_b. Using decompositions $\mathbf{u} = u_i \mathbf{e}_i$, $\mathbf{r} - \mathbf{r}_0 = r_j' \mathbf{e}_j$ we obtain

$$\oint_{S_b} \left((\mathbf{n} \times \nabla) \times \mathbf{u} \right) \times (\mathbf{r} - \mathbf{r}_0) \, \mathrm{d}s = \left(\left(\oint_{S_b} \mathbf{n} \times \nabla u_i r_j' \, \mathrm{d}s \right) \times \mathbf{e}_i \right) \times \mathbf{e}_j = 0 \tag{A3}$$

The second integral in (A2) is transformed as followes

$$\begin{aligned}
&-\oint_{S_b} \left(\mathbf{u} \times (\mathbf{n} \times \nabla) \right) \times (\mathbf{r} - \mathbf{r}_0) \, \mathrm{d}s = \\
&= \oint_{S_b} \mathbf{u} \left((\mathbf{n} \times \nabla) \cdot (\mathbf{r} - \mathbf{r}_0) \right) \mathrm{d}s - \oint_{S_b} \mathbf{n} \times (\mathbf{u} \cdot \nabla)(\mathbf{r} - \mathbf{r}_0) \, \mathrm{d}s - \oint_{S_b} \mathbf{n} \times \left(\mathbf{u} \times \left(\nabla \times (\mathbf{r} - \mathbf{r}_0) \right) \right) \mathrm{d}s = \\
&= \oint_{S_b} \mathbf{u} \left(\mathbf{n} \cdot \left(\nabla \times (\mathbf{r} - \mathbf{r}_0) \right) \right) \mathrm{d}s - \oint_{S_b} \mathbf{n} \times \mathbf{u} \, \mathrm{d}s = -\oint_{S_b} \mathbf{n} \times \mathbf{u} \, \mathrm{d}s = \\
&= -\oint_{S_b} \mathbf{n} \times \mathbf{u}_s \, \mathrm{d}s - \oint_{S_b} \mathbf{n} \times \mathbf{u}' \mathrm{d}s = -2\boldsymbol{\Omega} V_b - \oint_{S_b} \boldsymbol{\gamma} \, \mathrm{d}s
\end{aligned} \tag{A4}$$

Implying (A2)-(A4) to (A1) we obtain

$$\mathbf{M}_w = -\nu\rho \left(4\boldsymbol{\Omega} V_b + 2 \oint_{S_b} \boldsymbol{\gamma} \, \mathrm{d}s + \oint_{S_b} (\mathbf{r} - \mathbf{r}_0) \times (\mathbf{n} \times \boldsymbol{\omega}) \mathrm{d}s \right)$$

REFERENCE

[1] Dynnikova G. Y., An analog of the Bernoulli and Cauchy-Lagrange integrals for a time-dependent vortex flow of an ideal incompressible fluid. Fluid Dyn., 2000, 35, 24–32.
[2] Stepanyants Y. A., Yakubovich E. I. The Bernoulli Integral for a Certain Class of Non-Stationary Viscous Vortical Flows of Incompressible Fluid, Studies in Appl. Math., 2015, **135**, 3, 295-309.
[3] Golubkin V.N., Sizykh G.B., Some general properties of plane-parallel viscous flows. Fluid Dyn., 1987, 22, 479–481. https://doi.org/10.1007/BF01051932
[4] Uhlman Jr. J. S. An integral equation formulation of the equations of motion of an incompressible fluid, NUWC-NTP /Technical report 10,086. 15 July 1992. 30 p.
[5] Dynnikova G. Y. The integral formula for pressure field in the nonstationary barotropic flows of viscous fluid. Journal of Mathematical Fluid Mechanics, 2014, **16**, 145-162.
[6] Howarth L. The theoretical determination of the lift coefficient for a thin elliptic cylinder, Proc. R. Soc. Lond. Ser. A, 1935, 149, 558.
[7] Sears W. R. Unsteady motion of airfoil with boundary layer separation, AIAA J., 1951, 14, 216.
[8] Sears W. R., Some recent developments in airfoil theory, J. Aeronaut. Sci., 1956, 23, 490.
[9] Dynnikova G. Y., Forces exerted on a body in an unsteady vortex separation flow of an ideal incompressible fluid, Fluid Dyn.,2001, 36(2), 285.
[10] Golovkin M. A., Golovkin V. A., Kalyavin V. M. Vortex fluid mechanics, 2009, Moscow 264p. (in Russian).
[11] Burgers J. M. On the resistance of fluids and vortex motion, Proc. K. Akad. Wet. Amsterdam 1920, **23**, 774–782.
[12] Lighthill M. J. An Informal Introduction to Theoretical Fluid Mechanics Clarendon Press, Oxford, 1986.
[13] Wu J. C. Theory for aerodynamic force and moment in viscous flows, AIAA J., 1981, **19**, 432.
[14] Wu J. C. Elements of Vorticity Aerodynamics, Tsinghua University Press, Beijing, 2005.

[15] Quartapelle L., and Napolitano M. Force and moment in incompressible flows, AIAA Journal, 1983, **21,** 911–913.
[16] Chang C. C. Potential flow and forces for incompressible viscous flow, Proc. R. Soc. Lond. 1992, **437**, 517.
[17] Howe M. S. On the force and moment on a body in an incompressible fluid, with application to rigid bodies and bubbles at high and low Reynolds number, Q. J. Mech. Appl. Math., 1995, **48**, 401.
[18] Wells J. C. A geometrical interpretation of force on a translating body in rotational flow, Phys. Fluids, 1996, **8**, 442.
[19] Ragazzo C. G. & Tabak E. On the force and torque on systems of rigid bodies: A remark on an integral formula due to Howe, Phys. Fluids, 2007, **19**, 057108.
[20] Magnaudet J. A 'reciprocal' theorem for the prediction of loads on a body moving in an inhomogeneous flow at arbitrary Reynolds number, J. Fluid Mech., 2011, **689**, 564.
[21] Chien-C. Chang, Shih-Hao Yang and Chin-Chou Chu, A many-body force decomposition with applications to flow about bluff bodies, J. Fluid Mech., 2008, **600**, 95.
[22] Graham W.R. Decomposition of the forces on a body moving in an incompressible fluid, J. Fluid Mech., 2019, **881**, 1097-1122.
[23] Wu J. Z., and Wu J. M. Vorticity dynamics on boundaries, Adv. Appl. Mech., 1996, **32** 119-275.
[24] Wu J., Yang Y., Luo Y., & Pozdrikis C. Fluid kinematics on a deformable surface, J. Fluid Mech., 2005, **541**, 371-381.
[25] Wu J. Z., Ma H. Y & Zhou M. D. Vorticity and Vortex Dynamics, Springer –Verlag, 2006.
[26] Wu J.-Z., Lu X.-Y., and Zhuang L.-X. Integral force acting on a body due to local flow structures, J. Fluid Mech., 2007, **576**, 265.
[27] Zhu J. Y., Zhu F. L., Su W. D., Zou S. F., Liu L. Q., Shi Y. P., and Wu J. Z. A vorticity dynamics view of effective slip boundary with application to foil-flow control, Phys. Fluids, 2014, **26,** 123602.
[28] Liu L. Q. Unified Theoretical Foundations of Lift and Drag in Viscous and Compressible External Flows Springer, Singapore, 2018.
[29] Dynnikova G.Ya., Andronov P.R. Expressions of force and moment exerted on a body in a viscous flow via the flux of vorticity generated on its surface. European Journal of Mechanics, B/Fluids, 2018, 72, (6), 293–300. DOI:https://doi.org/10.1016/j.euromechflu.2018.06.002.
[30] Dynnikova G. Ya. General expression of aerodynamic force under different boundary conditions (slip, partial slip, no-slip). Physics of Fluids, 2021, **33**(063104).
[31] Korn G.A. & Korn T. M. Mathematical Handbook for Scientists and Engineers DOVER PUBLICATIONS, INC. Mineola, New York, 2000.
[32] Cottet G.-H., Koumoutsakos P. D. Vortex Methods: Theory and Practice, Cambridge University Press. 320p. 2000.
[33] Kempka S.N., Glass M.W., Peery J.S., Strickland J.H., Ingber M.S. Accuracy considerations for implementing velocity boundary conditions in vorticity formulations, SANDIA report. SAND96-0583, UC-700. 1996. 52 p.
[34] Dergachev S.A., Marchevsky I.K., Shcheglov G.A. Flow simulation around 3D bodies by using Lagrangian vortex loops method with boundary condition satisfaction with respect to tangential velocity components, Aerospace Science and Technology, 2019, V. 94. Art. 105374.
[35] van Oosterom A., Strackee J., The solid angle of a plane triangle // IEEE Trans. on Biomedical Eng, 1983, V. BME-30, No. 2. P. 125–126.

Interpolating Vortex Particle Methods using Splines Wavelets

Matthias Kirchhart[1*]

[1]*Applied and Computational Mathematics, RWTH Aachen University, Schinkelstraße 2, 52066 Aachen, Germany.*
**Corresponding Author: kirchhart@acom.rwth-aachen.de*

Conventional vortex particle methods interpret a given particle field as a quadrature rule. To obtain a smooth approximation, this quadrature rule is then regularised using so-called blob-functions. The resulting schemes have the advantage of simplicity, but either converge only very slowly or require frequent ‘remeshing’.

In this talk we first review our previous work on splines for particle methods. [1] This approach allowed us to perform long-term accurate, high-order simulations without remeshing and could compete with a state-of-the-art discontinuous Galerkin method, see Fig. 1. However, when flows develop steep gradients and particles begin to cluster the method becomes inefficient due to its lack of adaptivity.

We then present a novel approach that instead interprets a given particle cloud as a set of point values and constructs smooth interpolants on them. These interpolants make use of spline wavelets and are adaptive. On the one hand, the method is a natural extension of our previous approach. On the other hand, there is a close relationship with radial basis function interpolants. The resulting schemes have many beneficial properties and preliminary results are promising.

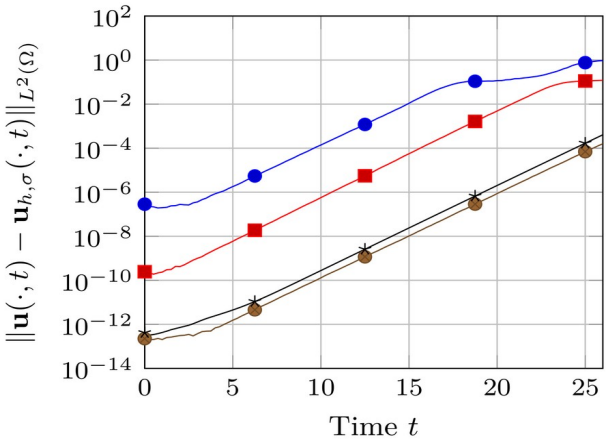

Fig. 1: Error-evolution of 4th, 6th, and 8th-order vortex particle methods using splines on a two-dimensional test-problem without remeshing. [1] Vortex methods using a spline regularisation are competitive with a state-of-the-art discontinuous Galerkin method.

References

[1] Kirchhart M, Rieger C. Discrete Projections: A Step Towards Particle Methods on Bounded Domains without Remeshing. SIAM Journal on Scientific Computing, 2021, 43(1):A609–A635.

Effect of Froude number on the motion of a sphere launched vertically upward in water

Kotaro Takamure[1*], Tomomi Uchiyama[1]

[1] *Institute of Materials and Systems for Sustainability, Nagoya University, Nagoya, Japan*
** Corresponding Author: kotaro.takamure@imass.nagoya-u.ac.jp*

A water exit refers to a situation in which an object is propelled from water into air. The water exit problem is highly complex because it involves nonlinear interference between the object and water surface. In most existing studies on the water exit problem, a primarily symmetrical spherical object was considered to clarify the relevant phenomena [1-2]. Several researches have utilized the Froude number (*Fr*), which is the ratio of gravity to inertial force, because the water exit is dominated by gravity when the sphere completely passes through the water surface [2-3]. By increasing the water exit velocity, the sphere spends less time submerged in entrained fluid and more time in a gravity-dominated regime. Haohao et al. [2] numerically investigated the effect of *Fr* ranging as $1.65 < Fr < 8.24$ by using the lattice Boltzmann method, which can effectively capture the large deformations of the air-water interface. Furthermore, Haohao et al. [2] indicated that *Fr* influenced the rupturing of the interfacial water sheet, which occurred when the sphere passes through the water surface. Thus, it can be considered that because the deformation of the water surface depends on *Fr*, the interface containing energy must also change accordingly.

To examine this aspect, in this study, a spherical sphere with a density of ρ_p=2640 kg/m^3 and diameter of d=25.4 mm was launched vertically toward the water surface. The value of *Fr* at the instant in which the sphere crossed the water surface was varied. The dependence of *Fr* on the sphere motion and water surface behavior was investigated.

An overview of the experimental apparatus is shown in Fig.1(a). The water tank using in this study was a cubic acrylic tank with a side length of 0.4 m. Water was stored in the tank, and a sphere launcher was installed at the center of the bottom of the tank. When the sphere was placed on the launcher, the coordinate origin was the center of the sphere when the sphere was placed in the launcher. The distance from the coordinate origin to the water surface was H, with H=3d for all the considered cases. Fig. 1 shows the schematic of the sphere launch system. When the sphere was placed on the launcher, the iron bar moved vertically downward, thereby compressing the coil spring. When the coil spring was released by pulling the trigger at time t=0, the iron bar moved upward, the small tab at the upper end of the iron bar impacted the sphere, and the sphere was ejected vertically upward. The launch velocity of the sphere was controlled via the compressive displacement of the coil spring.

Fig. 2 shows a snapshot of the instant at which the sphere reaches the maximum displacement position. For *Fr* = 2.86, a large amount of the water mass is attached around the sphere, and the water surface and sphere are clearly connected. For *Fr* = 3.4, a water mass is generated behind the sphere, and a water column is formed between the water surface and the sphere. For *Fr* = 4.92, most of the water mass separates from the sphere and distributes around the sphere as water droplets. In addition, the water column is elongated but still connects the water surface and sphere. For *Fr* = 5.9, no water mass is present around the sphere, and the water column is detached in certain regions. These results suggest that a larger *Fr* corresponds to a smaller influence of the water mass and water column on the sphere at the maximum displacement position of the sphere.

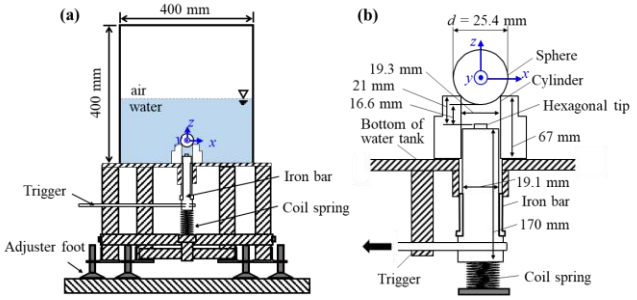

Fig. 1: Schematic of the sphere launch system. (a) Overview of experimental apparatus, (b) details of the launch system.

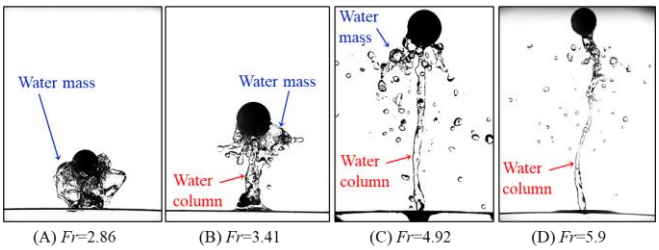

Fig. 2: Behavior of the water mass and water column when the sphere reaches the maximum displacement position.

Acknowledgement
This work was supported by the TOYOAKI SCHOLARSHIP FOUNDATION, Japan.

References

[1] Truscott TT, Epps BP, Munns, et al., Water exit dynamics of buoyant particles, Phys. Rev. Fluids, 2016 1(7): 074501.
[2] Haohao H, Yanping S, et al., Y. Jianyang, Numerical analysis of water exit for a particle with constant velocity using the lattice Boltzmann method, Appl. Ocean Res., 2019 84: 163-178.
[3] Wu Q, Ni B, et al., Experimental study on large deformation of free surface during water exit of a particle, Ocean Eng., 2017, 140: 369-376.

Analytical Description of the Vortex Ring Induced by a Ring Plume

Maria Stefanidou[1*], Aristeidis Bloutsos[1, 3], George Horsch[2], Athanassios Dimas[2] and Panayotis Yannopoulos[1]

[1]Environmental Engineering Laboratory, Department of Civil Engineering, University of Patras, 265 04 Patras, Greece
[2]Hydraulic Engineering Laboratory, Department of Civil Engineering, University of Patras, 265 04 Patras, Greece
[3]Hydraulics & Geotechnical Engineering Division, Department of Civil Engineering, University of West Attica, 122 43, Athens, Greece
** Corresponding Author: stefanidou.m@gmail.com*

The ring plume is a buoyant jet discharged vertically with low or without initial inertia and, thus, it is mainly dominated by buoyancy. It may be considered as the limiting case of a rosette-type diffuser with many nozzles discharging fluid into water bodies or in the atmosphere. The fluid may be wastewater, air pollutants or thermal effluents having a little different density than the density of the receiving fluid. The shear flow induced by the velocity right after the exit of the ring nozzle generates a vortex ring occupying the internal diameter of the nozzle. Since the internal diameter of the nozzle includes a solid bottom wall, located at z_0 under the ring exit level, the vortex ring remains stagnant.

In this paper the mathematical analysis of the flow related to a stagnant vortex ring is presented. Following Batchelor [1], for a single circular line vortex of a radius a and strength κ, for the element of integration in the axial plane including the line vortex, the streamlines are described in a cylindrical coordinate system (with the z axis vertical and in coincidence with the vortex ring centreline) by the relationship:

$$\psi(r,z) = \frac{\kappa\alpha r}{4\pi}\int_0^{2\pi}\frac{\cos\theta}{|\vec{s}|}\,\mathrm{d}\theta; \qquad (1)$$

and the velocities in the r and z direction, respectively, are:

$$u = \frac{\partial\psi}{r\partial z} = -\frac{\kappa\alpha}{4\pi}\int_0^{2\pi}\frac{(z-z_0-a)\cos\theta}{|\vec{s}|^3}\,\mathrm{d}\theta \qquad (2)$$

$$w = -\frac{\partial\psi}{r\partial r} = -\frac{\kappa\alpha}{4\pi r}\int_0^{2\pi}\frac{[(z-z_0-a)^2+a^2-ar\cos\theta]\cos\theta}{|\vec{s}|^3}\,\mathrm{d}\theta, \qquad (3)$$

where $|\vec{s}| = [(z-z_0-a)^2 + r^2 + a^2 - 2ra\cos\theta]^{1/2}$. If the vortex has a thin core of radius ε, a rough estimate is $\varepsilon \approx 0.13a$ [1]. Because Eqs. (1)-(3) are valid in an infinite space, while the stagnant vortex occurs in the semi-infinite space, the virtual image technique is applied, according to which a mirrored ring vortex of opposite vorticity is considered. The virtual vortex contributes to the replenishment of quantities lost out of the semi-infinite space.

The strength (or circulation) κ of the ring vortex is constant and independent of the shape of the curve containing the region of vorticity. For the present case, where the vortex ring is generated by the exit ring velocities, κ can be calculated by multiplying the tangential velocity with the perimeter of the maximum radius a of the circular vortex of the vortex ring and a shear stress coefficient c_s. The tangential velocity is considered to be about equal to the exit mean velocity w_0. Therefore, $\kappa = 2\pi a c_s w_0$. For a ring nozzle of a mean radius $R_0 = 6$ cm, the maximum vortex radius is $a = R_0/2 = 3$ cm. Thus, for $w_0 = 0.527$ m/s and $c_s = 0.005$, $\kappa = 5\times10^{-4}$ m^2/s and $\varepsilon \approx 0.39$ cm. In the present application, the internal solid bottom level is $z_0 = -0.005$ m. It is necessary that $|\vec{s}| \geq \varepsilon$, which implies that $(z-z_0-a)^2 + (r-a)^2 \geq \varepsilon^2$.

The streamlines and the velocity vector field derived by Eqs. (1)-(3) and using the values of parameters given above are shown in Fig. 1. The upward plume flow velocity field is not depicted in this diagram.

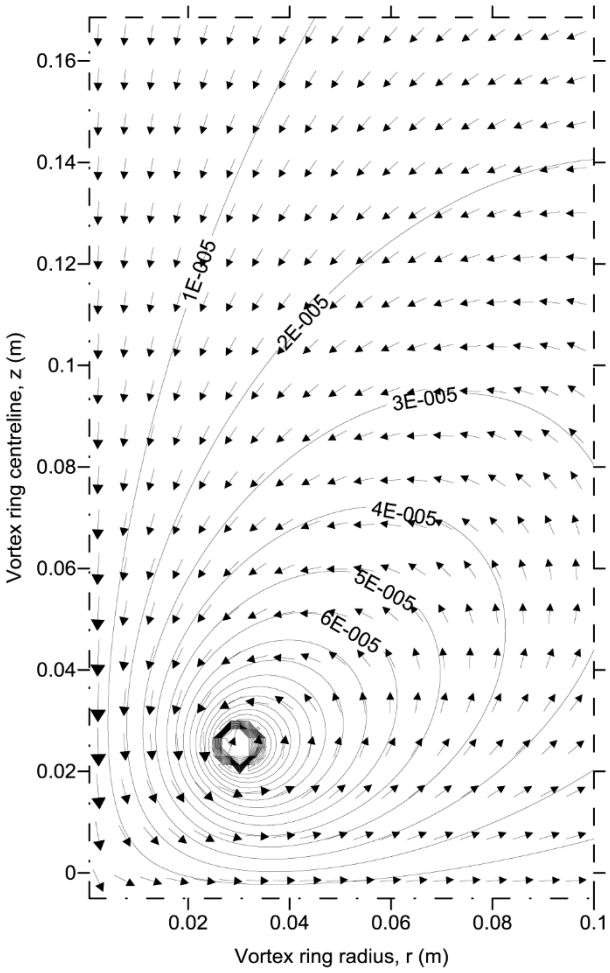

Fig. 1: Vertical cross-section of the vortex ring, showing the streamlines along with the velocity vectors on rz plane, as they are obtained by Eqs. (1)-(3), without the plume flow.

As shown in Fig. 1, the velocity vectors along the vortex ring centreline z, are directed downwards, and they become horizontal just above the solid bottom wall, as expected. In addition, the maximum values of velocities occur on z at the level of the vortex centre.

References

[1] Batchelor, G. K. *An Introduction to Fluid Dynamics*. Cambridge University Press, 2000.

Article S2.5

Flow visualization of transitional channel flow with polymer additive

Sattaya Yimprasert[1], P. Henrik Alfredsson[2], Masaharu Matsubara[1]*

[1]Department of Mechanical System Engineering Shinshu University, Nagano, Japan
[2]FLOW, Department of Engineering Mechanics, KTH Royal Institute of Technology, SE-100 44 Stockholm, Sweden
** Corresponding Author: mmatsu@shinshu-u.ac.jp*

ABSTRACT

The effects of polymer addition on flow fluctuations in transitional channel flow have been studied using flake particle flow visualization. In a certain Reynolds number range, a transitional state with coexistence of turbulent patches and streak structures, as also seen in Newtonian fluids, is here also observed. However, the transitional Reynolds number increases with the polymer concentration, indicating that the addition of polymers delays the transition to turbulence. It is also noted that as the polymer concentration increased, the streak spacing becomes wider and horizontally elongated streaks penetrate into the turbulent regions. These results indicate that the addition of polymers does not simply delay the turbulent transition, but also strongly affects the nature of the transitional flow.

KEYWORDS: Transitional channel flow, Polymers, Transition, Flow visualization

1. INTRODUCTION

Drag reduction by adding a polymer to wall bounded turbulent flows is known as the Toms Effect in honor of the discoverer of this phenomenon. It is still not fully understood and it is therefore still interesting to study the process and the causes of its occurrence. Lumley [1] was one of the first researchers to suggest that the flow dynamics can be altered by the expansion of the polymer molecules in water. This is consistent with the ideas by Bird et al. [2] and Toonder et al. [3] suggesting that the expansion and contraction of polymers are similar to a spring with a dashpot that absorbs fluctuating kinetic energy from the flow.

Another interesting aspect of polymer solutions affecting the flow is the phenomenon of transition from laminar to turbulent flow. Under Newtonian flow conditions, Patel and Head [4] conducted an experiment in a transitional channel flow to measure streamwise velocity fluctuation using a hot-wire anemometer and they observed intermittency in the range of $\mathbf{1380} \leq \boldsymbol{Re} \leq \mathbf{1800}$, where $\boldsymbol{Re}$ is defined with the mean (bulk) velocity and the channel width. Seki and Matsubara [5] estimated the transitional $\boldsymbol{Re}$ range from hot-wire measurements using the so called single slope method. They demonstrated that the transition starts at $\boldsymbol{Re} = \mathbf{1400}$ and ends at $\boldsymbol{Re} = \mathbf{2600}$. The flow visualization and drag measurement in a water channel flow performed by Yimprasert and Matsubara [6] supported this transitional *Re* range and found that in the middle of the transition the intermittency factor $\boldsymbol{\gamma}$ (turbulent fraction) increases linearly with $\boldsymbol{Re}$, forming a patchwork patten composed of turbulent and streaky regions.

Investigation of the effect of polymer addition on the transition in a pipe shear flow was done by Choueiri et al. [7] using Polyacrylamide (PAM) and Polyethylene Oxide (POE). The PAM experiments indicate that the skin friction coefficient at $\boldsymbol{Re} = \mathbf{3150}$ exceeds the Virk maximum drag reduction asymptote (MDR) [8] because of the transition delay due to the polymer addition. However, Chandra et al. [9] show that the skin friction asymptotes to the MDR line without going below the MDR limit. They also reported that polymer addition may cause relaminarization of the pipe flow.

In the present experiment, flow visualization experiments have been performed in order to investigate effects of polymer addition on flow fluctuations in a water channel flow, especially on the patchwork pattern that is observed in the middle of the transitional $\boldsymbol{Re}$ range in the pure water case.

2. EXPERIMENT SETUP

This experiment was carried out in a closed water channel flow facility. The channel is 7.1 mm wide and 7320 mm long and is connected to a nozzle with a contraction ratio of 25:1 installed in an upstream box. A tripping wire with a diameter of 0.9 mm and length of 220 mm is mounted on the sidewall 290 mm downstream of the nozzle to disturb the flow. By this wire disturbance and an expansion of the end wall spacing, which makes the Reynolds number 38 % lower, the flow at the inlet of the test section is highly disturbed. See [6] for details of the facility.

The flow visualization was performed 3000 mm downstream from the end of the wall expansion. To capture high-resolution photos and videos, pearl flakes with a density of 3.1 g/cm^3 and a particle size of 7 $\boldsymbol{\mu m}$ were added to the flow. Two inclined 500 watts halogen lights were used to illuminate the flow to detect the response of the flakes to the directions of the shear. The sizes and resolutions of the photo images are 182 × 122 $\boldsymbol{mm^2}$ and 4912 × 3264 pixels, where the numbers before and after the " × " sign represent the streamwise and spanwise directions, respectively. The polymer is Polyacrylamide (PAM, HF-840) which has a molecular weight of 1.1×10^7 g/mol. The polymer concentration is measured as the mass ratio $\boldsymbol{C = m/M}$, where $\boldsymbol{m}$ and $\boldsymbol{M}$ are the mass of the polymer and the solution, respectively. For convenience of analyses of the experimental results, Reynolds number $\boldsymbol{Re = U_m d/\nu}$, defined by the mean (bulk) velocity $\boldsymbol{U_m}$, the channel width d = 7.1 mm and viscosity of water ν, not the polymer solution, is used at first. Since viscosity of the aqueous polymer solution changes with both concentration of the PAM and shear of flow, the effective Reynolds number $\boldsymbol{Re_s}$ is determined from the skin friction coefficient $\boldsymbol{C_f = (\tau_w/0.5\rho U_m^2)}$ measured by the pressure drop in the laminar channel flow, where $\boldsymbol{\tau_w}$ is wall shear stress and $\boldsymbol{\rho}$ is density of the solution. $\boldsymbol{Re_s}$ is estimated from the relation

$$\boldsymbol{C_f = \frac{Re_s}{12}} \tag{1}$$

as a laminar channel flow of a Newtonian fluid. For high flow rates at which the flow is transitional or turbulent, extrapolation of the power law,

$$\boldsymbol{Re_s = aRe^n} \tag{2}$$

is used with a least-squares approximation to fix the constants $\boldsymbol{a}$ and $\boldsymbol{n}$. This power law is also used for interpolation at low flow rates.

3. EXPERIMENTAL RESULTS

3.1 TRANSITIONAL REYNOLDS NUMBER

Figure 1 shows typical flow visualization photographs at $Re_s = 1900$ at different polymer concentrations. The flow direction is from left to right. In a pure water case shown in Fig. 1a, as Yimprasert et al. [6] already reported, the flow is in a transitional state with a characteristic patchwork pattern involving turbulent patches and clusters of streaks. The typical streamwise and spanwise sizes of the turbulent patches are about $10d \times 5d$. The streak spacing z/d is approximately 0.64. The images at 10 to 30 ppm shown in Figs. 1b-d clearly indicate that the turbulent patches get sparser, shrinking in area, while the streaks become more noticeable due to their elongation. These tendencies continue with increasing polymer concentration up to $C = 70$ ppm. Comparing the cases of water and $C = 70$ ppm, it is obvious that the area covered by turbulent patches dramatically decreases and the streaks appear in higher contrast at $C = 70$ ppm. The length and spanwise spacing of the streaks increase with C. The widening of the streak spacing will be discussed later.

In order to quantitatively determine the delay of the transition to turbulence suggested by the apparent decrease in the area of turbulent patches in Fig. 1, a group of photographs at a certain $\boldsymbol{Re_s}$ was selected so that the intermittency ratio, the ratio of turbulent area to total area, is the same for each concentration, and the results are shown in Fig. 2. The number of photographs evaluated for each case is 10. The quantitative determination of $\boldsymbol{\gamma}$ follows the approach by Yimprasert et al. [6] for the water case. In Fig. 2a, $\boldsymbol{Re_s}$ for $\boldsymbol{\gamma}$= 0.03, 0.25 and 0.74 increase with the polymer concentration. This indicates that the addition of the polymer delay transition to turbulence, shifting the transitional $\boldsymbol{Re_s}$ range to higher values.

3.2 COMPARISON AT CONSTANT INTERMITTENCY FACTOR

Flow visualization at certain levels of the intermittency factor $\boldsymbol{\gamma}$ is presented for comparison of the patchwork patten and the structures of fluctuating flow. The first comparison shown in Fig. 3 is at $\boldsymbol{\gamma}$=0.03. Figure 3a shows a turbulent spot in a Newtonian flow (*C*=0 ppm) at *Re*=1400. In a video observation, the turbulence spot spreads into the laminar flow area in both the streamwise and spanwise directions. The spot has the characteristics of an arrowhead front, oblique waves on the side of the spot and streaks following the back of the spot, which first dissected by Carlson et al. [10]. These characteristics change with very small amount of the polymer addition as seen at *C*=10 ppm (Fig. 3b); the oblique waves disappear and the streaks downstream of the spot are almost parallel to the streamwise direction, getting longer and wider. The elongation and widening of the streaks are also seen at the upstream side of the spot. Increasing *C*, the streaks become longer and wider as seen in Figs. 3c-f, then the streaks at *C*=50 and 70 ppm, runs from the left edge to the right edge of the image, and some of the streaks penetrate into the turbulent spots.

As seen in Fig. 4, the flow changes to the patchwork pattern when γ increases to 0.25. In contrast to the lower γ flow, the turbulent and streak regions of the water flow at *Re*=1600 continuously contact each other, and the purely laminar parts disappear. Furthermore, the features of turbulent spots such as oblique waves described by Carlson et al. [10] are not seen around the turbulent parts except the streaks. Yimprasert et al. [6] pointed out that the transitional channel flow of pure water above *Re*=1500 is in an equilibrium state balancing generation and extinction of turbulence at boundaries between turbulent and non-turbulent laminar regions. The fact that the patchwork pattern is maintained even with increasing polymer concentration up to $C = 70$ ppm indicates that the flow at $\gamma = 0.25$ is in such an equilibrium state regardless of the polymer addition. The effects of polymer addition observed at γ = 0.03, such as the streaks observed at lower γ values become more pronounced and the tendency for the streaks to be more widely spaced, are also observed at γ = 0.25. Especially the penetration of the streak through the turbulent patches are observed, as seen in the bottom of Fig. 4f.

3.3 SPANWISE SPACINGS OF THE STREAKS

The measured spanwise spacings of the streaks z/d are shown in Fig. 5. For the quantification ten photographs are used for each case. Figure 5a is illustrated in the form at constant Re_s of 1500, 1700 and 1900. Regardless of the constant Re_s, which means the viscous force to the inertial force is effectively constant, the streak spanwise spacings z/d widen with increasing polymer concentration C. The ratios of the spacings at concentration of 70 ppm to those of the pure water flow are 1.66, 1.67, and 1.84 for Re_s= 1500, 1700 and 1900, respectively.

As shown in Fig. 5b illustrated in the form at constant γ of 0.03, 0.25 and 0.74, even at the constant γ, the streak spacing increases with C. The ratios of the spacing at C =70 ppm are 1.42, 1.37, and 1.52 for γ =0.03, 0.25 and 0.74, respectively. An explanation why the spacing expansion at constant γ are smaller than those at constant Re_s is that Re_s is higher for the same γ and the same C. In most turbulent flows attenuation by the viscosity prevents activity of the small-scale fluctuations of the flow, so that in general the scale of fluctuations becomes larger in average with decreasing Reynolds number. The fact that the drastic expansion of the streak spacings even measured at constant γ and that the streaks penetrate

through the turbulent patches demonstrate that polymer addition to water channel flow does not only delay transition to turbulence, but also strongly affects the structures of the flow fluctuations.

4. CONCLUSIONS

In order to investigate the effect of polymer addition on a transitional water channel flow, flow visualization was performed. The results show that the transitional Reynolds number increases with increasing polymer concentration. It was also found that spanwise spacing of the streaks increases with the addition of the polymer, and that the streaks became very long through the turbulent regions. These results indicate that the addition of the polymer not only delays the transition but also strongly affects the fluctuating structure of the flow.

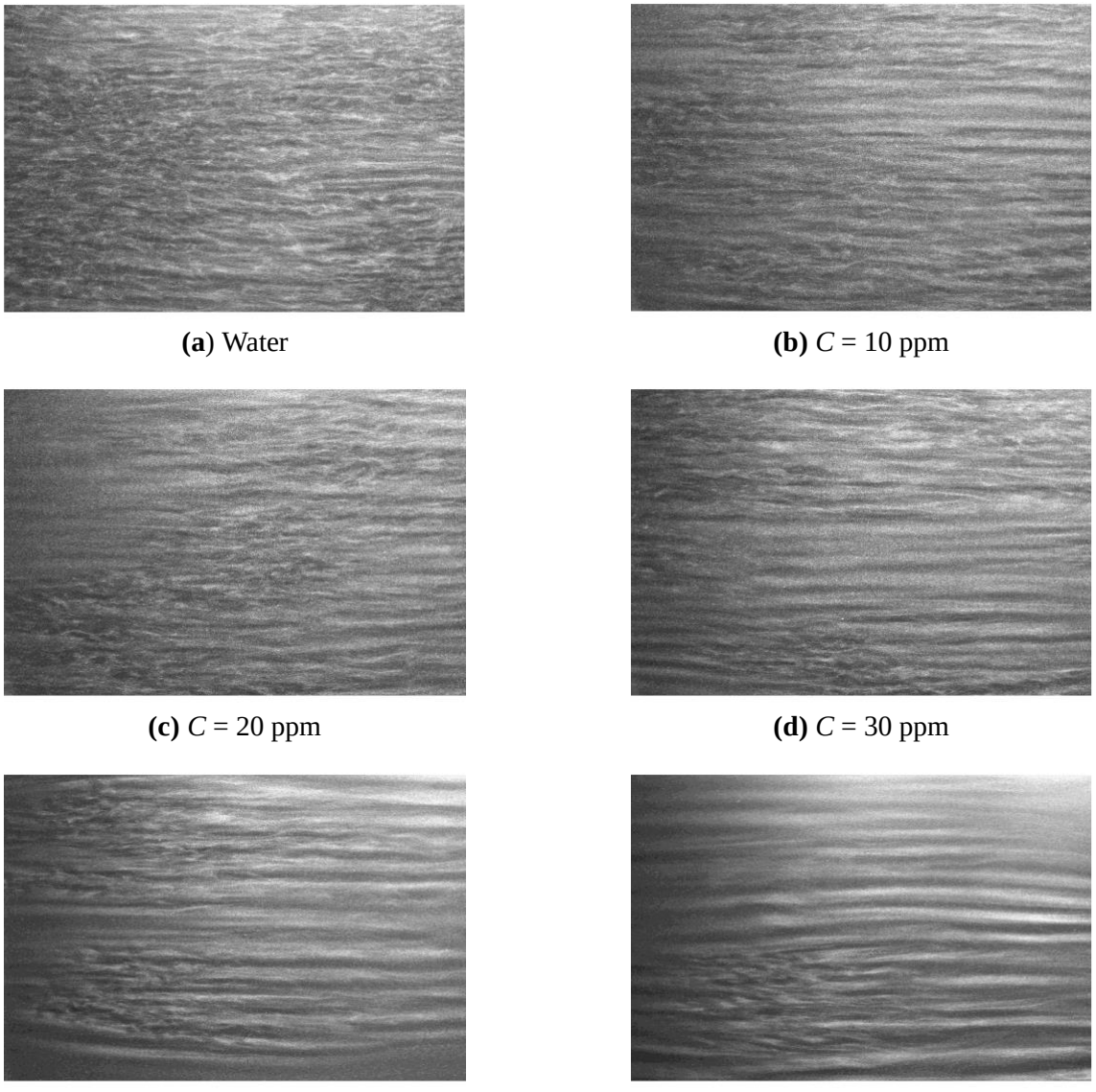

(a) Water

(b) C = 10 ppm

(c) C = 20 ppm

(d) C = 30 ppm

(e) C = 50 ppm

(f) C = 70 ppm

Fig. 1 Flow visualization at $\boldsymbol{Re_s = 1900}$.

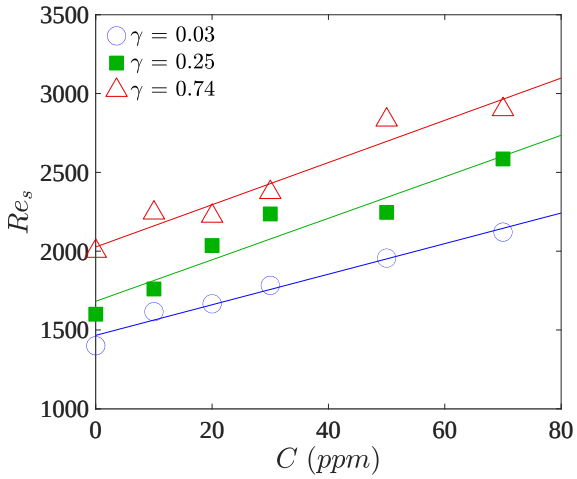

Fig. 2 Effect of the polymer addition on transition Reynolds number.

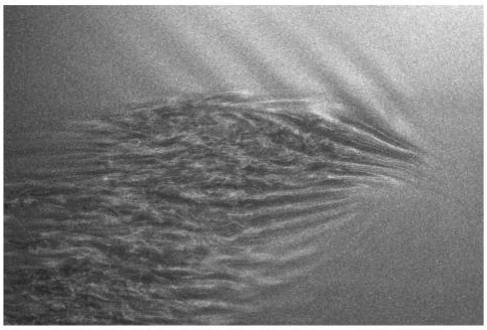

(a) Water (Re_s = 1400)

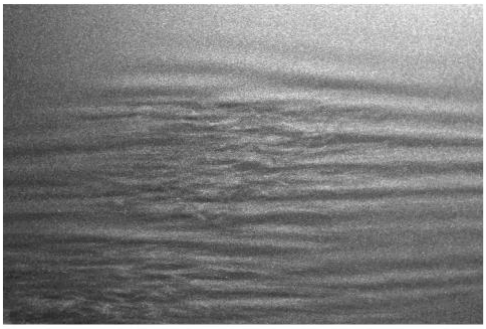

(b) C = 10 ppm (Re_s = 1623)

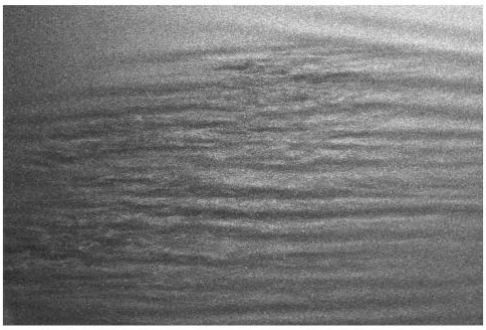

(c) C = 20 ppm (Re_s = 1671)

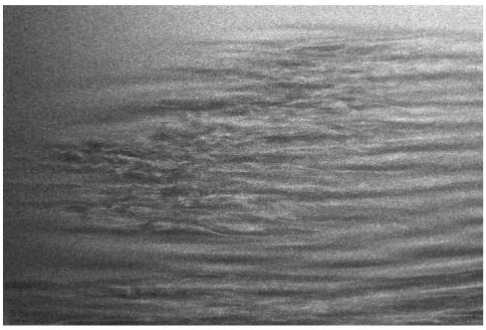

(d) C = 30 ppm (Re_s = 1711)

(e) C = 50 ppm (Re_s = 1916)

(f) C = 70 ppm (Re_s = 2100)

Fig. 3 Flow visualization at $\boldsymbol{\gamma = 0.03}$.

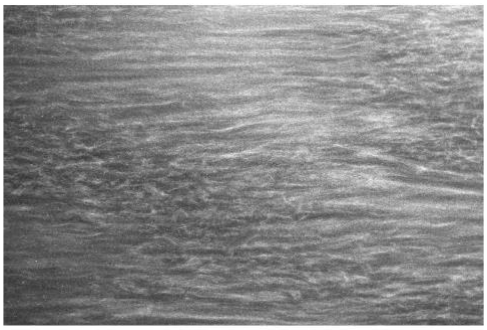

(a) Water (Re_s = 1600)

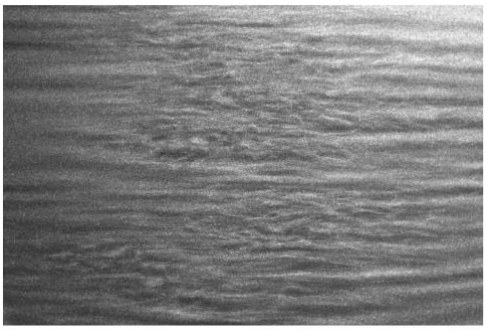

(b) C = 10 ppm (Re_s = 1770)

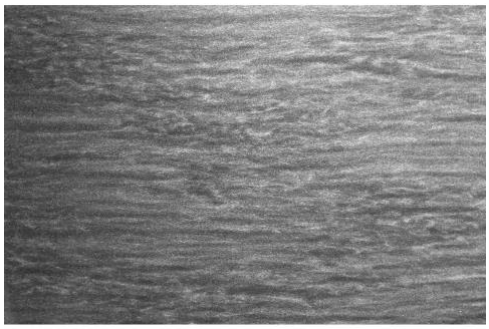

(c) C = 20 ppm (Re_s = 2048)

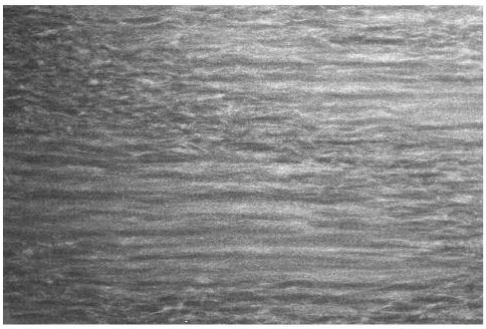

(d) C = 30 ppm (Re_s = 2151)

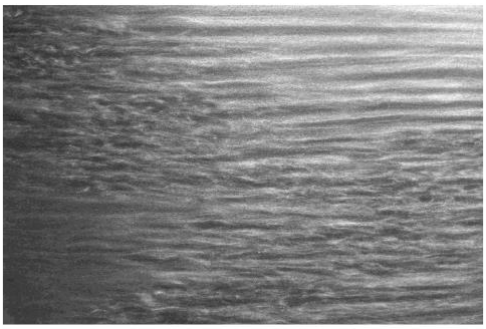

(e) C = 50 ppm (Re_s = 2206)

(f) C = 70 ppm (Re_s = 2572)

Fig. 4 Flow visualization at $\boldsymbol{\gamma = 0.25}$.

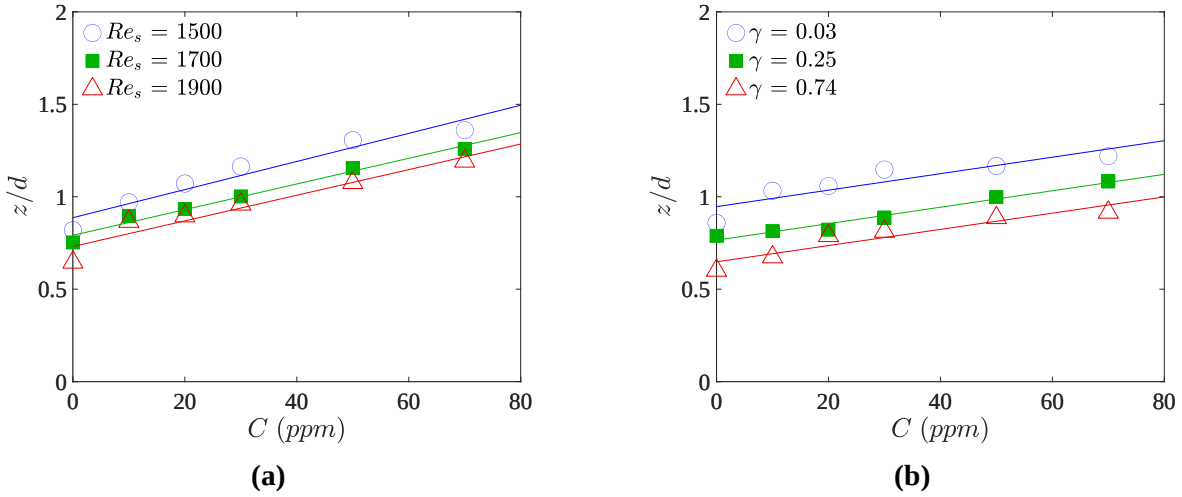

Fig. 5 Spanwise spacing of the streaks z/d versus polymer concentration C. (a) at constant Re_s. (b) at constant γ.

REFERENCE

[1] Lumley JL. Drag reduction in turbulent flow by polymer additives. J. Polym. Sci. Macromol. Rev., 1973, 7:263-290

[2] Bird RB, Dotson PJ, Johnson NL. Polymer solution rheology based on a finitely extensible bead-spring chain model. J. Non-Newtonian Fluid Mech., 1980, 7:213-235

[3] Den Toonder JMJ, Hulsen MA, Kuiken GDC, Nieuwstadt FTM. Drag reduction by polymer additive in a turbulent pipe flow: numerical and laboratory experiment. J. Fluid Mech., 1997, 337:193-231

[4] Patel VC, Head MR. Some observation on skin friction and velocity profile in fully developed pipe and channel flow. J. Fluid Mech., 1969, 38:181-201

[5] Seki D, Matsubara M. Experimental investigation of relaminarizing and transitional channel flows. Phys. Fluids, 2012, 24:1-23

[6] Yimprasert S, Kvick M, Alfredsson PH, Matsubara M. Flow visualization and skin friction determination in transitional channel flow. Exp. Fluids, 2021, 62(31):1-16

[7] Choueiri H George, Lopez M Jose, Hof B. Exceeding the Asymptotic Limit of Polymer Drag Reduction. Phys. Rev. Lett., 2018, 120(124501):1-5

[8] Virk PS. Drag reduction fundamentals. AlChE J., 1975, 21(4):625-656

[9] Chandra B, Shankar V, Das D. Early transition, Relaminarization and drag reduction in the flow of polymer solutions through microtubes. J. Fluid Mech., 2020, 885(A47):1-34

[10] Carlson DR, Widnall SE, Peeters MF. A flow visualization study of transition in plane Poiseuille flow. J. Fluid Mech., 1982, 121:485-505

Micropolar Theory on Turbulence Modulation

George Sofiadis[1*], Evangelos Karvelas[2] and Ioannis Sarris[2]
[1]*Department of Mechanical Engineering, University of Thessaly, 38334, Volos, Greece*
[2]*Department of Mechanical Engineering, University of West Attica, Athens, Greece*
** Corresponding Author: sofiadis@uth.gr*

Fluids with internal rigid microstructure, the so-called micropolar fluids, gain significant attention in many industrial, natural and biological systems. Typical examples of such fluids are dense suspensions, liquid crystals and blood flow. Here we study in detail their turbulent regime by considering an alternative formulation of the Navier-Stokes equation in which the linear and angular momentum is conserved for the fluid and its microstructure, respectively. Three cases of low-turbulence channel flow with Re = 3300, 5600 and 13800, based on mean velocity, channel height and the fluid kinematic viscosity are used to study the effect of polarity and Re.

Micropolar theory was originally developed by Eringen [1]. In his work, Eringen introduces a simple generalization of the usual Navier-Stokes equation system, the so-called micropolar equations, where due to internal fluid structure microrotation, an angular momentum conservation equation is also solved. In addition, new viscosity coefficients appear in the system of governing equations, as the main role of microrotation is to increase the dissipation of kinetic energy. These equations may be reduced to the classical Navier-Stokes equations when microrotation viscosity coefficients are diminished.

In the present study, Direct Numerical Simulations (DNS) of a turbulent channel flow with internal microstructure have been performed. The set of equations that has been solved (1) and (2), together with the incompressibility condition, $\nabla \cdot u = 0$, has been properly nondimensionalized as:

$$\frac{\partial \mathrm{u}}{\partial \mathrm{t}} + (\mathrm{u}\cdot\nabla)\mathrm{u} = -\nabla \mathrm{P} + \frac{1}{\mathrm{Re}}\nabla^2 \mathrm{u} + \frac{\mathrm{m}}{\mathrm{Re}}\nabla \times \omega \qquad (1)$$

$$\frac{JN}{m}\left(\frac{\partial \omega}{\partial t} + (u\cdot\nabla)\omega\right) = \frac{1}{Re}\nabla^2\omega + \frac{N}{Re}\nabla \times u - 2\frac{N}{Re}\omega \qquad (2)$$

where, u and ω are the linear and angular velocity, respectively, and P stands for pressure. Except of Reynolds number, the rest non-dimensional parameters are: $m = \kappa/(\mu + \kappa)$ the so-called vortex viscosity parameter where κ is the micropolar viscosity and μ the molecular one, $J = j/\delta^2$ the dimensionless microrotation based on δ^2, where j is the microinertia of the fluid, and $N = \kappa\delta^2/\gamma$ the so-called spin gradient viscosity parameter, where γ is the material coefficient of the fluid.

Three different Reynolds numbers are considered in the low Reynolds turbulent regime, while the ratio of micropolar to total viscosity *(m)*, has been varied as well, where micropolar viscosity is the one of the dispersed phase. Our findings support that turbulence behavior is affected by both *m* and *Re* [2]. Previous studies have also reported modulation of the turbulence activity in dilute suspensions, although the majority of these studies only considers the effect of particle diameter. They mostly report a turbulence attenuation when the particle diameter is less than the turbulent length scale. For low micropolar volume fractions, turbulence presents a monotonic enhancement as the Reynolds number increases. However, on the other hand, for sufficiently high-volume fractions, turbulence intensity drops, along with Reynolds number increment Fig. 1 [2]. This result is considered to be due to the effect of the micropolar force term on the flow, suppressing near-wall turbulence and enforcing turbulence activity to move further away from the wall.

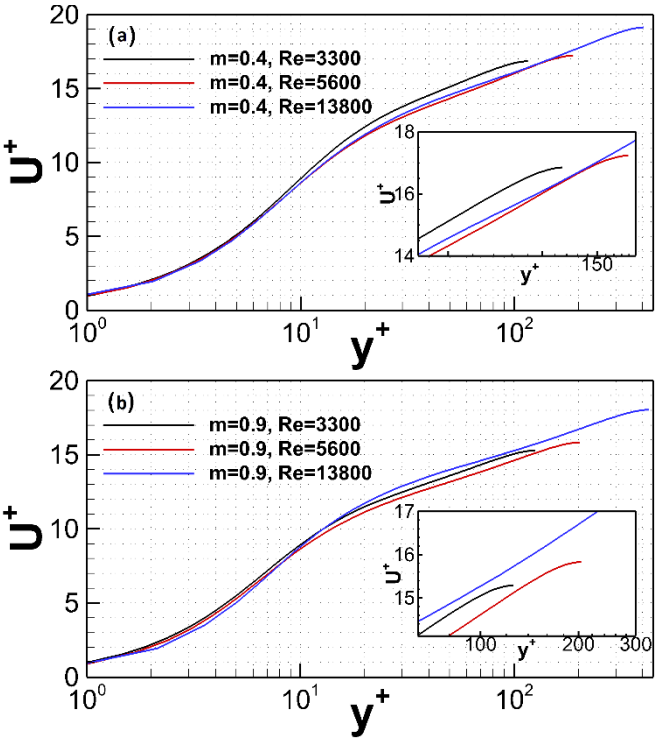

Fig. 1: Normalized mean streamwise velocity distributions along y+, for: m = 0.4, Re = 3300, 5600, 13800 and m = 0.9, Re = 3300, 5600, 13800 cases [2].

References

[1] Eringen, A.C. Theory of Micropolar Fluids; Technical Report; Purdue University: West Lafayette, Indiana, 1965; Volume 27.
[2] Sofiadis, G., and I. Sarris. Turbulence Intensity Modulation by Micropolar Fluids." Fluids 6, no. 6 (2021): 195.

Keynote Lecture

Oleg Goushcha
National Aeronautics and Space Administration (NASA), Langley, VA.
Adjunct Assistant Professor, Manhattan College, Riverdale, NY., USA

Oleg Goushcha combines his work at NASA with an Assistant Professorship in Mechanical Engineering. His research focuses on experimental fluid mechanics studying turbulent, transitional and vortical flows. Previous and current work include wind tunnel tests of passive-scalar mixing and energy harvesting in turbulent flows, fluid-structure interaction, and transition to turbulence and relaminarization in pulsating flows. His research is inspired by current needs in the clean technology and biomedical industries. Close interaction between academia and industry drives Dr. Goushcha to provide his students with theoretical tools and their practical applications in the industry.
Dr. Goushcha holds a B.S. and a M.S. in Aerospace Engineering, from the University of California, Irvine, and a Ph.D. in Mechanical Engineering, from The City College of New York. He has received several awards and grants from the City College of New York,

and

Yannis Andreopoulos
CUNY Distinguished Professor
Michael Pope Chair for Energy Research, Department of Mechanical Engineering
The Grove School of Engineering, The City College of New York, USA

Yannis Andreopoulos holds the Michael Pope Chair for Energy Research and is Professor of Mechanical Engineering at The Grove School of Engineering at The City College of New York. His research expertise is in the areas of fluid dynamics which impact transportation, manufacturing, medicine, biology, energy, the environment, built environment, climate change and defense and homeland security. Andreopoulos has developed several innovative experimental techniques and designed a large-scale wind tunnel and a unique high energy/enthalpy experimental shock tube research facility for studies in various configurations where high spatial and temporal resolution is required.
Andreopoulos holds an Engineering Diploma (Dipl.-Ing) in Mechanical and Electrical Engineering from the National Technical University in Athens, Greece, a M.Sc. (Aeronautics) from London University in England, a Diploma of Imperial College degree (D.I.C) and a PhD in aeronautical engineering from Imperial College of Science, Technology and Medicine of London University, UK. He held postdoctoral research appointments at the University of Karlsruhe, Germany, and at Princeton University where he gained extensive experience in laser techniques and optical methods.
Yannis Andreopoulos has been unanimously elevated by the CUNY Board of Trustees, to the rank of Distinguished Professor, the highest academic honor that CUNY can bestow upon faculty who have reached exceptional scholarly achievement.

Lecture title:

Vortices interacting with smart materials and structures: the case of energy harvesting

by Oleg Goushcha, Vahid Azadeh Ranjbar, Yiannis Andreopoulos

The lack of understanding and the complexity of vortex induced vibration (VIV) physics combined with a diverse range of applications have motivated a number of studies in this field. While large vibration amplitude due to VIV in general should be avoided in the design of engineering systems since the induced deflections can cause significant structural stresses, new applications related to harnessing small-scale energy from the ambient environment using VIV have emerged in the last decade which have revived the interest in this field. Recent advances in decreasing the power consumption of electronic devices, such as remote sensors, have bolstered the interest in clean and renewable energy harvesting. Converting ambient mechanical vibration to electrical power by using electromechanically coupled smart materials has been the main focus of the present energy-harvesting research. In the last several years, research has concentrated on harvesting energy from fluid flows, which otherwise is wasted, by using vibrating structures, mostly cantilever beams with piezoelectric layers, which are excited by fluid-structure interaction. The presentation will include configurations that can be classified as interactions with forcing stimuli provided by coherent fluid structures such as vortices with distinct travel frequency and spacing, like those in the wake of cylinders, discrete vortex rings, or randomly appearing turbulent eddies in boundary layers or grid turbulence. The excited motion of the structure with the piezoelectric transduction can lead to simple vibrations by flutter or complex VIV.

Keynote Lecture

Xiande Fang
Distinguished Professor
Nanjing University of Aeronautics and Astronautics (NUAA), China

Xiande Fang is a distinguished professor at Nanjing University of Aeronautics and Astronautics (NUAA), China. He received his Ph.D. in Engineering Thermophysics from University of Science and Technology of China, M. Sci. in Thermal Engineering from Tsinghua University, China, and B. Eng. in Altitude Equipment from NUAA. He is currently an Associate Editor, Aerospace Science and Technology (SCI indexed top journal), and the Editor-in-Chief, International Journal of Thermofluid Science and Technology. He worked as an associate researcher in USA for one year, and as a visiting professor and professional engineer in Canada over 5 years. In NUAA, he serves as the deputy director of Academic Committee of MIIT Key Laboratory of Aircraft Environment Control and Life Support and the director of Professional Committee of Building Environment and Energy Engineering and Aircraft Environment Control and Life Support Engineering. His research area is thermofluid science and technology and its applications to various industrial sectors. He has published over 200 papers and 4 books/book chapters, received 14 academic awards, and obtained 15 Chinese patents. He teaches thermofluid-related courses to international undergraduate, postgraduate, and doctoral students in China.

Lecture title:
Empirical Predictive Method for Two-Phase Flow Condensation Heat Transfer in Plain Channels

Keynote S4.K1

Empirical Predictive Method for Two-Phase Flow Condensation Heat Transfer in Plain Channels

Xiande Fang*, Xiaohuan Li, Zufen Luo

Key Laboratory of Aircraft Environment Control and Life Support, MIIT, Nanjing University of Aeronautics and Astronautics, 29 Yudao Street, Nanjing 210016, PR China
** Corresponding Author: Tel: 86-25-84896381, Email: xd_fang@nuaa.edu.cn*

ABSTRACT

The flow condensation heat transfer in plain channels has a variety of applications, which makes it important to accurately predict flow condensation heat transfer coefficient (HTC). Although a number of correlations, or called empirical predictive methods, for condensation HTCs exist, it is still in need to develop an accurate one for a broad application range. This paper presents a general correlation with high prediction accuracy for flow condensation heat transfer in plain channels of various sizes and a broad operational parameter range. A large compound database of condensation heat transfer containing 5607 data points and 30 fluids was compiled from 52 sources for developing the new correlation. The parameter range is diameter or hydraulic diameter D = 0.493–20 mm, vapor quality x = 0.003–0.992, mass flux G = 24–1533 kg/m^2 s, heat flux q = 2.9–422 kW/m^2, reduced pressure p_r = 0.04–0.95, liquid Prandtl number Pr_l = 1.7–8.5, liquid Reynolds number Re_l = 11.6–5.3×10^4, and gas Reynolds number Re_g = 75.1–9.1×10^5. The new correlation has very high accuracy, predicting the entire database, $D \le 3$ mm data, and $D > 3$ mm data with MADs of 14.1%, 16.8%, and 12.8%, respectively, much better than the best ΔT-independent correlation among the 37 existing correlations. The best ΔT-independent correlation predicts the entire database, $D \le 3$ mm data, and $D > 3$ mm data with MADs of 20.1%, 18.9%, and 22.3%, respectively. The applicability of the new and 37 existing correlations to individual fluids is assessed, which is helpful for choosing a proper correlation for the given application of the design and development of the related equipment and systems. The new correlation performs best for 10 fluids and appears 7 times for the others among the 21 fluids evaluated, in total 17 times as the top five correlations for the 21 individual fluids. Also proposed is the strategy for developing a new correlation.

KEYWORDS: flow condensation; heat transfer coefficient; correlation; conventional channel; minichannel.

1. INTRODUCTION

The flow condensation heat transfer in plain channels is widely used in many industrial sectors, such as refrigeration, air conditioning, process engineering, thermal power generation, and aerospace engineering [1–3]. It is important to predict accurately the flow condensation heat transfer coefficient (HTC) for the design and development of such equipment and systems [4, 5].

Two important events spurred the rapid development of flow condensation heat transfer in channels: Miniaturization and the Montreal protocol on substances that deplete the ozone layer. Miniaturization demands mini/micro-scale thermo-fluid systems, stimulating investigations of flow condensation heat transfer in mini/micro-channels [4, 6, 7]. The Montreal protocol [8] led to phase out CFCs and HCFCs refrigerants and promoted extensive research into flow condensation heat transfer of alterative refrigerants [9, 10].

The extensive studies of flow condensation heat transfer have yielded a large number of correlations, or called empirical predictive methods, for condensation HTC. Many reviews and assessments with

NOMENCLATURE

A	tube cross-sectional area (m^2)
Bd	Bond number
Ca	capillary number
c_p	specific heat at constant pressure (kJ/kg K)
D	tube diameter, hydraulic diameter (m)
D_h	hydraulic diameter (m)
Fa	Fang number
Fr	Froude number
G	mass flux (kg/m^2 s)
Ga	Galileo number
Gr	Grashof number
g	gravitational acceleration (m/s^2)
h	heat transfer coefficient (kW/m^2 K)
h_{lg}	latent heat of vaporization (kJ/kg)
J	dimensionless superficial velocity
J_g	dimensionless vapor velocity
Ja	Jakob number
L	length of tube (m)
Nu	Nusselt number
Pr	Prandtl number
p	pressure (Pa)
p_r	reduced pressure, $p_r = p/p_{crit}$
q	heat flux (kW/m^2)
Re	Reynolds number
Su	Suratman number
T	temperature (K)
ΔT	excess temperature (K), $\Delta T = T_{sat} - T_w$
We	Weber number
We^*	modified Weber number
X	Lockhart-Martinelli parameter
x	vapor quality

Greek Symbols	
α	void fraction
δ	thickness (m)
θ	angle (rad)
λ	thermal conductivity (W/m K)
μ	dynamic viscosity (Pa s)
ρ	density (kg/m^3)
σ	surface tension (N/m)
ϕ_g	gas friction multiplier
ϕ_{lo}^2	liquid only friction multiplier
Subscripts	
annul	annular flow
crit	critical
exp	experimental
film	film condensation
forced	forced condensation
g	gas (vapor)
go	Gas only
l	liquid
lo	liquid-only
pred	predicted
sat	saturation
slug	slug flow
strat	stratified flow
top	top
tp	two-phase mixture
trans	transition
tt	turbulent liquid–turbulent gas
w	wall
wavy	wavy flow

large compound database for condensation HTC in plain tubes have been reported, including several in the past decade, including Kim and Mudawar [11] (2014), Zhang et al. [12] (2015), Shah [13] (2019), Rifert et al. [14] (2020), and Moreira et al. [9] (2021).

Kim and Mudawar [11, 15] compiled a database of flow condensation heat transfer from 28 sources. It contained 4045 data points, including 3332 annular flow data corresponding to $We^* > 7X_{tt}^{0.2}$ and 713 slug and bubbly flow data. The definitions of the modified Weber number We^* and turbulent liquid–turbulent gas Lockhart-Martinelli parameter X_{tt} are provided later. The parameter range was the hydraulic diameter D_h = 0.424–6.22 mm, mass flux G = 53–1403 kg/m^{2}s, reduced pressure p_r = 0.04 to 0.91, vapor quality x = 0–1, and the liquid only Reynolds number Re_{lo} = 276–89,798. Based on the database, 12 HTC correlations of flow condensation were assessed, including [15] that was developed based on the database, Akers and Rosson [16], Moser et al. [17], Shah [18, 19], Wang et al. [20], Cavallini and Zecchin [21], Haraguchi et al. [22], Dobson and Chato [23], Koyama et al. [24], Huang et al. [25], Park et al. [26], and Bohdal et al. [27]. The results showed that three correlations had MAD ≤ 30%, which are Kim and Mudawar [15] having MAD = 16.0% for the entire database, and Akers and Rosson [16] having MAD = 27.3% and Moser et al. [17] having MAD = 27.7% for the annular flow data.

Zhang et al. [12] compiled an experimental database of flow condensation heat transfer in horizontal tubes, which consisted of 2563 data points from 26 published articles and included 17 different fluids,

with the parameter range of D_h = 0.493–20 mm, G = 24–1532.1 kg/m^{2}s, x = 0–1, heat flux q = 2.35–421.14 kW/m^2, and saturation temperature T_{sat} = (–25.6)–70.7 °C. With the database, they evaluated 28 correlations, among which 12 have MAD ≤ 30%, including Cavallini et al. [28] (MAD = 17.0%), Bivens and Yokozeki [29] (21.6%), Haraguchi et al. [22] (22.6%), Cavallini et al. [30] (22.7%), Koyama et al. [24] (23.6%), Koyama et al. [31] (24.3%), Dobson and Chato [23] (24.9%), Tang et al. [33] (25.0%), Thome et al. [34] (25.1%), Moser et al. [17] (25.4%), Huang et al. [25] (25.9%), and Chen et al. [35] (26.3%).

Shah [13] obtained a database of flow condensation heat transfer in channels of various shapes and orientations, which contains 5100 data points from 88 sources covering 40 fluids, with hydraulic diameter D_h = 0.08–49.0 mm, reduced pressure p_r = 0.0008–0.946, and mass flux G = 1.1–1400 kg/m^{2}s. The database included around 4000 data from that used in Shah [5]. With the database, seven existing correlations were evaluated and two new correlations were proposed. In Shah [5] and [13], each has two correlations, here just the better ones are included. Among the seven existing correlations, five had MAD ≤ 30%, which are Shah [5], Shah [36] which is identical to Shah [18] as implied by Shah [13], Ananiev et al. [37], Dorao and Fernandez [38], and Kim and Mudawar [15], with the mean absolute deviations (MADs) of 19.1%, 20.5%, 26.4%, 27.1%, and 27.9%, respectively. Among the two new correlations, the better one has an MAD of 18.6%. The rest two existing correlations evaluated were Moser et al. [17] and Akers et al. [39], with the MAD of 35.0% and 68.9%, respectively. Shah [13] indicated that the correlations of Cavallini et al. [28], Thome et al. [34], and Dobson and Chato [23] agreed with a wide range of data, and they were not included in the evaluation because they required either heat flux q or excess temperature ΔT to be known.

Rifert et al. [14] presented a comprehensive review of experimental research on condensation heat transfer inside plain tubes. More than 40 condensation HTC correlations were evaluated with the 14 sources of experimental data from different authors for different fluids and flow conditions. The correlations providing the deviation of ± 25% for individual data sources were those of the Cavallini et al. [28] (for 5 data sources), Thome et al. [34] (for 4 data sources), Shah [5] (for 4 data sources), Dobson and Chato [23] (for 2 data sources), and Zhuang et al. [40] (for 1 data source). Shah [18] and Dorao and Fernandez [38], which had good accuracy as per the Shah [13] assessment, did not predict any of the 14 sources in ± 25%. There was no any indication that how many data points were obtained from the data sources, and no MAD information provided, which makes the evaluation results not convincing.

Moreira et al. [9] compiled a database of flow condensation heat transfer of hydrocarbons, which contained 960 data points from 9 sources and involves four fluids, including R290, R600, R600a, and R1270, with channel hydraulic diameter D_h = 4–20.8 mm and mass flux G = 32–400 kg/m^{2}s. Eighteen correlations of flow condensation HTC were compared with the database, including Shah [18, 19], Kim and Mudawar [15], Moser et al. [17], Wang et al. [20], Cavallini and Zecchin [21], Haraguchi et al. [22], Dobson and Chato [23], Koyama et al. [24], Cavallini et al. [28], Thome et al. [34], Akers et al. [39], Jung et al. [41], Chang et al. [42], Jaster and Kosky [43], Traviss et al. [44], Tandon et al. [45], Macdonald and Garimella [46]. Among them, four had MAD ≤ 30%, which are Thome et al. [34] (MAD = 23.4%), Cavallini et al. [28] (24.5%), Shah [18] (25.3%), and Jung et al. [41] (28.0%).
The above recent evaluations of correlations for flow condensation HTC with large compound databases showed that the accuracy of the existing correlations remains an issue needing to be improved. Kim and Mudawar [15] reported that the correlation developed based on their database of 4045 data points predicted the database with MAD = 16.0%. Shah [13] reported that the correlation developed based on his database of 5100 data points predicted the database with MAD = 18.6%, and his equations [5, 15] had the MAD of 19.1% and 20.5%, respectively. However, evaluations from other researchers showed large discrepancy between theirs and the original authors'. Shah [13] found that the Kim and Mudawar [15] correlation had an MAD of 27.9% for his database of 5100 data points. Moreira et al. [9] found that the Shah [5] correlation had an MAD of 30.5% for their 428 microchannel data and the Shah [18] correlation had an MAD of 27.9% for the entire database of 1388 data points. Many researchers reported good predictions by the Cavallini et al. [28] correlation. However, it requires the excess temperature ΔT to be known [28, 13]. The prediction performance would be adversely affected if ΔT is unknown. The

necessity for a high accurate correlation of flow condensation HTC can also be seen from the fact that many new ones have been proposed continuously, such as Pham and Oh [47] (2021), Jacob and Fronk [48] (2021), and Moreira et al. [49] (2021).

The primary goal of the present study is to develop a general correlation for flow condensation HTC that has high accuracy for a wide range of parameters. A strategy for developing the new correlation is worked out to guide the whole process of the correlation development. The first step is to compile a large compound database of flow condensation HTC, which is the largest of this kind reported so far. Secondly, the existing correlations of flow condensation HTC, including the newest ones and those having a good record in any other assessment, are evaluated to unearth ideas for developing a new correlation. An emphasis is put on the ΔT-independent correlations that predict the present database with MAD ≤ 30%, including the mathematical expressions and the dimensionless parameters incorporated. From this point on, the relationships between the Nusselt number Nu and other two-phase flow dimensionless parameters are explored to identify different heat transfer regimes to guide the partition of heat transfer regimes for constructing a piecewise correlation. Then, several tentative model forms are constructed, from which computer tests with the methods of the least squares and error analysis are conducted, until a satisfied new correlation is obtained. The comparison between the new correlation and the best existing correlations are also made, and the top five correlations for each refrigerant are identified to provide guide for scientific and engineering applications.

2. DATABASE DESCRIPTION

A compound database of condensation heat transfer was compiled from 52 sources, containing 5607 data points and covers 30 fluids from both minichannels and conventional channels. Several classifications of channels have been proposed, as briefly discussed in [50, 51], among which the Kandlikar and Grande [52] method is more popular and adopted in the present paper to classify minichannels (0.2 mm < D_h ≤ 3 mm) and conventional channels (D_h > 3 mm).

The 30 fluids include 12 pure halocarbon refrigerants (R12, R123, R1234ze(E), R1234yf, R125, R161, R134a, R152a, R22, R245fa, R32, and R41) (Table 1), 9 halocarbon refrigerant blends (R404A, R407C, R410A, R417A, R448A, R449A, R454C, 60%R32/40%R125, and 60%R152a/40%R1234ze(E)) (Table 2), and 9 hydrocarbon refrigerants (R1270, R170, R290, R50, R600, R600a, CO_2, DME, and 50%R600/50%R290) (Table 3). Fig. 1 shows the data distribution as per fluid, where the mixtures include 60%R32/40%R125, 60%R152a/40%R1234ze(E), and 50%R600/50%R290.

The following is the ranges of important parameters of the database.

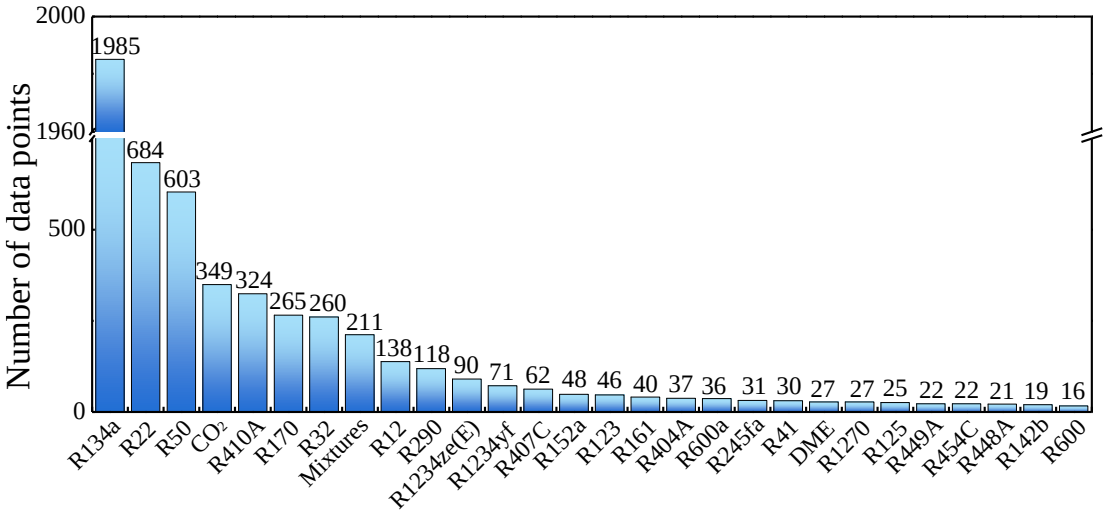

Fig. 1 Data distribution as per fluid

Table 1 Experimental data of pure halocarbon refrigerants.

Data source	Fluid	Parameter range: T_{sat} (°C)/p_{sat} (bar)/G (kg/m^2 s)/q (kW/ m^2)/x	Geometry range: D (mm)/L (mm)/ Orientation/Tube type	Data points
Azzolin et al. [7]	R134a	40/10.2/50–200/25–36/0.1–0.9	3.4/1020/H [a] & vertical downward/SCCT	111
Haraguchi et al. [22]	R22, R123, R134a	47.91–70.67/3.8–18.5/300/14.42–27.3 /0.03–0.95	8.4/6000/H [a]/SCCT	30
Jung et al. [41]	R12, R123, R125, R134a, R142b, R22, R32	40/5.23–24.78/100,300/7.5/ 0.1–1	8.82/1000/H/SCCT	188
Traviss et al. [44]	R12, R22	21.4–59/5.9–18.3/161.1–59/7.86–85.43/ 0.02–0.96	8.001/5029/H/SCCT	161
Dobson et al. [32, 53]	R22, R134a	35–45/8.9–27.6/69–512/3.12–16.08/ 0.08–0.96	4.572/NA[b]/SCCT	77
	R22, R134a	33.546.4/8.528.5/24812/2.9854.95/ 0.02–0.95	3.14, 7.04/NA/SCCT	445
Shin and Kim [54,55]	R134a	40/10.2/200/6–20/0.12–0.85	0.493/171/H/Single rectangular tubes, SCCT	37
	R134a	40/10.2/100–600/5–20/0.1–0.92	0.691/171/H/SCCT	74
Park et al. [56]	R22	40/5.3–16.5/100–300/7.3/0.1–1	8.8/530/H/SCCT [c]	27
Tang et al. [57]	R22	38.6/14.8/155–310/15/0.19–0.83	8.28/1104/H/SCCT	15
Derby et al. [58]	R134a	34/8.6/300/23.5–46/0.19–0.52	1/100/H/Multiport square; triangle; semi-circle copper tubes	25
Guo et al. [59]	R1234ze(E),R 134a,R41,R16 1,R32	35–45/12–53.9/200–400/8–30/0–0.95	2/1900/H/SCAT [d]	169
Kim et al. [60]	R22	45/17.3/200–600/10/0.21–0.85	1.41/45/H/MSAT [e]	10
Meyer et al. [61]	R134a	30–50/7.7–13.2/100–400/6.38/ 0.25–0.75	8.38/1488/[f]/SCCT	409
Olivier et al. [62]	R134a	40/10.2/100–300/5.11/0.10–0.90	8.38/1488/[g]/SCCT	228
Meyer and Ewim [63]	R134a	40/10.2/50–200/4.3–15.2/0.1–0.9	8.38/1500/H/SCCT	92
Aroonrat and Wongwises [64]	R134a	40–50/10.2–1.32/300–400/10–20/ 0.1–0.8	8.1/1500/H/SCCT	24
Rahman et al. [65]	R134a	30–35/7.7–8.9/50–200/8/0–1	0.81/852/H/MSAT	58
Del Col et al. [66]	R134a	40/10.2/400/29–130/0.17–0.96	1.23/230/H/Single square copper tube	44
Wen et al. [67]	R134a	8.18–11.01/3.8–5.1/115–290/10–46/0–1	4/274/H/MSAT	18
Keniar and Garimella [68]	R134a, R245fa, R1234ze(E)	30–50/1.7–7.7/50–200/2.3–6.7/0.1–0.9	0.98–1.55/240/H/SCCT	223
Hinde [69]	R12, R134a	35–60/8.5–16.8/75–300/2.35–15.52/ 0.1–0.83	4.57/2950/H/SCCT	50
Zhang [70]	R22, R134a	25–65/9.9–19.4/200–1403/8–12/ 0.19–0.83	3.25, 6.2/914/H/SCCT	48
	R134a	25–65/9.9–19.4/200–1403/8–12/ 0.19–0.83	0.96–2.13/508/H/SCAT	30
Cavallini et al. [71]	R125, R134a	40/10.2–20.1/65–200/4.4–9.7/0.22–0.78	8/1600/H/SCCT	15
Zilly et al. [72]	R22	(–25)–10/2.5–6.8/400/7.07–43.5/ 0.1–0.81	6.1/150/H/SCCT	14
Aprea et al. [73]	R22	37.1–39.6/14.3–15/45.5–120/8.69–42.76/ 0.08–0.88	20/6600/H/SCCT	66
Jang and Hrnjak [74]	R22	(–20)–20/2.5–9.1/400/10.2–18.1/ 0.1–0.9	6.1/150/H/SCCT	5
Kim and Shin [75]	R22	45/17.3/280.4/11/0.15–0.82	8.7/920/H/SCCT	5
Wang et al. [76]	R32, R134a, R1234yf	40–50/10.2–24.8/100–401/5.5–31.7/ 0.11–0.92	4/3400/H/SCCT	90
Yan and Lin [77]	R134a	25–50/6.7–13.2/100–200/10–20/ 0.08–0.96	2/200/H/NA	76
Baird et al. [78]	R123	20.9–55.31/2.9–3/170/14.13–68.71/ 0.11–0.97	1.95/30/H/NA	18
Wen et al. [79]	R134a	40/10.2/205–320/5.2/0.12–0.84	2.46/3850/H/SCCT	16
Matkovic et al. [80]	R32, R134a	40–40.4/10.2–25/100–1200/12.4–325.46/ 0.01–0.99	0.96/225/H/SCCT	359
Del Col et al. [81]	R1234yf	39.83–40.58/10.1–10.3/800/54.98–140.86/ 0.2–0.85	0.96/230/H/SCCT	11

Table 1 Continued

Data source	Fluid	Parameter range: T_{sat} (°C)/p_{sat} (bar)/G (kg/m^2 s)/q (kW/ m^2)/x	Geometry range: D (mm)/L (mm)/ Orientation/Tube type	Data points
Oh and Son [82]	R22, R134a	40/10.2–15.3/450–1050/29.65–421.14/ 0.22–0.87	1.77/1220/H/SCCT	72
Zhang et al. [83]	R22	40/15.3/300–600/12.09–146.17/ 0.01–0.88	1.088,1.289/200/H/ SCSST	79
Liu et al. [84]	R152a	40–50/9.1–11.8/200–800/20.31–136.75/ 0.11–0.9	1.152/336/H/SCSST	48
Total				3467

[a] Horizontal, the same in Tables 2 and 3.
[b] Not available, the same in Tables 2 and 3.
[c] Single circular copper tube, the same in Tables 2 and 3.
[d] Single circular aluminum tube, the same in Tables 2 and 3.
[e] Multiport square aluminum tube, the same in Tables 2 and 3.
[f] Including: 37 horizontal data points; 37 vertical upward data points; 38 vertical downward data points; incline upward data points of 36, 37, 25, 25, and 25 for incline angles of 60°, 30°, 15°, 10°, and 5° respectively; and incline downward data points of 37, 37, 25, 25, and 25 for incline angles of –60°, –30°, –15°, –10°, and –5° respectively.
[g] Including: 12 horizontal data points; 12 vertical upward data points; 12 vertical downward data points; and incline upward data points of 12 each for incline angles of 75°, 60°, 45°, 30°, 20°, 15°, 10°, and 5°; and incline downward data points of 12 each for incline angles of –75°, –60°, –45°, –30°, –20°, –15°, –10°, and –5°.

Table 2 Experimental data of zeotropic halocarbon refrigerant blends

Data source	Fluid	Parameter range: T_{sat} (°C)/p_{sat} (bar)/G (kg/m^2 s)/q (kW/ m^2)/x	Geometry range: D (mm)/L (mm)/ Orientation/Tube type	Data points
Huang et al. [25]	R410A	40/24.3/200–600/4.23–19.07/0.19–0.82	4.18/1720/H/SCCT	21
Dobson et al. [32, 53]	60%R32/ 40%R125	35–45/8.9–27.6/69–512/3.12–16.08/ 0.08–0.96	4.572/NA/H/SCCT	53
	R410A, 60%R32/ 40%R125	33.5–46.4/8.5–28.5/24–812/2.98–54.95/ 0.02–0.95	3.14, 7.04/NA/H/SCCT	202
Kim et al. [60, 85]	R410A	45/27.3/100–400/10/0.14–0.8	5/1000/H/ SCSST [h]	14
Zhang [70]	R404A	25–65/9.9–19.4/200–1403/8–12/ 0.19–0.83	3.25, 6.2/914/H/SCCT	16
Kim and Shin [75]	R410A	45/27.3/280.3/11/0.15–0.82	8.7/920/H/SCCT	6
Wang et al. [76]	R410A	40/24.3/200–600/4.23–19.07/0.19–0.82	1.6/1720/H/SCCT	14
Oh and Son [82]	R410A	40/4.3/450–1050/29.65–421.14/0.22–0.87	1.77/1220/H/SCCT	36
Zhang et al. [83]	R407C, R410A	40/17.5–24.3/300–600/12.09–146.17/ 0.01–0.88	1.088,1.289/200/H/ SCSST	81
Jung et al. [86]	R407C, R410A	40/17.4–24.2/100–300/7.7/0–1	8.82/1000/H/SCCT	46
		45/27.3/200–600/10/0.21–0.85	1.41/45/H/MSAT	9
Vu et al. [87]	R410A	48/29.3/200–320/9,12/0.12–1	6.61, 7.45, 9.2/1200/H/SCCT	53
Kim et al. [88, 89]	R404A,R448A,R449A,R454C	45/15.8–20.5/380–760/6/0.2–0.8	0.8–5.6/NA/H/MSAT	86
Li et al. [90]	60%R152a/ 40%R1234ze(E)	30–40/6.9–7.9/173–462/5–10/0.1–0.9	4/870/H/Single circular tube	46
Total				683

[g] Single circular stainless steel tube, the same in Table 3.

Table 3 Experimental data of hydrocarbon refrigerants

Data source	Fluid	Parameter range: T_{sat} (°C)/p_{sat} (bar)/G (kg/m^2 s)/q (kW/ m^2)/x	Geometry range: D (mm)/L (mm)/ Orientation/Tube type	Data points
Park et al. [56]	DME, R1270, R290, R600a	40/5.31–16.49/100–300/7.3/0.1–1	8.8/530/H/SCCT	102
Guo et al. [59]	R290	35–45/12–15.3/200–400/9.5–15/0–0.95	2/1900/H/SCAT	48
Zilly et al. [72]	CO_2	(–25)–(–15)/16.7–22.9/200–400/7.07–43.5/ 0.1–0.81	6.1/150/H/SCCT	28
Jang and Hrnjak [74]	CO_2	(–25.6)–(–15.6)/16.5–22.5/197.1–406.2/8–36.4/ 0.1–0.9	6.1/150/ H/SCCT	85
Wen et al. [79]	R290, R600, 50%R600/ 50%R290	40/3.8–13.7/205–320/5.2/0.12–0.84	2.46/3850/H/SCCT	48
Zhuang et al. [40, 91]	R50	(–108.15)–(–92.15)/20–35/99–255/8.7–76.5/ 0–1	4/200/H/SCCT	499
	R170	(–32)–3/10.1–25.6/100–257/55.3–96.3/0–0.93	4/200/H/ SCSST	265

Table 3 Continued

Data source	Fluid	Parameter range: T_{sat} (°C)/p_{sat} (bar)/G (kg/m^2 s)/q (kW/ m^2)/x	Geometry range: D (mm)/L (mm)/ Orientation/Tube type	Data points
Kondou and Hrnjak [92]	CO_2	22.0–28.7/60,70/100–200/3–15/0–1	6.1/150/H/SCCT	103
Maråk [93]	R50	(–132.3)–(–85.72)/6.7–41.7/160–700/6.4–26.4/ 0.1–0.89	1/50/Vertical downward/SCCT	104
Murphy [94]	R290	47–74/16.0–27.9/75–150/12.14–46.49/ 0.10–0.79	1.93/135.1/Vertical downward / SCAT	27
Agra and Teke [95]	R600a	43/5.7/92/7.57–25.71/0.45–0.9	4/NA/ H/SCCT	15
Kim et al. [96]	CO_2	(–25)/16.8/200–800/8.77–85.12/0.09–0.9	3.48/1000/H/SCCT	20
Park and Hrnjak [97]	CO_2	(–25)–(–15)/16.7–22.9/200–800/6.13–28.7/ 0.09–0.9	0.89/150/H/SCAT	113
Total				1457

(1) The liquid Reynolds number Re_l = 11.6–5.3×10^4, with most of data having Re_l = 100–2.5×10^4. The gas Reynolds number Re_g = 75.1–9.1×10^5, with most of data having Re_g = 1000–3.5×10^5. Fig. 2(a) shows the laminar/turbulent flow distribution, from which it can be seen that about 98.9% of the data are in the turbulent liquid or turbulent gas regions and 66.1% in the turbulent liquid–turbulent gas (*tt*) region when taking Re = 2000 as a criterion.

(2) Diameter or hydraulic diameter D = 0.493–20 mm, with 1866 minichannel (0.2 mm < D ≤ 3 mm) data and 3741 conventional channel (D > 3 mm) data (Fig. 2(b)), as per the Kandlikar and Grande [52] method. For convenience, symbol D is used to represent both inner diameter and hydraulic diameter in this paper.

(3) Vapor quality x = 0.003–0.992. For x > 0.1, the number of the data points decreases with increasing vapor quality (Fig. 2(c)).

(4) Mass flux G = 24–1533 kg/m^2 s, with most of data having G < 800 kg/m^2 s (Fig. 2(d)).

(5) Heat flux q = 2.9–422 kW/m^2, with most of data having q < 100 kW/m^2 (Fig. 2(e)).

(6) Reduced pressure p_r = 0.04–0.95.

(7) Liquid Prandtl number Pr_l = 1.7–8.5.

(8) Orientation: horizontal, 4849 data points; vertical downward, 170 data points; incline upward, 295 data points; incline downward, 293 data points.

(9) Both single and multiport channels are involved, including circular, square, and rectangular cross section shapes, with 5286 single channel data and 321 multiport channel data.

3. NEW CORRELATION

3.1 STRATEGY FOR DEVELOP NEW CORRELATION

The strategy for developing a new correlation is summarized below and elaborated in the subsequent subsections of this section:

(1) Conducting evaluation analysis of existing correlations for flow condensation HTC to unearth ideas for developing a new correlation. The correlations predicting the present database with MAD ≤ 30% are analyzed, and the dimensionless parameters involved are counted, with an emphasis put on the ΔT-

independent correlations.

(2) Exploring relationships between the Nusselt number *Nu* and other two-phase flow dimensionless parameters to identify different heat transfer regimes, which is important to construct piecewise correlations. The dimensionless parameters counted and information obtained from step (1) are used as reference.

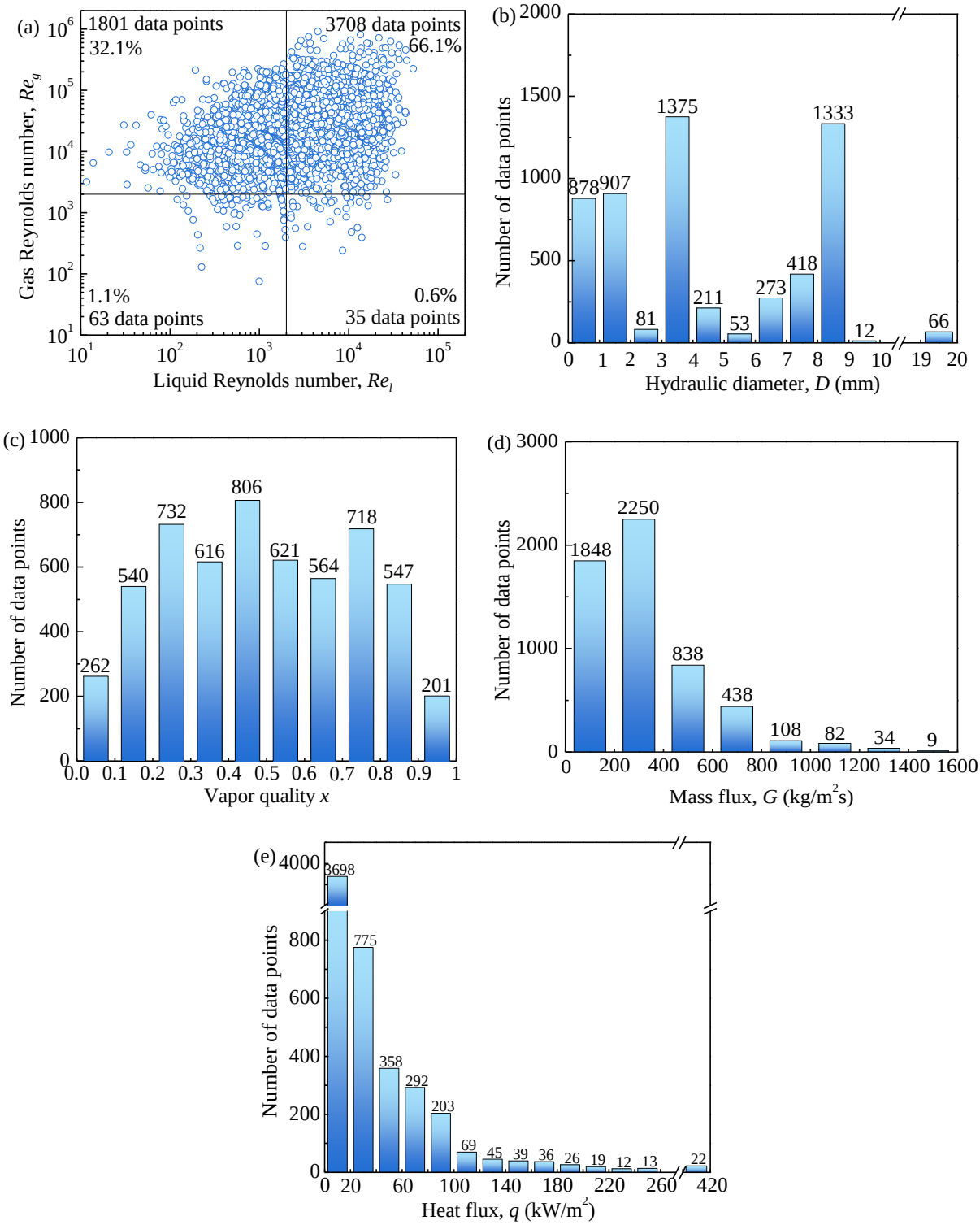

Fig. 2 Distribution of data points related to: (a) laminar/turbulent flow regime, (b) channel size, (c) vapor quality, (d) mass flux, (e) heat flux.

(3) Based on the work of steps (1) and (2) and the authors' experience, several tentative model forms

are constructed, from which computer tests with the methods of the least squares and error analysis are conducted to select the candidate baseline model forms. Then, using the methods of the least squares and error analysis along with adding and/or removing some dimensionless parameters included but not limited to those identified in step (1), computer tests are repeated to modify the candidate baseline model forms.

(4) Step (3) is repeated until the mean absolute deviation (MAD) cannot be reduced at the mean relative deviation (MRD) around zero.

$$\mathrm{MAD} = \frac{1}{N}\sum_{i=1}^{N}\left|\frac{y(i)_{pred} - y(i)_{exp}}{y(i)_{exp}}\right| \tag{1}$$

$$\mathrm{MRD} = \frac{1}{N}\sum_{i=1}^{N}\frac{y(i)_{pred} - y(i)_{exp}}{y(i)_{exp}} \tag{2}$$

where $y(i)_{pred}$ is the predicted value of the condensation HTC of point i, $y(i)_{exp}$ is the measured value of the condensation HTC of point i, and N is the number of the total data points in the database.

3.2 EVALUATION ANALYSIS OF EXISTING CORRELATIONS FOR FLOW CONDENSATION HTC

With the present database, 36 existing correlations are evaluated, including Patel et al. [4], Shah [5, 13, 19, 36, 50], Kim and Mudawar [15], Akers and Rosson [16], Moser et al. [17], Wang et al. [20], Cavallini and Zecchin [21], Haraguchi et al. [22], Dobson and Chato [23], Koyama et al. [24, 31], Huang et al. [25], Park et al. [26], Bohdal et al. [27], Cavallini et al. [28, 30], Bivens and Yokozeki [29], Tang et al. [33], Thome et al. [34], Chen et al. [35], Ananiev et al. [37], Dorao and Fernandino [38, 98], Akers et al. [39], Zhuang et al. [40], Jung et al. [41], Li et al. [90], Hosseini et al. [99], Song et al. [100], Camaraza-Medina et al. [101], Moreira et al. [102], and Barshar et al. [103]. Among them, except for those of Shah [5, 19, 36, 50], Dorao and Fernandino [98], and Koyama et al. [31], 15 have MAD ≤ 30%, including seven ΔT-independent and eight ΔT-dependent ones (Tables 4 and 5).

If an author or an author team has several similar correlations with MAD ≤ 30%, only the one having the highest prediction accuracy is counted as having MAD ≤ 30%. The correlations of Shah [5, 19, 36, 50], Dorao and Fernandino [98], and Koyama et al. [31] all have MAD ≤ 30%.The Shah [5, 19, 36, 50] correlations are similar to each other and are the basis of Shah [13] correlation, which is the last improved version and has the highest prediction accuracy among the Shah correlations. Similarly, the Dorao and Fernandino [38] correlation evolves from Dorao and Fernandino [98] and is better. The correlations of Koyama et al. [24] and [31] have similar forms and the former has a higher prediction accuracy. The Koyama et al. [24] and Park et al. [26] correlations are modified versions of the Haraguchi et al. [22] correlation, and they are counted in Table 5 because of different author groups.

The prediction deviation of the new correlation is listed in Table 4 for facilitating the comparison with the existing ones, and the detail comparison with the best existing ones is provided in the following section.

Table 4 Deviations of ΔT-independent correlations with MAD ≤ 30% (%)

Correlations	Total points		D > 3 mm		D ≤ 3 mm	
	MAD	MRD	MAD	MRD	MAD	MRD
New correlation	14.1	–1.1	12.8	–1.1	16.8	–1.1
Dorao and Fernandino [38]	20.1	0.8	18.9	2.2	22.3	–2.1
Shah [13]	20.2	3.9	20.3	4.1	20.1	3.8
Huang et al. [25]	22.5	–2.0	20.9	2.7	25.6	–11.3
Hosseini et al. [99]	22.8	–6.1	18.9	–6.5	30.6	–5.2
Moser et al. [17]	26.1	3.0	25.0	0.9	28.1	7.3
Tang et al. [33]	26.3	3.9	26.1	0.6	26.7	10.5
Chen et al. [35]	28.1	–11.7	28.2	–11.3	27.9	–12.5

Table 5 Deviations of ΔT-dependent correlations with MAD ≤ 30% (%)

Correlations	Total points		D > 3 mm		D ≤ 3 mm	
	MAD	MRD	MAD	MRD	MAD	MRD
Cavallini et al. [28]	16.9	2.5	15.0	2.8	20.6	1.7
Haraguchi et al. [22]	20.8	6.9	20.5	10.0	21.4	0.6
Zhuang et al. [40]	21.6	–7.6	18.0	0.6	28.9	–24.1
Koyama et al. [24]	21.9	6.3	21.1	10.7	23.6	–2.4
Thome et al. [34]	24.3	–19.8	24.9	–21.2	23.1	–17.0
Park et al. [26]	26.8	–13.2	22.7	–5.8	35.1	–28.0
Song et al. [100]	28.5	0.1	27.3	6.2	31.1	–12.3
Cavallini et al. [30]	29.3	–11.5	32.1	–20.9	23.6	7.4

The mathematical expressions of the seven ΔT-independent existing correlations are listed in Table 6, and the eight ΔT-dependent ones are listed in Table 7. Except for thermophysical or operational parameter ratios, the dimensionless parameters appearing in the seven ΔT-independent existing correlations are given in Table 8, of which some also appear in the eight ΔT-dependent ones, and the dimensionless parameters appearing only in the eight ΔT-dependent correlations are listed in Table 9. The word criteria in the first lines of Tables 8 and 9 means the criteria for partitioning heat transfer regimes. The Nusselt number Nu is defined as

$$Nu = hD/\lambda_l \tag{3}$$

The dimensionless parameters of thermophysical or operational parameter ratios, which appear in the 15 correlations at least twice, are the vapor quality x, viscosity ratio (μ_l/μ_g), density ratio (ρ_l/ρ_g), void fraction α, and reduced pressure p_r.

Table 6 ΔT-independent existing correlations with MAD ≤ 30%

Source	Correlation	Comments
Shah [13]	(1) Heat transfer regimes (a) Heat transfer regimes are the same as in Shah [36] correlation for both horizontal and vertical downflow if any of the following conditions are applicable: • Fluid is a hydrocarbon, Regime is I and $p_r < 0.4$ • Fluid is hydrocarbon and Regime is III • $Re_{lo} < 100$ Heat transfer regimes in Shah [36] $\begin{cases} \text{Regime I: } J_g \geq 0.98\left(Z+0.263\right)^{-0.62} \\ \text{Regime III: } J_g < 0.95\left(1.254+2.27Z^{1.249}\right)^{-1} \\ \text{If the Regime is neither I nor III , it is Regime II} \end{cases}$ where Z is the correlating parameter, $Z = \left(1/x-1\right)^{0.8} p_r{}^{0.4}$ (b) If none of the above conditions is applicable, heat transfer regimes are determined as follows. • For horizontal flow $\begin{cases} J_g \geq 0.98\left(Z+0.263\right)^{-0.62} \text{ and } We_{go} \geq 100 \text{ and } Fr_{lo} > 0.012 \text{ for Regime I} \\ J_g < 0.95\left(1.254+2.27Z^{1.249}\right)^{-1} \text{ and } Fr_{lo} > 0.012 \text{ for Regime III} \\ \text{If the Regime is neither I nor III , it is Regime II} \end{cases}$ • For vertical downflow $\begin{cases} J_g \geq 1/\left(2.4Z+0.73\right) \text{and } We_{go} \geq 100 \text{ for Regime I} \\ J_g \leq 0.89-0.93\exp\left(-0.087Z^{-1.17}\right) \text{ for Regime III} \\ \text{If the Regime is neither I nor III , it is Regime II} \end{cases}$ (2) Correlation	(1) Based on 5100 data points from 88 sources covering 40 fluids. D = 0.08–49.0 mm. G = 1.1–1400 kg/m^2 s. p_r = 0.0008–0.946. x = 0.01–0.99. (2) Regime partition criteria: J_g, We_{go} and Fr_{lo}.

Table 6 Continued

Source	Correlation	Comments
Shah [13]	$h = \begin{cases} h_{\mathrm{I}} & \text{for Regime I} \\ h_{\mathrm{I}} + h_{Nu} & \text{for Regime II} \\ h_{Nu} & \text{for Regime III} \end{cases}$ (4) $h_{Nu} = 1.32\left(Gr/Re_{lo}\right)^{1/3} \lambda_l / D$ (5) For horizontal flow when D ≤ 3 mm: $h_{\mathrm{I}} = h_{lo}\left[1 + 1.128x^{0.817}\left(\frac{\rho_l}{\rho_g}\right)^{0.3685}\left(\frac{\mu_l}{\mu_g}\right)^{0.2363}\left(1-\frac{\mu_g}{\mu_l}\right)^{2.144} Pr_l^{-0.1}\right]$ (6) $h_{lo} = 0.023 Re_{lo}^{0.8} Pr_l^{0.4} \lambda_l / D$ (7) For horizontal flow when D > 3 mm and for vertical channels of all diameters: $h_{\mathrm{I}} = h_l\left(1 + 3.8/Z^{0.95}\right)\left[\mu_l/\left(14\mu_g\right)\right]^{\left(0.0058+0.557\,p_r\right)}$ (8) $h_l = 0.023 Re_l^{0.8} Pr_l^{0.4} \lambda_l / D$ (9)	
Dorao and Fernandino [38]	$Nu = \left[Nu_{\mathrm{I}}^9 + Nu_{\mathrm{II}}^9\right]^{1/9}$ (10) $Nu_{\mathrm{I}} = 0.023 Re_{tp}^{0.8} Pr_{tp}^{0.3}$ $Re_{tp} > 10^8 D^{1.5}$ (11a) $Nu_{\mathrm{II}} = 41.5 D^{0.6} Re_{tp}^{0.4} Pr_{tp}^{0.3}$ $Re_{tp} < 10^8 D^{1.5}$ (11b) where D is in m.	Based on 3937 data points. D = 0.0667–20 mm. G = 45.5–1360 kg/m^2 s. T_{sat} = (–132.3)–94°C.
Huang et al. [25]	Huang et al. [25] modified the Haraguchi et al. [22] correlation. $Nu = 0.0152 Re_l^{0.77}\left(-0.33 + 0.83 Pr_l^{0.8}\right)\phi_g / X_{tt}$ (12a) where ϕ_g is given below: $\phi_g = 1 + 0.5\left(J_g / x\right)^{0.75} X_{tt}^{0.35}$ (12b)	Test with R410A data. D = 1.6 and 4.18 mm.
Hosseini et al. [99]	(a) For $G \le 200$ kg/m^2 s $Nu = 0.0022 Re_{tp}\left(1-\rho_g/\rho_l\right) + 0.0342 We_{go}\left(1-\rho_g/\rho_l\right)^2 - Pr_{tp} + \frac{\sin\left(39.8963\,p_r\right) - \ln We_{go}}{-0.0298 - 0.2203 Fr_{lo}}$ (13) (b) For $G > 200$ kg/m^2 s $Nu = \mathrm{ABS}\left\{\begin{array}{l} 0.0169 Re_{tp}^{0.862} - 0.00146\, Re_{tp}/\left[Pr_{tp}\left(1-\rho_g/\rho_l\right)\right] + Y \\ +17.948\sin\left(Y\right) + \tan\left(27.6370106546243\left(1-\rho_g/\rho_l\right)\right) \\ -\tan\left(369.8572 + Y\right) \end{array}\right\}$ (14a) $Y = \left(0.0036 + 0.0171 We_{go}\right)/Fr_{lo}$ (14b)	Based on genetic programming with 6521 data points. D = 0.133–20.8 mm. G = 13.1–1200 kg/m^2 s. p_r = 0.0005–0.952. x = 0.001–0.99. (2) Regime partition criterion: G.
Moser et al. [17]	$Nu = \frac{0.0994^{C_1} Re_l^{C_2} Re_{eq}^{1+0.875C_1} Pr_l^{0.815}}{\left(1.58\ln Re_{eq} - 3.28\right)\left(2.58\ln Re_{eq} + 13.7 Pr_l^{2/3} - 19.1\right)}$ (15a) where C_1, C_2 and Re_{eq} defined as below. $C_1 = 0.126 Pr_l^{-0.448}$ (15b) $C_2 = -0.113 Pr_l^{-0.563}$ (15c) $Re_{eq} = \phi_{lo}^{8/7} Re_{lo}$ (15d) $\phi_{lo}^2 = (1-x)^2 + x^2 \frac{\rho_l f_{go}}{\rho_g f_{lo}} + \frac{3.24 x^{0.78}(1-x)^{0.224} H}{Fr_{tp}^{0.045} We_{tp}^{0.035}}$ (16a) $H = \left(\rho_l/\rho_g\right)^{0.91}\left(\mu_g/\mu_l\right)^{0.19}\left(1-\mu_g/\mu_l\right)^{0.7}$ (16b) where We_{tp}, Fr_{tp}, f_{lo} and f_{go} are respectively defined as below. $We_{tp} = G^2 D/\left(\sigma\rho_{tp}\right)$ (16c)	Based on 1197 data points of R11, R12, R125, R22, R134a and R410A. D = 3.14–20 mm.

Table 6 Continued

Source	Correlation	Comments
Moser et al. [17]	$Fr_{tp} = G^2 / \left(gD\rho_{tp}^2 \right)$ (16d) $f_{ko} = \begin{cases} 64/Re_{ko} & Re_{ko} < 2000 \\ 0.316/Re_{ko}^{0.25} & 2000 \le Re_{ko} < 20000 \\ 0.184/Re_{ko}^{0.2} & Re_{ko} \ge 20000 \end{cases}$ (16e) where $k=l$ for the liquid phase, $k=g$ for the gas phase, the form of Two–phase flow density ρ_{tp} defined as below. $\rho_{tp} = \left[(1-x)/\rho_l + x/\rho_g \right]^{-1}$ (17)	
Tang et al. [33]	$Nu = 0.023 Re_l^{0.8} Pr_l^{0.4} \left[1 + 4.863 \left(-x/(1-x) \ln p_r \right)^{0.836} \right]$ (18)	Based on data of R22, R134a, and R410A. D = 8.81 mm. T_{sat} = 35–45°C. G = 250–810 kg/m^2 s. q = 5.5–37 kW/m^2.
Chen et al. [35]	$Nu = 0.018 \left(\rho_l/\rho_g \right)^{0.39} \left(\mu_g/\mu_l \right)^{0.078} Re_l^{0.2} \left(Re_{lo} - Re_l \right)^{0.7} Pr_l^{0.65}$ (19)	Based on analytical and empirical results with experimental data in vertical tubes.

Table 7 ΔT-dependent existing correlations with MAD ≤ 30%

Source	Correlation	Comments
Haraguchi et al. [22]	$Nu = \left(Nu_{film}^2 + Nu_{forced}^2 \right)^{1/2}$ (20) $Nu_{film} = 0.725 H(\alpha) \left(Ga_l Pr_l / Ja \right)^{0.25}$ (21a) $Nu_{forced} = 0.0152 Re_l^{0.77} \left(1 + 0.6 Pr_l^{0.8} \right) \phi_g / X_{tt}$ (21b) $\phi_g = 1 + 0.5 \left(J_g / x \right)^{0.75} X_{tt}^{0.35}$ (22) $H(\alpha) = \alpha + \left\{ 10 \left[(1-\alpha)^{0.1} - 1 \right] + 1.7 \times 10^{-4} Re_{lo} \right\} \alpha^{0.5} \left(1 - \alpha^{0.5} \right)$ (23) $\alpha = \left\{ 1 + \left(\frac{\rho_g}{\rho_l} \right) \left(\frac{1-x}{x} \right) \left[0.4 + 0.6 \left(\frac{\rho_l/\rho_g + 0.4(1-x)/x}{1 + 0.4(1-x)/x} \right)^{1/2} \right] \right\}^{-1}$ (24)	Test on R22, R134a, R123 condensating in 8mm horizontal tube. Pr_L = 2.5–4.5, Re_L = 200–20000, Re_{LO} = 3000–30000, X_{tt} = 0–1300, $Ga_L Pr_L / H_{LV}$ = 4.8×10^9–9.5×10^{10}.
Koyama et al. [24]	They modified Haraguchi et al. [22] method by replacing Eq. (22) with $\phi_g^2 = 1 + 21 \left[1 - \exp(-0.319D) \right] X_{tt} + X_{tt}^2$ (25)	Experiment on R134a in 1.11 mm and 0.8 mm rectangular tubes.
Park et al. [26]	They used Haraguchi et al. [22] Eq. (20), where Nu_{film} and Nu_{forced} are calculated by $Nu_{film} = 0.746 \left[1 - \exp\left(-0.85 Bd^{0.5} \right) \right] H(\alpha) \left(Ga_l Pr_l / Ja \right)^{0.25}$ (26) $Nu_{forced} = 0.0055 Re_l^{0.7} Pr_l^{1.37} \phi_g / X_{tt}$ (27) $\phi_g^2 = 1 + 13.17 \left(\frac{\mu_l}{\mu_g} \frac{\rho_g}{\rho_l} \right)^{0.17} \left[1 - \exp\left(-0.6 Bd^{0.5} \right) \right] X_{tt} + X_{tt}^2$ (28) $H(\alpha) = \alpha + \left[10 (1-\alpha)^{0.1} - 8.9 \right] \alpha^{0.5} \left(1 - \alpha^{0.5} \right)$ (29) where the void fraction α is calculated with Eq. (24).	Experiment on R1234ze, R134a and R236fa in 1.45 mm multi-port extruded rectangular aluminum tubes. T_{sat} = 25–70 °C, G = 50–260 kg m^{-2} s^{-1}, q = 1–62 kW m^{-2}, x = 0–1.

Table 7 Continued

Source	Correlation	Comments
Thome et al. [34]	$h=\left[\theta h_{film}+(2\pi-\theta)h_{forced}\right]/(2\pi)$ (30a) $h_{film}=0.728\left(GrPr_l/Ja\right)^{0.25}\left(\lambda_l/D\right)$ (30b) $h_{forced}=0.003Re_{l,\delta}^{0.74}Pr_l^{0.5}f_i\left(\lambda_l/\delta\right)$ (30c) $f_i=\left(\frac{\rho_l}{\rho_g}\frac{x}{1-x}\frac{1-\alpha}{\alpha}\right)^{1/2}Bd^{0.25}\left(\delta/D\right)^{0.5}$ (30d) $Re_{l,\delta}=4G(1-x)\delta/\left[(1-\alpha)\mu_l\right]$ (31) $\alpha=\left(\alpha_h-\alpha_{ra}\right)/\ln\left(\alpha_h/\alpha_{ra}\right)$ (32a) $\alpha_h=\left[1+\left(\rho_g/\rho_l\right)(1-x)/x\right]^{-1}$ (32b) $\alpha_{ra}=\frac{x}{\rho_g}\left\{[1+0.12(1-x)]\left(\frac{x}{\rho_g}+\frac{1-x}{\rho_l}\right)+\frac{1.18(1-x)\left[g\sigma\left(\rho_l-\rho_g\right)\right]^{0.25}}{G\rho_l^{0.5}}\right\}^{-1}$ (32c) $\theta=\begin{cases}0 & \text{for } G>G_{wavy}\\ \theta_{strat}\left[\left(G_{wavy}-G\right)/\left(G_{wavy}-G_{strat}\right)\right]^{0.5} & \text{for } G_{strat}<G\le G_{wavy}\\ \theta_{strat} & \text{for } G\le G_{strat}\end{cases}$ (33a) $\theta_{strat}=2\pi-2\begin{cases}\pi(1-\alpha)+(3\pi/2)^{1/3}\left[1-2(1-\alpha)+(1-\alpha)^{1/3}-\alpha^{1/3}\right]\\ -0.05\alpha(1-\alpha)\left[1-2(1-\alpha)\right]\left[1+4(1-\alpha)^2+\alpha^2\right]\end{cases}$ (33b) If $\delta'<D/2$, $\delta=\delta'$ if $\delta'\ge D/2$, $\delta=D/2$ (34a) $\delta'=0.5\left\{D-\left[D^2-8A_L/(2\pi-\theta)\right]^{0.5}\right\}$ (34b) $G_{wavy}=\left\{\frac{16A_{Vd}^3gD\rho_l\rho_g\left[\left(0.04\pi^2/H_{Ld}^2\right)\left(We_l/Fr_l\right)^{-1.023}+1\right]}{x^2\pi^2\sqrt{1-\left(2H_{Ld}-1\right)^2}}\right\}^{1/2}+B$ (35a) $B=50-75\exp\left[-\frac{\left(x^2-0.97\right)^2}{x(1-x)}\right]$ (35b) $G_{strat}=\left\{226.3^2A_{Ld}A_{Vd}^2\rho_g\left(\rho_l-\rho_g\right)\mu_l g/\left[x^2(1-x)\pi^3\right]\right\}^{1/3}+20x$ (36) $A_L=(1-\alpha)D^2\pi/4$, $A_{Ld}=(1-\alpha)\pi/4$, $A_{Vd}=\alpha\pi/4$ (37a) $H_{Ld}=0.5\left\{1-\cos\left[(2\pi-\theta_{strat})/2\right]\right\}$ (37b)	Proposed a new simplified flow structures of the flow regimes, and compared to test data for 15 fluids with: D = 3.1–21.4 mm, G = 24–1022 kg m^{-2} s^{-1}, x = 0.03–0.97, p_{rd} = 0.02–0.8.
Zhuang et al. [40]	(a) For annular flow ($We^*\ge 18.9X_{tt}^{0.33}$) $h=0.0043Re_{l,\delta}^{0.8}Pr_l^{0.3}f_i\left(\lambda_l/\delta\right)$ (38a) $\delta=D/\left[2\left(1-\alpha^{0.5}\right)\right]$ (38b) $f_i=\left(\frac{\mu_g}{\mu_l}\right)^{0.32}\left(\frac{\rho_l}{\rho_g}\frac{x}{1-x}\frac{1-\alpha}{\alpha}\right)^{0.73}Bd^{0.16}\left(\delta/D\right)^{0.32}$ (38c) where $Re_{l,\delta}$ is calculated by Eq. (31), and the void fraction α is calculated by Eq. (32). (b) For non-annular flow ($We^*<18.9X_{tt}^{0.33}$)	(1) Based on their own experimental data of R50 in horizontal channels. D = 4 mm. G = 99–255 kg/m^2 s. p = 2–3.5 MPa. (2) Regime partition criterion: We^*.

Table 7 Continued

Source	Correlation	Comments
Zhuang et al. [40]	$h=\frac{\lambda_l}{D}\left[Nu_{film}+Nu_{forced}\ \arccos\left(2\alpha-1\right)/\pi\right]$ (39a) $Nu_{film}=\frac{0.0053Re_{go}^{0.41}}{1+0.48X_{tt}^{0.73}}\left(\frac{GrPr_l}{Ja}\right)^{1/4}$ (39b) $Nu_{forced}=0.0195Re_l^{0.8}Pr_l^{0.4}\left(1.376+c_1/X_{tt}^{c_2}\right)^{0.5}$ (39c) $c_1=\begin{cases}4.172+5.48Fr_l-1.564Fr_l^2 & \text{for } 0<Fr_l\le 0.7\\ 7.242 & \text{for } Fr_l>0.7\end{cases}$ (39d) $c_2=\begin{cases}1.773-0.169Fr_l & \text{for } 0<Fr_l\le 0.7\\ 1.655 & \text{for } Fr_l>0.7\end{cases}$ (39e)	
	(b)	
Cavallini et al. [30]	(a) For $J_g\ge 2.5$, annular flow $Nu_{annul}=\left(\rho_l c_{p,l}/T^+\right)\left(\tau/\rho_l\right)^{0.5}\left(D/\lambda_l\right)$ (40a) $T^+=\begin{cases}\delta^+Pr_l & \text{if } \delta^+\le 5\\ T^+=5\left\{Pr_l+\ln\left[1+Pr_l\left(\delta^+/5-1\right)\right]\right\} & \text{if } 5<\delta^+<30\\ T^+=5\left[Pr_l+\ln\left(1+5Pr_l\right)+0.495\ln\left(\delta^+/30\right)\right] & \text{if } \delta^+\ge 30\end{cases}$ (40b) $\delta^+=\begin{cases}\left(Re_l/2\right)^{0.5} & \text{if } Re_l\le 1145\\ 0.0504Re_l^{7/8} & \text{if } Re_l>1145\end{cases}$ (40c) $\tau=0.5\phi_{lo}^2 f_{lo}G^2/\rho_l$ (40d) $\phi_{lo}^2=(1-x)^2+x^2\frac{\rho_l f_{go}}{\rho_g f_{lo}}+\frac{1.262x^{0.6978}H}{We_{go}^{0.1458}}$ (40e) $H=\left(\rho_l/\rho_g\right)^{0.3278}\left(\mu_g/\mu_l\right)^{-1.181}\left(1-\mu_g/\mu_l\right)^{3.477}$ (40f) $f_{ko}=\begin{cases}16/Re_{ko} & \text{for } Re_{ko}\le 2000\\ 0.046/Re_{ko}^{0.2} & \text{for } Re_{ko}>2000\end{cases}$ (40g) where subscript $k=l$ for liquid, and $k=g$ for gas. (b) For $J_g<2.5$ and $X_{tt}<1.6$, annular–stratified flow transition and stratified flow $Nu_{trans}=\left(Nu_{annul,J_g=2.5}-Nu_{strat}\right)\left(J_g/2.5\right)+Nu_{strat}$ (41a) $Nu_{strat}=0.725\left[1+0.82\left(\frac{1-x}{x}\right)^{0.268}\right]^{-1}\left(\frac{GrPr_l}{Ja}\right)^{0.25}+Nu_{lo}\left(1-x\right)^{0.8}\left(1-\frac{\theta}{\pi}\right)$ (41b) $\theta=\pi-\arccos(2\alpha-1)$ (41c) $\alpha=\left[1+\left(\rho_g/\rho_l\right)^{2/3}\left(1-x\right)/x\right]^{-1}$ (41d) $Nu_{lo}=0.023Re_{lo}^{0.8}Pr_l^{0.4}$ (42) (c) For $J_g<2.5$ and $X_{tt}>1.6$, stratified-slug transition and slug flow $Nu_{slug}=Nu_{lo}+x(Nu_{trans,x1.6}-Nu_{lo})/x_{1.6}$ (43a) $x_{1.6}=\left(\mu_l/\mu_g\right)^{1/9}\left(\rho_g/\rho_l\right)^{5/9}\Big/\left[1.686+\left(\mu_l/\mu_g\right)^{1/9}\left(\rho_g/\rho_l\right)^{5/9}\right]$ (43b) where $Nu_{trans,x1.6}$ is calculated by Eq. (41) with $x=x_{1.6}$.	(1) Based on 600 data points of R22, R134a, R125, R32, R236ea, R407C, and R410A. D = 8 mm. G = 100–750 kg/m^2 s. T_{sat} = 30–50°C. (2) Regime partition criteria: J_g, X_{tt}.

Table 7 Continued

Source	Correlation	Comments
Cavallini et al. [28]	$J_g^T = \left\{ \left[7.5/\left(4.3X_{tt}^{1.111}+1\right) \right]^{-3} + C_T^{-3} \right\}^{-1/3}$ (44) For hydrocarbons, C_T= 1.6; other refrigerants, C_T= 2.6 (a) For $J_g > J_g^T$, ΔT is independent of flow regime $Nu_{annul} = Nu_{lo}\left[1+1.128x^{0.817}\left(\frac{\rho_l}{\rho_g}\right)^{0.3685}\left(\frac{\mu_l}{\mu_g}\right)^{0.2363}\left(1-\frac{\mu_g}{\mu_l}\right)^{2.144} Pr_l^{-0.1} \right]$ (45) where Nu_{lo} is calculated by Eq. (42). (b) For $J_g \le J_g^T$, ΔT is dependent on flow regime. $Nu = \left[Nu_{annul}\left(J_g^T/J_g\right)^{0.8} - Nu_{strat} \right]\left(J_g/J_g^T\right) + Nu_{strat}$ (46a) $Nu_{strat} = 0.725\left[1+0.741\left(\frac{1-x}{x}\right)^{0.3321} \right]^{-1}\left(\frac{GrPr_l}{Ja}\right)^{1/4} + Nu_{lo}\left(1-x^{0.087}\right)$ (46b)	(1) Developed from an extensive analysis of 425 data points, and compared against 4471 data points. D > 3 mm. (2) Regime partition criterion: J_g.
Song et al. [100]	$S_c = Fr_g Bd^{-0.15} Ca_l^{-0.1}\left(1+Bo^{0.25}\right)$ (47) (a) for $S_c > \left(20+X_{tt}\right)^{0.86}$ and $S_c > 83.4X_{tt}^{1.62}$, annular flow $Nu = h\frac{D}{\lambda_l} = \frac{Pr_l Re_l^{0.9}}{T^+} f\left(X_{tt}\right)$ (48a) $T^+ = 4.625Re_l^{0.149}Pr_l^{1.1945}Bd^{-0.1}$ (48b) $f\left(X_{tt}\right) = 0.15\left(1/X_{tt} + 2.85/X_{tt}^{0.476}\right)$ (48c) (b) for $S_c < \left(20+X_{tt}\right)^{0.86}$ or $S_c < 83.4X_{tt}^{1.62}$, non-annular flow They used Haraguchi et al. [22] Eq. (20), where Nu_{film} and Nu_{forced} are calculated by $Nu_{film} = 0.555\left(GrPr_l/Ja\right)^{1/4}$ (49a) $Nu_{forced} = 0.023Re_l^{0.8}Pr_l^{0.3} f$ (49b) $f = 1+\left(Re_g/Re_l\right)^{0.728} Bd^{0.066}$ (49c)	(1) Based on their own experimental data of R14 and 1370 data points from 9 published literatures. D = 4 mm. G=200–650 kg/m^2 s. p = 1–3 MPa. q = 8.3–28.2 kW/m^2. (2) Regime partition criterion: S_c.

Table 8 Dimensionless parameters appearing in the ΔT-independent correlations, with some also appearing in the ΔT-dependent correlations

Dimensionless number	definition	Times of occurrences	
		In equations	In criteria
liquid only Froude number	$Fr_{lo} = G^2/\left(gD\rho_l^2\right)$	[99]	[13]
Grashof number	$Gr = \rho_l g\left(\rho_l-\rho_g\right)D^3/\mu_l^2$	[13, 30]	
dimensionless vapor velocity	$J_g = xG/\left[gD\rho_g\left(\rho_l-\rho_g\right) \right]^{0.5}$		[13]
gas Prandtl number	$Pr_g = c_{pg}\mu_g/\lambda_g$	[38,99]	
liquid Prandtl number	$Pr_l = c_{pl}\mu_l/\lambda_l$	[13, 17, 22, 28, 30, 33, 34,35, 40, 100]	
two-phase Prandtl number	$Pr_{tp} = Pr_l(1-x)+Pr_g x$	[38, 99]	
gas Reynolds number	$Re_g = xGD/\mu_g$	[30, 38, 99, 100]	
liquid Reynolds number	$Re_l = (1-x)GD/\mu_l$	[13, 17, 22, 24, 25, 26, 30, 33, 35, 40, 100]	
liquid only Reynolds number	$Re_{lo} = GD/\mu_l$	[13, 17, 24, 26, 28, 30, 35]	

Table 8 Continued

Dimensionless number	definition	Times of occurrences	
		In equations	In criteria
two-phase Reynolds number	$Re_{tp} = Re_g + Re_l$	[30, 38, 99]	
gas only Weber number	$We_{go} = G^2 D / (\rho_g \sigma)$	[99]	[13]
Lockhart-Martinelli parameter	$X_{tt} = \left(\frac{1-x}{x}\right)^{0.9} \left(\frac{\rho_g}{\rho_l}\right)^{0.5} \left(\frac{\mu_l}{\mu_g}\right)^{0.1}$	[22, 24, 25, 26, 40, 100]	
gas friction multiplier	ϕ_g	[22, 24, 25, 26]	
liquid only friction multiplier	ϕ_{lo}^2	[17, 30]	

Table 9 Dimensionless parameters appearing only in the ΔT-dependent correlations

Dimensionless number	definition	Times of occurrences	
		In equations	In criteria
film condensation group	$Ga_l Pr_l / Ja$	[22, 24, 26]	
film condensation group	$GrPr_l / Ja$	[28, 30, 34, 40, 100]	
Bond number	$Bd = g(\rho_l - \rho_g) D^2 / \sigma$	[26, 34, 40, 100]	[100] $S_c = Fr_g Bd^{-0.15} Ca_l^{-0.1} \left(1 + Bo^{0.25}\right)$
boiling number	$Bo = q / (G h_{lg})$		
liquid capillary number	$Ca_l = \mu_l G / (\sigma \rho_l)$		
gas Froude number	$Fr_g = (xG)^2 / (gD\rho_g^2)$		
liquid Froude number	$Fr_l = [(1-x)G]^2 / (gD\rho_l^2)$	[40]	
liquid Galileo number	$Ga_l = gD^3 (\rho_l / \mu_l)^2$	[22, 24, 26]	
Jakob number	$Ja = c_{pl} \Delta T / h_{lg}$, where $\Delta T = T_{sat} - T_w$	[22, 24, 26, 28, 30, 34, 40, 100]	
gas only Reynolds number	$Re_{go} = GD / \mu_g$	[40]	
modified Weber number	$We^* = \begin{cases} 2.45 Re_g^{0.64} \Big/ \left[Su_g^{0.3} \left(1 + 1.09 X_{tt}^{0.039}\right)^{0.4} \right] & Re_l \le 1250 \\ \dfrac{0.85 Re_g^{0.79} X_{tt}^{0.157} \left[\left(\mu_g / \mu_l\right)^2 \left(\rho_l / \rho_g\right) \right]^{0.084}}{Su_g^{0.3} \left(1 + 1.09 X_{tt}^{0.039}\right)^{0.4}} & Re_l > 1250 \end{cases}$ where gas Suratman number is defined as $Su_g = \rho_g \sigma D / \mu_g^2$		[40]

3.3 ANALYSIS OF RELATIONSHIPS BETWEEN NU AND OTHER DIMENSIONLESS PARAMETERS

The diagrams of *Nu* with every other two-phase flow dimensionless parameter appears in Tables 8 and 9 are plotted to identify different heat transfer regimes, with an emphasis on those appear in the partition criteria. The gas only Weber number We_{go} and the Grashof number *Gr* come out as the prominent partition criteria, as shown in Fig. 3 and Fig. 4.

From Fig. 3, it can be seen that the variation of *Nu* with We_{go} shows two different regimes, with the boundary around We_{go} = 500. Fig. 4 shows that the variation of *Nu* with *Gr* may have three regimes, with the boundaries around $Gr = 2\times10^6$ and $Gr = 4\times10^8$. The final boundary will be refined in steps (3) and (4) of the strategy.

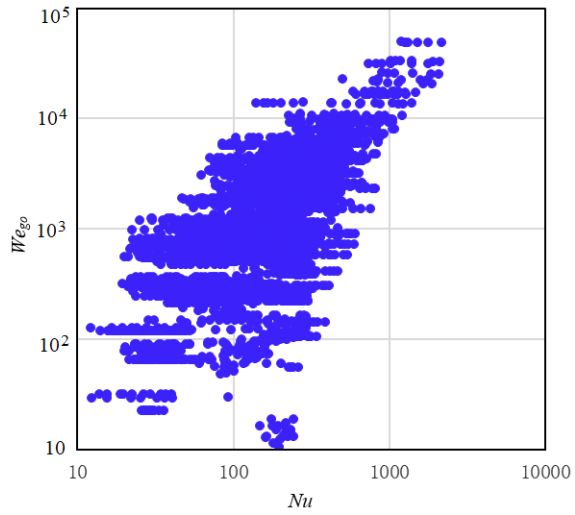

Fig. 3 variation of Nu with We_{go}

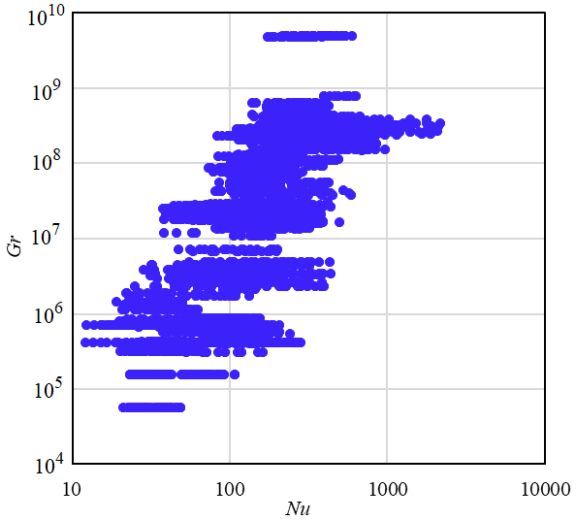

Fig. 4 variation of Nu with Gr

3.4 NEW CORRELATION

Steps (3) and (4) of the strategy are performed to obtain the new correlation. The ΔT-dependent form is avoid in constructing tentative correlation forms. This form may yield a correlation with very small MAD, as can be seen from Table 5, where the Cavallini et al. [28] correlation has a MAD of 16.9%, the smallest one among the existing correlations. However, in common engineering practice, ΔT is an unknown parameter. Two major problems may arise in using a ΔT-dependent correlation: accuracy loss and time consuming in iteration process. Uncertainties will be caused in the iteration process to obtain ΔT, which decreases the prediction accuracy.

In step 3, the other two-phase flow dimensionless numbers not appearing in the existing correlations with MAD ≤ 30% are also tried. It is interesting to note that the Fang number Fa plays an important role in the new correlation, though it was originally obtained in developing a correlation for flow boiling HTC [104, 105]. It implies that the Fang number relates the fundamental mechanisms of two-phase heat transfer, both boiling and condensation heat transfer. The Fang number Fa is defined as

$$Fa = (\rho_l - \rho_g)\sigma \Big/ \left(G^2 D\right) \tag{50}$$

The resultant new general correlation of the Nusselt number Nu for condensation heat transfer is of the form

For $We_{go} \le 500$

$$Nu = \begin{cases} 0.4314\left(Gr^{0.256} + \left|Gr^{0.61} - 1\times10^4\right|^{0.267}\right) Pr_l^{0.395} Pr_g^{-0.374} Fa^{-0.1} \left(\dfrac{x}{1-x}\right)^{0.25} \left(\dfrac{\mu_l}{\mu_g}\right)^{-0.15} & Gr < 4\times10^6 \\ 1.51 Gr^{0.315} Pr_l^{-0.17} Re_{lo}^{-0.446} Pr_g^{0.283} Fa^{-0.32} \left(\dfrac{x}{1-x}\right)^{0.185} \left(\dfrac{\mu_l}{\mu_g}\right)^{0.786} & 4\times10^6 \le Gr < 1.5\times10^8 \\ 26.98 Gr^{0.107} Pr_g^{-0.367} \left(\dfrac{x}{1-x}\right)^{0.14} & Gr \ge 1.5\times10^8 \end{cases} \tag{51}$$

For $We_{go} > 500$

$$Nu = \begin{cases} 0.00126(1-x)^{-0.1}\left(Gr^{0.2} + \left|Gr - 2\times10^6\right|^{0.24}\right)(Re_g + 0.43Re_l)^{0.5} Pr_l^{0.35} Fa^{0.1} We_{go}^{0.33} & Gr < 4\times10^6 \\ 1.977\left(Gr - 2\times10^6\right)^{0.076} Re_g^{0.344} Re_{lo}^{-0.35} We_{go}^{0.369} & 4\times10^6 \le Gr < 1.5\times10^8 \\ 0.0227\left(Re_g + 5\times10^4\right)^{0.69} We_{go}^{0.177} Fr_{lo}^{-0.0495} & Gr \ge 1.5\times10^8 \end{cases} \quad (52)$$

where all the fluid physical properties are obtained using the REFPROP of NIST, the Nusselt number Nu is determined by Eq. (3), and the dimensionless numbers Fr_{lo}, Gr, Pr_g, Pr_l, Re_g, Re_l, Re_{lo}, and We_{go} are given in Table 8.

4. COMPARISON WITH EXISTING CORRELATIONS

4.1 COMPARISON BASED ON ENTIRE DATABASE

Based on the present database, the new correlation is validated. It is also compared with 37 existing correlations, as indicated in Section 3.2including. The results of the deviations of the correlations with MAD ≤ 30% are listed in Tables 4 and 5, from which the following results can be obtained:

(a) The new model performs best with a huge lead for all the categories. It predicts the entire database, $D \le 3$ mm data, and $D > 3$ mm data with MADs of 14.1%, 16.8%, and 12.8%, respectively, while the best ΔT-independent correlation predicts the entire database, $D \le 3$ mm data, and $D > 3$ mm data with MADs of 20.1%, 18.9%, and 22.3%, respectively.

(b) The Cavallini et al. [28] correlation has the highest prediction accuracy among the existing correlations, predicting the entire database, $D \le 3$ mm data, and $D > 3$ mm data with MADs of 16.9%, 20.6%, and 15.0%, respectively. However, it is a ΔT-dependent correlation. As aforementioned, ΔT is often an unknown in common engineering practice. This may cause accuracy loss and time consuming in iteration process, resulting in uncertainties in the iteration process to obtain ΔT, which decreases the prediction accuracy in usage.

The error distribution of the new correlation for the entire database is shown in Fig. 5, where the error distributions of the top three best existing correlations are given for comparison. It can be seen that the error distribution of the new correlation is fairly even except although it under-predicts a couple of points at very low HTC. The Cavallini et al. [28] correlation under-predicts largely when the HTC is between 3 and 20 kW/m^2 K. Similar to the Cavallini et al. [28] correlation, the Shah [13] and Dorao-Fernandino [38] correlations under-predict largely when the HTC is between 2 and 20 kW/m^2 K.

4.2 COMPARISON BASED ON INDIVIDUAL FLUIDS

The applicability of the new and 37 existing correlations to individual fluids is assessed. The deviations of the top five correlations in prediction accuracy for individual fluids are listed in Table 10, where the first number in the brackets is MAD (%) and the second is MRD (%). Table 10 listed 21 fluids. Those with data points less than 30 are not included, considering that the results based on so few data points may not be reliable. From Table 19 the following points can be seen:

(a) The new correlation performs best for 10 fluids among the 21 ones, including R12, R1234ze(E), R134a, R22, R245fa, R404A, R407C, R50, CO_2, and 60R32/40R125, roughly half of the fluids. Besides, it appears 7 times for the other fluids, totally 17 times as the top five correlations for individual fluids.

(b) The Cavallini et al. [28] correlation appears 13 times, with three times as the best. The Shah [13] correlation appears 9 times, with one time as the best. The Dorao-Fernandino [38] correlation appears

10 times, but none is the best.

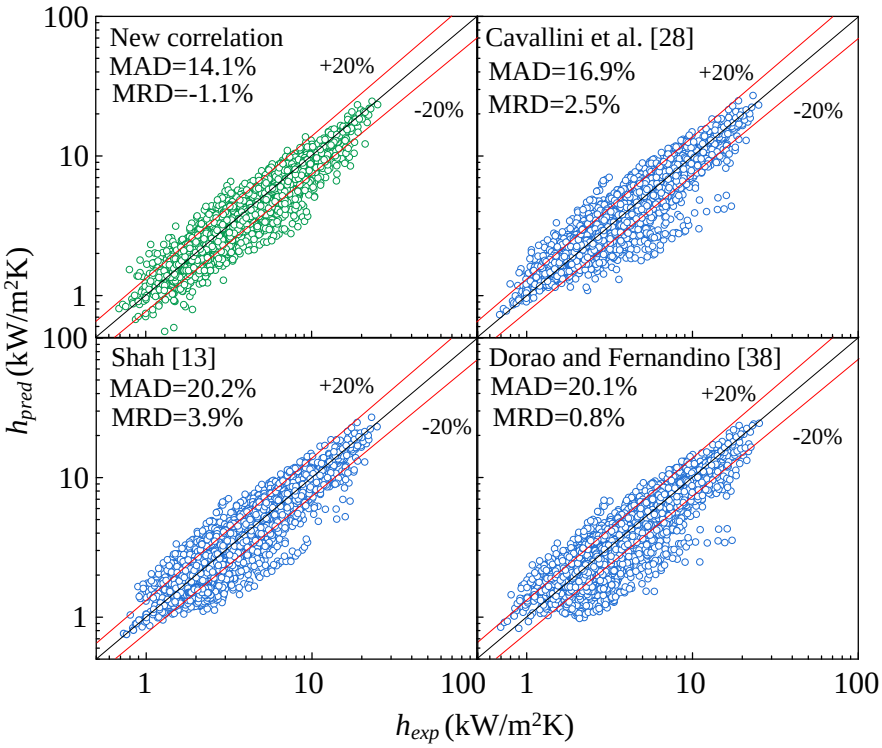

Fig. 5 Comparison of error distributions: New correlation vs. top three best ones

Table 10 Deviations of the top five correlations in prediction accuracy for individual fluids (%)

Fluid	No. 1	No. 2	No. 3	No. 4	No. 5
R12	New correlation (13.5, –9.8)	Zhuang et al. [40] (14.4, –7.6)	Cavallini et al. [28] (16.5, –15.1)	Shah [13] (16.5, –13.0)	Tang et al. [33] (18.8, –13.6)
R123	Thome et al. [34] (15.7, –4.9)	Dorao-Fernandino [38] (16.8, 4.3)	Shah [13] (16.9, 11.5)	Zhuang et al. [40] (17.2, 1.1)	Cavallini et al. [28] (18.1, –15.1)
R1234yf	Shah [13] (15.8, –12.6)	Cavallini et al. [28] (16.4, –14.7)	Koyama et al. [31] (17.2, –9.2)	New correlation (17.5, –15.2)	Haraguchi et al. [22] (18.6, –16.3)
R1234ze(E)	New correlation (19.8, –10.7)	Haraguchi et al. [22] (20.8, 6.1)	Huang et al. [25] (21.5, 0.8)	Koyama et al. [24] (21.9, 5.1)	Thome et al. [34] (22.3, –17.1)
R134a	New correlation (12.9, 0.4)	Cavallini et al. [28] (14.1, –3.6)	Shah [13] (15.7, –4.4)	Dorao-Fernandino [38] (16.7, –8.3)	Haraguchi et al. [22] (18.7, 16.4)
R152a	Thome et al. [34] (12.3, –2.9)	Dorao-Fernandino [38] (12.4, 6.3)	New correlation (12.9, 10.8)	Haraguchi et al. [22] (12.9, –6.2)	Chen et al. [35] (16.6, 4.7)
R161	Cavallini et al. [30] (12.4, –3.1)	Cavallini et al. [28] (14.4, –4.4)	Shah [13] (14.4, –4.4)	Song et al. [100] (16.4, –2.6)	Tang et al. [33] (16.6, 13.7)
R170	Koyama et al. [24] (13.4, 3.1)	Haraguchi et al. [22] (13.5, –1.7)	Hosseini et al. [99] (14.1, 8.3)	Zhuang et al. [40] (16.8, 10.0)	New correlation (17.9, 13.1)
R22	New correlation (13.1, –1.9)	Cavallini et al. [28] (14.9, –1,7)	Zhuang et al. [40] (16.9, –6.4)	Shah [13] (17.7, –1.8)	Song et al. [100] (18.1, –4.7)
R245fa	New correlation (13.0, –8.5)	Park et al. [26] (17.0, –9.0)	Koyama et al. [31] (17.0, 16.8)	Haraguchi et al. [22] (19.6, 12.4)	Huang et al. [25] (20.3, 10.4)
R290	Cavallini et al. [28] (15.6, –9.3)	Shah [50] (15.6, –8.5)	Moser et al. [17] (18.0, –1.1)	Dorao-Fernandino [98] (18.6, –15.9)	Cavallini et al. [30] (19.1, –12.6)
R32	Cavallini et al. [28] (7.6, –1.0)	Shah [13] (8.6, –1.5)	Dorao-Fernandino [38] (9.0, –0.3)	New correlation (11.9, –8.7)	Cavallini et al. [30] (13.7, –8.2)
R404A	New correlation (12.7, –3.9)	Cavallini et al. [28] (13.6, 4.8)	Shah [13] (14.1, 8.8)	Zhuang et al. [40] (14.5, –8.1)	Song et al. [100] (17.3, 4.1)
R407C	Park et al. [26] (17.8, –6.6)	Zhuang et al. [40] (19.4, 10.6)	Koyama et al. [31] (19.5, 19.2)	Huang et al. [25] (20.3, 8.8)	New correlation (20.9, 19.8)
R41	Haraguchi et al.[22] (10.8, 0.3)	Huang et al. [25] (14.0, –6.6)	Cavallini et al. [30] (16.9, –2.4)	Koyama et al. [24] (17.9, 8.3)	New correlation (20.9, 17.6)

Table 10 Continued

Fluid	No. 1	No. 2	No. 3	No. 4	No. 5
R410A	New correlation (20.2, –6.5)	Zhuang et al. [40] (22.9, –7.8)	Cavallini et al. [28] (25.2, –3.3)	Koyama et al. [31] (26.3, –5.4)	Tang et al. [33] (29.8, –18.1)
R50	New correlation (8.3, –5.0)	Hosseini et al. [99] (12.3, –5.1)	Dorao-Fernandino [98] (14.6, 11.0)	Zhuang et al. [40] (14.6, 1.9)	Haraguchi et al. [22] (14.8, 5.1)
R600a	Cavallini et al. [28] (9.7, –4.4)	Haraguchi et al. [22] (10.0, 2.8)	Shah [50] (10.6, –5.4)	Koyama et al. [24] (10.7, 1.9)	Huang et al. [25] (10.7, –3.1)
CO_2	New correlation (13.1, 6.5)	Thome et al. [34] (16.7 –7.7)	Dorao-Fernandino [38] (22.1, 19.0)	Cavallini et al. [28] (22.8, 19.3)	Zhuang et al. [40] (22.9, 4.9)
60%R32/ 40%R125	New correlation (10.6, –5.1)	Cavallini et al. [28] (11.9, 1.6)	Shah [13] (13.3, 1.0)	Dorao-Fernandino [38] (14.6, –3.4)	Zhuang et al. [40] (17.1, –1.2)
60%R152 /40%R1234 ze	Thome et al. [34] (19.3 –8.4)	Hosseini et al. [99] (20.4, –9.6)	Dorao-Fernandino [98] (21.6, –4.8)	Song et al. [100] (22.0, 0.4)	New correlation (22.0, –0.7)

5. EDDY AND VERTEX PHENOMENA IN TWO-PHASE PIPE FLOW

Gas-liquid two-phase eddy and vertex phenomena often appear in helically coiled tubes. Due to their compact structure, ease of manufacture, and high heat transfer efficiency, helically coiled tube heat exchangers have long been used in a number of industries and processes, such as in nuclear, food, and power generation industries and in refrigeration, heat recovery, space heating, and air-conditioning processes [106–108]. Compared to straight tubes, helically coiled tubes yield enhanced heat transfer characteristics due to the vertex-like secondary flow (Fig. 6), perpendicular to the axial fluid direction, which results in an improved fluid mixing and thus reduces the thickness of the thermal boundary layer. Fig. 7 is the velocity vector drawing at the cross section of the inlet tube of a once-through steam generator [108]. There are many eddies and vortexes in the upward cavity near the inlet nozzle due to the unique sudden expansion structure in the once-through steam generator, which have a great impact on the pressure drops and flow distribution and thus affect heat transfer.

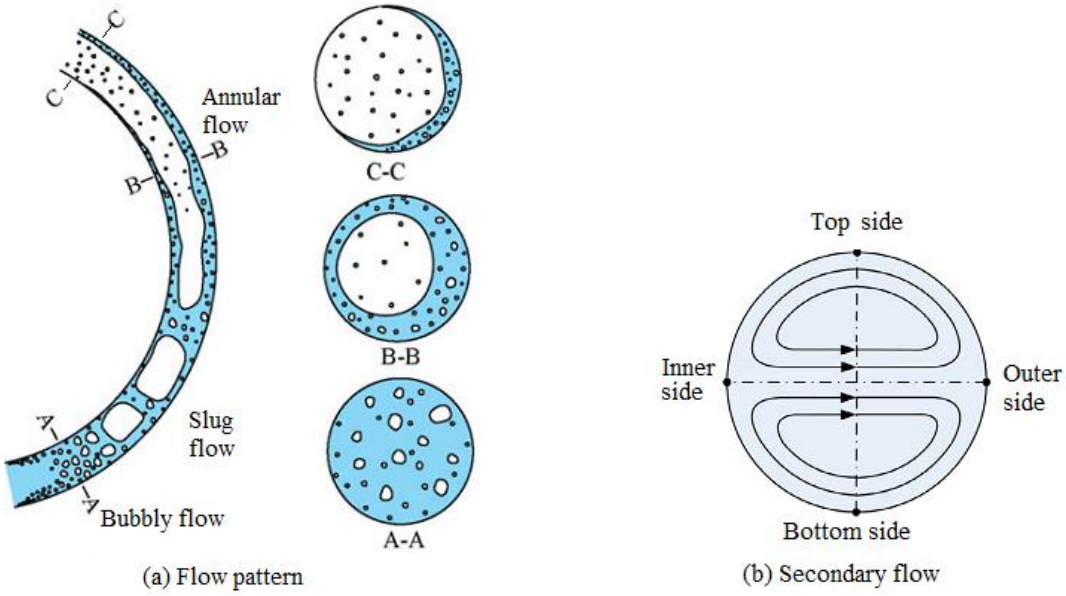

Fig. 6 Eddy and vertex phenomena in helically coiled tubes [107]

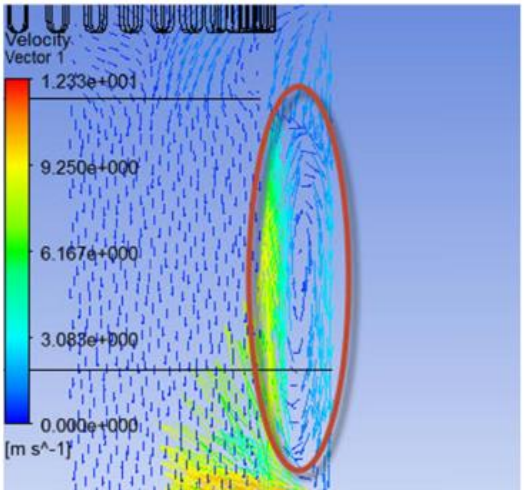

Fig. 7 Velocity vector drawing at inlet tube [108]

6. CONCLUSION AND DISCUSSION

It is important to predict accurately the HTC of flow condensation in plain channels for the design and development of related thermal equipment and systems. The present paper presents a new such correlation with high prediction accuracy. The following results are obtained.

(1) A compound database of condensation heat transfer containing 5607 data points was compiled from 52 sources. It is the largest database of this kind. It covers 30 fluids, including 12 pure halocarbon refrigerants, 9 halocarbon refrigerant blends, and 9 hydrocarbon refrigerants. The parameter range is D = 0.493–20 mm, x = 0.003–0.992, G = 24–1533 kg/m^2 s, q = 2.9–422 kW/m^2, p_r = 0.04–0.95, Pr_l = 1.7–8.5, Re_l = 11.6–5.3×10^4, and Re_g = 75.1–9.1×10^5.

(2) Based on the database, a new correlation with high accuracy is developed. It predicts the entire database, $D \le 3$ mm data, and $D > 3$ mm data with MADs of 14.1%, 16.8%, and 12.8%, respectively, much better than the best ΔT-independent one.

(3) Thirty-six existing correlations are evaluated against the database. The top two ΔT-independent correlations in prediction accuracy are the Dorao-Fernandino [38] and Shah [13] and correlations. The former predicts the entire database, $D \le 3$ mm data, and $D > 3$ mm data with MADs of 20.1%, 18.9%, and 22.3%, respectively, and the latter predicts the entire database, $D \le 3$ mm data, and $D > 3$ mm data with MADs of 20.2%, 20.1%, and 20.3%, respectively.

(4) The existing correlation with the smallest MAD is Cavallini et al. [28], which predicts the entire database, $D \le 3$ mm data, and $D > 3$ mm data with MADs of 16.9%, 20.6%, and 15.0%, respectively. However, because it is ΔT-dependent, the actual accuracy in practice may deteriorate noticeably due to the uncertainties caused by the unknown ΔT. Besides, it is time consuming in the iteration process to get ΔT.

(5) The applicability of the new and 37 existing correlations to individual fluids is assessed. The new correlation performs best for 10 fluids among the 21 evaluated, and it appears 7 times for the other fluids, 17 times in total as the top five correlations for individual fluids. The Cavallini et al. [28] correlation appears 13 times, with three times as the best. The Shah [13] correlation appears 9 times, with one time as the best. The Dorao-Fernandino [38] correlation appears 10 times, but none is the best.

(6) The strategy for developing a new correlation is suggested. It is useful for proposing a new correlation for engineering applications where no prediction method exists or the existing models cannot give an accurate prediction. The Fang number Fa plays an important role in the new correlation,

implying that it relates the fundamental mechanisms of two-phase heat transfer, both boiling and condensation heat transfer.

ACKNOWLEDGMENT

This study is supported by National Natural Science Foundation of China (52076107, 51576099) and funded by the Priority Academic Program Development of Jiangsu Higher Education Institutions.

CONFLICT OF INTEREST STATEMENT

There is no conflict of interest.

REFERENCE

[1] Mashaei P R, Shahryari M, Madani S. Analytical study of multiple evaporator heat pipe with nanofluid; A smart material for satellite equipment cooling application[J]. Aerospace Science and Technology, 2016, 59:112–121.
[2] Oh H U, Shin S, Baek C W. Thermal control of spaceborne image sensor using heat pipe cooling system[J]. Aerospace Science and Technology, 2013, 29 (1):394–402.
[3] Li Y, Li C, Chen E, Ying Y. Pressure wave propagation characteristics in a two-phase flow pipeline for liquid-propellant rocket[J]. Aerospace Science and Technology, 2011, 15 (6):453–464.
[4] Patel T, Parekh A D, Tailor P R. Experimental analysis of condensation heat transfer and frictional pressure drop in a horizontal circular mini channel[J]. Heat and Mass Transfer, 2020, 56:1579–1600.
[5] Shah M M. Comprehensive correlations for heat transfer during condensation in conventional and mini/micro channels in all orientations[J]. Int. J. Refrigeration, 2016, 67:22–41.
[6] Goss Jr G, Passos J C. Heat transfer during the condensation of R134a inside eight parallel microchannels[J]. Int. J. Heat Mass Transfer, 2013, 59:9–19.
[7] Azzolin M, Berto A, Bortolin S, Col D. Condensation heat transfer in minichannels: a review of available correlations[C]. Phys.: Conf. Ser., 2019, 1224:012038.
[8] United Nations Environment Programme (UNEP), Montreal protocol on substances that deplete the ozone layer[M]. 2006 MBTOC Assessment Report, 2006.
[9] Moreira T A, Furlan G, Oliveira G H, Ribatski G. Flow boiling and convective condensation of hydrocarbons: A state-of-the-art literature review[J]. Applied Thermal Engineering, 2021, 182:116129.
[10] Mauro A W, Napoli G, Pelella F, Viscito L. Flow pattern, condensation and boiling inside and outside smooth and enhanced surfaces of propane (R290). State of the art review[J]. Int. J. Heat Mass Transfer, 2021, 174:121316.
[11] Kim S M, Mudawar I. Review of databases and predictive methods for heat transfer in condensing and boiling mini/micro-channel flows[J]. Int. J. Heat Mass Transfer, 2014, 77:627–652.
[12] Zhang H, Fang X, Shang H, Chen W. Flow condensation heat transfer correlations in horizontal channels[J]. Int. J. Refrigeration, 2015, 59:102–114.
[13] Shah M M. Improved correlation for heat transfer during condensation in conventional and mini/micro channels[J]. Int. J. Refrigeration, 2019, 98:222–237.
[14] Rifert V, Sereda V, Gorin V, Barabash P, Solomakha A. Heat transfer during film condensation inside plain tubes, Review of experimental research[J]. Heat and Mass Transfer, 2020, 56:691–713.
[15] Kim S M, Mudawar I. Universal approach to predicting heat transfer coefficient for condensing mini/micro-channel flow[J]. Int. J. Heat Mass Transfer, 2013, 56(1):238–250.
[16] Akers W W, Rosson H F. Condensation inside a horizontal tube[J]. Chemical Engineering Progress Symposium Series, 1960, 56:145–149.
[17] Moser K W, Webb R L, Na B. A new equivalent Reynolds number model for condensation in smooth tubes[J]. J. Heat Transfer, 1998, 120:410–417.
[18] Shah M M. An improved and extended general correlation for heat transfer during condensation

in plain tubes[J]. HVAC&R Research, 2009, 15 (5):889–913.
[19] Shah M M. A general correlation for heat transfer during film condensation inside tube[J]. Int. J. Heat Mass Transfer, 1979, 22:547–556.
[20] Wang W W, Radcliff T D, Christensen R N. A condensation heat transfer correlation for millimeter-scale tubing with flow regime transition[J]. Experimental Thermal Fluid Science, 2002, 26(3):473–485.
[21] Cavallini A, Zecchin R. A dimensionless correlation for heat transfer in force convection condensation[C]. In: Proc. 5th Int. Heat Transfer Conference, 1974, 2: 309–313.
[22] Haraguchi H, Koyama S, Fujii T. Condensation of refrigerants HCFC22, HFC134a and HCFC123 in a horizontal smooth tube (2nd report, proposals of empirical expressions for the local heat transfer coefficient) [J]. Transactions of the Japan Society of Mechanical Engineers Part B, 1994, 60(574):2117–2124.
[23] Dobson M K, Chato J C. Condensation in smooth horizontal tubes[J]. J. Heat Transfer, 1998, 120(1):193–213.
[24] Koyama S, Kuwahara K, Nakashita K, Yamamoto K. An experimental study on condensation of refrigerant R134a in a multi-port extruded tube[J]. Int. J. Refrigeration, 2003, 24(4):425–432.
[25] Huang X, Ding G, Hu H, Zhu Y, Peng H, Gao Y, Deng B. Influence of oil on flow condensation heat transfer of R410A inside 4.18 mm and 1.6 mm inner diameter horizontal smooth tubes[J]. Int. J. Refrigeration, 2010, 33:158–169.
[26] Park J E, Vakili-Farahani F, Consolini L, Thome J R. Experimental study on condensation heat transfer in vertical minichannels for new refrigerant R1234ze (E) versus R134a and R236fa[J]. Experimental Thermal and Fluid Science, 2011, 35(3):442–454.
[27] Bohdal T, Charun H, Sikora M. Comparative investigations of the condensation of R134a and R404A refrigerants in pipe minichannels[J]. Int. J. Heat Mass Transfer, 2011, 54(9):1963–1974.
[28] Cavallini A, Del Col D, Doretti L, Matkovic M, Rossetto L, Zilio C, Censi G. Condensation in horizontal smooth tubes: a new heat transfer model for heat exchanger design[J]. Heat Transfer Engineering, 2006, 27(8):31–38.
[29] Bivens D B, Yokozeki A. Heat transfer coefficient and transport properties for alternative refrigerants[J]. Proc. Int. Refrigeration and Air Conditioning Conference, Purdue, Indiana, 1994, 299–304.
[30] Cavallini A, Censi G, Del Col D, Doretti L, Longo G A, Rossetto L. In-tube condensation of halogenated refrigerants[J]. ASHRAE Transactions, 2002,108 (1):146–161.
[31] Koyama S, Kuwahara K, Nakashita K, Yamamoto K. Condensation of refrigerant in a multi-port channel[C]. In: Proc. ICMM2003 Microchannels and Minichannels, New York, 2003, 193–205.
[32] Dobson M K, Chato J C, Wattelet J P, Gaibel J A, et al. Heat transfer and flow regimes during condensation in horizontal tubes[D]. ACRC TR-57, Air Conditioning and Refrigeration Center, University of Illinois at Urbana–Champaign, 1994.
[33] Tang L, Ohadi M M, Johnson A T. Flow condensation in smooth and microfin tubes with HCFC-22, HFC-134a, and HFC-410 refrigerants[J]. Part II: Design equations. J. Enhanced Heat Transfer, 2000, 7(5): 311–325.
[34] Thome J R, J. El Hajal, Cavallini A. Condensation in horizontal tubes, Part 2: new heat transfer model based on flow regimes[J]. Int. J. Heat Mass Transfer, 2003, 46(18):3365–3387.
[35] Chen S L, Gerner F M, Tien C L. General film condensation correlations[J]. Experimental Heat Transfer, 1987, 1(2):93–107.
[36] Shah M M. General correlation for heat transfer during condensation in plain tubes: further development and verification[J]. ASHRAE Trans. 2013, 119(2):3–11.
[37] Ananiev E P, Boyko I D, Kruzhilin G I. Heat transfer in the presence of steam condensation in horizontal tubes[J]. Int. Dev. Heat Transf., 1961, 2:290–295.
[38] Dorao C A, Fernandino M. Simple and general correlation for heat transfer during flow condensation inside plain pipes[J]. Int. J. Heat Mass Transfer, 2018, 122: 290–305.
[39] Akers W W, Deans H A, Crosser O K. Condensing heat transfer within horizontal tubes[J]. Chemical Engineering Progress Symposium Series, 1959, 55:171–176.
[40] Zhuang X R, Chen G F, Zou X, Song Q L, Gong M Q. Experimental investigation on flow condensation of methane in a horizontal smooth tube[J]. Int. J. Refrigeration, 2017, 78:193–214.
[41] Jung D, Song K H, Cho Y, Kim S J. Flow condensation heat transfer coefficients of pure

refrigerants[J]. Int. J. Refrigeration, 2003, 26: 4–11.
[42] Chang Y S, Kim M S, Ro S T. Performance and heat transfer characteristics of hydrocarbon refrigerants in a heat pump system[J]. Int. J. Refrigeration, 2000, 23:232–242.
[43] Jaster H, Kosky P G. Condensation heat transfer in a mixed flow regime[J]. Int. J. Heat Mass Transfer, 1976, 19(1):95–99.
[44] Traviss D P, Rohsenow W M, Baron A B. Forced convective condensation in tubes: a heat transfer correlation for condenser design[J]. ASHRAE Transactions, 1973, 79(1):157–165.
[45] Tandon T N, Varma H K, Gupta C P. Heat transfer during forced convection condensation inside horizontal tube[J]. Int. J. Refrigeration, 1995, 18:210–214.
[46] Macdonald M, Garimella S. Hydrocarbon condensation in horizontal smooth tubes: Part II – Heat transfer coefficient and pressure drop modelling[J]. Int. J. Heat Mass Transfer, 2016, 93:1248–1261.
[47] Pham Q V, Oh J T. Condensation heat transfer characteristics of R1234yf inside multiport mini-channel tube[J]. Int. J. Heat Mass Transfer, 2021, 170:121029.
[48] Jacob T A, Fronk B M. A heat transfer model to predict superheated and saturated condensation of HFC/HFO refrigerant mixtures[J]. Int. J. Heat Mass Transfer, 2021, 170:120947.
[49] Moreira T A, Ayub Z H, Ribatski G. Convective condensation of R600a, R290, R1270 and their zeotropic binary mixtures in horizontal tubes[J]. Int. J. Refrigeration 2021, 130:27–43.
[50] Shah M.M. A correlation for heat transfer during condensation in horizontal mini/micro channels[J]. Int. J. Refrigeration, 2016, 64:187–202.
[51] Fang X, Zhou Z, Li D. Review of correlations of flow boiling heat transfer coefficients for carbon dioxide[J]. Int. J. Refrigeration, 2013, 36:2017–2039.
[52] Kandlikar S G, Grande W J. Evolution of microchannel flow passages – thermohydraulic performance and fabrication technology[J]. Heat Transfer Engineering, 2003, 24 (1):3–17.
[53] Dobson M K, Chato J C, Wang S P, Hinde D K, Gaibel J A. Initial condensation comparison of R-22 with R-134a and R-32/R-125[R]. Air Conditioning and Refrigeration Center, College of Engineering, University of Illinois at Urbana–Champaign, 1993.
[54] Shin J S, Kim M H. An experimental study of flow condensation heat transfer inside circular and rectangular mini-channels[J]. Heat Transfer Engineering, 2005, 26:36–44.
[55] Shin J S, Kim M H. An experimental study of condensation heat transfer inside a mini-channel with a new measurement technique[J]. Int. J. Multiphase Flow, 2004, 30(3):311–325.
[56] Park K J, Jung D, Seo T. Flow condensation heat transfer characteristics of hydrocarbon refrigerants and dimethyl ether inside a horizontal plain tube[J]. Int. J. Multiphase Flow, 2008, 34:628–635.
[57] Tang S C, Liu X, Tao W Q. Experimental study on condensation heat transfer of R22 in horizontal micro-fin and smooth tube[J]. J. Zhengzhou University of Light Industry: Natural Science, 2007, 22:42–45.
[58] Derby M, Lee H J, Peles Y, Jensen M K. Condensation heat transfer in square, triangular, and semi-circular mini-channels[J]. Int. J. Heat and Mass Transfer, 2012, 55:187–197.
[59] Guo Q, Li M, Gu H. Condensation heat transfer characteristics of low-GWP refrigerants in a smooth horizontal mini tube[J]. Int. J. Heat Mass Transfer, 2018, 126:26–38.
[60] Kim N H, Cho J P, Kim J O, Youn B. Condensation heat transfer of R-22 and R-410A in flat aluminum multi-channel tubes with or without micro-fins[J]. Int. J. Refrigeration, 2003, 26:830–839.
[61] Meyer J P, Dirker J, Adelaja A O. Condensation heat transfer in smooth inclined tubes for R134a at different saturation temperatures[J]. Int. J. Heat Mass Transfer, 2014, 70:515–525.
[62] Olivier S P, Meyer J P, Paepe M D, Kerpel K D. The influence of inclination angle on void fraction and heat transfer during condensation inside a smooth tube[J]. Int. J. Multiphase Flow, 2015, 80:1–14.
[63] Meyer J P, Ewim D R E. Heat transfer coefficients during the condensation of low mass fluxes in smooth horizontal tubes[J]. Int. J. Multiphase Flow, 2018, 99:485–499.
[64] Aroonrat K, Wongwises S. Experimental study on two-phase condensation heat transfer and pressure drop of R-134a flowing in a dimpled tube[J]. Int. J. Heat Mass Transfer, 2017, 106:437–448.
[65] Rahman M M, Kariya K, Miyara A. An experimental study and development of new correlation for condensation heat transfer coefficient of refrigerant inside a multiport minichannel with and

without fins[J]. Int. J. Heat Mass Transfer, 2018, 116:50–60.
[66] Del Col D, Bortolin S, Cavallini A, Matkovic M. Effect of cross sectional shape during condensation in a single square minichannel[J]. Int. J. Heat and Mass Transfer, 2011, 54:3909–3920.
[67] Wen T, Zhan H, Zhang D. Flow condensation heat transfer characteristics of R134a in multiport mini-channel by jet impingement cooling[J]. Applied Thermal Engineering, 2019, 147:399–409.
[68] Keniar K, Garimella S. Experimental investigation of refrigerant condensation in circular and square micro- and mini-channels[J]. Int. J. Heat Mass Transfer, 2021, 176:121383.
[69] Hinde D K. Condensation of refrigerants 12 and 134a in horizontal tubes with and without oil[R]. Air Conditioning and Refrigeration Center, College of Engineering, University of Illinois at Urbana-Champaign, 1992.
[70] Zhang M. A new equivalent Reynolds number model for vapor shear-controlled condensation inside smooth and micro-fin tubes[M]. Ph.D. dissertation, Department of Mechanical Engineering, Pennsylvania State University, 1998.
[71] Cavallini A, Censi G, Del Col D, Diretti L, Longo G A, Rossetto L. Experimental investigation on condensation heat transfer and pressure drop of new HFC refrigerants (R134a, R125, R32, R410A, R236ea) in a horizontal smooth tube[J]. Int. J. Refrigeration, 2001, 24(1):73–87.
[72] Zilly J, Jang J, Hrnjak P S. Condensation of CO_2 at low temperature inside horizontal microfinned tubes[R]. Air Conditioning and Refrigeration Center, College of Engineering, University of Illinois at Urbana–Champaign, 2003.
[73] Aprea C, Greco A, Vanoli G P. Condensation heat transfer coefficients for R22 and R407C in gravity driven flow regime within a smooth horizontal tube[J]. Int. J. Refrigeration, 2003, 26(4):393–401.
[74] Jang J, Hrnjak P S. Condensation of CO_2 at low temperatures[R]. Air Conditioning and Refrigeration Center, College of Engineering. University of Illinois at Urbana-Champaign, 2004.
[75] Kim M H, Shin J S. Condensation heat transfer of R22 and R410A in horizontal smooth and microfin tubes[J]. Int. J. Refrigeration, 2005, 28(6):949–957.
[76] Wang L, Dang C, Hihara E. Experimental study on condensation heat transfer and pressure drop of low GWP refrigerant HFO1234yf in a horizontal tube[J]. Int. J. Refrigeration, 2012, 35(5):1418–1429.
[77] Yan Y Y, Lin T F. Condensation heat transfer and pressure drop of refrigerant R-134a in a small pipe[J]. Int. J. Heat Mass Transfer, 1999, 42(4):697–708.
[78] Baird J R, Fletcher D F, Haynes B S. Local condensation heat transfer rates in fine passages[J]. Int. J. Heat Mass Transfer, 2003, 46(23):4453–4466.
[79] Wen M Y, Ho C Y, Hsieh J M. Condensation heat transfer and pressure drop characteristics of R-290 (propane), R-600 (butane), and a mixture of R-290/R-600 in the serpentine small-tube bank[J]. Applied Thermal Engineering, 2006, 26(16):2045–2053.
[80] Matkovic M, Cavallini A, Del Col D, Rossetto L. Experimental study on condensation heat transfer inside a single circular minichannel[J]. Int. J. Heat Mass Transfer, 2009, 52(9):2311–2323.
[81] Del Col D, Torresin D, Cavallini A. Heat transfer and pressure drop during condensation of the low GWP refrigerant R1234yf[J]. Int. J. Refrigeration, 2010, 33(7):1307–1318.
[82] Oh H K, Son C H. Condensation heat transfer characteristics of R-22, R-134a and R-410A in a single circular microtube[J]. Experimental Thermal and Fluid Science, 2011, 35(4):706–716.
[83] Zhang H Y, Li J M, Liu N, Wang B X. Experimental investigation of condensation heat transfer and pressure drop of R22, R410A and R407C in mini-tubes[J]. Int. J. Heat Mass Transfer, 2012, 55(13):3522–3532.
[84] Liu N, Li J M, Sun J, Wang H S. Heat transfer and pressure drop during condensation of R152a in circular and square microchannels[J]. Experimental Thermal and Fluid Science, 2013, 47:60–67.
[85] Kim N H, Lee E J, Byun H W. Condensation heat transfer and pressure drop in flattened smooth tubes having different aspect ratios[J]. Experimental Thermal and Fluid Science, 2013, 46:245–253.
[86] Jung D, Cho Y, Park K. Flow condensation heat transfer coefficients of R22, R134a, R407C, and R410A inside plain and microfin tubes[J]. Int. J. Refrigeration, 2004, 27:25–32.
[87] Vu P Q, Chien N B, Taek O J. An experimental investigation of condensation heat transfer

coefficient of R-410A in horizontal circular tubes[J]. Applied Mechanics and Materials, 2015, 75: 3113–3118.
[88] Kim C H, Shah Y, Kim N H. Condensation heat transfer and pressure drop of low GWP R-404A alternative refrigerants in a multiport tube[J]. Int. J. Heat Mass Transfer, 2021, 179:121722.
[89] Kim C H, Kim N H. Condensation heat transfer and pressure drop of low GWP R-404A-alternative refrigerants (R-448A, R-449A, R-455A, R-454C) in a 7.0-mm outer-diameter horizontal microfin tube[J]. Int. J. Refrigeration, 2021, 126:181–194.
[90] Li B, Feng L, Wang L, Dai Y. Experimental investigation of condensation heat transfer and pressure drop of R152a/R1234ze(E) in a smooth horizontal tube[J]. Heat Transfer Research, 2021, 52:35–54.
[91] Zhuang X R, Gong M Q, Zou X, Chen G F, Wu J F. Experimental investigation on flow condensation heat transfer and pressure drop of R170 in a horizontal tube[J]. Int. J. Refrigeration, 2016, 66:105–120.
[92] Kondou C, Hrnjak P. Heat rejection from R744 flow under uniform temperature cooling in a horizontal smooth tube around the critical point[J]. Int. J. Refrigeration, 2011, 34:719–731.
[93] Maråk K A. Condensation heat transfer and pressure drop for methane and binary methane fluids in small channels[D]. Doctoral thesis. Department of Energy and Process Engineering, Norwegian University of Science and Technology, 2009.
[94] Murphy D. Condensation heat transfer and pressure drop of propane in vertical minichannels[D]. Master thesis, Georgia Institute of Technology, 2014.
[95] Agra O, Teke I. Experimental investigation of condensation of hydrocarbon refrigerants (R600a) in a horizontal smooth tube[J]. International Communications in Heat and Mass Transfer, 2008, 35(9):1165–1171.
[96] Kim Y J, Jang J, Hrnjak P S, Kim M S. Condensation heat transfer of carbon dioxide inside horizontal smooth and microfin tubes at low temperatures[J]. Journal of Heat Transfer, 2009, 131(2):021501.
[97] Park C Y, Hrnjak P. CO_2 flow condensation heat transfer and pressure drop in multi-port microchannels at low temperatures[J]. Int. J. Refrigeration, 2009, 32(6):1129–1139.
[98] Dorao C A, Fernandino M. Dominant dimensionless groups controlling heat transfer coefficient during flow condensation inside pipes[J]. Int. J. Heat Mass Transfer, 2017, 112:465–479.
[99] Hosseini S H, Moradkhani M A, Valizadeh M, Zendehboudi A, Olazar M. A general heat transfer correlation for flow condensation in single port mini and macro channels using genetic programming[J]. Int. J. Refrigeration, 2020, 119:376–389.
[100] Song Q, Chen G, Xue H, Zhao Y, Gong M. R14 flow condensation heat transfer performance: Measurements and modeling based on two-phase flow patterns[J]. Int. J. Heat Mass Transfer, 2019, 136:298–311.
[101] Camaraza-Medina Y, Hernandez-Guerrero A, Luviano-Ortiz J L, Cruz-Fonticiella O M, García-Morales O F. New model for heat transfer calculation during film condensation inside pipes[J]. Int. J. Heat Mass Transfer, 2019, 141:180–190.
[102] Moreira T A, Ayub Z H, Ribatski G. Convective condensation of R600a, R290, R1270 and their zeotropic binary mixtures in horizontal tubes[J]. Int. J. Refrigeration, 2021, 130:27–43.
[103] Bashar M K, Khairul K, Kariya K, Miyara A. Condensation heat transfer of R1234yf in a small diameter smooth and microfin tube and development of correlation[J]. Int. J. Refrigeration, 2020, 120:331–339.
[104] Fang X. A new correlation of flow boiling heat transfer coefficients for carbon dioxide[J]. Int. J. Heat Mass Transfer, 2013, 64:802–807.
[105] Awad M M. A look on Fang number [J]. ASME Journal of Heat Transfer, 2014, 136:064502.
[106] Chen S, Hu Z, Xiao Y, Gu H. Experimental investigation of subcooled flow boiling heat transfer in helical coils[J]. Nuclear Engineering and Design, 2018, 327:187–197.
[107] Niu X, Yuan H, Quan C, Bai B, Zhao L. Flow boiling heat transfer of R134a in a vertical helically coiled tube[J]. Heat Transfer Engineering, 2019, 40(6):1393–1402.
[108] Ye K, Zhang Y, Sheng X, Li N, Yang Y, Chen Y. Numerical analysis of the flow behavior in a helically coiled once through steam generator[J]. Nuclear Engineering and Design, 2018, 330:187–198.

Keynote Lecture

Toshihiko Shakouchi
Professor, Emeritus
Graduate School of Engineering
Mie University, Japan

B.S. Eng., 1969 and M.S. Eng., 1971, Ehime University, and Dr. Eng., 1984, Nagoya University, Japan
Guest researcher, 1992-1993, Erlangen-Nuremberg University, Germany.
Chairperson of *The 1st Int.Conf,on Jets, Wakes and Separated Flows, ICJWSF-2005*, 2005, Toba-shi, Japan.
President of *Japan Soc. for Multiphase Flow, JSMF*, 2009.
Fellow of *Japan Soc. of Mechanical Engineers, JSME.*
Emeritus member of *JSMF*.

Interests

- Jets, wakes and separated flows
- Coanda reattached jet, Resonance jet, Oscillating jet, Edge-tone
- Supersonic Jet; Vector control, Gas atomization, Ejector
- Flow control
- Fluidics
- Gas-solid flow; Air classification of fine solid particles, Jet mill, Blaster
- Gas-liquid flow; Drag reduction, Gas absorption, Jet oscillation, FAC
- Heat transfer; Impinging jet, Oscillating jet, Heat exchanger
- Desalination of sea water by decompressed boiling

Lecture title:

Flow and Control of Some Jets and Separated Flows

One of the major purposes of fluid mechanics and engineering is to reduce the flow resistance caused by flow friction, flow separation, vortex generation, and others. To reduce the flow resistance, in general, flow control is carried out by a passive or an active method in order to reduce or increase the flow resistance depending on the needs. Passive flow control is performed by changing the configuration of flow channel or object a little and reducing the total flow resistance. On the other hand, active flow control uses a device requiring power, but it can perform various complex flow controls. In this lecture, the passive flow control of jets and separated flows is examined with flow characteristics, control methods, and some applications because jets and separated flows include the essence of fluid dynamics, such as, boundary layer flow, turbulent flow, shear flow, vortex flow and flow mixing. In particular, the effects of the nozzle shape, the tab, rib and vortex generator, and the orifice or notched orifice on the flow characteristics of sub- and supersonic jets are examined. Furthermore, the control and suppression of high speed jet noise by a chevron nozzle, some examples of active flow control, and other areas are examined. Globular formation of fine solid particles by flow control, lift control of airplane wings, and the flow control of a NOTAR helicopter without tail rotor are also addressed.

Experimental study on the heat transfer characteristics and frequency control of flashing spray cooling under varying operating conditions

Shang-Ming Wang, Zhi-Fu Zhou, Bin Chen*

State Key Laboratory of Multiphase Flow in Power Engineering, Xi'an Jiaotong University, Xi'an 710049, China
** Corresponding Author: chenbin@mail.xjtu.edu.cn*

As electronic chips tend to become more and more compact, traditional cooling methods can hardly satisfy the requirement of extremely high power density and low working temperature. With high heat transfer coefficient and critical heat flux (CHF) at low surface temperature, flashing spray cooling is considered as one of the most promising thermal management technologies, and its in-depth research has far-reaching significance for the optoelectronic manufacturing industry[1].

In this work, a close loop experimental rig was constructed to study the heat transfer characteristics of flashing spray cooling by R410A in steady-state, varying operating conditions and the frequency conversion, especially the effects of compressor frequency conversion on system parameters including mass flow rate, chamber outlet pressure, time required to reach steady state, and system cooling performance. The experimental system consists of an inverter compressor, a condenser, a spray chamber and a liquid-vapor separator and other accessories. The discharge pressure of the compressor can be up to 4.1 MPa. As shown in Fig. 1, the spray chamber is made of stainless steel high-pressure resistant cavity with tempered glass window. A nozzle with inner diameter of 0.8 mm sprays R410A droplets onto the smooth flat copper cooling surface. The distance between nozzle orifice and the cooling surface is 24.5 mm. To simulate chip heating, the bottom of the cooling surface is supported by a copper heating body, which is embedded with 10 evenly distributed heating rods and the heating power is changed by a voltage regulator. Two probe type K-type thermocouples are embedded at 9mm and 13.8mm below the cooling surface, and the recorded temperature is used to obtain the heat flux of the cooling surface by Fourier heat conduction.

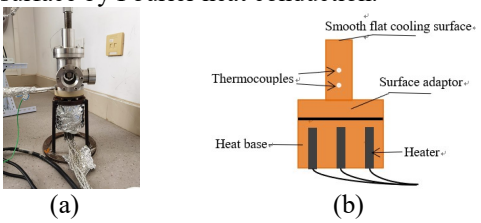

Fig. 1: Spray chamber (a) and test section (b)

The experimental results show that system takes 1200-1800s to reach the steady state. With increasing the heating voltage, phase change of the refrigerant inside the chamber can be observed. The heat transfer process of flashing spray cooling will experience three stages: single-phase heat transfer, two-phase boiling and partial drying, In the stage II, the heat transfer effect and cooling performance of the spray cooling system are the best. With increasing the compressor frequency, the mass flow rate of refrigerant in the system increases. The outlet pressure of the spray chamber has a linear negative correlation with frequency, and it is less influenced by the heat flux. In addition, an increase in compressor frequency can shorten the time consumed for the system to reach steady state.

From the Fig. 2 and Fig. 3 we can analyze the cooling performance of the system for different compressor frequency. When the compressor frequency is 10Hz, 15Hz and 20Hz, for smooth flat surface, CHF can reach 162.89 $W \cdot cm^{-2}$, 168.31 $W \cdot cm^{-2}$ and 175.02 $W \cdot cm^{-2}$, separately, at the condensation temperature of 26℃. In the heat transfer stage II with good heat transfer effect, the heat transfer coefficient falls within the interval [53.71, 72.28], [64.15, 88.62], [72.64, 99.94] $kW \cdot m^{-2} \cdot k^{-1}$, respectively. Meanwhile, the temperature of the chip surface can be maintained below 35℃, 30℃ and 25℃ in this stage. It is shown that the increase of compressor frequency can effectively improve the refrigeration performance of the whole system.

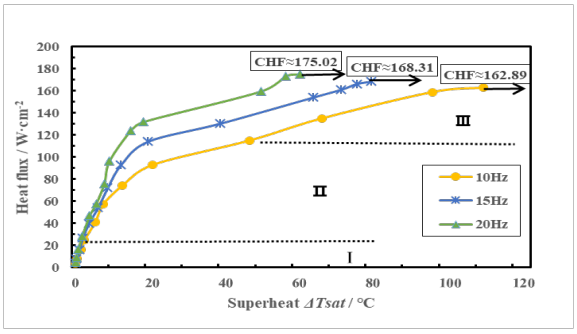

Fig. 2: Heat flux as a function of surface superheat for different compressor frequencies

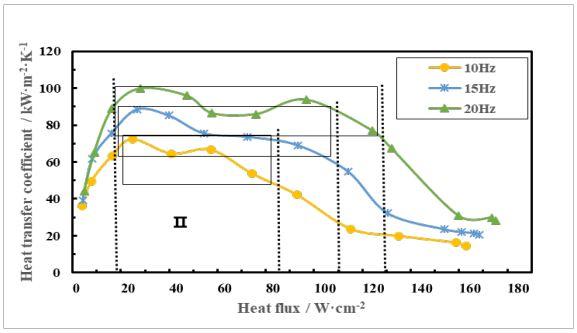

Fig. 3: Heat transfer coefficient as a function of heat flux for different compressor frequencies

References

[1] Bostanci Huseyin and Yata Vishnu V. R. and Kaluvan Suresh. Flow-Controlled Spray Cooling Approaches for Dynamic Thermal Management[J]. Journal of Electronic Packaging, 2021, 143(3):1-8.

Article S5.2

Influence of the inlet local annular swirling zone on an axisymmetric turbulent jet

Yevhenii Shkvar[1]*, Shi-ju E[1], Dmytro Redchyts[2], Svitlana Moiseienko[3]

[1]College of Engineering, Zhejiang Normal University,688 Yingbin Road, Jinhua, Zhejiang Province, 321004, China
[2]Institute of Transport Systems and Technologies of the NASU, Pysarzhevskoho str., 5, Dnipro, 49005, Ukraine
[3]Kherson National Technical University, Beryslavske highway, 24, Kherson, 73008, Ukraine
** Corresponding author: shkvar.eugene@qq.com*

ABSTRACT

A method for control of formation and further development of a turbulent free axisymmetric jet by creating a local annular swirling region at the inlet is considered. The main goal of this flow modification is to improve local mixing and increase the circumferential and radial uniformity of the flow as well as the characteristics transferred by it, such as heat. Particular attention was paid to the study of the effect of local annular swirl on the formation of a jet in a nozzle with a system of specially proposed impeller and deflector, as well as the localization and dynamics of the swirling region in the process of further jet development. Numerical model based on the Reynolds-averaged Navier-Stokes equations (RANS), closed by the Spalart-Allmaras (SA) turbulence model is developed. In order to verify the constructed mathematical model, the corresponding experimental studies of measuring the dynamic and thermal characteristics of the flow were carried out, which showed the existence of an acceptable for applied purposes correspondence between the numerical and experimental distributions of the maximum velocity and temperature in the jet along the axis of its development. The obtained results of parametric calculations demonstrated the effect of displacement of the local swirl region to the axis of symmetry with intensification of vorticity along the direction of the jet development.

KEYWORDS: Turbulent jet control, Local annular swirl zone, Numerical and experimental flow modeling, RANS

1. INTRODUCTION

Vortex formation is an effective mechanism for changing the structure of various flows, capable of enhancing mixing and purposefully influencing the distribution of turbulence and heat and mass transfer characteristics. There are many designs of efficient injectors that form swirling jets, which are effectively used in various technical devices and, in particular, in hydro-cyclones, in burners of combustion chambers of various jet engines for preparation of air-droplet fuel mixtures etc. [1-4]. In order to improve the characteristics of such devices and ensure the completeness of combustion, it is important to intensively mix flowing air with droplets of the fuel fraction, which are unevenly distributed over the area of the inlet section. Another example with a non-uniform distribution of parameters is a heat gun, where the temperature and flow velocity distributions at the outlet of the heating element are non-uniform due to different technological reasons not only in the radial, but also in the circumferential direction, and these factors negatively affect the direction, geometry and properties of the generated jet. Swirling the flow is capable of intensifying mixing and contributing to the uniformity of the flow in the circumferential direction, but it leads to additional losses of the jet energy in the longitudinal direction. Thus, annular swirling can be a reasonable alternative, since energy losses will be reduced in comparison with the global swirl, and the mixing effect can be realized locally in the most relevant region of the jet cross-section in its inlet. Therefore, the issue of optimal localization of the annular swirling region of the jet is an urgent problem for research. Moreover, the scope of application of such a technological solution can be much wider, including nozzles of jet rocket and aircraft engines, including also spacecraft engines, which control their positioning in space in order to form and stabilize the properties of the output jet.

2. PROBLEM STATEMENT AND AERODYNAMIC DESIGN FORMALIZATION

The **object of study** is a high-temperature ($t \leq 650$℃) axisymmetric free turbulent jet ($U \leq 30$ m/s), typical for many engineering applications, in which a swirl is created inside a nozzle head 2 only for a certain inlet annular zone 3 using a specially proposed impeller 4 with blades 12 installed on the core of the outlet section 5 of the air heating element 6 (Fig. 1). In particular, such a flow can be generated, for example, using a typical heat gun, which makes it easy to investigate this kind of flow also experimentally, although the scope of its possible applications is much wider.

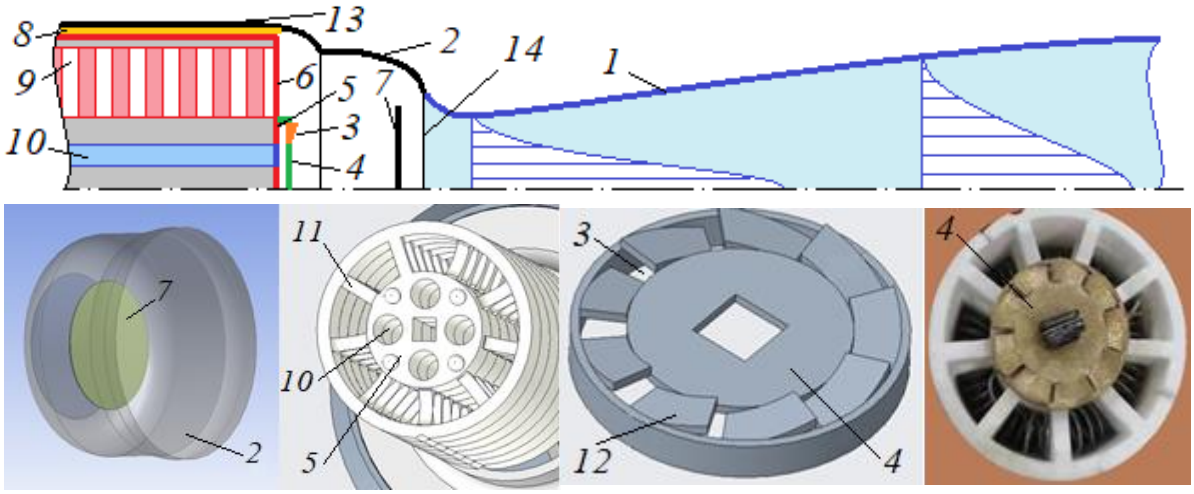

Fig. 1 Schematics of a swirl jet flow (due to axial symmetry only a half is illustrated) and the principal elements of a nozzle: 1 – axisymmetric free jet, 2 – nozzle head, 3 – local swirling annular zone, 4 - specially proposed impeller for purposeful generating the swirl zone, 5 - core of the outlet section of the air heater 6, 7 – nozzle head deflector, 8 – heat insulator between cylindric nozzle case unit 13 and heater 6, 9 – hot air channel, 10 – technological internal cold air channel, 11 – heater baffles, 12 – impeller blades, 14 – nozzle head outlet

To be more specific in the further modeling process, let's in addition to speed and temperature determine a number of basic geometric dimensions as a possible example: external diameter of the cylindric nozzle case 13 is 35mm, diameter of the nozzle head 2 is 30mm and its rounding radius is 6mm, diameter of the nozzle outlet 14 is 23mm, distance from outlet section of ceramic heater 5 to the head outlet is 18mm, distance between nozzle head outlet 14 and flow deflector 7 is 7mm and the diameter of this deflector is 20mm. As can be seen from Fig. 1, the radial baffles of the heater 11 and the technological channels of its core 10 are sources of uneven flow in the circumferential direction (Fig. 2*a*). The **basic idea** on the way to improve the flow uniformity is to create a tangential component of the input flow velocity 15 by the blades 12 of the impeller 4, which locally swirls the flow (Fig. 2*b*).

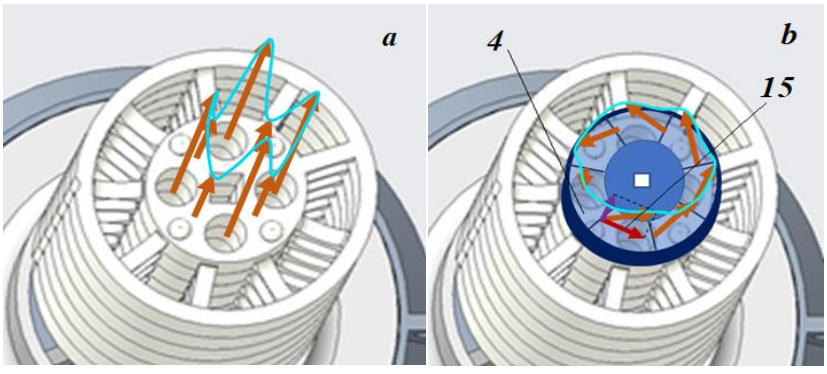

Fig. 2 Creating the local annular swirling flow by internal impeller 4

The **main goal** of the conducted research was to analyze the influence of the effect of local swirling of the inner annular part of the flow on the distribution of velocity and temperature in the axial *x*, radial *r*, and angular φ directions for the flow regions located both inside and outside the nozzle.

2. MATHEMATICAL MODEL

Due to flow symmetry we simplify the consideration by the axisymmetric case of turbulent free jet swirl flow, generated by the nozzle head, but the jet properties are strongly dependent on the shape of structural elements of the nozzle head, so the modeling of internal flow inside the exit part of nozzle has been a subject of special attention in the research. Despite the small flow speed, intensive local heating and temperature gradients require using the compressible flow model.

2.1 GOVERNING EQUATIONS

To simulate the jet flow from the heat gun nozzle, the following system of Reynolds-averaged Navier–Stokes (RANS) governing equations has been solved under the assumption of stationary incompressible (but density is temperature dependent) turbulent flow that completely corresponds to the formulated above working conditions:

$$\begin{cases} \nabla \cdot (\rho \bar{V}) = 0; \\ \rho(\bar{V} \cdot \nabla)\bar{V} = -\nabla p + \nabla \cdot (\mu \nabla \bar{V} + \sigma_t); \\ \rho c_p (\bar{V} \cdot \nabla)\bar{T} = \nabla \cdot (\lambda \nabla \bar{T} + q_t); \\ p = \rho R \bar{T}, \end{cases} \quad (1)$$

where $\sigma_t = -\rho\overline{u_i' u_j'}$ (i,j=1-3), q_t – the additional Reynolds stresses and heat flux density that are the result of turbulent exchange dissipative mechanism; p is the pressure; ρ is density; $\bar{T}$ is the average temperature; $\bar{V} = \{u_i\}$ – the average flow velocity; R=287 J/(kg K); μ, λ – molecular viscosity and heat conductivity coefficients respectively. The order of accuracy of the finite-volume discretization was chosen as second for diffusive terms and third for convective terms of all governing equations including the transport equation of turbulence model. The residuals for all computational variables were taken as $\varepsilon = 10^{-6}$.

2.2 TURBULENCE MODELING

According to the Boussinesq approach, the Reynolds stresses can be directly connected with the strain rate components similarly to the laminar case, but by the use of additional viscosity (so-called eddy- or turbulent viscosity μ_t) that reflects the dissipative mechanism of the turbulent vortical system: $\sigma_{t\,ij} = -\rho\overline{u_i' u_j'} = \mu_t \nabla \bar{V}$. Similarly, q_t can be found from the Fourier law $q_t = \lambda_t \nabla \bar{T}$ and the turbulent heat conductivity λ_t can be linked with μ_t based on the Prandtl's hypotheses as follows: $\lambda_t = \mu_t c_p / Pr_t$, where c_p – specific heat at p=const; Pr_t – the turbulent Prandtl number. According to the RANS approach, the turbulent viscosity μ_t must be modeled with the use of additional semi-empirical model of turbulence. Within the framework of ANSYS software, the Spalart–Allmaras turbulence model [5] was chosen for closing (1) as the most appropriate for the external flows and computationally efficient.

2.3 BOUNDARY CONDITIONS

The boundary conditions were established according to the ANSYS Fluent formalism as follows: All faces of surfaces of a nozzle and deflectors — Velocity Magnitude 0 m/s (wall); External lateral (top) and outlet (right) surface of domain — Gauge Pressure 0 Pa (pressure-outlet); Axis of flow – "Axis" boundary condition; Flow input (left) face surface of domain – Inlet (Velocity Magnitude is determined by the profile, associated with the geometry of outlet of ceramic heater for the flux 500 l/min). In particular, the input velocity was determined as nonuniform in radial direction, especially, in the heater core region (0≤r≤4mm) velocity was taken as 0 and in the region with small technological holes (4mm≤r≤8mm) velocity according to the corresponding experimental measurements was determined as its averaged value 10 m/s and swirl velocity there in case of its taking into account was given equal to 2 m/s. Velocity in the region of air heating element

(9mm≤r≤15mm) was taken equal to 4.5 m/s based on the experimental data.

2.4 COMPUTATIONAL DOMAIN AND MESH

The trapezoidal computational domain was selected based on the presence of a predominant longitudinal flow direction. Then it was covered by structured mesh, having the smallest cells and detailed structure in the neighborhood of the wall surfaces inside input sections and nozzle (Fig. 3). This mesh is structured and well-adjusted to free jet-flow as well as to the nozzle geometry. The total number of mesh nodes is 65206 that satisfies the condition y_1^+ <1.5 for near-wall nodes and further refinement of the grid no longer leads to any noticeable change in the solution properties.

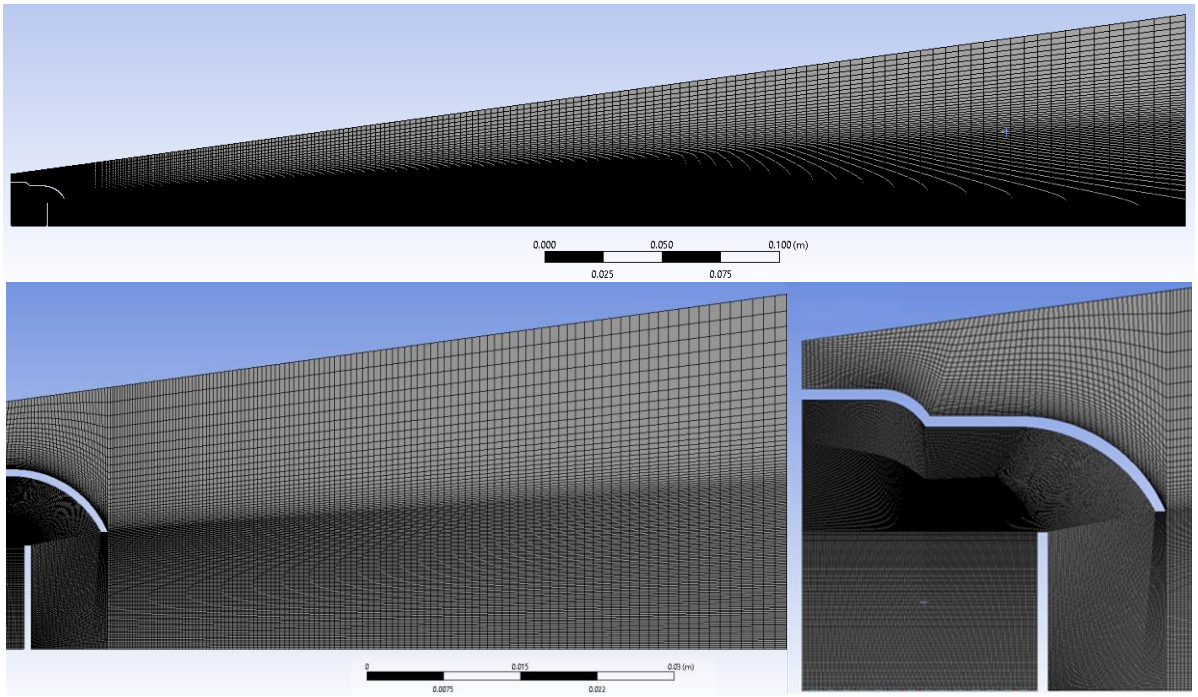

Fig. 3 Geometric model of the nozzle head, domain and computational mesh

3. RESULTS AND DISCUSSION

3.1 NUMERICAL MODEL VERIFICATION

The maximum velocity and temperature distributions along *x* coordinate, codirected with longitudinal axis of symmetry of the turbulent jet from the outlet of the heat gun nozzle and along the most interesting from the point of view of the intensity of formation of the initial flow region have been tested experimentally (Prandtl-Pitot velocimetry, attached to the differential digital manometer, high-temperature thermo-sensor and digital resistor-meter) and predicted numerically for the basic case of swirl absence (Fig. 4). As it follows from the comparison, the numerical predictions, obtained on the basis of the developed numerical model, correlate satisfactorily for most practical purposes with the experimental data for the analyzed jet flow region.

3.2 PARAMETRIC STUDY: FLOW PARAMETERS VS NOZZLE GEOMETRY

The most important of geometrical nozzle characteristics from the point of view of jet flow rate control are: angle α, distance between outlet and deflector H and angle of inclination of the deflector β (Fig. 5). The results of parametric numerical analysis for jet flow without swirl are presented below in the form of dimensionless coefficients $kU_\alpha = U/U_{\alpha=0}$, $kU_\beta = U/U_{\beta=0}$, $kU_H = U/U_{H=6mm}$. As it follows from the presented by Fig. 5 data the most rational values of the geometric nozzle head parameters α, β and H for the considering jet flow are: α=10-15°, β =0-14° and H=6-6.5mm and the following fixed values α=10°, β =0° and H=6.5mm will be applied in the following stages of flow simulation.

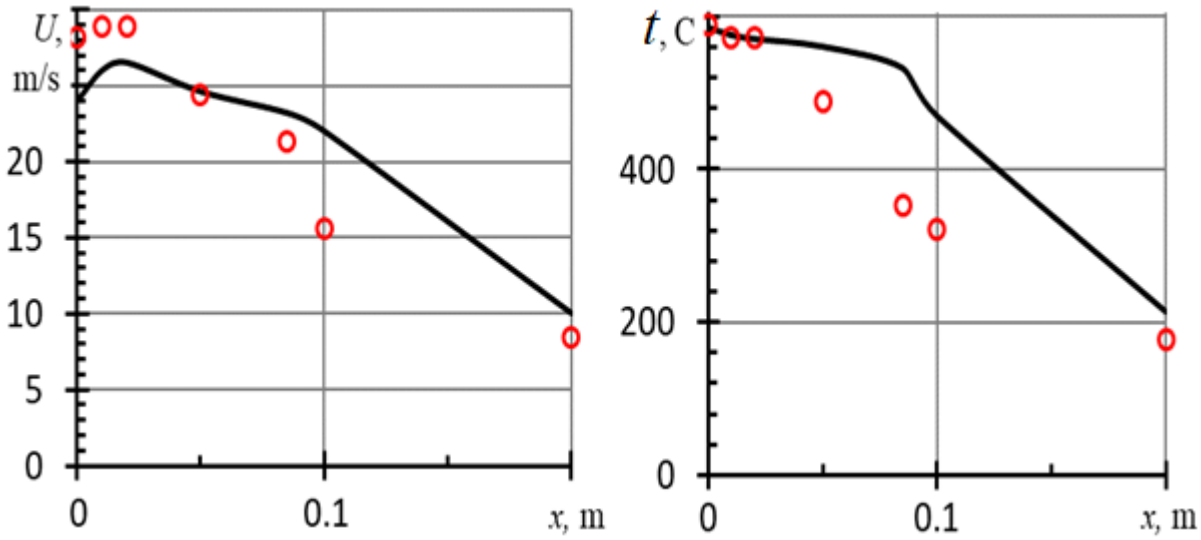

Fig. 4 Maximum velocity (left) and temperature (right) vs *x* (points – experiment, lines - predictions)

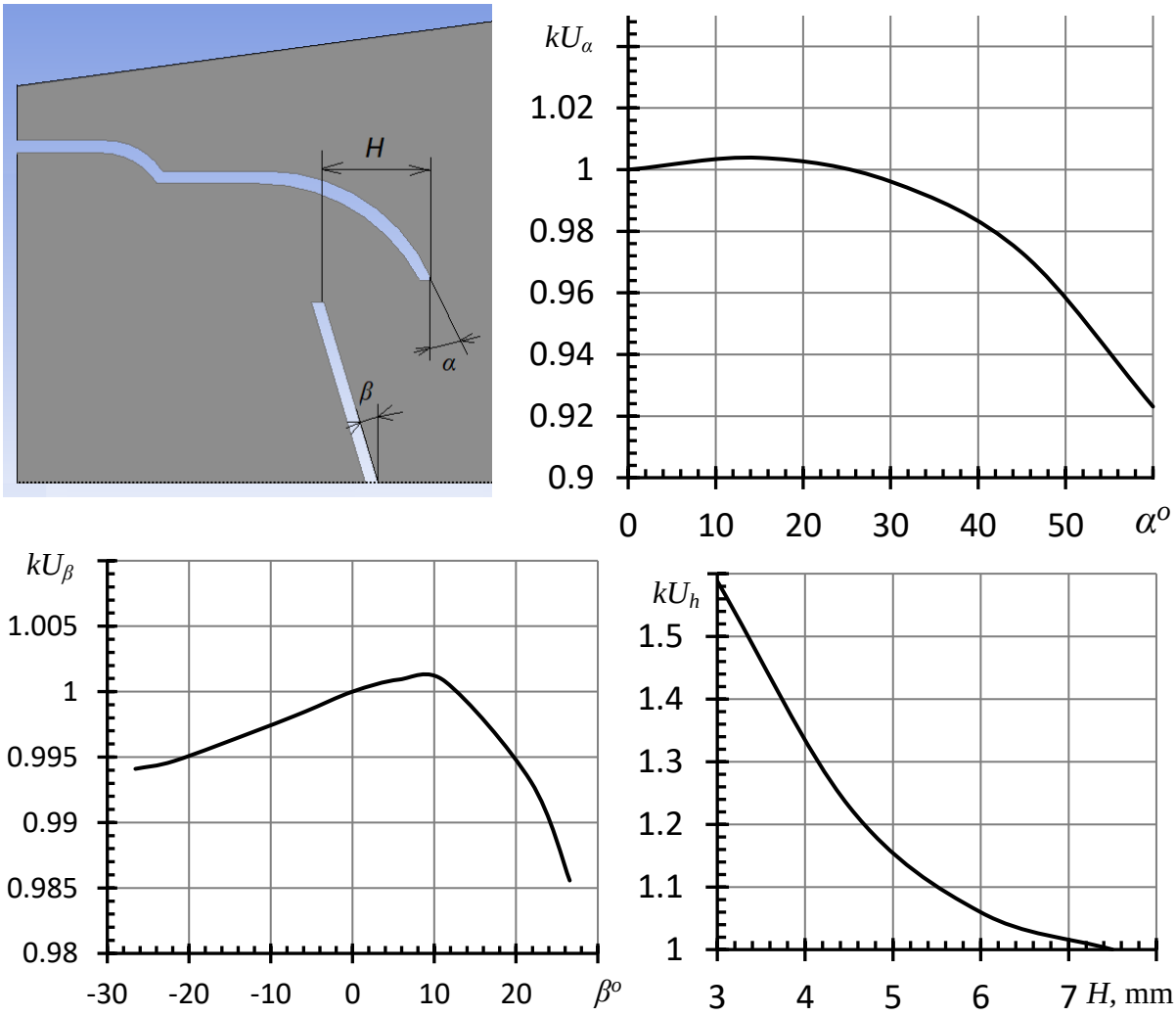

Fig. 5 Dependencies of dimensionless velocity coefficients vs the most principal geometrical parameters of the nozzle head α, *β* and *H*

3.3 LOCAL PARAMETERS OF THE SWIRLING JET (NUMERICAL STUDY)

The process of flow formation inside the nozzle head and the further development of the jet is represented by visualizations of numerically obtained fields of axial velocity u_x (*a*), temperature *t(y)* (*b*) and swirl velocity $u_\theta(y)$ (*c*) inside the computational domain in Fig. 6. Distinctive features here are: intensive transformation of the flow in the short nozzle head with its strong turn at the sharp outer edge of the circular deflector and further acceleration and narrowing of the flow at the initial region of the free jet. But the most interesting in connection with the objectives of this study is the process of swirling intensification at the initial region of the jet directly behind the deflector due to the displacement of the local swirling zone to the jet axis according to the 2-nd Helmholtz 'theorem. The practically important for various engineering applications effect of this swirling growth is the intensification of mixing in the central region of the jet and the transfer of the hot gas from the periphery of the jet to its central region with a lower temperature. As a result, the desired process of alignment of the temperature and velocity fields takes place in both the radial and circumferential directions.

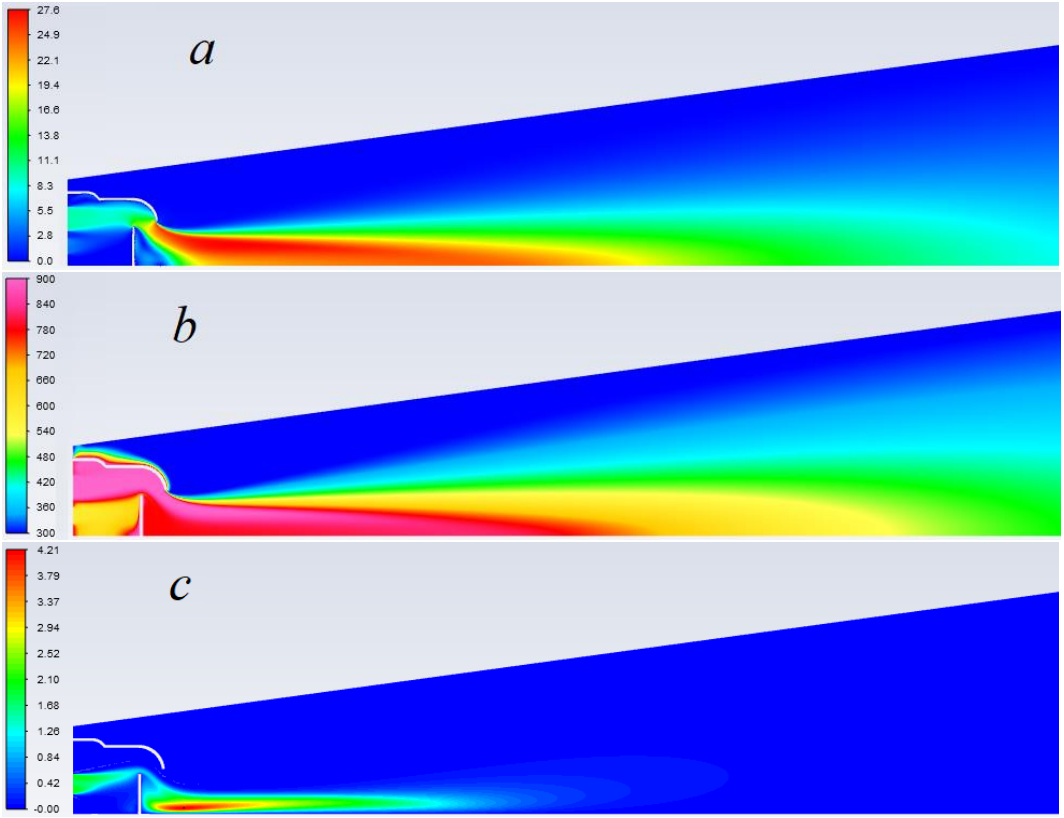

Fig. 6 Visualized numerical predictions of axial velocity $u_x(y)$ (*a*), temperature *t(y)* (*b*) and swirl velocity $u_\theta(y)$ (*c*) distributions in a swirl jet

For a more detailed quantitative assessment of the discussed process, Fig. 7 shows the profiles of the mentioned above simulated flow characteristics in several jet sections along its longitudinal axis. One can see that the axial velocity and temperature profiles (Fig. 7*a*, Fig. 7*b*) at the initial jet region have a non-monotonic distribution with a zone of slowed flow that surrounds the jet symmetry axis. In addition, Fig. 7*c* allows to estimate the doubled increase in the swirl velocity at the initial jet region (4 m/s) in comparison with its initial value in the local annular region of the impeller (2 m/s). In this case, the temperature on the jet axis increases by 50-70 degrees in comparison with the jet without local swirling, while the profiles of other characteristics, including the peripheral temperature, remain practically unchanged. Fig. 6*c* and Fig. 7*c* also allow us to conclude that the area of the most intense effect of swirling on the properties of the jet is limited precisely by its initial region.

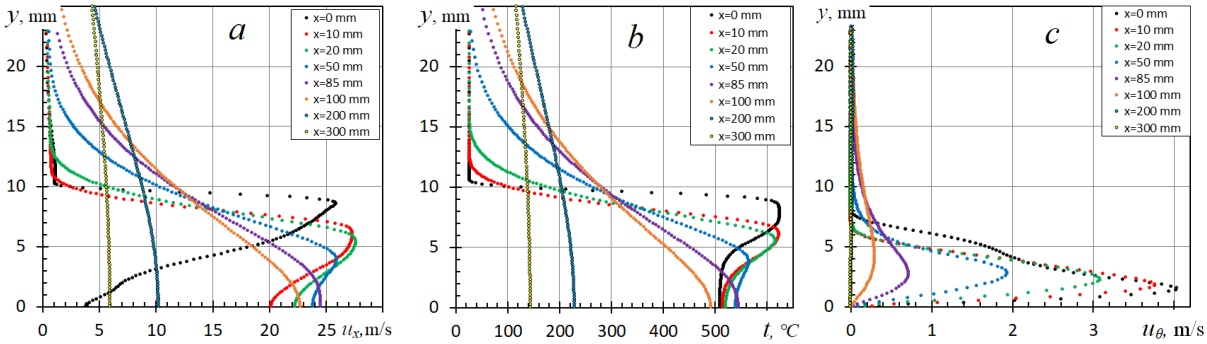

Fig. 7 Profiles of axial velocity $u_x(y)$ (*a*), temperature $t(y)$ (*b*) and swirl velocity $u_\theta(y)$ (*c*) in a swirl jet for different sections along x

3.4 INFLUENCE OF LOCAL ANNULAR SWIRL ON THE CIRCUMFFERENTIAL JET INHOMOGENEITY (EXPERIMENTAL STUDY)

Due to the difficulties of numerical simulation of the jet in 3D setting with the reproduction of the geometry of the impeller blades of small dimensions and various technological reasons for the non-uniformity of the flow, at this stage, the effectiveness of the proposed approach to improving the uniformity of the distribution of the jet parameters in the circumferential direction was experimentally tested. The velocity and temperature measurements were carried out with a Prandtl-Pitot tube and a high-temperature sensor at a distance of several millimeters from the nozzle head outlet in 18 sections (twice the number of ceramic heater baffles) in the circumferential direction with an angle step of 20º for 3 radiuses: r = 4mm (yellow line), r = 8mm (orange line), r = 10mm (blue line) and are represented by radial diagrams for cases where the impeller is absent (Fig. 8) and its presence (Fig. 9).

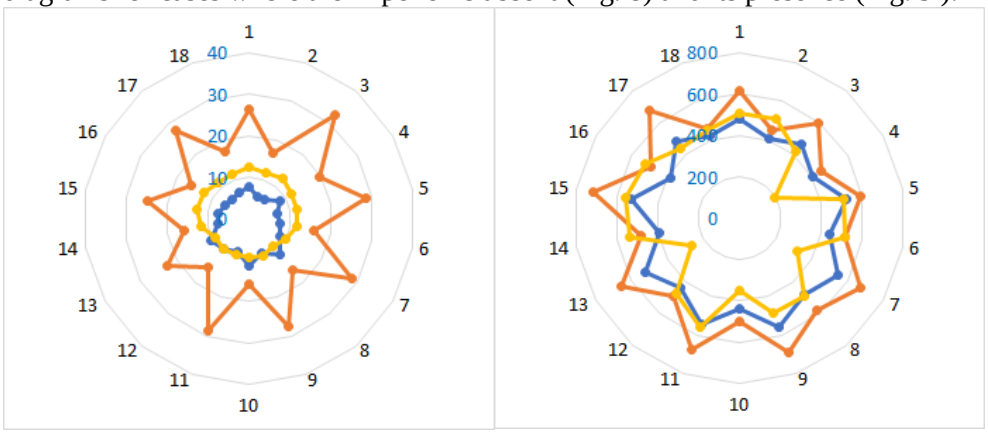

Fig. 8 Radial diagrams for axial velocity $u_x(\theta)$, m/s (left) and temperature $t(\theta)$,℃ (right) in the basic case of no swirl

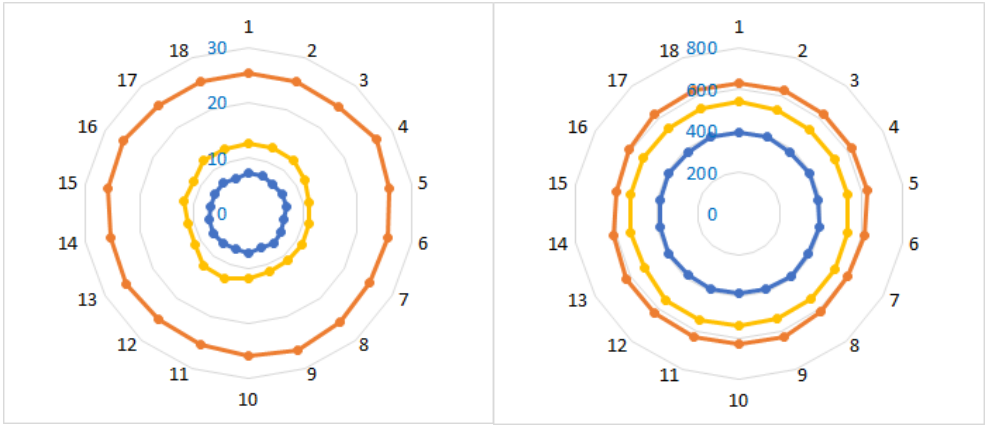

Fig. 9 Radial diagrams for axial velocity $u_x(\theta)$, m/s (left) and temperature $t(\theta)$,℃ (right) in the basic case present local annular swirl

As can be seen on the basis of such a fairly simple experiment, the presence of local swirling makes it possible to practically eliminate the effect of circular non-uniformity of the velocity and temperature distributions, which is caused, in particular, by the elements of the heating element design.

4. CONCLUSIONS

1. The analyzed turbulent axisymmetric jet flow, generated by a variety of heat guns and other devices, having similar functionality, is characterized by significant radial and circumferential nonuniformities, having various technologically determined reasons.

2. The theoretical numerical model of turbulent jet development has been worked out and successfully verified by the corresponding experimental measurements (Fig. 5). The developed model allowed to find the optimized superposition of the nozzle head parameters, namely: α=10-15^o, β =0-14^o and H=6-6.5mm.

3. The internal impeller with special design, containing the local annular zone with inclined blades for swirl generation, has been elaborated for covering the ceramic core of air heater with small technological holes (Fig. 1). The results of experimental testing and numerical simulation proved that installing such an impeller allowed to substantially improve the flow uniformity in both radial and circumferential directions without any tangible loss of energy of the main stream in axial direction.

4. The generated local internal swirling flow in the nozzle head strongly changes the further jet structure and parameters inside the initial region of flow development by creating the intensive swirling core. In this limited region, the swirl of the jet is localized in the region adjacent to the axis of symmetry, and the swirl velocity is doubled in comparison with its value at the outlet of the impeller.

5. Thus, an efficient method for purposful control of a thermal turbulent free jet by creating a local annular swirling zone of the incoming flow at the inlet has been developed. Its further improvement may consist in finding the optimal geometry and number of impeller blades in the local annular swirling zone, depending on the operating parameters of the technical device.

REFERENCE

[1] Vasilyev A.Yu., Sviridenkov A.A., Tretyakov V.V. Experimental investigations of fluid atomization by model frontal devices of combustion chambers [J]. Samara State Aerospace University Bulletin, 2011, 5 (29):55-64.

[2] Jiautheen, P.B., Tiwari, S., Annamalai, M. Three-dimensional Numerical Investigations on Ejector of Vapour Jet Refrigeration System [J]. International Refrigeration and Air Conditioning Conference. Paper, 2014, 1433.

[3] Shtern, V., Hussain, F. and Herrada, M. (2000) New features of swirling jets [J]. Physics of Fluids, 12: 2868-2877.

[4] Yang, Y., Zou, D., Sun, W. et al. A swirling jet from a nozzle with tangential inlets and its characteristics in breaking-up rocks [J]. Pet. Sci. 2012, 9: 53–58.

[5] Spalart P, Allmaras P. A one-equation turbulence model for aerodynamic flow [J]. AIAA, 1992, 12(1): 439-478.

Article S5.3

Experimental Study on Coaxial Swirling Jets

A. Naxakis, A. Romeos, A. Giannadakis, K. Perrakis, Th. Panidis*

Department of Mechanical Engineering & Aeronautics, University of Patras
Rion-Patras, 26504, Greece
* Corresponding Author: panidis@upatras.gr

ABSTRACT

Experimental results on coaxial swirling flows are presented, aiming to contribute to the investigation and understanding of vortical flows close to vortex breakdown conditions. Two swirling jets are issuing from parallel coaxial straight tubes of two sizes in a coaxial cylinder of diameter equal to the largest tube. Swirl is introduced by two rotating vanes located close to the outlets of both jets respectively. Initial conditions, flow rates and swirling strengths can be parametrically controlled. The mean flow fields are monitored on the axial central plane, based on measurements of all three velocity components, using Stereoscopic PIV. Refractive index matching is utilized to eliminate optical distortions. In the present experiments three inner and six annular flow rates were combined with four inner jet and three annular jet swirls comprising a relatively large number of inlet conditions. Two modified dimensionless numbers, Ro_{tot} and S_2, are introduced, to support the classification of the flow patterns and the discussion of the characteristic trends. An experimental map of flow conditions, based on the combination of the two dimensionless numbers, has been constructed, to classify the flow patterns. Four typical flow patterns can be identified for different inlet conditions. A "downstream core flow" (DCF) in test cases with no recirculation, a "closed bubble" type (CB) vortex breakdown, an "asymmetric recirculation" (AR) and an "intense recirculation" (IR) pattern.

KEYWORDS: Coaxial, Swirling flows, Vortex Breakdown,3DPIV

1. INTRODUCTION

Swirling motion is commonly observed in natural (tornadoes [1], twisters, typhoons) and artificial flows. Swirling flows cover an important scientific field in engineering. Swirl can enhance diffusion and mixing, and control vorticity and flow stabilization and the estimation of performance of systems using swirling flows, in various conditions, is of primary importance for their design and optimal operation. Therefore, swirling flows have been widely studied in relation to several engineering applications [2-10]. In combustion systems, the steep momentum and pressure gradients imposed by swirl are critical, defining the combustion chamber design [11-13]. The exploitation of the positive characteristics and the control of the negative features of swirling flows is a yet difficult task due to their complexity and diversity. The methods of producing swirling motion can be active or passive depending on whether the means of swirling are rotating or not. Various mechanisms, used in previous studies and applications include guide vanes (radial, axial, with a twist, or combinations of different types of guide vanes), tangential inlets and rotating parts (pipes, walls, rods, honeycombs) among others [14].

Swirling jets are broadly classified as low swirl jets or high swirl jets with recirculation. Generally, in swirling flows, "the presence of a strong azimuthal velocity component induces a strong radial pressure gradient in the flow close to the nozzle exit" [15]. Therefore, intensive swirl endorses the formation of strong flow reversals in internal recirculation zones [15]. A characteristic phenomenon associated with axially rotating flows, is the "vortex breakdown" or "vortex bursting" [16-18] phenomenon, first observed on delta wings by Petcham and Atkinson [19]. According to Leibovich [20], vortex breakdown is defined as "a disturbance characterized by the formation of an internal

stagnation point on the vortex axis, followed by a reversed flow in a region of limited axial extent". To have better control over swirling flows and the phenomenon of vortex breakdown, several researchers have studied experimentally axially rotating flows confined in tubes. Early work on vortex breakdown was mostly relying on flow visualization [21, 22], although theoretical and mathematical analysis [16, 23-24] and numerical simulations have been also advanced, as outlined in excellent past reviews [14, 25].

2. EXPERIMENTAL SETUP

The experimental facility is the same as in Naxakis et al. [26]. The main components are shown in figure 1. Two upward flow streams issuing from inlet preconditioning coaxial tubes are interacting within a transparent Plexiglas tube of internal diameter equal to that of the outer tube. The test section is encased in a transparent rectangular box, filled with 99.9% pure glycerin, for refractive index matching, to alleviate refraction problems in optical measurements [27-28]. Swirl can be applied at both streams independently with the use of rotating impellers equipped with 8 flat blades each, at angles of attack $a_i=a_o=0°$ for the inner and the annular tubes respectively. The inner impeller has length $l_1=100$mm, with its trailing edge 30mm downstream of the trailing edge of the annular impeller, which has length $l_2 = 40$mm. Induced swirl is regulated with inverters guiding the motors, which control the rotational speed of the inner and the annular impellers. Filtered, deionized tap water is used as the working fluid. To avoid pump induced oscillations and achieve steady flowrates, the flow in both streams is regulated by controlling the free surface height of two overflow tank systems, supplied from the same 200 litters storage tank. The flowrate of each stream was monitored with variable area flowmeters, with an uncertainty of $u_{fm}=5$ lit/h. More details on the experimental facility can be found in Naxakis et a. [26].

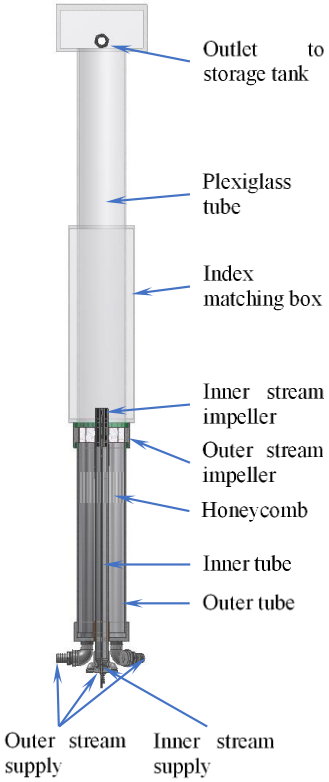

Fig. 1 Experimental Setup

Measurements of the three velocity components were obtained on a central axial plane, downstream the stream interaction, with three-dimensional Particle Image Velocimetry (3D PIV) [29-30]. The flow was seeded, through the storage tank, with hollow glass spheres of 60 μm mean diameter [31]. A

double-pulse Nd:YAG laser (Quantel EverGreen) operating at 532 nm generated the laser light sheet of 2 mm thickness. Pairs of field images were captured by two CCD cameras (LaVision Imager Pro X 2M), fitted with Nikon AF Micro Nikkor 60 mm lenses (f/4) and bandpass filters with spectral range 525-550 nm. Scheimpflug adapters on both cameras were used to achieve high quality focus. The cameras were positioned on opposite sides of the laser sheet, in a backward-backward scattering setup, at 30° to the normal to the measuring plane [26]. Spatial calibration was performed prior to each measuring session. A homemade calibration plate (following the design of LaVision's type 11-3D calibration plate) was used in a plexiglass mockup, simulating accurately the index matching box and the test section. The 1200 pixel×1600 pixel imaged field was 126 mm wide by 168 mm tall. 800 pairs of images were recorded at 7 Hz for each test case, to achieve convergence of mean values. LaVision Davis 8.2.2 software was used for the processing of the raw data. For the first three passes, the interrogation window was 64 pixels × 64 pixels with a 50% overlap. For the last pass, an interrogation window of 32 pixels × 32 pixels with a 75% overlap was used. Further details about the instrumentation can be found in [26].

The results in this work are referred to a Cartesian coordinate system, which is related to the cylindrical coordinate system defined by the tube axis as follows: x and y lay on the axial plane where measurements were obtained, with x in the radial direction and y in the axial direction, whereas z is normal to them, in the tangential direction. The origin of the coordinate system is located on the axis of the test section, 24 mm downstream of the outlet of the internal tube.

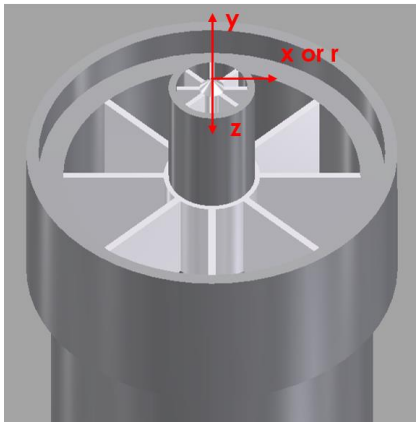

Fig. 2 Coordinate system

A revolution counter was used for the calibration of the inverters that controlled the inner and the annular swirler. Plots depicting the relation between inverter frequency settings and revolutions per minute for each inverter respectively are shown if figure 3. These plots indicate that the rotation rate of both swirlers changed almost linearly with the frequency setting of the inverters.

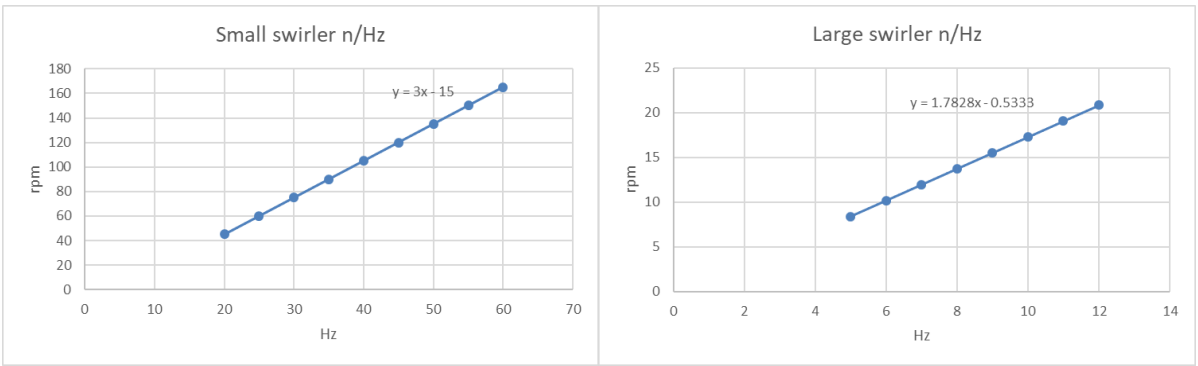

Fig. 3 RPM vs inverter frequency plots for the inner and annular swirler

3. DEFINITION OF MODIFIED DIMENSIONLESS NUMBERS, RO_{TOT}, S_2

The results of this study are discussed mainly in relation to streamline plots based on the x and y components of the mean velocity on the measuring plane, which provide the topological characteristics of the flow field in relation to the volume flowrate and rotational speed of the two streams. Since the flow field is three-dimensional, with significant values of the velocity component in z direction, vertical to the xy plane, these lines do not represent trajectories of actual mean flow but help to distinguish flow patterns and understand and discuss the characteristics of the flow field and its topology. Besides, in these plots, iso-contour distributions of the axial (longitudinal) average velocity are included, indicating the recirculation areas in the flow field.

Swirling flows are customarily presented in terms of a suitable swirl number and/or Rossby number. Following the reasoning of previous investigations and the analysis of Giannadakis et al. [32], the Rossby number represents the relationship between the linear and the angular momentum in the flow, depending on the specifics of the experimental setup. In the present experiments, the difference between the internal and external mean longitudinal velocities was considered to represent the linear momentum affecting the flow field, while the co-rotating angular velocities were expected to have an additional effect on the angular momentum and their ratio was used as a reference number Ro_{tot}. The modified Rossby number Ro_{tot} is calculated using the longitudinal and tangential velocity of the inner and outer stream $V_{y,i}$ and $V_{y,o}$ based on the measurements of two independent flowmeters. $V_{\theta,i}$ and $V_{\theta,o}$ are the inner and the annular tangential velocity at the tip of the inner impeller blade, where ω is the angular velocity of the inner and the annular impeller respectively.

$$V_{\theta,i} = \omega_i r_{bl,i} \tag{1}$$

$$V_{\theta,o} = \omega_o r_{bl,i} \tag{2}$$

$$Ro_{tot} = \frac{V_{y,i} - V_{y,o}}{V_{\theta,i} + V_{\theta,o}} \tag{3}$$

An interesting observation is that the Rossby number is not adequate to uniquely describe these trends and determine the flow pattern. There are several test cases with the same or similar Rossby number but quite different flow pattern that are not show in this work. Moreover, test cases with similar patterns may have quite different Rossby numbers. Other definitions of the Rossby number were also considered, but this inconsistency was not alleviated. It thus became clear that complementary criteria should be sought to identify flow patterns. Therefore, an attempt was undertaken to define suitable nondimensional numbers which should take the same values for test cases displaying similar flow patterns and similar Ro numbers. In this quest it was plausible to assume that the required nondimensional number would be a function of several variables depending on inlet conditions. The modified dimensionless number S_2 which balances the ratio of the angular to axial momentum of the internal stream with the inverse ratio of the axial shear layer to the tangential shear layer jumps is devised by solving a suitable nonlinear system of equation for test cases with similar flow patterns and quite Ro_{tot} numbers.

$$S_2 = \frac{V_{\theta,i}}{V_{y,i}} \frac{(V_{y,i} - V_{y,o})}{(V_{\theta,i} + V_{\theta,o})} \tag{4}$$

4. EXPERIMENTAL RESULTS

The main body of the results includes six combinations of inner and outer flow rates, comprising three flow rates of the internal stream and six of the external. For each of these combinations twelve test cases were studied, imposing four frequency settings to the inverter driving the internal stream impeller and three for the external one. The characteristics of the test cases are shown in Table 1. Test cases are characterized by four numbers, the first two indicating the flow rates of the internal and the external stream in l/h and the third and fourth indicating the frequency settings in Hz of the inverters driving the internal and external stream impellers respectively. The ID of each test case comprises a capital letter indicating the flow rates combination and a lowercase letter, indicating a combination of rotational speeds of the internal and external impeller. Although several other combinations of inlet conditions were studied, they are not included in this systematic presentation, since in most of these no indication of recirculation was observed, close to the orifice exit.

Table 1 Inlet conditions

ID	Inlet conditions	$U_{y,i}$ (m/s)	$U_{y,o}$ (m/s)	ω_i (rad/s)	ω_o (rad/s)	Ro_{tot}
A.a	400-330-030-07	0.1682	0.0083	9.27	1.25	1.05
A.b	400-330-030-10	0.1682	0.0083	9.27	1.81	1.00
A.c	400-330-030-13	0.1682	0.0083	9.27	2.37	0.95
A.d	400-330-050-07	0.1682	0.0083	15.55	1.25	0.66
A.e	400-330-050-10	0.1682	0.0083	15.55	1.81	0.64
A.f	400-330-050-13	0.1682	0.0083	15.55	2.37	0.62
A.g	400-330-070-07	0.1682	0.0083	21.83	1.25	0.48
A.h	400-330-070-10	0.1682	0.0083	21.83	1.81	0.47
A.i	400-330-070-13	0.1682	0.0083	21.83	2.37	0.46
A.j	400-330-100-07	0.1682	0.0083	31.26	1.25	0.34
A.k	400-330-100-10	0.1682	0.0083	31.26	1.81	0.33
A.l	400-330-100-13	0.1682	0.0083	31.26	2.37	0.33
B.a	400-215-030-07	0.1682	0.0054	4859	460	9.27
B.b	400-215-030-10	0.1682	0.0054	4859	460	9.27
B.c	400-215-030-13	0.1682	0.0054	4859	460	9.27
B.d	400-215-050-07	0.1682	0.0054	4859	460	15.55
B.e	400-215-050-10	0.1682	0.0054	4859	460	15.55
B.f	400-215-050-13	0.1682	0.0054	4859	460	15.55
B.g	400-215-070-07	0.1682	0.0054	4859	460	21.83
B.h	400-215-070-10	0.1682	0.0054	4859	460	21.83
B.i	400-215-070-13	0.1682	0.0054	4859	460	21.83
B.j	400-215-100-07	0.1682	0.0054	4859	460	31.26
B.k	400-215-100-10	0.1682	0.0054	4859	460	31.26
B.l	400-215-100-13	0.1682	0.0054	4859	460	31.26
C.a	400-200-030-07	0.1682	0.0051	4798	428	9.27
C.b	400-200-030-10	0.1682	0.0051	4798	428	9.27
C.c	400-200-030-13	0.1682	0.0051	4798	428	9.27
C.d	400-200-050-07	0.1682	0.0051	4798	428	15.55
C.e	400-200-050-10	0.1682	0.0051	4798	428	15.55
C.f	400-200-050-13	0.1682	0.0051	4798	428	15.55
C.g	400-200-070-07	0.1682	0.0051	4798	428	21.83
C.h	400-200-070-10	0.1682	0.0051	4798	428	21.83
C.i	400-200-070-13	0.1682	0.0051	4798	428	21.83
C.j	400-200-100-07	0.1682	0.0051	4798	428	31.26
C.k	400-200-100-10	0.1682	0.0051	4798	428	31.26
C.l	400-200-100-13	0.1682	0.0051	4798	428	31.26

D.a	375-425-030-07	0.1577	0.0107	4555	909	9.27
D.b	375-425-030-10	0.1577	0.0107	4555	909	9.27
D.c	375-425-030-13	0.1577	0.0107	4555	909	9.27
D.d	375-425-050-07	0.1577	0.0107	4555	909	15.55
D.e	375-425-050-10	0.1577	0.0107	4555	909	15.55
D.f	375-425-050-13	0.1577	0.0107	4555	909	15.55
D.g	375-425-070-07	0.1577	0.0107	4555	909	21.83
D.h	375-425-070-10	0.1577	0.0107	4555	909	21.83
D.i	375-425-070-13	0.1577	0.0107	4555	909	21.83
D.j	375-425-100-07	0.1577	0.0107	4555	909	31.26
D.k	375-425-100-10	0.1577	0.0107	4555	909	31.26
D.l	375-425-100-13	0.1577	0.0107	4555	909	31.26
E.a	375-280-030-07	0.1577	0.0071	4555	599	9.27
E.b	375-280-030-10	0.1577	0.0071	4555	599	9.27
E.c	375-280-030-13	0.1577	0.0071	4555	599	9.27
E.d	375-280-050-07	0.1577	0.0071	4555	599	15.55
E.e	375-280-050-10	0.1577	0.0071	4555	599	15.55
E.f	375-280-050-13	0.1577	0.0071	4555	599	15.55
E.g	375-280-070-07	0.1577	0.0071	4555	599	21.83
E.h	375-280-070-10	0.1577	0.0071	4555	599	21.83
E.i	375-280-070-13	0.1577	0.0071	4555	599	21.83
E.j	375-280-100-07	0.1577	0.0071	4555	599	31.26
E.k	375-280-100-10	0.1577	0.0071	4555	599	31.26
E.l	375-280-100-13	0.1577	0.0071	4555	599	31.26
F.a	250-175-030-07	0.1051	0.0044	3037	375	9.27
F.b	250-175-030-10	0.1051	0.0044	3037	375	9.27
F.c	250-175-030-13	0.1051	0.0044	3037	375	9.27
F.d	250-175-050-07	0.1051	0.0044	3037	375	15.55
F.e	250-175-050-10	0.1051	0.0044	3037	375	15.55
F.f	250-175-050-13	0.1051	0.0044	3037	375	15.55
F.g	250-175-070-07	0.1051	0.0044	3037	375	21.83
F.h	250-175-070-10	0.1051	0.0044	3037	375	21.83
F.i	250-175-070-13	0.1051	0.0044	3037	375	21.83
F.j	250-175-100-07	0.1051	0.0044	3037	375	31.26
F.k	250-175-100-10	0.1051	0.0044	3037	375	31.26
F.l	250-175-100-13	0.1051	0.0044	3037	375	31.26

In figure 4 the test cases studied in this work are depicted in an S_2 vs Ro_{tot} chart. Data points have been arranged in groups with similar patterns (indicated by the letter G and a number), and representative pictures for each group have been included. Based on this graph, a flow pattern map can be constructed, where four zones are identified, corresponding to the typical patterns discussed previously. The upper left zone corresponds to the "downstream core flow" (DCF) pattern, where no recirculation is observed. Next to this zone, for lower Ro and higher S2 values, is the "closed bubble" (CB) pattern zone and following this the "asymmetric recirculation" (AR) pattern zone. The lower, right side of the map, corresponding to low Ro_{tot} and high S_2 numbers, is occupied with symmetric "intense recirculation" (IR) patterns. The location of the zone boundaries is tentative, since there are several areas on the map which are not populated and therefore, despite the quite large number of the test cases investigated in this work, further experiments are needed to verify the value of this approach and better define the form of the boundaries. It should also be noted that patterns of neighboring zones can be identified on both sides close to the boundaries.

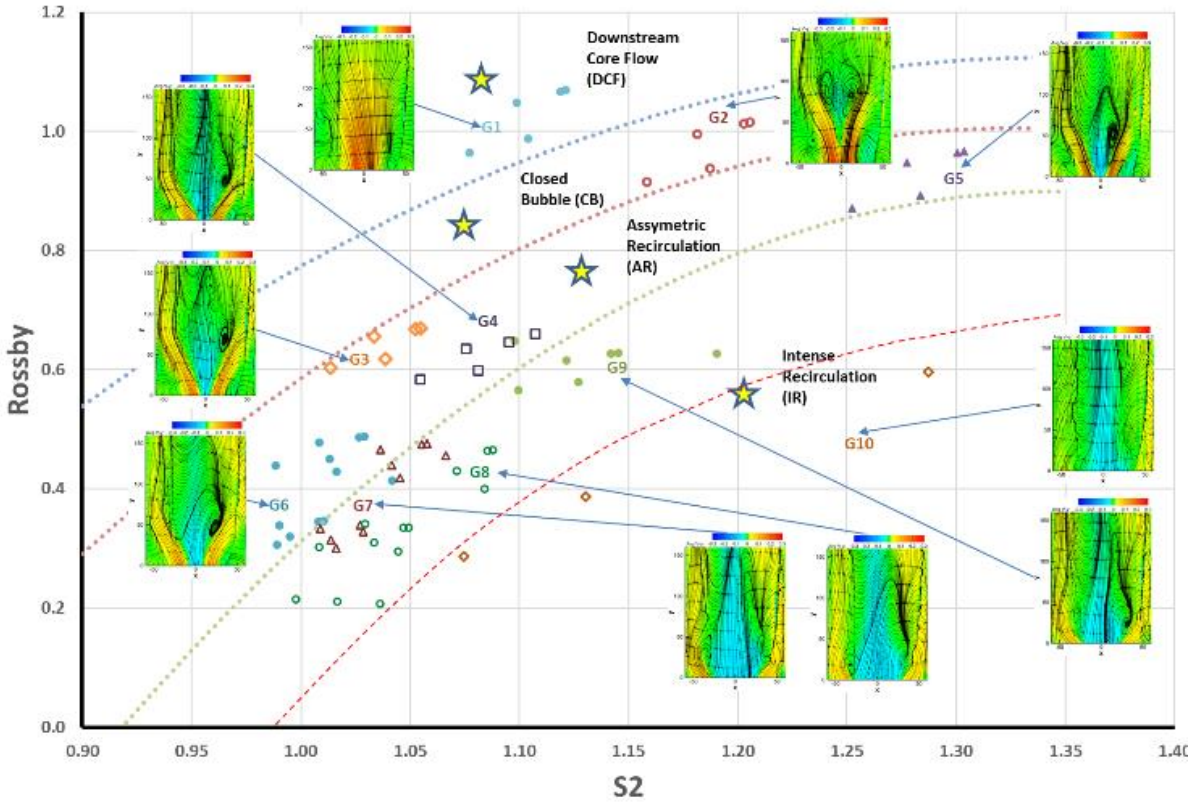

Figure. 4 Flow map in accordance with Ro and S2

5. CONCLUSIONS

The development of the flow field of a swirling jet and a coaxial annular swirling stream interacting in a tube has been studied. A significant number of combinations of inlet conditions, comprising several internal and external streams, flowrates and rotational rates, have been considered. Streamlines and mean longitudinal velocity contour maps, based on 3D-PIV measurements on the central, axial plane, are presented. This work focuses on the topological characteristics of the flow field and attempts to describe the trends resulting from the variation of the inlet conditions. Key to this approach is the identification of the recirculation pattern formed in the vicinity of the internal flow exit.

The use of an appropriately modified Rossby number was not proven adequate to uniquely describe the observed trends and determine the flow pattern. Therefore, a complementing non dimensional number, S_2, was sought and devised, by solving a suitable nonlinear system of equations for test cases with similar flow patterns, in order to support the identification of the flow pattern in relation to the inlet conditions. Based on both Ro and S_2, a map was constructed which effectively classified the flow patterns, for the test cases that were tested in four zones.

Four typical flow patterns are identified for the different inlet conditions that were considered. The “downstream core flow” (DCF) pattern corresponds to test cases with no recirculation. In the cases characterized as “closed bubble” (CB) type a closed recirculating bubble is developing downstream of the internal nozzle exit, whereas in the “asymmetric recirculation” (AR) cases the recirculation area appears open and secondary recirculation zones are observed. Usually associated with high rotation rates is the “intense recirculation” (IR) pattern, comprising two rather symmetrical, radially separated recirculation structures, very close to the internal nozzle outlet and a significant (in radial and axial extent) zone of reverse flow.

REFERENCE

[1] Rotunno R. The fluid dynamics of tornadoes, Annual Review of Fluid Mechanics, 2013, 45, pp 59-84.
[2] Lefebvre A H, McDonell V G. Atomization and Sprays. Combustion: An International Series. CRC Press, Taylor & Francis, 2017).
[3] Yazdabadi P A, Griffiths A J, Syred N. Characterization of the PVC phenomena in the exhaust of a cyclone dust separator. Experiments in Fluids, 1994, 17(1–2):84–95
[4] Rocha A D, Bannwarta A C, Ganzarollib M. M. Numerical and experimental study of an axially induced swirling pipe flow. International Journal of Heat and Fluid Flow, 2015, 53:81-90.
[5] Rafiee S E, Sadeghiazad M M. Efficiency evaluation of vortex tube cyclone separator. Applied Thermal Engineering, 2017, 114:300-327
[6] Wang X, Yang V. Supercritical Mixing and Combustion of Liquid-Oxygen/ Kerosene Bi-Swirl Injectors. Journal of propulsion and power, 2017, 33(2):316-322
[7] Sheikholeslami M, Gorji-Bandpy M, DomiriGanji D. Review of heat transfer enhancement methods: Focus on passive methods using swirl flow devices. Renewable and Sustainable Energy Reviews, 2015, 49:444-469
[8] Zhixiang C, Wang Y, Duan M, Zhu H. Study of the vortex principle for improving the efficiency of an exhaust ventilation system. Energy and Buildings, 2017, 142:39-48
[9] Peake N, Parry A B. Modern Challenges Facing Turbomachinery Aeroacoustics. Annual Review of Fluid Mechanics, 2012, 44:227-248
[10] Skripkin S, Tsoy M, Kuibin P, Shtork S. Swirling flow in a hydraulic turbine discharge cone at different speeds and discharge conditions. Experimental Thermal and Fluid Science, 2019, 100:349–359
[11] Terhaar S, Reichel T G, Schrödinger C, Rukes L, Paschereit C O, Oberleithner K. Vortex Breakdown Types and Global Modes in Swirling Combustor Flows with Axial Injection. Journal of Propulsion and Power, 2015, 31(1):219-229
[12] Lilley D G. Swirl Flows in Combustion: A Review. AIAA journal, 1977, 15(8):1063-1078
[13] Rajamanickam K, Roy S, Basu S. Novel fuel injection systems for high-speed combustors. Droplets and Sprays, 2018,:183–216
[14] Lucca-Negro O, O' Doherty T. Vortex breakdown: a review, Progress in Energy and Combustion Science, 2001, 27(4):431-481
[15] Gupta A K, Lilley D G. Syred N. Swirl Flows. Abacus Press Tunbridge Wells England, 1984
[16] Benjamin T B. Theory of the vortex breakdown phenomenon. J. Fluid Mech, 1962, 14(4):593-629
[17] Batchelor G K. An Introduction to Fluid Dynamics. Cambridge University Press, 1967
[18] Lambourne N C, D. Bryer W. The Bursting of Leading-Edge-Vortices Some Observations and Discussion of the Phenomenon. London HMSO, 1962
[19] Peckham D H, Atkinson S. Preliminary results of low speed wind tunnel tests on a Gothic wing of aspect ratio 1.0. Royal Aircraft Establishment. Technical note AERO, 1957, 2504
[20] Leibovich S. The Structure of Vortex Breakdown. Annual Review of Fluid Mechanics, 1978, 10:221-246
[21] Nuttall J B. Axial Flow in a Vortex. Natural, 1953,172:582-583
[22] Harvey J. K. Some observations of the vortex breakdown phenomenon. J. Fluid Mech, 1962,14(4):585-592
[23] Hall M G. Vortex breakdown". Annual Review of Fluid Mechanics, 1972, 4:195-218
[24] Spall R, Gatski T, Grosch C. A criterion for vortex breakdown. Phys. Fluids, 1987, 30(11):3434-3440
[25] Escudier M. Vortex breakdown: Observations and explanations. Progress in Aerospace Sciences, 1988,25(2):189-229
[26] Naxakis A, Perrakis K, Panidis T. Experimental study on swirling jets. International Review of Mechanical Engineering, 2018 12(6):533-539
[27] BudwigR. Refractive Index Matching Methods for Liquid Flow Investigations. Experiments in Fluids, 1994, 17(5):350-355
[28] Wiederseiner S. Andreini N, Epely-Chauvin G, Ancey C. Refractive-index and density matching in concentrated particle suspensions: a review. Experiments in Fluids, 2011, 50(5):1183-1206

[29] Adrian R J. Particle-Imaging Techniques for Experimental Fluid Mechanics. Annual Review of Fluid Mechanics, 1991, 23:261-304
[30] Prasad A K. Stereoscopic particle image velocimetry. Experiments in Fluids, 2000, 29(2):103-116
[31] Melling A. Tracer particles and seeding for particle image velocimetry. Measurement Science and Technology, 1997, 8(12):1406-1416
[32] Giannadakis A, Naxakis A, Romeos A, Perrakis K, Panidis T. An experimental study on a coaxial flow with inner swirl: vortex evolution and flow field mixing attributes. Aerospace Science and Technology, 2019, 94:105373

Patient–Specific Diastolic Vortex Flow Patterns in the Left Ventricle

Dimitris Zantzas[1*], Vasileios G. Gkoutzamanis[1] Vasiliki Kantartzi[2] Vasileios Sachpekidis[2] and Anestis Kalfas[1]
[1]Aristotle University of Thessaloniki, School of Mechanical Engineering, GR-54124 Thessaloniki, Greece,
[2]Papageorgiou General Hospital 2nd Cardiology Department, GR-56429 Thessaloniki, Greece
** Corresponding Author: dzantzas@auth.gr*

This paper presents a numerical model for the analysis of blood flow in a human left ventricle during the diastolic phase. Patient–specific data from Real-Time 3-Dimensional Echocardiography is used in order to reconstruct the geometry of left ventricle. Vortex flow pattern analysis is conducted in order to quantify the role of vortical structures in the optimal throughput of the heart flow.

In order to broaden our knowledge about the heart function and to counter the increasing cardiovascular diseases novel approaches are required. Computational engineering could be very productive for this purpose. The vortex formation in the left ventricle is suggested to critically contribute to efficient blood pump function[1]. For that reason, this paper is focused on the qualitative analysis of the role of the vortex that appears in the left ventricle.

In this paper, the geometry of the model is reconstructed from patient-specific data. The segmentation process is made manually with the use of semi-automatic algorithms. The temporal resolution of the echo data is too low for the numerical simulation, so cubic splines interpolation is used to fit the requirement of the CFD calculation with the reconstructed geometries[2]. The calculation is performed using a Navier-Stokes solver with the use of the arbitrary Lagrangian Eulerian formulation. The working fluid simulating blood is taken to be a Newtonian fluid with constant viscosity and density.[3]

Analysis of the results shows that the velocity and the pressure inside the left ventricle are in reasonable agreement with in-vivo data which have been acquired by clinicians. In figure 1 and 2, cross-sectional view of the blood pressure and the 3D vortex ring with velocity vector is presented in two consecutive timesteps of the diastolic phase. The vortex ring is considered to assist ventricular function[4].

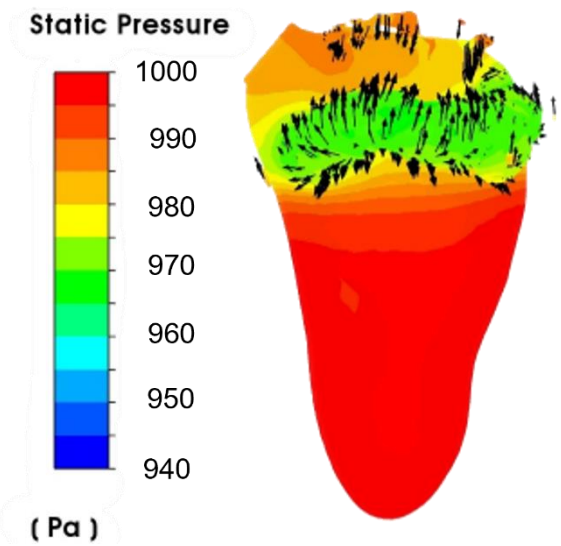

Fig. 1: Static pressure and 3D vortex at early diastole.

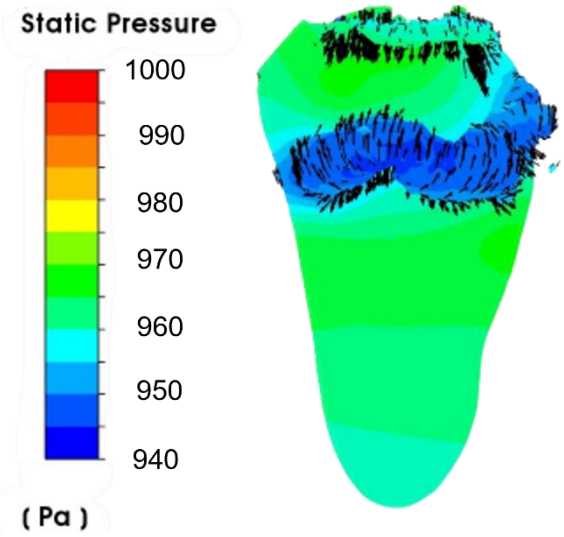

Fig. 2: Static pressure and 3d vortex at mid-diastole.

This vortical motion has been found to occur in the early diastolic phase as shown in figure 1. Furthermore, this vortical motion is found to persist almost the whole diastolic phase of the cardiac cycle. As depicted from the two figures, the 3D vortex ring is found in the region of minimum pressure and is migrated to the apex with the evolution of diastolic phase.

References

[1] Gharib, Morteza & Rambod, Edmond & Kheradvar, Arash & Sahn, David & Dabiri, John. (2006). Optimal vortex formation as an index of cardiac health. Proceedings of the National Academy of Sciences of the United States of America. 103. 6305-8. 10.1073/pnas.0600520103.

[2] Schenkel T, Malve M, Reik M, Markl M, Jung B, Oertel H: MRI-based CFD analysis of flow in a human left ventricle: methodology and application to a healthy heart. Ann Biomed Eng. 2009, 37: 503-15. 10.1007/s10439-008-9627-4.

[3] Khalafvand, Seyed Saeid & Zhong, Liang & Ng, Eddie. (2014). Three-dimensional CFD/MRI modeling reveals that ventricular surgical restoration improves ventricular function by modifying intraventricular blood flow. International Journal for Numerical Methods in Biomedical Engineering. 30. 10.1002/cnm.2643.

[4] Krueger PS, Gharib M: The significance of vortex ring formation to the impulse and thrust of a starting jet. Phys Fluids 15:1271-1281, 2003

Article S6.1

Hot-wire measurement of asymptotic characteristics of lobed jet flow

Ren Fukui[1*], Mamoru Takahashi[1], Koichi Tsujimoto[1], Toshitake Ando[1], Toshihiko Shakouchi[1], Ryuichi Momiyama[2]
[1]Graduate school of Engineering, Mie University, Tsu, Mie, Japan
[2]Faculty of Engineering, Mie University, Tsu, Mie, Japan
** Corresponding Author: 421M149@m.mie-u.ac.jp*

ABSTRACT

Diffusion characteristics of the turbulent jet can be controlled by modifying the initial condition, namely the nozzle shapes. Lobed jet is one of the non-circular jets, supplied from the nozzle with wave-shaped edges. In this study, we measured the self-similarity of the velocity fields of two lobed jets with six lobe peaks but different curvatures (6L and 6S), and compared their diffusion characteristics with those of a round jet. The results show that the mean streamwise velocity distribution display the self-similarity in $x/D_e \gtrsim 10$ and the RMS value of fluctuating velocity $x/D_e \gtrsim 30$ for all of the investigated jets. The flow rate of the lobed jets are lower in the self-similar state than that of the round jet. In contrast, the difference of the flow rate between the two lobed jets is small, proposing that the diffusion characteristics of the lobed jet is almost independent of the curvature of the nozzle shape.

KEYWORDS: Lobed jet, Turbulent diffusion, Self-Similarity

1. INTRODUCTION

Diffusion characteristics of the turbulent jet can be controlled by modifying the initial condition, namely the nozzle shapes [1]. Lobed jet is one of the non-circular jets, supplied from the nozzle with a wave-shaped edge. Originally this idea is from the noise reduction of the jet engine but has potential for more applications in mixing enhancement problems.

Owing to the generation of intense turbulence at the jet exit by the non-circular nozzle edge, the lobed jets show the better mixing performance than the round jet in the near field from the jet exit [2-4]. However, Nastase and Meslem [4] investigated the lobed jets with six lobes and they found lower mixing efficiency of the lobed jets than the round one in the far-field from the exit. They showed the results obtained only in $x \lesssim 10D_e$, where x is the streamwise distance from the nozzle exit and De is the equivalent diameter of the jet exit. In order to understand the whole area of the jet flow field, measurement of the asymptotic (self-similarity) characteristics of the jet is desired. Wygnanski et al. [5] showed that the half-width of the mean velocity of the turbulent wake depends on the initial condition, even though that of the mean velocity profile itself does not. This suggests that the lobed jets have different diffusion characteristics from the round jet in the self-similarity state.

In the present study, we investigated the asymptotic diffusion characteristics of two lobed jets which have six lobes. The results were compared with that of the round jet. The flow fields of the jet flows were measured by mean of hot-wire anemometry. We evaluated the development of the flow rate of those jet flows in the self-similarity state. Especially, we gave careful consideration for the mixing performance variation on the edge curvature of the nozzle lobes.

2. EXPERIMENTAL SETUP AND CONDITIONS

2.1 EXPERIMENTAL SETUP

The jet flows are generated in the laboratory experiment. Figure 1 shows the diagram of experimental equipment. The air flow was supplied by a blower, and cooled by a radiator, before being ejected from the nozzle of a wind tunnel into the still air. The flow rate was monitored by a digital manometer connected to a flowmeter, and we adjust the flow rate with the valve installed between the radiator and the flowmeter. The jet flows were measured by a hot wire anemometer with I-type probe. The hot-wire

sensor was a tungsten wire of 5 μm in diameter and 1 mm in length. The hot wire probes were installed on the three-dimensional traverse systems (SUS XA-42L and XAK-P50). The strokes of the traverse system are 2,000 mm in the mainstream direction and 400 mm in the perpendicular direction. The stroke length of the traverse device is 2,000 mm in the main flow direction and 400 mm in the direction perpendicular to the main flow direction. The output voltage from the hot wire anemometer (KANOMAX 1010) is converted to digital data by the data logger (NI USB-6361) and recorded in the experimental PC.

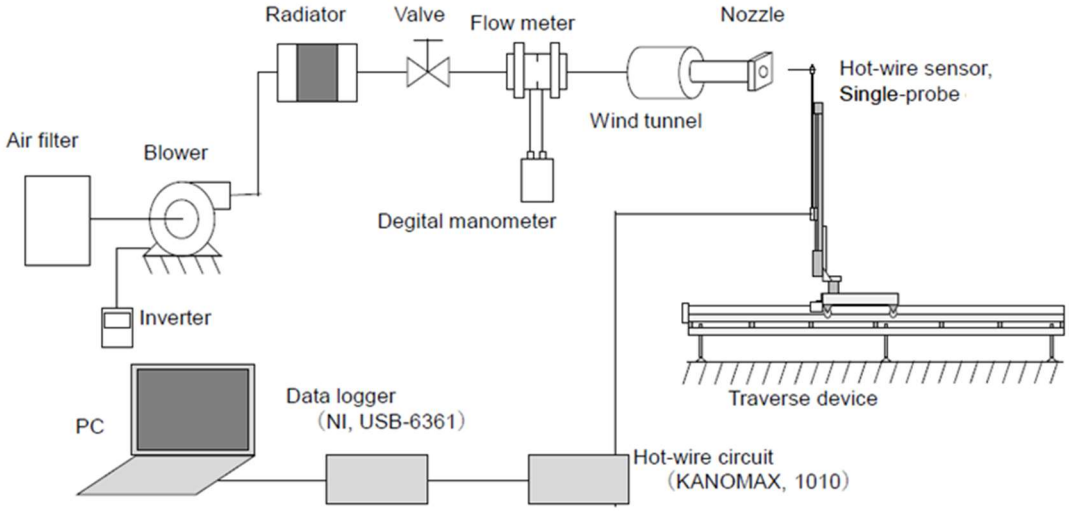

Fig. 1 Diaguram of experimental equipment.

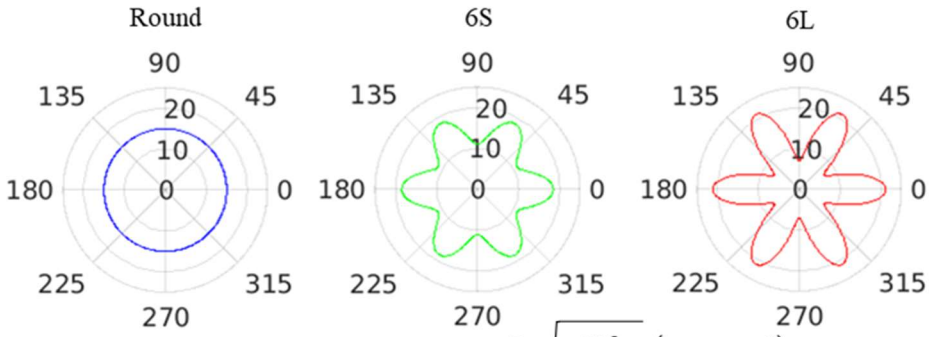

Fig. 2 Shape of the nozzles.

The lobed nozzles employed in the previous studies [2-4] are subtly different from each other and a wide range of factors seems to be required to determine their shapes. In this study, we introduced a closed curve containing only two factors that determine the nozzle outline (the number of lobes and the curvature), which clarifies the dependency between the mixing performance of the lobed jets and the nozzle shape characteristics. Figure 2 shows the edge shapes of the round and lobed nozzles. The shapes of the lobed nozzles are given by

$$r(\theta) = D_e\sqrt{\frac{2b^2}{2b^2+1}}\left(1+\frac{\cos a\theta}{b}\right), \tag{1}$$

where the parameter a and b are the number of lobes and curvature of the edge, respectively. In the present study, we used a=6 and b=4 (small curvature, 6S) or 2 (large curvature, 6L) since the lobed nozzles with six lobes have been often studied. The (equivalent) diameter of the nozzles were 15 mm.

The nozzles can form the top-hat initial mean velocity profiles, which is generally achieved by a smooth contraction nozzle.

2.2 EXPERIMENTAL CONDITIONS

The coordinate system is the Cartesian coordinate system, with the x-axis in the mainstream direction, the y-axis perpendicular to the jet and the z-axis in the span direction. Reynolds number $\mathrm{Re}\equiv D_e U_J/\nu$ is 70,000, where U_J is the mean velocity at the jet exit ($\simeq$70 m/s) and ν is the kinematic viscosity of the air ($\simeq 1.5\times10^{-5}$ m^2/s). 524,288 instantaneous samples are obtained with 20 kHz sampling frequency.

3. RESULT AND DISCUSSION

3.1 RADIAL PROFILE OF VELOCITYSTATIDTICS

Figure 3 and 4 shows the radial profile of the mean streamwise velocity U in lobed jets 6S and 6L, respectively, (a) is for the profile along the major-axis and (b) for the minor-axis. The vertical axis is non-dimensionalized by the mean velocity on the central axis U_{max} and the horizontal axis by the half-width of the mean velocity profile $r_{0.5}$. From Fig. 3 and 4, We can confirm that both 6S and 6L display their self-similarity in $x/D_e \gtrsim 10$.

Figure 5 and 6 show the radial profile of the RMS values u_{rms} in lobed jets 6S and 6L, respectively, (a) is for the profile along the major-axis and (b) for the minor-axis. The vertical axis is non-dimensionalized by U_{max} and the horizontal axis by $r_{0.5}$. Fig. 5 and 6 show that both 6S and 6L show the self-similarity in $x/D_e \gtrsim 20$. The same self-similarity asymptotic property is observed in the round jet, which is not included in this paper.

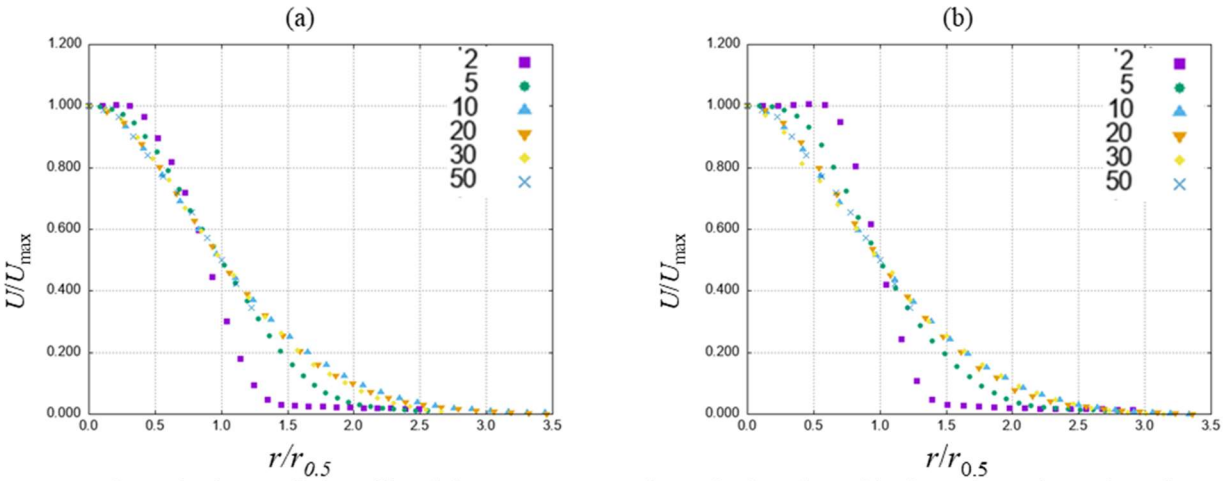

Fig. 3 Dimensionless radial profile of the mean streamwise velocity of 6S, (a) along the major-axis and (b) the minor-axis.

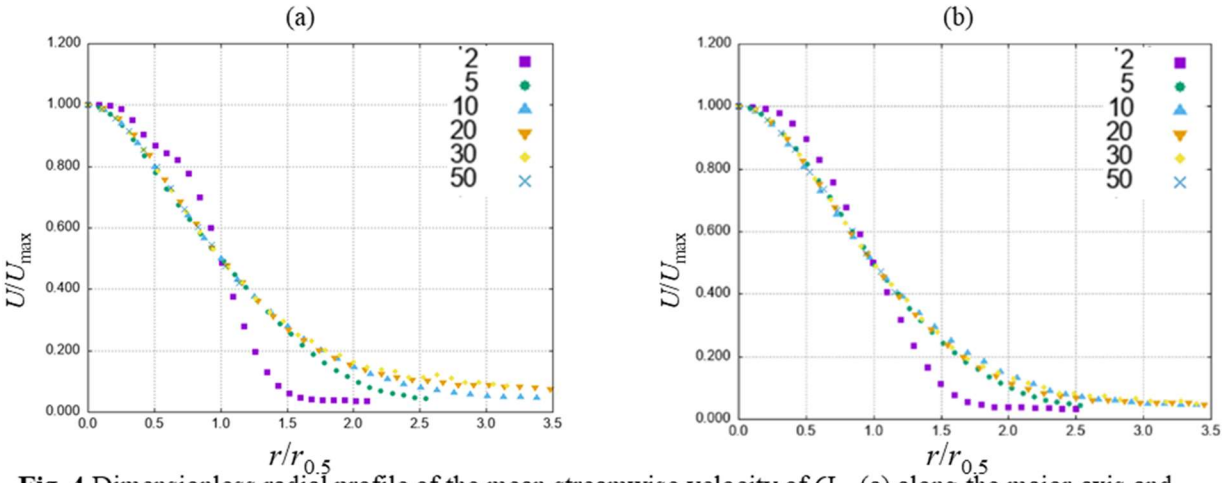

Fig. 4 Dimensionless radial profile of the mean streamwise velocity of 6L, (a) along the major-axis and (b) the minor-axis.

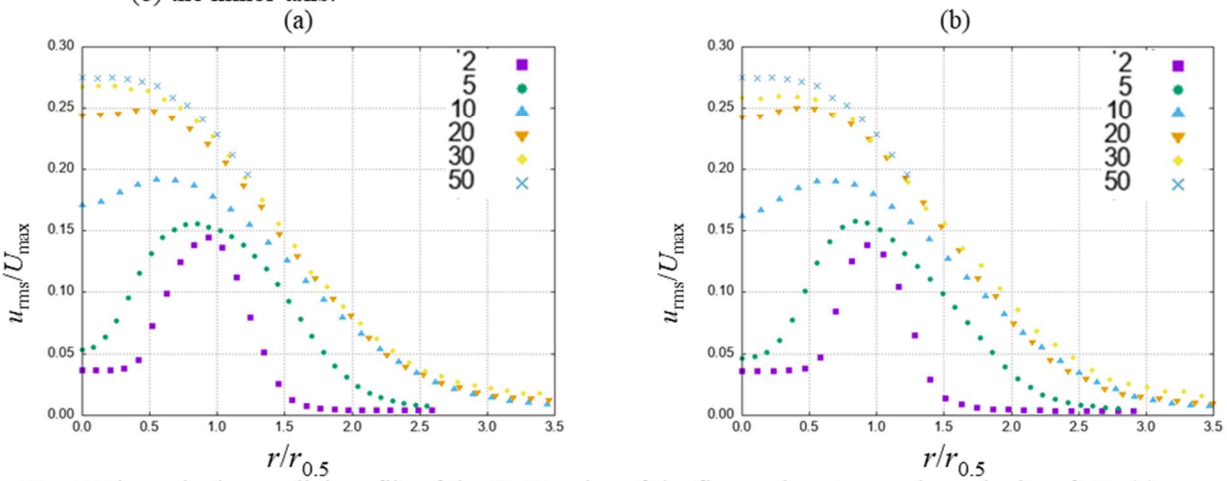

Fig. 5 Dimensionless radial profile of the RMS value of the fluctuating streamwise velocity of 6S, (a) along the major-axis and (b) the minor-axis.

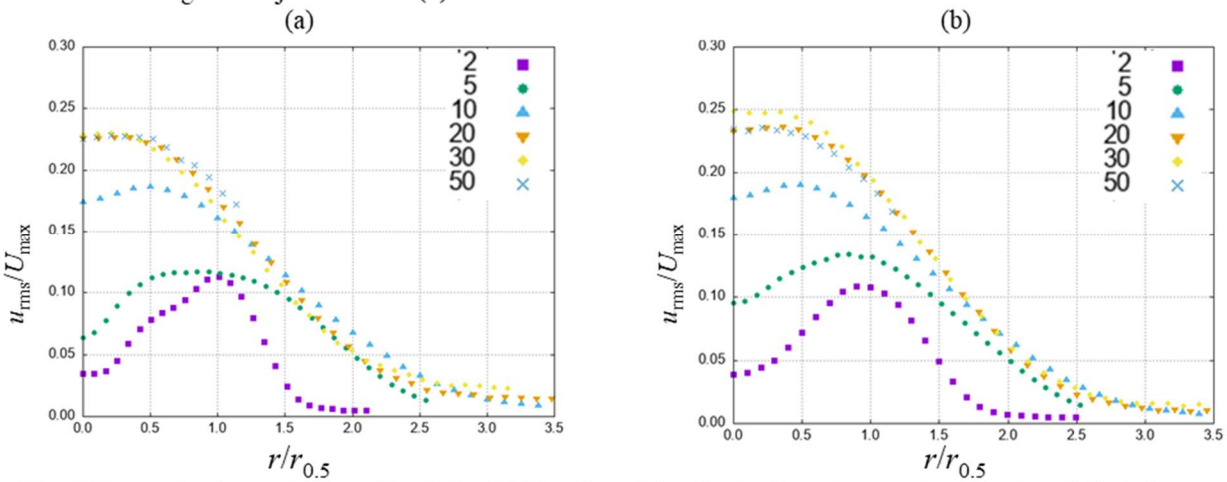

Fig. 6 Dimensionless radial profile of the RMS value of the fluctuating streamwise velocity of 6L, (a) along the major-axis and (b) the minor-axis.

3.2 FLOW RATE

Figure 2 shows the development of the flow rate of the round and lobed jets. The flow rate is non-dimensionalized using that at the nozzle exit (Q_0) and the distance x using D_e. The flow rate was obtained by integrating the mean velocity over the cross-streamwise (y-z) plane, which was measured

by moving the hot-wire probe, at each measurement distance. In particular, the following equation was used to obtain the flow rate values.

$$Q(x) = \iint_{-\infty}^{\infty} \bar{U}(x, y, z)\, dy\, dz, \quad \bar{U} \geq 0.1U. \tag{2}$$

It can be observed that the flow rate of the lobed jets is smaller than that of the round jet in the far-field. In contrast, there is small difference between the flow rate of the two lobed jets with different curvatures.

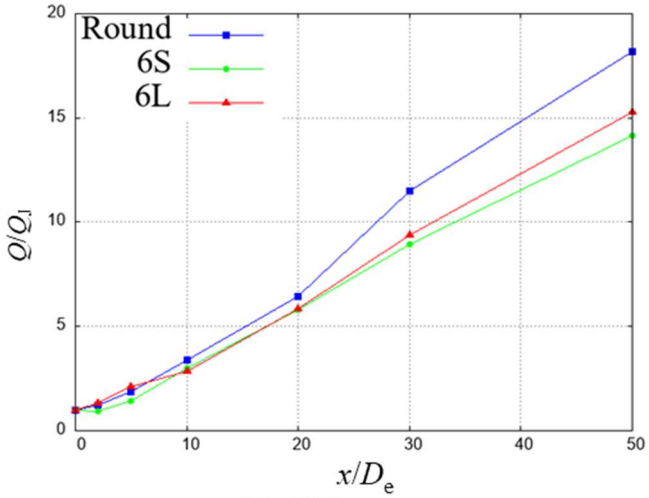

Fig. 7 Flow rate.

4. CONCLUSIONS

(1) For all of the round jet, 6S and 6L, the mean velocity in the main flow direction is $x/D_e \gtrsim 5$ and the RMS of the fluctuating velocity in the main flow direction is $x/D_e \gtrsim 20$ for all jets.
(2) The flow rate of the lobed jet is smaller than that of the round jet in the far field.
(3) The asymptotic diffusion characteristics of the lobed jets are independent of the curvature of the nozzle edge.

ACKNOWLEDGMENT

Funding from the Okasan-Kato Foundation is gratefully acknowledged.

REFERENCE

[1] Aleyasin S S, Tachie M F, Koupriyanov M. PIV measurements in the near and intermediate field regions of jets issuing from eight different nozzle geometries. Turbulence and Combustion, 2017, 99(2):329-351
[2] Hui H, Toshio K, Toshio K, Nobuyuki T. Mixng process in a lobed jet flow. AIAA Joumal, 2002, 40(7):1339-1345
[3] Shakouchi T, Iriyama S, Kawashima Y, Tsujimoto K, Ando T. Flow characteristics of submerged free jet flow from petal-shaped nozzle. Journal of Fluid Science and Technology, 2014, 9(3): JFST0037–JFST0037
[4] Nastase I, Meslem A. Vortex dynamics and mass entrainment in turbulent lobed jet with and without lobe deflection angles. Experiments in Fluids, 2010, 48(4):693-714
[5] Wygnanski I, Champagne F, Marasli B. One the large-scale structures in twodimensional, small-deficit, turbulent wakes. Journal of Fluid Mechanics, 1986, 168:31-71

Vortex Structure Produced by a Sweeping Jet in a Cross Flow

Masaki Fuchiwaki[1*], Eisei Kobayashi[1], Surya Raghu [2]

[1] Kyushu Institute of Technology, Kawazu6804, Iizuka, Japan
[2] Advanced Fluidics LLC, 8860 Columbia 100 Parkway, Suite 204, Columbia, MD 21045, USA
** Corresponding Author:futiwaki@mse.kyutech.ac.jp*

Fluidic Oscillator generates a sweeping jet with high frequency and large amplitude and is characterized by its capability for jet ejection over a wide range. Recently, the sweeping jet from the Fluidic Oscillator has been attracted attention from the viewpoint of an active flow control techniques. The studies on the active flow control techniques using the sweeping jet have been already reported [1]-[3]. However, these studies focused on the characteristics of the dynamic forces acting on an airfoil in conjunction with a fluidic oscillator. There have been no studies about the flow structure or flow mechanism. Actually, the sweeping jet from the Fluidic Oscillator ejected into a main flow is the jet in cross flow, and it is well known that this flow field will be more complex flow structure. It is expected that the interaction between the sweeping jet and the main flow occurs and the complex vortex structure will be generated in the wake. In near future, in order to apply as the active flow control devise using the sweeping jet from the Fluidic Oscillator, it is required to be understood the complex flow structure and the flow mechanism by the interaction between the sweeping jet and the main flow.

The authors have already reported the flow characteristic produced by interactions between the sweeping jet from the fluidic oscillator and the main flow using a stereo particle image velocimetry (PIV) measurement [4]. However, the detailed of the flow structure or flow mechanism produced by the interaction between the sweeping jet and the main flow have not been understood sufficiently.

The purpose of the present study is to investigate the detailed vortex structure produced by the interaction between the sweeping jet from the Fluidic Oscillator and the main flow. Especially, the detailed vortex structure and flow mechanism produced by these interactions is visualized by a stereo PIV measurement and a numerical simulation using ANSYS-CFX.

The three-dimensional velocity vectors in x-y plane produced by the interaction between the sweeping jet and the main flow at a location 30 mm from the outlet of the jet obtained by the stereo PIV is shown in Figure 1(a) and 1(b). Figures 1(a) and 1(b) shows the results at $V_j/V_0 = \infty$ (Vo = 0.0 m/s) and 80.00, respectively. These results are time-averaged results during 0.5 sec. At $V_j/V_0 = \infty$, as shown in Fig. 1(a), the sweeping jet from the fluidic oscillator shows high-speed flow to the right and left. All velocity vectors are linear and the rotational component of the velocity field is not seen. On the other hand, at V_j/V_0 = 80.0, as shown in Fig. 1(b), the high-speed jet is especially prominent in the center and the maximum velocity of the sweeping jet is much higher than that at $V_j/V_0 = \infty$. The higher velocity vectors at the center of the sweeping jet are surrounded by the low velocity vectors with a strong rotational component at the outside of the sweeping jet. It is expected that the low velocity vectors with a strong rotational component at the outside is produced by the interaction between the sweeping jet and the main flow and the higher velocity at the center is induced by the interaction. Moreover, the spreading angle of the sweeping jet is greater than at $V_j/V_0 = \infty$. The PIV measurement results will be related with the numerical simulation results, and finally, the authors will discuss about the more details of flow structure and the flow mechanism by the interaction between the sweeping jet and the main flow

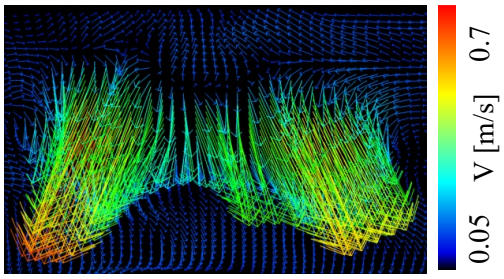

(a) $V_j/V_0 = \infty$

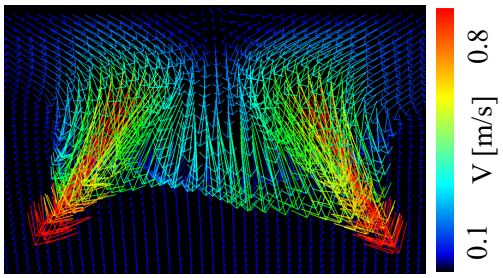

(b) V_j/V_0 = 80.0

Fig. 1: Three-dimensional velocity vectors in x-y plane produced by the interaction between the sweeping jet and the main flow

References

[1] Raghu, S., Raman, and G., Miniature fluidic devices for flow control, *ASME-JSME joint fluids engineering conference*, 1999, ASME FEDSM 99-7256.

[2] Raghu, S., Gregory, J., W., and Sullivan, J., P., Modulated high frequency fluidic actuators for flow control, 2005, *International conference on jets, wakes and separated flows*.

[3] Raghu S., Fluidic Oscillator for flow control, 2013, *Experiments in Fluids*, 54:1455, DOI 10.1007/s00348-012-1455-5.

[4] Fuchiwaki, M., and Raghu S., Flow structure formed by a sweeping jet ejected into a main flow, 2018, *ASME 2018 5th Joint US-European Fluids Engineering Summer Conference,* FEDSM2018-83045

Supersonic Under-Expanded Reattached Jet with Vortex Region

Tetsuji Ohmura[1,2], Toshihiko Shakouchi[1*], Ryota Matsui[1] and Koichi Tsujimoto[1]

[1]Mie University, Kurimamachiya-cho 1577, Tsu-shi, Japan
[2]Fukuda Metal Foil & Powder Co., Ltd., Kyoto, Japan
** Corresponding Author: shako@mach.mie-u.ac.jp*

If there is a wall near the incompressible jet, it reattaches to the wall surface by the Coanda effect enclosing a large vortex region (Fig. 1) [1]. The supersonic jet also reattaches to he wall, however the flow characteristics of supersonic reattached jet have not been revealed enough. The reattached jet is one of the basic flow in the fields of fluid- and thermo-dynamics. In this study, the flow characteristics such as the velocity, pressure, density distributions and the effects of offset distance on the two-dimensional supersonic under-expanded reattached jet are examined by numerical and experimental analyses.

Figures 1(a),(b) show, respectively, the velocity and pressure distributions by a 2-D numerical analysis using CFD software of the FlowSimulation with k-ε turbulence model. The supply pressure is $P_0 = 0.4$ MPa and offset distance is $D/b = 5.0$ (b: nozzle width = 2.5 mm, Aspect ratio: **4.0). Read colored area is a high speed area. The under-**expanded jet spreads just after the nozzle exit and appears the expansion region with a high speed and the compression region. This is the so called 1st shock cell. The 1st to 5th shock cells can be seen. The expansion and compression regions have negative low and positive high pressure areas (Fig. 1(b)). The dark blue and red colored areas in Fig. 1(b), respectively, are them. The jet reattaches to the side wall by the Coanda effect and there are major vortex region of clockwise and minor vortex region of counterclockwise near

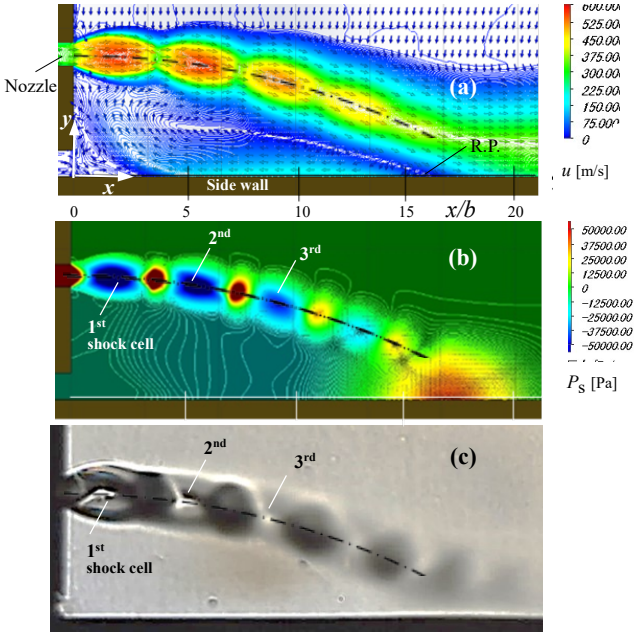

Fig. 1: Supersonic under-expanded reattached jet ($P_0 = 0.4$ MPa, $D/b = 5.0$)

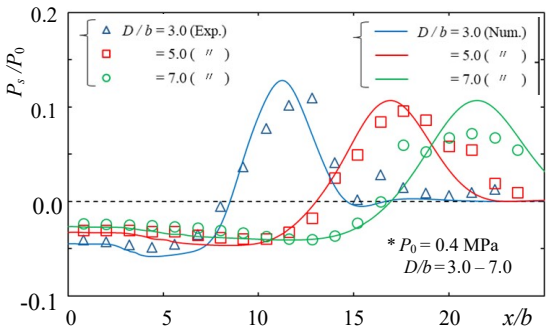

Fig. 2: Pressure distribution on side wall

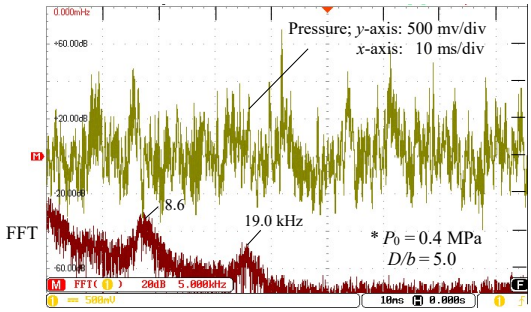

Fig. 3: Pressure fluctuation near reattachment point

the corner. However, the pressure distribution in the major vortex region is different from the incompressible reattached jet [1] and it does not have a cleat vortex center. Figure 1(c) shows the visualized flow pattern by a Schlieren method. The white and dark colored areas are the expansion and compression regions, respectively. The flow pattern by numerical analysis can express well the experimental one.

Figure 2 shows the pressure distribution P_s/P_0 on the side wall for the offset distance of $D/b = 3.0 - 7.0$. The pressure corresponding the vortex region is negative and it takes a maximum around the reattachment point, R.P (Fig. 1(a)). The position of the maximum pressure x/b moves to the downstream and the maximum pressure decreases as increasing the offset distance D/b. The numerical analysis can express well the experimental results.

Figure 3 shows the pressure fluctuation at $x/b = 16.4$ near the reattachment point, R.P. (Fig. 1(a)). The pressure fluctuates irregularly with the dominant frequencies of f_d = 8.6 and 19.0 kHz. This means that the reattached jet flows under the fluctuation with the same dominant frequencies.

References

[1] Bourque, C. and Newman, B.G., Reattachment of a 2-D, incompressible jet to an adjacent flat plate, *Aeronautical Quarterly*., 1960, **11**, 201-232.

Article S6.4

Fundamental Study on Design Methodology of a Solar Car Considering Aerodynamic and Power Generation Performance

Arata Muto[1]*, Ichiro Uto[2] , Kota Fukuda[3] , Kouhei Sagawa[4] and Hideki Kimura[4]

[1]Course of Mechanical Engineering, Graduate School of Engineering, Tokai University
[2]Department of Human and Information Science, School of Information Science and Technology, Tokai University
[3]Department of Aeronautics and Astronautics, School of Engineering, Tokai University
[4]Department of Electrical and Electronic Engineering, School of Engineering, Tokai University
4-1-1 Kitakaname, Hiratsuka, Kanagawa, 259-1292, Japan
** Corresponding Author: 0CEMM082@mail.u-tokai.ac.jp*

ABSTRACT

For the development of solar cars, the power consumption should be reduced since the solar irradiance is very low. Furthermore, the balance between power generation and aerodynamic performance is crucial for the design of the solar car. Therefore, in this study, a design methodology is proposed and applied to a solar car, called Tokai Challenger, which the Tokai University Solar Car Team developed for the Bridgestone World Solar Challenge (BWSC). In the methodology, both aerodynamic and power generation performance are considered by combining the flow simulation and a power generation simulation. By using the proposed methodology, total performance can be evaluated.

KEYWORDS: CFD, Aerodynamics, Solar Car, Power generation simulation

1. INTRODUCTION

Recently, various energy efficiency standards for automobiles have been released in various countries in order to achieve a Carbon-Neutral, Carbon-Free Society. For these reasons, many electric vehicles have been developed and automobile manufacturers have tried to improve the efficiency of automobiles. Bridgestone World Solar Challenge (BWSC) is one of international solar car challenges and a competition of technologies on eco-friendly car. The Tokai University Solar Car Team has participated in the BWSC in the past years. The distance of the BWSC is around 3,000 km and only energy obtained from sunlight can be used.

1.1 TOKAI UNIVERSITY SOLAR CAR TEAM

Tokai University Solar Car Team won many trophies in several solar car challenges all over the world, and we have a history of about 25 years. We established a solar car project in 1991, and we firstly participated in World Solar Challenge (WSC) in 1993. Since then, we have many solar car race experience, and we won the six victories in the international competitions since 2008.Almost all parts of our solar car were developed based on Japanese advanced technologies, Toray's light weight and strong carbon fiber bodies, Mitsuba's high efficiency motors, and Bridgestone's low resistance tires and so on. Our aim of participating race is to pursue the technology of clean energy and energy conservation and accelerate the development of these technologies.

1.2 BRIDGESTONE WORLD SOLAR CHALLENGE

BWSC is the most famous solar car race in the world, which started in 1987. More than 40 teams from 20 countries are participating in this competition. The distance of BWSC is around 3,000 km and only energy obtained from sunlight can be used. The weight of solar cars of the top teams is only 140 kg because the state-of-the-art technologies, such as carbon fiber reinforced plastic technologies, have been introduced. This race takes place in the desert area in Australia called the Outback. BWSC is a grueling challenge with temperatures exceeding 40 degrees Celsius in the northern area and winds as strong as 20 m/s in the south area. Fig. 1 shows the 2017 Tokai Challenger of the Tokai University

Solar Car Team and the length, width, and height of the solar car is 5.0m, 1.2m, and 1.0m respectively. Fig. 2 shows the BWSC route.

Fig. 1 The 2017 Tokai Challenger

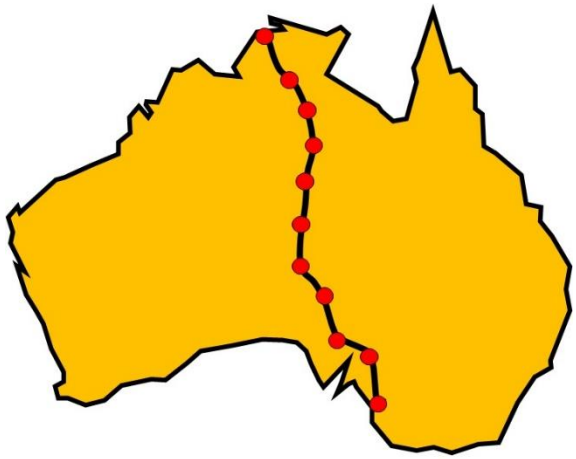

Fig. 2 Route map

2. DESIGN METHODOLOGY

The total area of solar cells is limited within 4m² for the silicon type solar cells, which generate about 900W. Even though the generated power is very low, the cruising speed of the top team's solar car can run at about 85 km/s. In order to make this possible, the running resistance should be reduced to the utmost limit. In particular, reduction of aerodynamic drag and improvement of power generation are major factors for the development of the solar cars and realization of victories. For these reasons, we developed the aerodynamic design and estimation methodologies of the power generation of solar array.

2.1 AERODYNAMIC SIMULATION

In this study, a flow simulation was carried out by using SCRYU/Tetra, a 3D fluid analysis software based on an unstructured grid, developed by Software Cradle Corporation, Japan. Various shapes were examined based on the RANS simulation results. The calculation condition is shown in Table 1. Total number of mesh element is about 150 million. Fig.3 shows an example of comparison of the canopy shape. Canopy covers the driver's cabin space and is installed on the roof of the solar car where the solar array is placed. The canopy shape has a significant impact on the performance of a solar car, since the canopy generates vortices and shadow around it. As shown in Fig. 1, the canopy protrudes from the roof of the solar car in many solar cars. Therefore, it is necessary to consider both aerodynamic

performance and power generation performance. The route of the BWSC is from the north to the south of Australia and Australia is in the Southern Hemisphere, so the sun delivers light from the rear of the body. The position of sun changes from east to west as time goes on. Fig. 3 shows comparison of two types. One is the 2017 Tokai Challenger called 17TC and another type called C1 has longer streamlined shape. Table 2 shows comparison of drag force and lift force between 17TC and C1 model. The drag force and lift force of the C1 model is smaller than 17TC. Figs. 4-7 shows the analyzed flow field. Fig. 4 and Fig.5 show that the adverse pressure gradient at the rear part of the canopy is weaker than the 17TC and the turbulent energy in the wake becomes weak than the 17TC. Fig.6 shows that the velocity distribution. The result shows that the wake region of C1 model is smaller than the one of the 17TC. These results indicate that the C1 model is superior to the 17TC in terms of aerodynamic performance. Fig. 8 shows comparison of shoulder shape. The shoulder generates strong vortices due to the pressure difference between side and roof of the solar car especially when side wind occurs. In the southern Australia, winds will exceed 15 m/s. Two models were compared as shown in Figs. 8-9. One is the 2017 Tokai Challenger, and another model called S1 has a modified shoulder shape. Table 3 shows comparison of drag force and lift force between 17TC and S1 model. The drag force of the S1 model is almost the same as the one of 17TC. The Lift force of the S1 model is smaller than 17TC. Figs. 10-11 shows the analyzed flow field. Fig. 10 shows that the high turbulent energy region of the 17TC is suppressed in the S1 model as shown in the red circle. Fig. 11 shows that the vortices at the top of the shoulder are suppressed in the modified shape.

Table 1 Calculation condition

Vehicle speed [m/s]	25
Fluid density [kg/m³]	1.206
Viscosity coefficient [Pa・s]	1.83×10^{-5}
Fluid temperature [℃]	20
Governing equation	Navier-Stokes equation, Equation of continuity
Discretization method	Finite volume method
Analytical method	RANS
Turbulence model	SST k-ω
Pressure field solution	SIMPLEC method
Spatial discretization scheme	2nd order QUICK
Time discretization scheme	2nd order implicit method
Grid type	Unstructured grid (Tetra, Prism)
Grid width [mm]	Max 440, Min 3.44
Number of boundary layer meshes	7 layers
Outlet conditions	Standard atmosphere

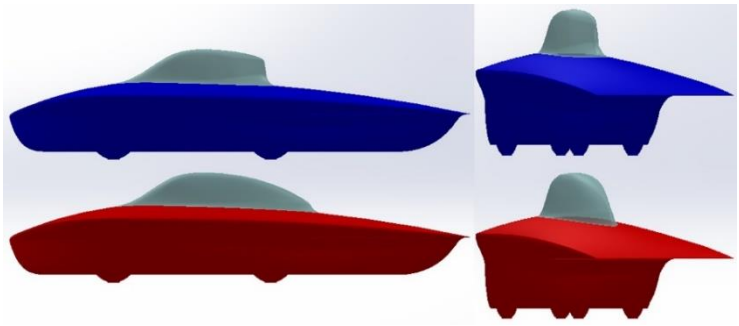

Fig. 3 Comparison of canopy shape (blue:17TC, red: C1)

Table 2 Drag force and lift force of C1 model compared to 17TC

Drag force	-0.30%
Lift force	-6.22%

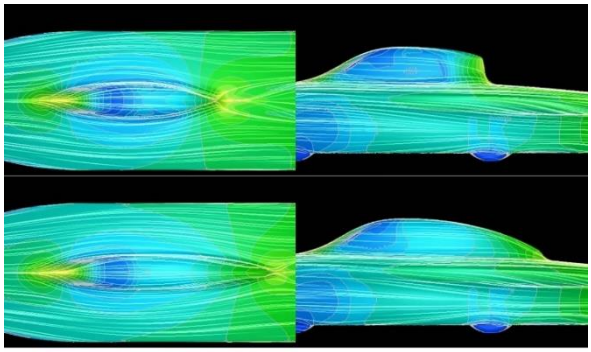

Fig. 4 Surface pressure distribution and surface streamline

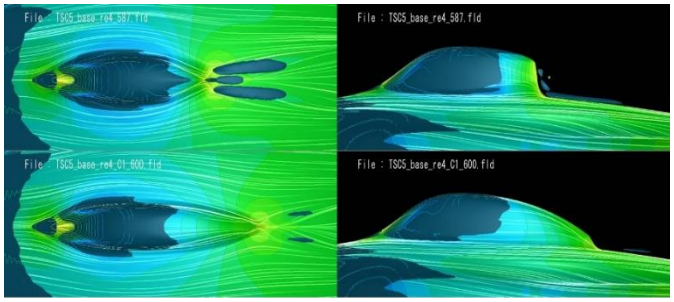

Fig. 5 Surface pressure distribution and iso-surface of turbulent kinetic energy
(Comparison of canopy shape, left:17TC, right: C1)

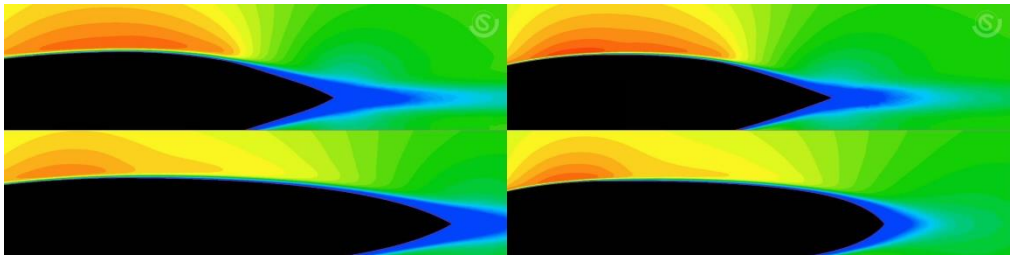

Fig. 6 Velocity distribution
(top view, left:17TC, right: C1, upper side: *y*=0.75m, lower side: *y*=0.85m)

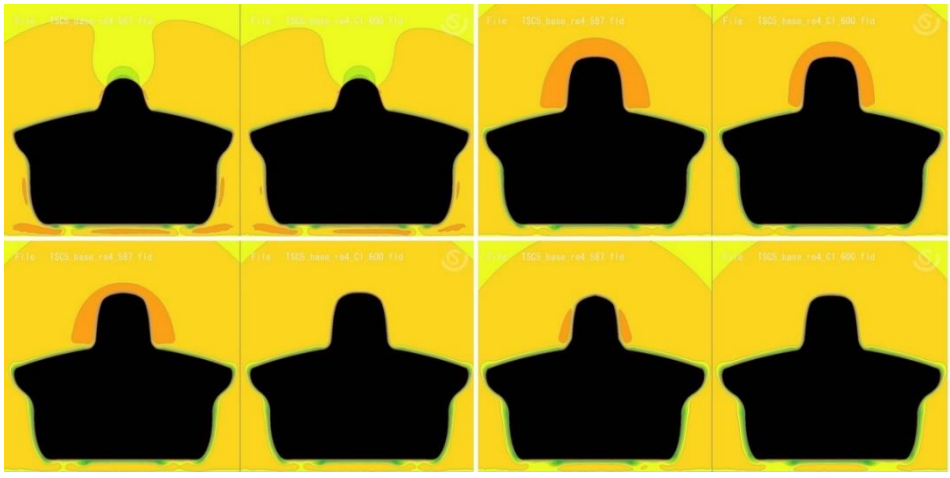

Fig. 7 Velocity distribution (left:17TC, right: C1,
upper left : *x*=1.6m, upper right : *x* =2.0m, lower left : *x*=2.2m, lower right : *x* =2.4m)

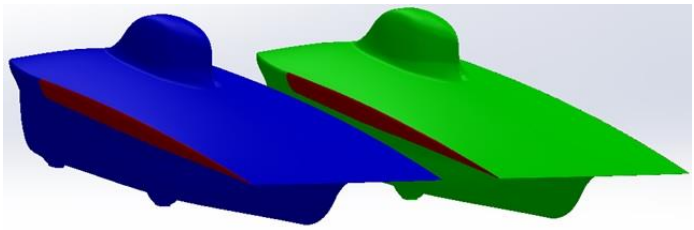

Fig. 8 Comparison of shoulder shape (blue:17TC, green: S1)

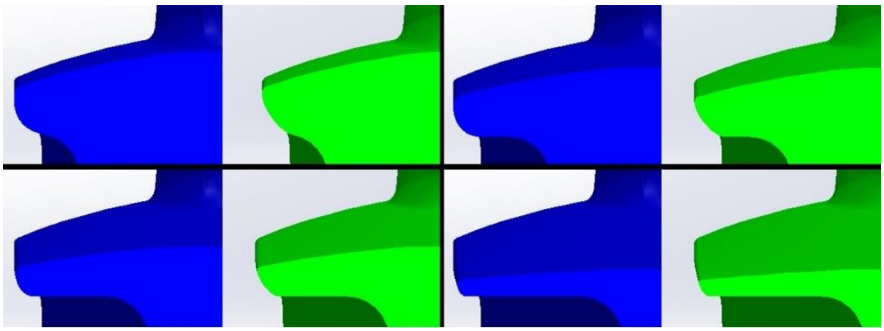

Fig. 9 Rear view of the cross section (blue:17TC, green: S1,
upper left : *x*=3.0m, upper right : *x* =3.5m, lower left : *x*=4.0m, lower right : *x* =4.5m)

Table 3 Drag force and lift force of S1 model compared to 17TC

Drag force	0.04%
Lift force	-4.87%

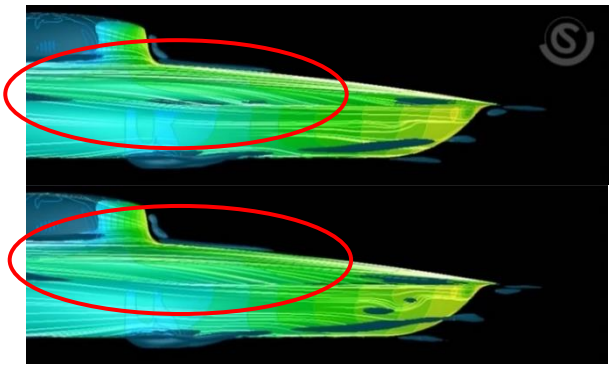

Fig. 10 Surface pressure distribution and iso-surface of turbulent kinetic energy
(upper: 17TC, lower: S1)

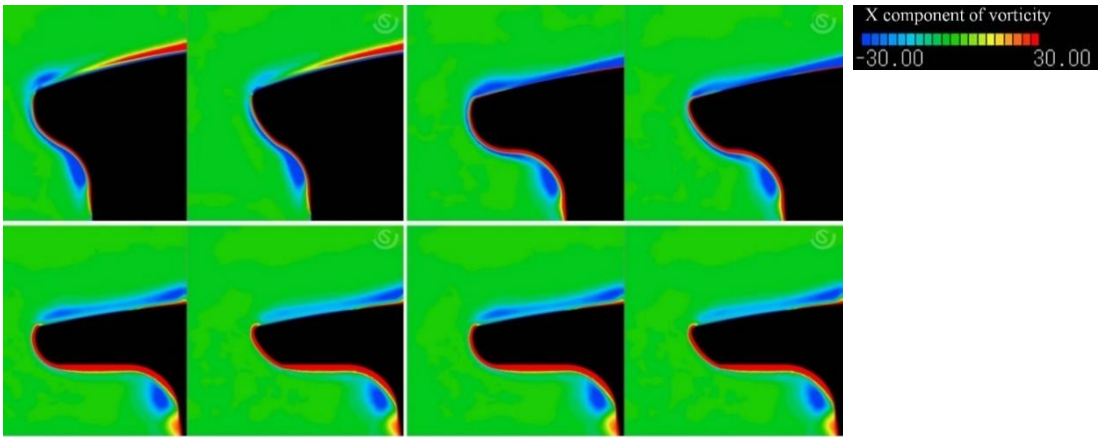

Fig. 11 vorticity distribution (*x* component, left:17TC right: S1,
upper left : *x*=1.6m, upper right : *x* =2.0m, lower left : *x*=2.2m, lower right : *x* =2.4m)

3.1 SIMULATION OF SOLAR POWER GENERATION

The comparison of the power generation performance between the 17TC model and the C1 model was carried out. The solar radiation analysis was performed using the SCRYU/Tetra. In the analysis, the sun was set at an arbitrary position. In this study, sun position was decided based on each time in Adelaide on the 15th of October 2019 and amount of generated power was estimated. Table 4 shows the calculation condition and Fig. 12 shows the temperature distribution of the solar cells at 9:00. Fig. 13 shows the comparison between solar cell array layout and temperature distribution at 9:00 am, 10:30 am, and noon. Fig. 12 shows that the shadow of the canopy expands on the solar array in the morning and afternoon. Due to the characteristics of the solar array, the current of the solar arrays with shadows is reduced. The reduction of the current of the cells reduces the power output of the module which includes the cells. Furthermore, if there is a cell with zero power generation in a module, the power generation of that module will become zero. In practice, electrical systems such as bypass diodes can ignore low cells and prevent from reducing the loss of power. However, the amount of power generated by the module is reduced. Therefore, reduction of the shadow area is crucial for the realization of high-performance solar cars. Fig. 13 shows that the C1 model has larger shadows than in the 17TC. In addition, the C1 type canopy interferes with the solar array, so it is necessary to be relocated to the front or increase the overall width. However, the power generation at the front of the vehicle is low because the BWSC is held in the southern hemisphere and the aerodynamic performance is deteriorated if the vehicle width is increased. In order to estimate the quantity of power generation, our group developed a estimation methodology based on the "New Solar Energy Utilization Handbook" of the Solar Energy Society of Japan and other sources [1]-[5]. By combining the aerodynamic simulation and the estimation methodology of power generation, both aerodynamic performance and power generation performance can be examined. Table 5 and Fig.15 show the total power generation of the C1 model at each time compared to 17TC. The result was evaluated by considering the global irradiation based on direct solar irradiation, diffused solar irradiation. In the results, the cell angle and the effect of the shadows mentioned above were considered. In the estimation, the power generation was set to zero if more than half of the cell was in shadow, even though the effect on the module should be considered in the actual system. The result shows that the power generation of the C1 model was decreased compared to the 17TC. The reduction is 5% in maximum, while the improvement of the aerodynamic performance is 0.5%. The result shows that the total performance of the 17TC as a solar car is better than the C1 model. Finally, even though the C1 model has better aerodynamic performance than the 17TC, but the 17TC model was selected by considering the total performance as the final model.

Table 4 Calculation condition

Physical property value	Solar Array：Glass, Canopy：Acrylic Air：incompressible flow 25[℃]
Radiation	VF (View Factor) method
Type of VF method	single band, solar radiation
Condition：panel , body	Emissivity：0.9, Absorption rate：0.75
Condition：canopy	Emissivity：0.1, Absorption rate：0.90

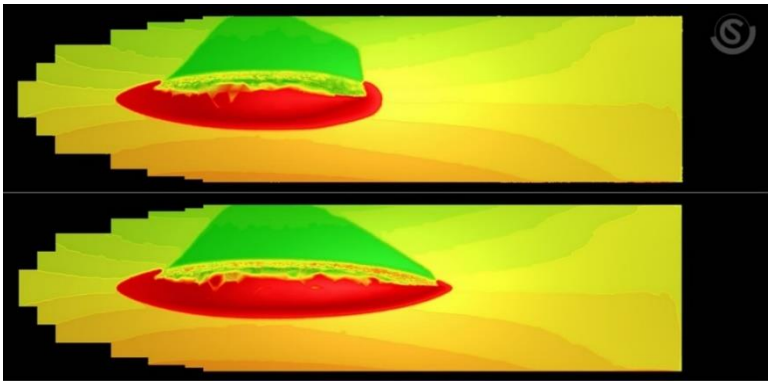

Fig. 12 Temperature distribution of solar cell array (upper: 17TC, lower:C1)

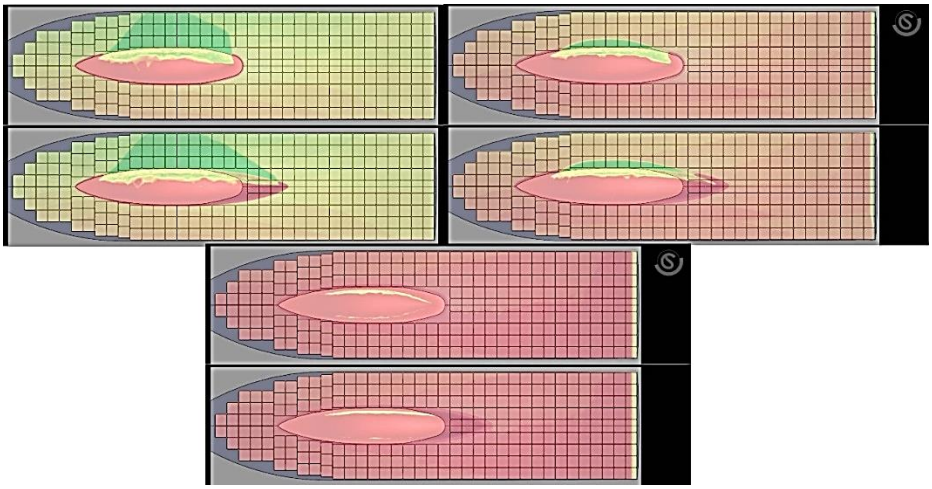

Fig. 13 Comparison between solar cell array layout and temperature distribution (upper: 17TC, lower:C1, upper left: 9:00 am, upper right: 10:30 am, lower: noon)

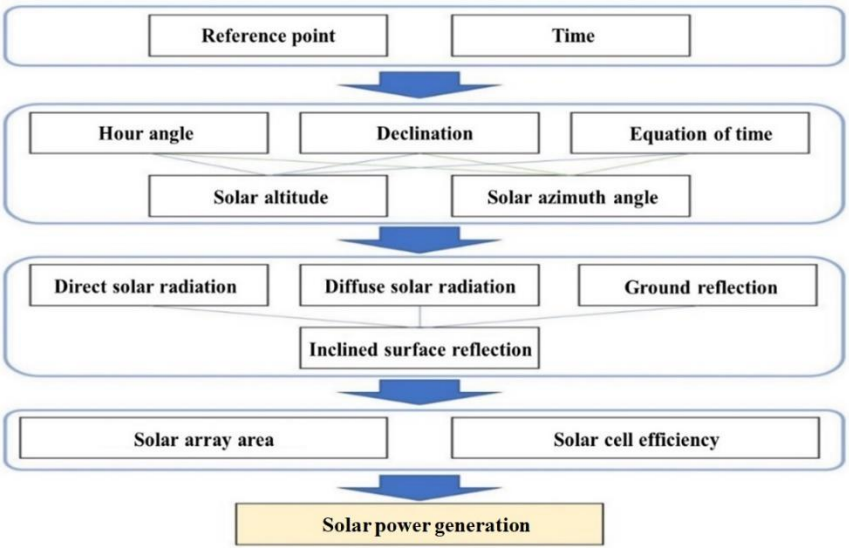

Fig. 14 Flow of solar power generation simulation

Table 5 Total power generation of C1 type compared to 17TC

time	9:00	10:30	12:00	13:30	15:00
C1 model	-5.0%	-2.4%	-2.4%	-2.4%	-5.0%

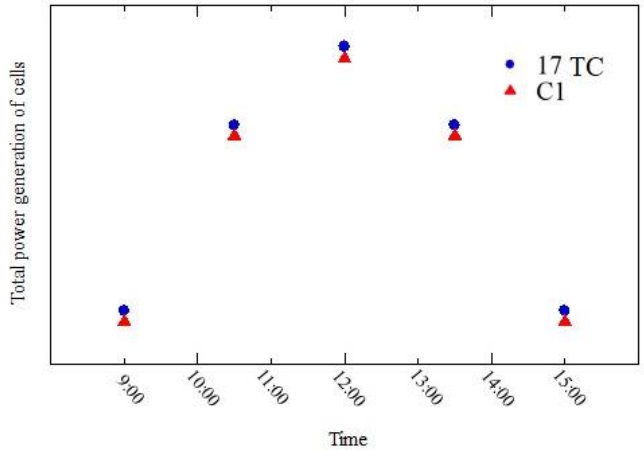

Fig. 15 Power generation at each time

3. CONCLUSIONS

In this study, a design methodology was proposed and applied to the solar car called Tokai Challenger, which the Tokai University Solar Car Team developed for the BWSC. In the methodology, both aerodynamic and power generation performance are considered by combining the flow simulation and a power generation simulation. By using the proposed methodology, total performance can be evaluated. The results showed that the methodology is effective to develop high performance solar cars.

REFERENCE

[1] Japan Solar Energy Society, "Revised Handbook for New Solar Energy Applications"
[2] Meteorological Data System Co., Ltd, Calculating the Sun Position, Sourced on 15 Sep 2021, https://www.metds.co.jp/wp-content/uploads/2019/03/TE_SunPosition_160401.pdf
[3] Meteorological Data System Co., Ltd, Calculation of direct solar radiation separation and slope solar radiation, Sourced on 15 Sep 2021, TE_Radiation_200530.pdf (metds.co.jp)
[4] Japan Sustainable Building Consortium, Energy consumption performance calculation program (residential version), Chapter 9 Renewable Energy Utilization Facilities, Oct 2019
[5] National Astronomical Observatory of Japan,Chronological Scientific Tables 2019", MARUZEN-YUSHODO Co., Ltd,

Article S6.5

Study on Drag Reduction of Superstructure of Ships and Improvement of Fuel Consumption

Kodai Fukushima[1], Kota Fukuda[2], Takao Kashiwagi[3], Takashi Danno[4], Koeki Onishi[5], and Koyu Kimura[6]

[1]Tokai University, 1cemm080@mail.u-tokai.ac.jp, Kanagawa, Japan
[2]Tokai University, fukuda@tokai-u.jp, Kanagawa, Japan
[3]Mitsui O.S.K.Lines, Ltd., takao.kashiwagi@molgroup.com, Tokyo, Japan
[4]Mitsui O.S.K.Lines, Ltd., takashi.danno@molgroup.com, Tokyo, Japan
[5]Mitsui O.S.K.Lines, Ltd., koeki.onishi@molgroup.com, Kanagawa, Japan
[6]Akishima Laboratories (MITSUI ZOSEN) Inc., kimurak@ak.mes.co.jp, Tokyo, Japan
** Corresponding Author: 1cemm080@mail.u-tokai.ac.jp*

ABSTRACT

In this study, reduction of aerodynamic drag of ship superstructure and the fuel consumption during navigation were examined. Large ships used in service for international freight are composed of a hull and a superstructure. Since the superstructure which includes ship bridge, residential area of crew and so on is a huge structure, strong aerodynamic drag force is generated by the superstructure. Various pioneering works on reduction of frictional drag of ships below the waterline have been carried out. For example, bulbous bows have been used to reduce the drag force. On the other hand, there are few studies on the reduction of aerodynamic drag force of superstructures. In this study, some aerodynamic parts were proposed to reduce drag force of superstructure. The effects of aerodynamic parts were examined by wind tunnel test and numerical simulation. At first, the validation of the numerical simulation was carried out by comparing with the experimental data. The analyzed data was in good agreement with the wind tunnel data and the effect of aerodynamic parts were reasonably simulated. Furthermore, the detail effect of the aerodynamic parts and flow characteristics were investigated by numerical simulation. The results showed that the wake and high turbulent energy region were reduced by installing the aerodynamic devices. Furthermore, the fuel consumption in the actual sea route was evaluated by using the obtained data. The results showed that the installation of the device improved fuel efficiency.

KEYWORDS: Ship, Superstructure, Aerodynamic device, CFD, Wind Tunnel test, Fuel consumption

1. INTRODUCTION

There are various types of ships depending on the operation and purpose, and many ships are in operation all over the world. Most of them are powered by diesel engines, which use petroleum as their fuel source. Diesel engines have the advantage of thermally high efficiency, low fuel consumption. The fuel consumption is only about half of the one of steam turbine engines to achieve the same output. As a result, ships emit less carbon dioxide and air pollutants per unit of transportation than other transportation. However, cargo ships, passenger ships, and other mass transit vessels travel long distances on most of the world's oceans and consume large amounts of fuel to keep their engines running without stopping from the port that they leave to the next port. For this reason, the International Maritime Organization (IMO) set its own greenhouse gas reduction targets in 2018, categorizing them into three levels: short-term, medium-term, and long-term. The short-term goal is to improve the average fuel efficiency of all ships by about 40% by 2030, the medium-term goal is to reduce total greenhouse gas emissions by 50% by 2050, and the long-term goal is to reduce total greenhouse gas emissions to zero(1). Among these three reduction targets, for the short-term target, the introduction of drag-reducing technologies during navigation, more efficient ship operations, and the use of low-carbon fuels have been studied as possible improvements.

A ship can be divided into two parts based on its structure: one is the hull, which is just a vessel that can float on the water surface. The other part is called superstructure, which is installed on top of the hull and contains the crew's living facilities. The reduction of drag during ship navigation has been studied from various viewpoints. Since the hull of a ship is always in the water, it receives a large amount of drag from the water during navigation. For this reason, various measures to reduce drag have already been studied and implemented. For example, a large amount of microbubbles are generated to cover the bottom of the ship to reduce the contact area between the water and the hull, and the microbubbles can reduce the frictional resistance [(2)]. In addition, there are bulwark bows, which are valve-shaped protrusions on the bow. The bulwark bows generate waves and reduce wave resistance due to the wave interference [(3)]. As described above, practical methods for the resistance reduction have already been established for hull sections that receive resistance from the water during navigation. On the other hand, on the reduction of aerodynamic drag force generated by superstructures and other parts, there are few studies. One example is the "SUPER ECO SHIP 2050," which reduces air resistance by making the superstructure itself streamlined shape [(4)]. Another example is the "Wind Challenger," which reduces greenhouse gas emissions by installing huge hard-wing sails on the deck to be powered not only by diesel engines but also by wind. These systems will be introduced into new ships to reduce greenhouse gas emission [(5)]. When similar modifications are made to existing ships, the necessary audits and certifications for operation must be obtained again. Research on drag reduction technology to improve existing ships have also been conducted. The examples are changing the container layout of container ships [(8)] and installing aerodynamic devices in the superstructure [(6, 7)]. In this study, aerodynamic devices that can be installed on the superstructure of an existing ship without the need for re-certification were proposed to reduce the aerodynamic drag during navigation.

2. NUMERICAL METHOD

In this study, computational fluid dynamics (CFD) and wind tunnel tests were conducted to investigate the effect of the aerodynamic device on the very large crude carrier (VLCC) of superstructure. Flow simulation was carried out by using "scFLOW Version 2021", a 3D fluid analysis software based on an unstructured grid, developed by Software Cradle Corporation, Japan. The analysis was based on the shape data of the wind tunnel model of the superstructure provided by the Akishima Laboratories (MITSUI ZOSEN) Inc., as shown in Fig.1. The dimensions of the base model are overall length L = 368[mm], overall width W = 600[mm], and overall height H = 307[mm], respectively. The calculation region was set as 11W in length, 24L in width, and 10H in height as shown in Fig.2. Turn table of the wind tunnel is circular and 1600 [mm] in diameter, but the viscous wall region was limited as shown in Fig. 3 in order to reduce the number of calculation meshes and calculation time. For the crosswind analysis, the model was rotated on the turn table. The calculation condition is shown in Table 1. The density was set to 1.206 [kg/m3]. The surface of the analytical model and the turntable were analyzed as viscous walls. The calculation mesh is shown in Fig.4. The mesh sizes near the device and the superstructure were reduced to 0.78[mm] and 1.56[mm], respectively, in order to analyze the detail flow phenomena. The mesh size is gradually increased as it moves away from the object. Twenty layers of boundary layer mesh were inserted in the superstructure and the turntable. For the wind tunnel tests, a low-speed wind tunnel at the Akishima Laboratories (MITSUI ZOSEN) Inc was used. The wind tunnel is the Goettingen type, and the dimensions of the measurement section are 2000 [mm] in length, 2000 [mm] in width, and 3000 [mm] in height. Fig.5 shows the wind tunnel test model and the measurement section of the wind tunnel. The test was conducted at a wind speed of 20.5 [m/s], and the wind direction was changed in the range of 0 [deg] to 180 [deg], every 10 [deg]. The analytical model is shown in Fig.6. In this study, two types of aerodynamic devices, Type A and Type B, are installed. Their cross-sectional shapes are shown in Fig.7. Type A is based on the shape of Type B, but the shape is simplified to reduce the cost of production [(10)]. No.1 is the base model and No.2 is the case in which Type A device is set with Wing, Side and Prop, No.3 is the case in which Type B is set with Wing, Side and Prop. The coordinate axes of the superstructure in this study are shown in Fig.8, where the angle between the mainstream V_∞ [m/s] and the centerline of the superstructure is the yaw angle β [deg]. The drag coefficient Cf_x, and the lateral force coefficient Cf_y is evaluated. Since the coordinate axes are fixed to the superstructure and rotated with the rotation of the superstructure.

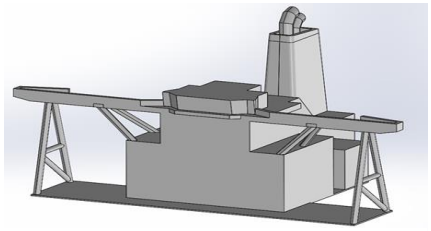

Fig.1 Shape of superstructure

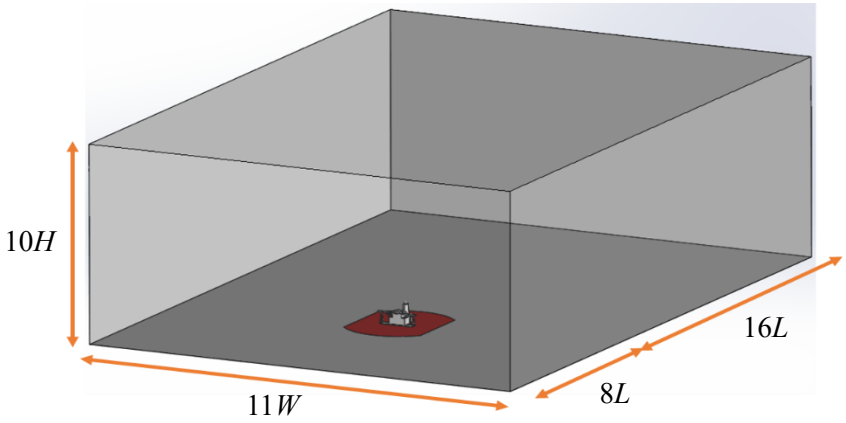

Fig.2 Calculation region

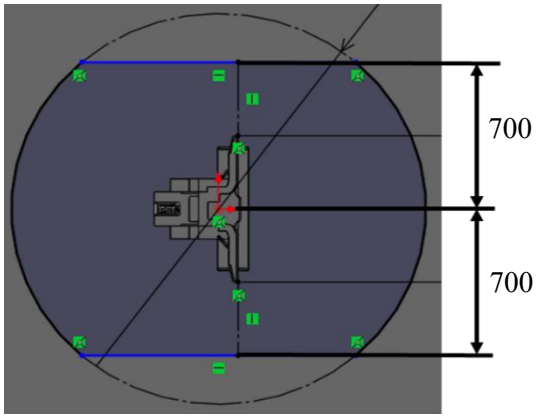

Fig.3 Turn table

Table.1 Calculation conditions

Governing equation	Navier-Stokes equation, Equation of continuity
Fluid	Air（incompressible 20°C）
Inflow condition (velocity) [m/s]	20
Model yaw angle [deg]	0~180（Δ30）
Outflow condition	Atmospheric pressure
Maximum grid width [mm]	200
Minimum grid width [mm]	0.78
Boundary layer mesh	20 layers
Turbulence analysis	RANS
Turbulence model	SST k-ω
Pressure field solution	SIMPLEC
Spatial discretization scheme	2nd order MUSCL

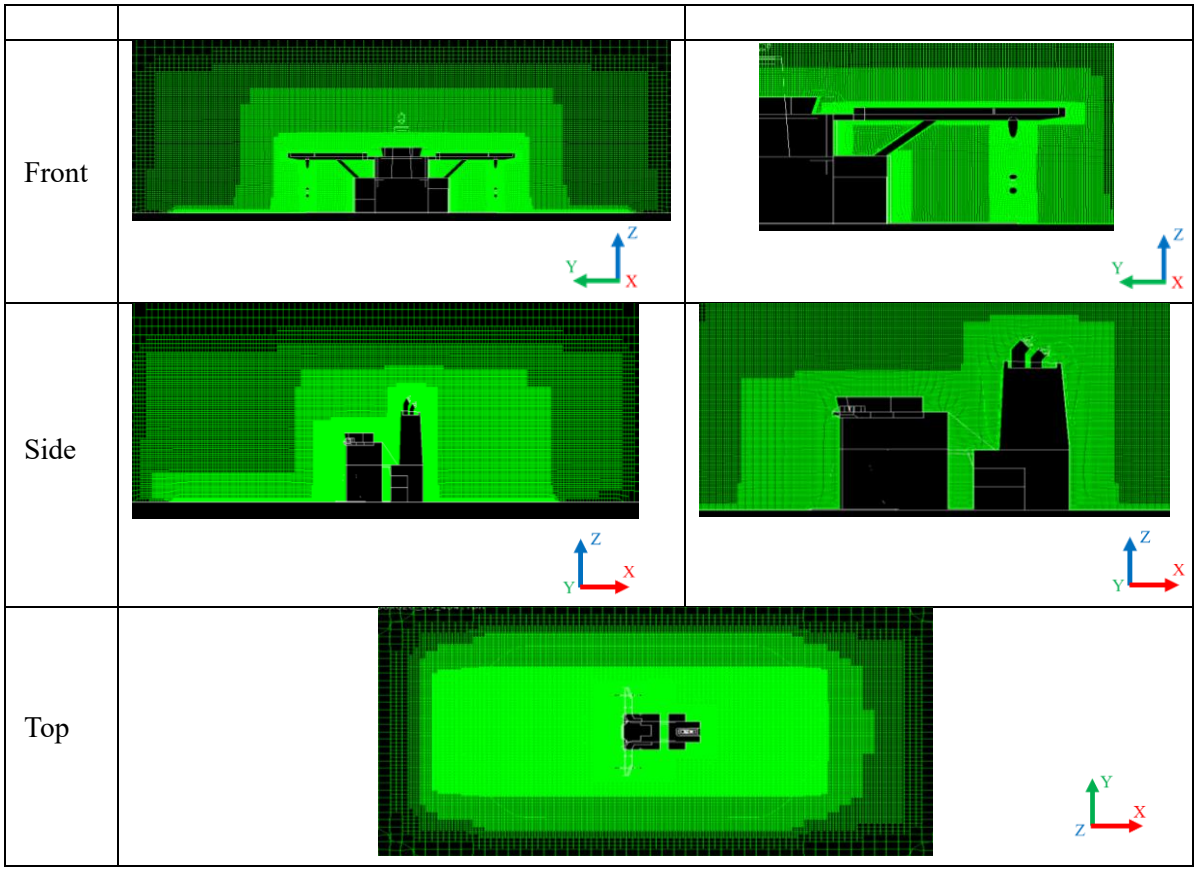

Fig.4 Computational mesh (cross section, 0deg)

Fig.5 Wind tunnel model and measurement section

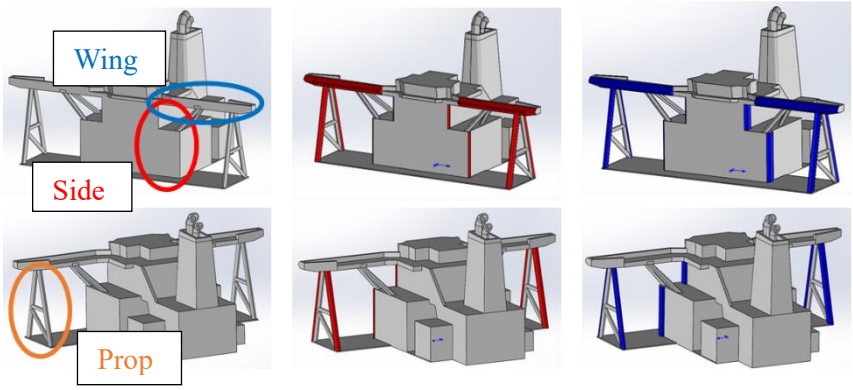

No.1 (Base model) No.2 (Type A) No.3 (Type B)

Fig.6 Analysis models

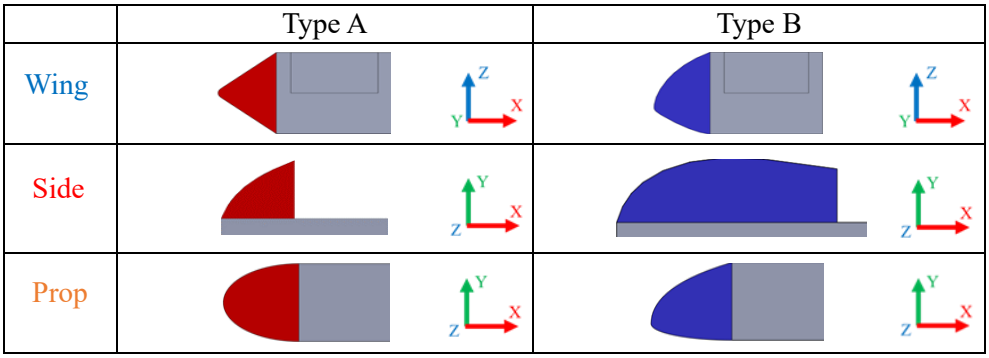

Fig.7 Aerodynamic Devices

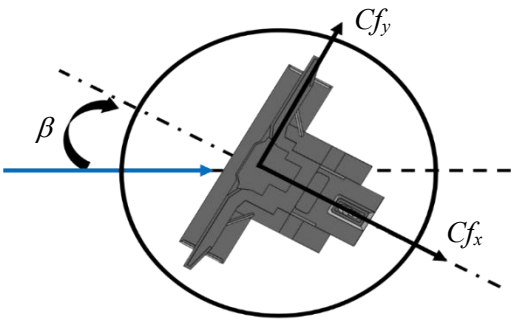

Fig.8 Coordinate axes

3. RESULTS

3.1. VALIDATION RESULTS AND EFFFECT OF AEODYNAMIC DEVICES

Figs.9-11 show the analyzed fluid force for each yaw angle and experimental data obtained in the wind tunnel tests. Although there is discrepancy at some angle, the analyzed drag coefficient and lateral force coefficient are generally in good agreement with the experimental data. Fig.12 and Fig.13 show the percentage change in the drag and lateral force coefficients from the base model due to the installation of the device. The change of drag coefficient and lateral force coefficient have different characteristics at each angle. The results show that the type B aerodynamic devices improves the aerodynamic performance of the superstructure compared to the type A. In order to examine detail effect and flow characteristics, comparison of the visualization results for each shape at 0[deg], 60[deg], and 100[deg] are shown in the next section.

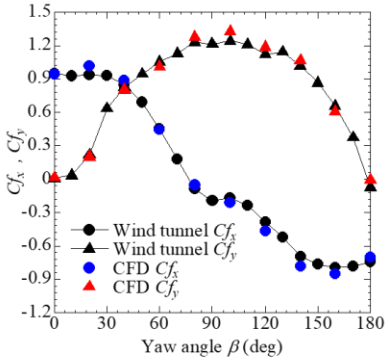

Fig.9 Cf_x-β, Cf_y-β (No.1)

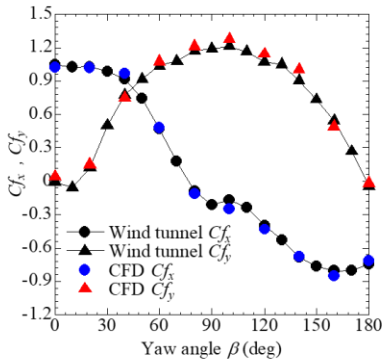

Fig.10 Cf_x-β, Cf_y-β (No.2)

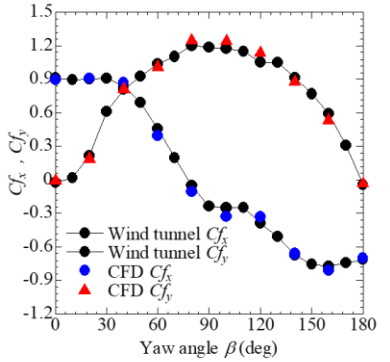

Fig.11 Cf_x-β, Cf_y-β (No.3)

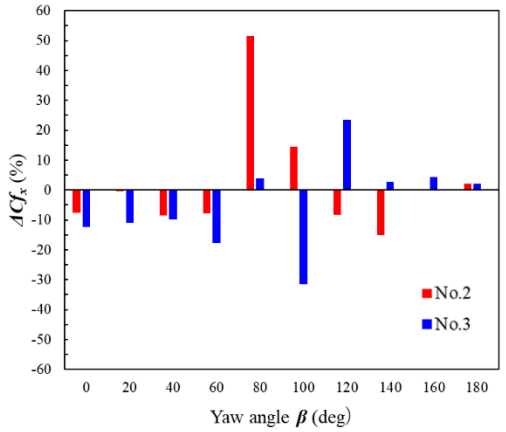

Fig.12 ΔCf_x - β

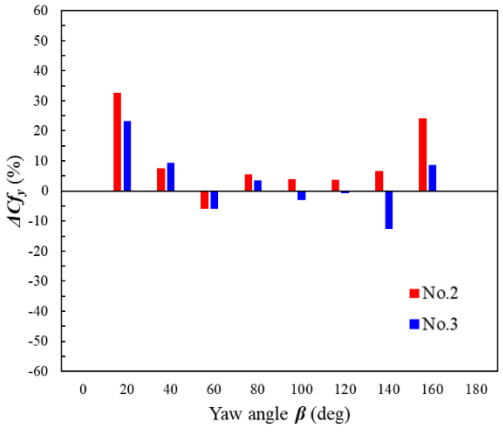

Fig.13 ΔCf_y - β

3.1.1. Yaw angle 0 [deg]

The flow field at yaw angle of 0[deg] is shown in Fig.14. Fig.14 shows the cross section at 200 [mm] from the center of the structure to port. The pressure distribution shows that the high pressure region in front of the structure is larger in No.1 than in No.2 and No.3. The velocity distribution shows that the stagnation region and wake region in No.2 and No.3 is smaller than in No.1. These results show that Type A and type B devices reduce the stagnation pressure and wake region, and the type B is more effective than the type A.

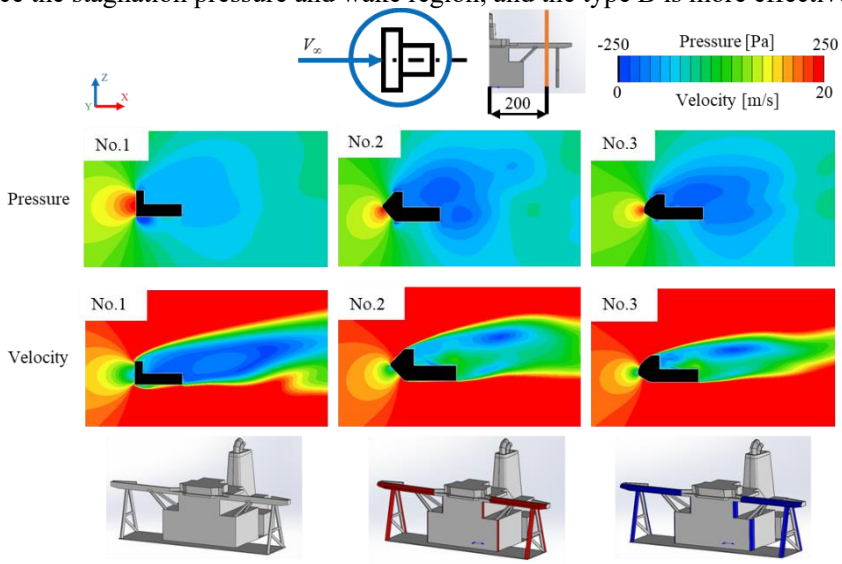

Fig.14 Flow pattern (0deg)

3.3.4. Yaw angle 60 [deg]

Fig.15 shows the analyzed flow field at 70 [mm] in the height direction from the bottom of the structure. The Comparison results of each model showed that the base model has wider stagnant and high pressure region in front and side of the structure than in No.2 and No.3. The high pressure region is narrowed due to the installation of the aerodynamic devices. The Type A device installed in No.2 has a larger high pressure region around the front of the residential area than in No.3. Furthermore, it is confirmed that the wake region behind the pillar is larger in No.3 than other cases since the total frontal projected area of the Prop device in No.3 is larger than the one in the No.1. These results show that Type A and type B devices reduce the stagnation pressure and wake region, and the type B is more effective than the type A. Fig.16 shows the pressure distribution on the cross section at 70[mm] in the height direction from the bottom of the structure and the structure. From the results, it is confirmed that the installation of device to the prop area increases the high pressure region in front of the prop structure compared to No.1. In the case of No.2 and No. 3, although the high pressure region in front of the prop structure is expanded by the installation of the prop device, the high pressure region at the side of the main structure is contracted since the wake region behind the prop structure in No.2 and No.3 is larger

than the one in No.1. As a result, the lateral force coefficient in No.2 and No.3 is reduced compared to in No.1.

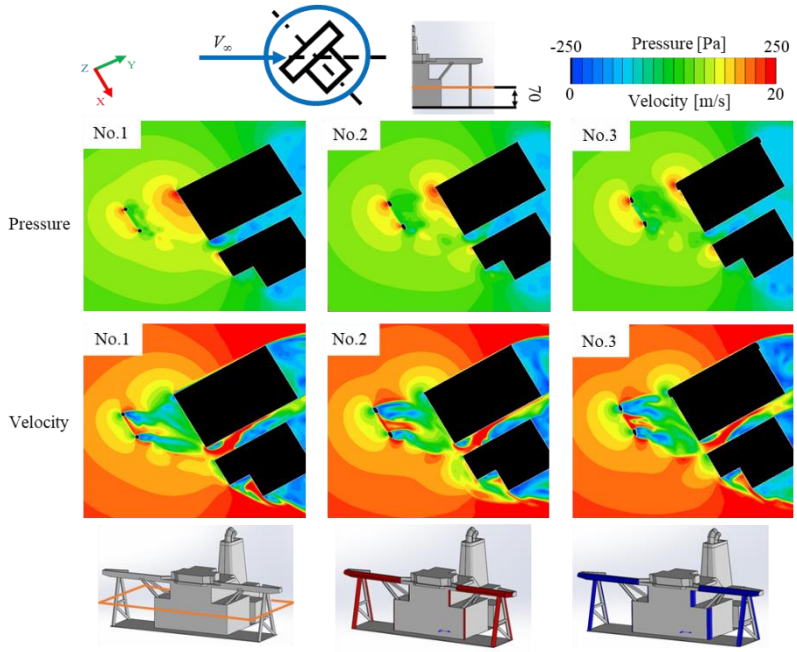

Fig.15 Flow pattern (60deg)

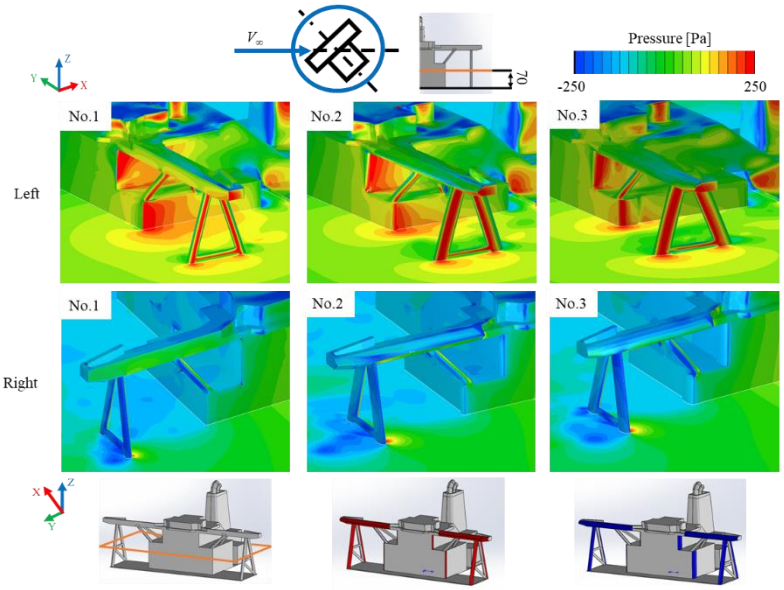

Fig.16 Pressure distribution around the device (60deg)

3.3.6. Yaw angle 100 [deg]

Fig.17 shows the pressure distribution at the cross section of the structure at 70[mm] in the height direction from the bottom and the surface pressure distribution. The result shows that the low pressure region at the frontal side of the structure in No.3 was expanded compared to in No.1. The low pressure region generates the pushing force in the direction of the ship and reduce the drag force. On the other hand, the drag coefficient of No.2 is increased because the negative pressure region is limited than the one in No.1. Furthermore, in No.3, the high pressure region at the upstream side and low pressure region at the downstream side is contracted compared to in No.1 and the lateral force is reduced.

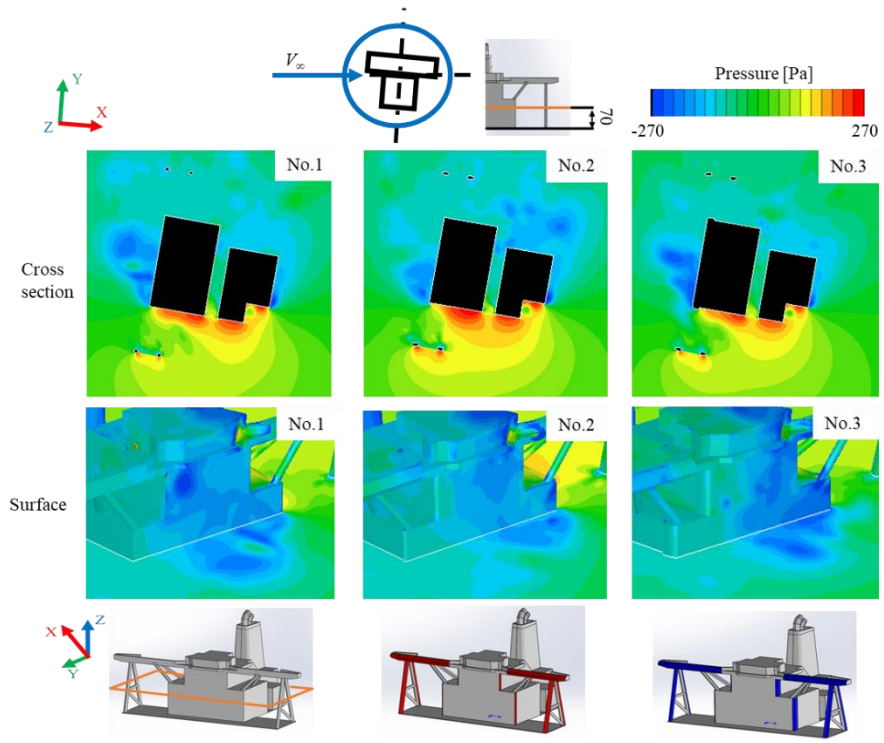

Fig.17 Pressure distribution around the device (100deg)

3.2. FUEL CONSUMPTION

In this study, based on the results of CFD analysis, the effect of the installation of aerodynamic devices in actual shipping routes was investigated in terms of brake horse power (BHP), fuel consumption, fuel cost, and CO_2 emissions. The analyzed aerodynamic characteristics were applied to route of tanker ships from Japan to the Persian Gulf via Singapore and the Malacca Strait [(11)] in this study. A schematic diagram of the route is shown in Fig.18. The tanker ship sails without crude oil on the outbound leg and with a full load of crude oil on the inbound leg. Therefore, the effect of the installation of aerodynamic devices was investigated in the case of full load with the crude oil and ballast without the crude oil. First, the relative wind direction occurrence frequency was evaluated from the data provided by the Akishima Laboratories (MITSUI ZOSEN) Inc. and the histogram of the occurrence frequency of relative wind direction is shown in Fig.19. The results show that the most dominant relative wind direction was 0 [deg], the most dominant wind speed was Beaufort scale 4 (6.75 [m/s]), and the most dominant ship speed was 14.5 [kts] (7.46 [m/s]) when the ship was fully loaded and 16.0 [kts] (8.23 [m/s]) when the ship was empty. The relationship between the braking horsepower and relative wind direction for each model is shown in Fig.20 and Fig.21. In both the fully loaded and unloaded cases, the braking horsepower of all models with aerodynamic devices was reduced compared to the base model in the relative wind direction between 0 [deg] and 80 [deg]. Furthermore, based on the estimated braking horsepower, the annual fuel consumption [t], fuel cost, and CO_2 emissions [t] when the frequency of relative wind direction is 0 [deg] were compared between the base model and No.3. The assumed fuel is C fuel oil, which is commonly used in large ships. The overview of C fuel oil is shown in Table.2[(12)(13)]. When the fuel consumption is E [kl], the calorific value per unit consumption is J [GJ/kl], and the carbon emission per unit calorific value is K [tC/GJ], the CO_2 emission Q [t] is calculated by the following equation [(12)(13)].

$$Q = E \times J \times K \times 44 / 12 \quad (1)$$

Table.3 shows the fuel consumption [t], fuel cost, and CO_2 emissions [t] estimated from the data provided by Akishima Laboratories (MITSUI ZOSEN) Inc and Equation (1). The fuel consumption [t], fuel cost, and CO_2 emissions [t] are estimated to decrease with the reduction of braking horsepower by the installation of the device in the case of full load and ballast. This suggests that the installation of aerodynamic devices on the superstructure can improve the fuel efficiency in actual shipping routes.

Fig.18 JPN-PG route [13]

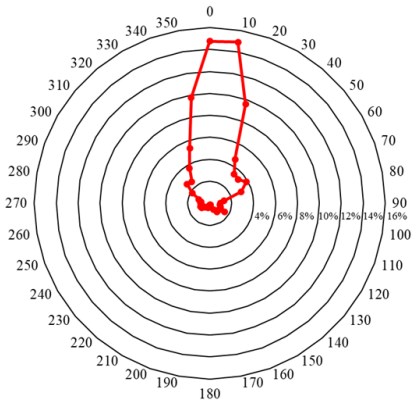

Fig.19 Relative wind direction occurrence frequency

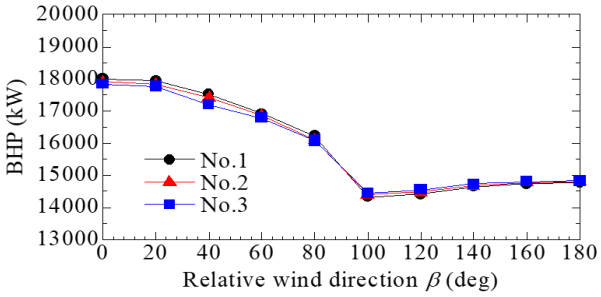

Fig.20 BHP-β graph (Full)

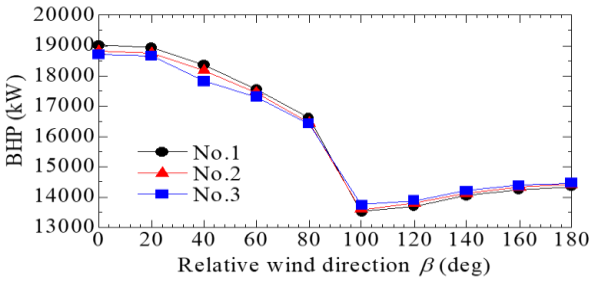

Fig.21 BHP-β graph (Ballast)

Table.2 Overview of C fuel oil

Specific gravity	0.935
Unit price [Yen/kl]	40,000
Calorific value per unit use [GJ/kl]	41.9
Carbon emissions per unit calorific value [tC/GJ]	0.0195

Table.3 Fuel consumption effect at relative wind direction 0 [deg] (per year)

	Full		Ballast	
	No.1	No.3	No.1	No.3
Fuel usage [t]	17285	17110	17635	17460
Fuel expenses [Yen]	739,480,000	732,000,000	754,440,000	746,920,000
CO_2 of emissions [t]	55461	54900	56583	56019

4. CONCLUSIONS

In this study, some aerodynamic parts were proposed to reduce drag force of superstructure. The effects of aerodynamic parts were examined by wind tunnel test and numerical simulation. At first, the validation of the numerical simulation was carried out by comparing with the experimental data. The analyzed data was in good agreement with the wind tunnel data and the effect of aerodynamic parts were reasonably simulated. Furthermore, the detail effect of the aerodynamic parts and flow characteristics were investigated by numerical simulation. The results showed that the wake and high turbulent energy region were reduced by installing the aerodynamic devices. Furthermore, the fuel consumption in the actual sea route was evaluated by using the obtained data. The results showed that the installation of the device improved fuel efficiency. We aimed to reduce the drag force of the superstructure without reexamination, but the effect on fuel efficiency in actual shipping routes was about 1[%]. Therefore, further studies will be necessary to achieve the short-term goal of the initial greenhouse gas reduction strategy announced by the IMO. Furthermore, for the medium-term target of the Initial Strategy for Greenhouse Gas Reduction, it is necessary to conduct research on the premise of introduction to new ships and large-scale refurbishment, such as optimization of the shape of the superstructure itself in addition to small-scale refurbishment.

REFERENCE

[1] Shin Imai, " GHG Reduction Measures in the International Shipping Sector: Recent International Trends and Japan's Policy", Maritime Bureau, Ministry of Land, Infrastructure, Transport and Tourism, pp.1-6, 2019, (in Japanese)

[2] Koji Takahashi, Akira Kadokawa, and Yoshiaki Kodama, “Flow direction distribution of frictional resistance reduction by microbubbles”, Proceedings of the Japan Shipbuilding Society, 1997 (in Japanese).

[3] Takeo Inui, Tetsuo Takahei, and Michio Kumano, “Tank Tests on the Effect of a Spherical Bow on Wave Formation”, Proceedings of the Japan Shipbuilding Society, 1960 (in Japanese).

[4] Nippon Yusen, News Release 2018, “The Challenge of Decarbonization: NYK Super Eco Ship 2050”, https://www.nyk.com/news/2018/20181114_01.html, (Date viewed:2020/5/6)

[5] Takehiro Shirai, Kiyoshi Uzawa, Manabu Kimura, Syunsuke Tamura, Mizuho Sawada, Hideki Yodawara, Yamato Nagahama, Izumi Osugi, Ichiro Aoki, Kazuyuki Ouchi, “Results of Sail Performance Test and Study of Wing Control by Large Hard-wing Sail Demonstrator”, Proceedings of the Japan Society of Marine Engineers Lectures, 21, pp.167-170, 2015 (in Japanese)

[6] Tsuneishi Shipbuilding Co.,Ltd., “Wind pressure reduction structure for ships”, International Bureau of the World Intellectual Property Organization, WO 2013/005671 A1, pp.1-12, 2013

[7] Shipbuilding Industry Association of Japan, “Japan Shipbuilding Digest No.24”, 2011 (in Japanese)

[8] K Ouchi, Y Tanaka, A Taniguchi, J Takashina, N Matsubara, K Kimura, “A STUDY ON AIR DRAG REDUCTION ON THE LARGE CONTAINER SHIP IN THE SEA”, The Royal Institution of Naval Architects, pp1-6, 2014

[9] Software Cradle Co., Ltd., “scFLOW Version 2021 User's Guide Analysis Methods”, 2020 (in Japanese)

[10] Hiroki Yanagisawa, “Numerical Simulation on Drag Reduction of Hull Superstructure”, Master's Thesis, Tokai University, pp.30-34, 2020 (in Japanese)
[11] Izumi Kawamura, “Basic Knowledge of Tankers”, Analysys Oil and Natural Gas Review, pp.25, 2016 (in Japanese)
[12] Ministry of the Environment, “List of Calculation Methods and Emission Factors in the Calculation, Reporting, and Publication System”, pp.1-7
[13] Ministry of the Environment, “List of Formulae and Emission Factors for Calculating Greenhouse Gas Emissions”, pp.1-2

Keynote Lecture

Frank Holzäpfel
Senior Scientist (Dr.-Ing. habil.)
Institute of Atmospheric Physics
German Aerospace Center, Germany

Dr.-Ing. habil. Frank Holzäpfel graduated as a mechanical engineer from the University of Karlsruhe (TH) in 1990. He then specialized in measurement and modelling of turbulent swirling flows at the Engler Bunte Division of Combustion Technology in Karlsruhe, where he obtained his Dr.-Ing. in 1996. In 1997 he became a Research Scientist at the Institute of Atmospheric Physics, DLR (German Aerospace Center) in Oberpfaffenhofen, where he concentrates on wake vortex research, including large eddy simulation, real-time wake vortex model development, field experiments, wake vortex advisory systems, risk analysis, and wake vortex decay enhancement. In 2005 he obtained his Habilitation in Fluid Dynamics at the Faculty of Mechanical Engineering of the Technical University Munich where he was an associate lecturer from 2007 to 2009. In 2014 he was awarded the title Senior Scientist.

Lecture title:
Mitigating Aircraft Wake Vortex Risks During Final Approach via Plate Lines
by Frank Holzäpfel, Anton Stephan, Grigory Rotshteyn, Dennis Vechtel

Mitigating Aircraft Wake Vortex Risks During Final Approach via Plate Lines

Frank Holzäpfel[1*], Anton Stephan[1], Grigory Rotshteyn[1], Dennis Vechtel[2]

[1]*Deutsches Zentrum für Luft- und Raumfahrt, Institut für Physik der Atmosphäre, 82234 Oberpfaffenhofen, Germany*
[2]*Deutsches Zentrum für Luft- und Raumfahrt, Institut für Flugsystemtechnik, 38108 Braunschweig, Germany*
** Corresponding Author: frank.holzaepfel@dlr.de*

As an unavoidable consequence of lift, every flying vehicle generates counter-rotating regions of turbulence known as wake vortices (see Fig. 1). These long-lived trailing vortices constitute a potential threat to following air traffic. Aircraft must therefore keep to a predetermined minimum separation distance. These aircraft separations limit the capacity of congested airports in a basically rapidly growing aeronautical environment. Decades of research on effective aircraft modifications aiming at the alleviation of the wake vortex hazard did not lead to operational use until today.

Fig. 1: Numerical simulation of wake vortex evolution generated by landing A340 aircraft with plate line.

The highest risk to encounter wake vortices prevails in ground proximity, where the vortices cannot descend below the glide path but tend to rebound due to the interaction with the ground surface. Weak crosswinds may compensate the self-induced lateral propagation of the upwind vortex, such that it may hover over the runway directly in the flight path of the following aircraft. That's why aircraft experience wake vortex encounters time after time, even under adherence to separation standards.

So-called plate lines mitigate the risk of wake vortex encounters during final approach and may help to enhance runway capacity. One plate line consists of several upright plates that are installed underneath the approach glide path at the ends of runways (Figs. 1 and 3). Plate lines are passive, cost-effective, robust and safe.

Since the first idea developed in the year 2008, the functionality of the patented plate lines was first demonstrated in towing tank experiments [1]. Next, using high-performance numerical simulations, the underlying physical mechanism was analyzed in detail, the size of the plate lines was optimized, and the influence of wind was investigated [1]. Flight tests with the DLR research aircraft HALO (Gulfstream G550) at the special airport Oberpfaffenhofen showed that the lifetime of the longest-lived vortices can be reduced by about 30%.

When a vortex gets close to the plates, strong Ω-shaped secondary vortices (SV) are induced at the plate's surface that actively approach the wake vortices (WV) by self-induced motion, (see Fig. 2, left). Then the secondary vortices are wrapped around the wake vortices by the primary wake vortex flow (Fig. 2, center). Finally, the secondary vortices propagate along either side of the wake vortices again driven by self-induced motion and accelerate their decay (Fig. 2, right). In Fig. 2 curved arrows denote the rotational direction of the vortices while straight arrows denote their self-induced directions of propagation.

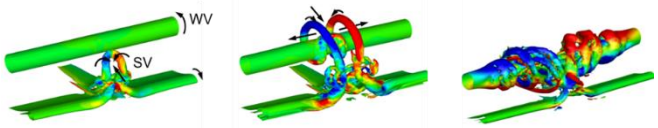

Fig. 2: Ω-shaped secondary vortex (SV) approaches wake vortex (WV) and wraps around it leading to premature wake vortex decay [1].

In the year 2019, the effectivity of the plate lines was demonstrated in a large-scale measurement campaign at Vienna International Airport [2]. Two temporary plate lines were installed underneath the glide path to runway 16. During a six-month period, wake vortex decay was measured for 9473 landings using lidar. It was found that plate lines reduce the lifetime of the most safety-relevant wake vortices by 22% for Medium category aircraft and by up to 37% for Heavy category aircraft. Depending on the aircraft pairing, plate lines allow for a potential separation reduction of 12% to 20% compared to the RECAT-EU separation scheme.

Fig. 3: Overflight of A380 of one of the experimental plate lines installed at runway 16 of Airport Vienna.

References

[1] Stephan, A. et al. (2014). Enhancement of aircraft wake vortex decay in ground proximity, CEAS Aeronautical Journal, 5, 109-125, http://dx.doi.org/10.1007/s13272-013-0094-8.

[2] Holzäpfel, F. et al. (2021). Mitigating Wake Turbulence Risk During Final Approach via Plate Lines, AIAA Journal, accepted, https://doi.org/10.2514/1.J060025.

Acknowledgments: This project has received funding within the framework of the SESAR Joint Undertaking "Increased Runway and Airport Throughput" project (PJ.02 EARTH) and the "Safely Optimized Runway Throughput" project (VLD3-W2 SORT) within the European Union's Horizon 2020 research and innovation programme under grant agreement Nos 731781 and 874520 as well as from the German Aerospace Research Center (DLR) project "Wetter und disruptive Ereignisse".

Article S7.1

Comparison of Synthetic Inflow Generation Methods for Atmospheric Boundary Layer Flows

Henry Plischka[1*], **Johann Turnow**[1], **Nikolai Kornev**[1]

[1] *University of Rostock, Albert-Einstein-Str. 2, 18059 Rostock, Germany*
[*] *Corresponding Author: henry.plischka@uni-rostock.de*

ABSTRACT

In the present work full scale large eddy simulations of atmospheric boundary layer flow for two roughness lengths are presented and compared with wind tunnel experiments. Periodic boundary conditions and four synthetic turbulence generation techniques are introduces with reviewing two input methods for the Reynolds stress. The horizontal homogeneity in stream wise direction of the velocity, the Reynolds stresses and the velocity spectra are discussed. The ability to reproduce the provided length scales is also considered. It is shown, that high differences in horizontal homogeneity of vertical profiles and velocity spectra are present between the inflow methods. The prediction of two synthetic inflow methods quickly adapt to the profile of periodic boundary conditions and are in good agreement with experimental data.

KEYWORDS: Large Eddy Simulation, synthetic turbulence, atmospheric boundary layer

1 INTRODUCTION

Large-eddy simulation (LES) has become a very prominent numerical tool for studying transport processes in the atmospheric boundary layer during the last 50 years [1]. More recently, due to increasing computational resources, also the urban boundary layer including dispersion processes inside a densely build-up environment is investigated with LES. Since these investigations are still time-consuming and numerical expensive, methods to speed up the simulation are worthwhile, especially in non academic applications, as e.g. the security analysis of gas propagation due to hazardous incidents. One way to the above mentioned intention is the effective reproduction of the incoming wind field by synthetic generated turbulence. A vast amount of methods and modifications have been presented in last decades. Some reviews were made by [2] and [3]. Four of these methods are analyzed in this study for the applicability to atmospheric boundary layer flow, using two roughness conditions. The results will be compared with measurement data from the open-return boundary layer wind tunnel facility of the Meteorological Institute of the University of Hamburg and wind profiles generated with periodic boundary conditions.

2 COMPUTATIONAL METHODS

In the following section the geometrical and boundary conditions as well as the numerical setup of the simulations are described. The software tool used in this work is OpenFOAM® (v1906) [4].

2.1 COMPUTATIONAL DOMAIN

All simulations are performed in full scale. The vertical and lateral dimensions (z- and y-direction, respectively) are set to $H = 600$ m, whereby a minor influence of the top boundary as well as a negligible acceleration due to blockage in later simulations of build-up areas can be ensured. The stream-wise extension (x-direction) is chosen to be $7H$, to provide minor correlation and a naturally developed turbulent boundary layer when periodic boundary conditions are used. A pure hexaedral block structured grid with uniform cell size in horizontal direction and a grading in vertical direction is used. Within a grid resolution study, performed with cyclic boundary conditions, the final cell size in stream- and span-wise direction for comparison of the various inflow methods is $\Delta x_g = \Delta y_g = 9$ m . Perpendicular to the ground a grading of 1.1 for $z < H/6$ and 1.03 for $z > H/6$ is applied, starting with a height of $\Delta z_{g1} = 1.5$ m for the wall adjacent cell.

2.2 BOUNDARY CONDITIONS

2.2.1 Inlet condition

Two methodologies of time-varying turbulent velocity inflow are used in this study. The first one can be assigned to as precurser method (PM), where the velocity field from inside the domain is mapped to the inlet patch. As in [5] and [6] the re-scaling is neglected in this study due to the assumption of fully developed boundary layer over constant roughness height. To impose the horizontal pressure gradient, the mean patch velocity at the inlet is enforced to be $\overline{U}_{\text{inlet}} = 6$ m/s. As second method the inlet is defined by a synthetically prescribed turbulent velocity field. Various methods of so-called turbulence generators (TG) have been presented in the literature and a few of them are review in the following paragraphs.

In the method of Klein et al. [7] the mathematical properties of the digital filters, which were determined in the LDA measurement technology, have been applied for the generation of the velocity fluctuations. The velocity signal is represented as a linear series of random numbers multiplied with the filter coefficients $b_{x,y,z} = b_x b_y b_z$ which are chosen to reproduce desired integral lengths. The coefficients b_α, $\alpha = -N_\alpha, N_\alpha$ are calculated in each coordinate directions for the autocorrelation function of the Gaussian type. The length of the series is dictated by the length scales of the generated turbulence. Extension to arbitrary autocorrelation functions has been proposed in [8]. It is based on the solution of nonlinear equations using the Newtonian method which is a very challenging procedure in terms of convergence. The anisotropy of Reynolds stress is taken into account by the Lund's transformation [9]. Both the integral lengths and the Reynolds stress can be variable in space. The method shows many advantages over other methods (simplicity, number of nodes is arbitrary, no periodicity of the signal in time, adaptation to conditions of the experiment, consideration of anisotropy of length scales). The disadvantages of this method include the requirement of a constant time step width and the use of uniform grids. Note that the application of the Lund's transformation changes the length scales specified for the computation of b_α. Also the resulting signal is not divergence free.
The group of the methods proposed in [10] and [11] belong to the structure based ones. The idea is based on the generation of structures with a certain inner distribution of the velocity in front of the inlet. When moving through the inlet the structures induce the velocity at the inlet. The method has no restrictions with respect to the time step and the computational grid.
The initial version of this method, called the turbulent spot method, has been developed for inhomogeneous non-solenoidal turbulent fields [12]. A motivation for the development of the turbulent spots (TS) method were works in which turbulence was simulated by a set of stochastically distributed vortex structures. Townsend [13] and Lundgren [14] obtained the vortex structures from a local linearized solution of the Navier- Stokes equation and proved which energy spectrum results from a collection of such vortices. On the contrary, in TS developments we proceeded from a prescribed energy spectrum and obtained the fluid structures corresponding to this spectrum. A few theoretical relations were taken from a comprehensive theoretical study of statistical parameters of turbulence produced by set of stochastic vortices published by Pullin and Saffman [15]. The idea of TS method was also inspired by works of Sergent (see, for instance, [16]), who used two dimensional vortices to generate the turbulence within a plane.
A few years after the publication of [12] the Synthetic Eddy Method [10] appeared, which formalism is the same as in [12]. The difference is that an additional two steps procedure was developed in [12] to reproduce the integral lengths. The Synthetic Eddy Method utilizes a tent like inner distribution of the velocity in all three coordinate directions. It can be shown analytically that the size of the eddy is not equal to the integral scale and an additional procedure is necessary to overcome this shortage [12]. The Reynolds stress is taken into account by the Lund's [9] transformation. The velocity field is not divergence free and reproduces non controllable correlation functions.
A way to reproduce desirable correlation functions of arbitrary shape was found in [17]. This can be achieved by choice of function f which describes the inner velocity distribution inside of the turbulent spot. f is found from a nonlinear integral equation derived in [17]. Since the numerical solution of this nonlinear equation is laborious and unstable due to ambiguity of the solution, this way has not been used in practical simulations. Instead of this, exact analytic solutions for f were found in [18] for the homogeneous turbulence case using the convolution theorem. A modified Lund's transformation which preserves the autocorrelation functions was developed in [17]. In [19] the turbulent spot method was extended to obey the continuity condition $\nabla \mathbf{u} = 0$ by deriving the inner velocity distribution from a vector potential $\mathbf{A}$. Then the velocity field obtained as $\mathbf{u} = \nabla \times \mathbf{A}$ satisfies the continuity condition

$\nabla\mathbf{u} = \nabla(\nabla\times\mathbf{A}) = 0$ automatically. It was also shown that the shape of the vector potential distribution is dictated by the energy spectrum. Analytical solutions were found for two typical spectra.
We called this new spots, carriers of the vector potential with corresponding divergence-free velocity fields as "vortons" following the term introduced by [20]. The vorton has an orientation $\boldsymbol{\gamma}$ and dipole like vorticity $\nabla\times\mathbf{u}$ distribution. If the orientation vector $\boldsymbol{\gamma}$ is uniformly distributed on the sphere, with other words if the vorton has no preferential orientation, the velocity field generated by a set of vortons stochastically distributed in space is isotropic. If any preferential orientation $\boldsymbol{\gamma}$ is introduced, the turbulent field becomes anisotropic. Unfortunately, as shown in [11], only a weak anisotropy could be reproduced in such a way.
New exact analytical solution allowing to generate divergence free turbulent fields with arbitrary anisotropy and two prescribed integral lengths was derived in [11] by stretching the coordinates to obtain a diagonal Reynolds stress tensor

$$\mathbf{A} = \exp\left[-\frac{1}{2}\left(\frac{x^2}{\sigma_x^2}+\frac{y^2}{\sigma_y^2}+\frac{z^2}{\sigma_z^2}\right)\right]\begin{pmatrix} x\gamma_x \\ y\gamma_y \\ z\gamma_z \end{pmatrix} \tag{1}$$

$$\mathbf{U} = \exp\left[-\frac{1}{2}\left(\frac{x^2}{\sigma_x^2}+\frac{y^2}{\sigma_y^2}+\frac{z^2}{\sigma_z^2}\right)\right]\begin{pmatrix} \left(\frac{\gamma_y}{\sigma_z^2}-\frac{\gamma_z}{\sigma_y^2}\right) yz \\ \left(\frac{\gamma_z}{\sigma_x^2}-\frac{\gamma_x}{\sigma_z^2}\right) xz \\ \left(\frac{\gamma_x}{\sigma_y^2}-\frac{\gamma_y}{\sigma_x^2}\right) xy \end{pmatrix} \tag{2}$$

By aligning the x, y, z-directions of the vorton with the principal directions of the Reynolds stress tensor, arbitrary anisotropic Reynolds stresses can be reproduced (see explanations in [11]). The stretching parameters σ_x, σ_y and σ_z and strength vector components γ_x, γ_y and γ_z are used to match the prescribed Reynolds stresses and integral length scales, which are expressed in a simple analytic form (see derivations in [11]). The analytic solution is only possible for specified Reynolds stresses and two arbitrary lengths. The third integral lengths can not be arbitrary and it is found from the condition of solvability of the problem.
Finally, we list differences with the divergence free SEM method [21]:

- The present method is based on simple analytic function (2) which has smooth derivatives of arbitrary order. As a result the divergence free condition is satisfied everywhere within the computational domain.

- The most serious advantage is that, at least two integral lengths L_i can be explicitly prescribed and exactly reproduced in simulations. The method with approximate reproduction of three integral lengths is presented in [11].

In this study the approaches of Klein et al. [7] (TG1), Jarrin et al. [10] (TG2), Kröger et al. [11] (TG3) and a simple Random velocity field generator (TG4) are used. In the case of TG1 and TG4 the original in OpenFOAM implemented versions are applied. It should be noted, that contrary to the original version this implementation uses only the length scales at one height. The uniform virtual grid of TG1 is chosen to resolve the numerical grid described in section 2.1 in both directions. The detailed input values for all used TG are prescribed in section 2.2.2. For comparison reasons the velocity field at the inlet patch of all inflow generation techniques is saved with a time step of $\Delta t = 1$ s. In the simulation of the boundary layer the field is temporally interpolated with a time step of $\Delta t = 0.25$ s.

2.2.2 Generation of input parameter for synthetic inflow generation

The synthetic turbulence generation methods TG1-TG4 require prescribed input values for the mean velocity $\langle U\rangle$, the Reynolds stresses R_{ij} and the integral length scales L_{ij}. The height dependent velocity

profile of rough atmospheric boundary layers can easily be estimated from the logarithmic relation

$$\langle U_x \rangle (z) = U_{\log}(z) = U_{\text{ref}} \frac{\ln\left(\frac{z+z_0}{z_0}\right)}{\ln\left(\frac{z_{\text{ref}}+z_0}{z_0}\right)}, \tag{3}$$

where $\langle U_x \rangle$ is the mean stream-wise velocity, U_{ref} is a reference velocity at height z_{ref}, z is the height above ground and z_0 is the roughness length. For providing the Reynolds stresses, usually experimental data or computationally expensive LES can be used (e.g. [22], [23]). Calculating the R_{ij}-tensor from a Reynolds Average Navier-Stokes Equations simulation of an atmospheric boundary layer is also possible, whereat it still is inconvenient and horizontal homogeneity must be ensured (see e.g. [24], [25] and [26]). Less elaborate, R_{ij} can be generated from empirical relations, for which various methods have been presented in the literature (e.g. [27], [28], [29]). In this work we use the Boussinesq approximation

$$R_{ij} = \frac{2}{3} k \delta_{ij} - 2\nu_t \left[S_{ij} - \frac{1}{3} tr\left(S_{ij}\right) \delta_{ij} \right], \tag{4}$$

where the turbulent kinetic energy is calculated with

$$k = \frac{u^{*2}}{\sqrt{C_\mu}}, \tag{5}$$

δ_{ij} is the Kronecker delta and S_{ij} is the strain rate tensor. The turbulent viscosity and the friction velocity are defined as

$$\nu_t = \frac{u^* z \kappa}{\ln\left((z+z_0)/z_0\right)} - \nu \tag{6}$$

and

$$u^* = \frac{U_{\text{ref}} \kappa}{\ln\left((z+z_0)/z_0\right)}, \tag{7}$$

respectively. The von Karman constant κ and the k-ϵ model constant C_μ are set to 0.41 and 0.09, respectively. With the assumption of $U_y = U_z = 0$ and $dU_x/dx = dU_x/dy = 0$ the normal stresses result from $u'u' = v'v' = w'w' = 2/3k$ and the only non zero flux is $u'w' = -\nu_t(dU_x/dz)$.
The R_{ij} from LES (only the resolved stresses are used) and from the Boussinesq approach are compared with experimental data in Fig. 1. The LES data is generated with a grid of $\Delta x_g = \Delta y_g = 9\,\text{m}$ and $\Delta z_{g1} = 1.5\,\text{m}$. It can be observed, that the analytical normal stresses are constant, whereas experimental and LES values decrease with height. The LES does predict the lateral and vertical stress as well as the vertical momentum flux of medium roughness well. The stream-wise normal stress is overestimated, though the slope is well met. For higher roughness $u'u'$ is in better agreement with the measurements, but on the other hand the lateral and vertical stresses are slightly underestimated. It can be seen, that $u'u'$ and $v'v'$ of (4) is in good comparison with the measurements, whereas the vertical flux is highly underestimated. Overall the Boussinesq approximation produces estimations for the Reynolds-stresses comparable with a LES. The influence of using LES or (4) for the generation of the Reynold-stresses as input data for the TG is discussed in section 3.
For the used synthetic inflow generation techniques different integral turbulent length scales L_{ij} must be provided. Whereas TG2 and TG3 use the height dependent normal components L_{11}, L_{22} and L_{33}, all nine components of L_{ij} for only one height ($L_{ij}(z = 15\,\text{m})$ was used in this study) must be supplied for the employed implementation of TG1. Various formulations for the estimation of L_{ij} are known for the atmospheric boundary layer. In this study the approach of [30] is used, which is based on the review of several publications of wind tunnel and open field measurements

$$L_{11}^{\text{Cou}}(z) = L_{11} = C z^{1/n}, \tag{8}$$

where C and $1/n$ can be read from Fig. 13 in [30]. This formula is valid for heights of $10\,m \leq z \leq 240\,m$. Measurements above 240 m indicate that L_{11} decrease with further increase of height, which is supposed to be caused by a decreasing intermittency factor (whereas a boundary layer height of 600 m is assumed) [30]. In the region below 10 m a rapid decrease of L_{11} with decrease of height can be assumed, due to the proximity of the ground, which can be included as linear interpolation to $L_{11}(z = 0\,\text{m}) = 0\,\text{m}$.

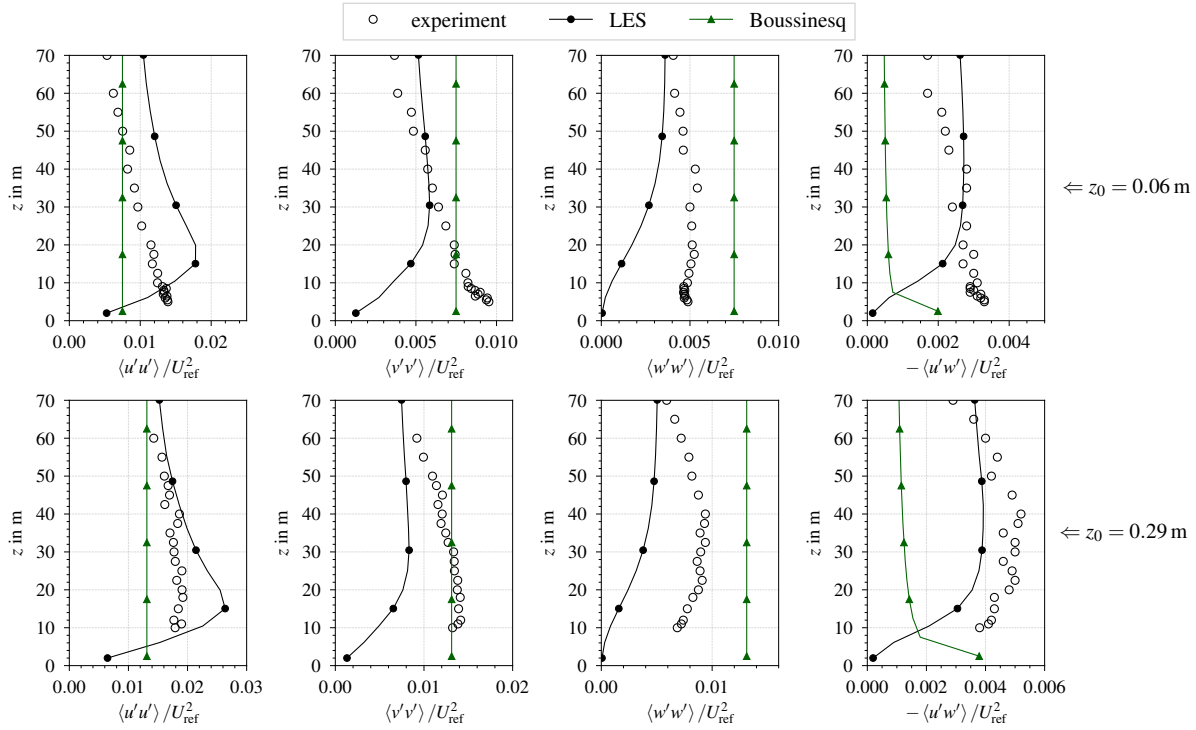

Fig. 1 Normalized profiles of the normal stresses $\langle u'u' \rangle$, $\langle v'v' \rangle$, $\langle w'w' \rangle$ and the vertical momentum flux $\langle u'w' \rangle$ of three approaches for $z_0 = 0.06\,\mathrm{m}$ (left) and $z_0 = 0.29\,\mathrm{m}$ (right).

Three other calculations of L_{11} are compared in [31] for different roughness heights. A comparison of all four approximations is shown on the left hand side of Fig. 2. The figure shows high differences between these four estimations. As [32] as well as [33] stated, an correct approximation is depending only on the roughness length is difficult. In this study the approximation of [30] is used for L_{11} with an additional rapid decrease in the surface region and constant L_{11} for $z > 0.4H$. The other turbulent length scales can be calculated with empirical formula as functions of L_{11} (shown in [31]). The increasing of the ratio between L_{11} and the other turbulent length scales, mentioned in [31], is neglected in this study.

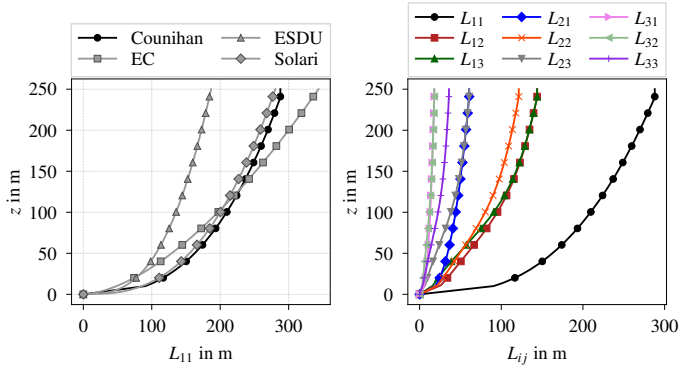

Fig. 2 Comparison of turbulent length scale profile (L_{11}) of various methods (left) and profiles of the used bundle of length scales L_{ij} (right) for a roughness height of $z_0 = 0.29\,\mathrm{m}$.

The simplest method introduced here is TG4, which superimposes a randomized signal on the mean velocity field by

$$U_i^n = (1-\alpha)\,U_i^{n-1} + \alpha\left(U_{\log} + s_i C_{\mathrm{rand}} U_{\log}\right), \tag{9}$$

where U_i^n and U_i^{n-1} are the current and previous instantaneous velocities, $U_{\log}$ is the mean logarithmic velocity, s_i is the fluctuation scale in the spatial direction i and C_{rand} is a random value in the range of $-0.5 \leq C_{\mathrm{rand}} \leq 0.5$. The weighting α between old instantaneous velocity and the randomized value is

chosen to be 0.1 here. The fluctuation scale in the three spatial directions is estimated from the measured velocity fluctuation at 15 m height with (0.14, 0.11, 0.09) and (0.19, 0.16, 0.12) for the medium and high roughness lengths, respectively. Note, that because there is a dependence of U_i^n on U_i^{n-1} the resulting signal is not correlated in space but in time.

2.2.3 Ground

For the simulation of atmospheric boundary layer flows wall modeled LES in combination with the Monin-Obukhov similarity theory (MOST) [34] is the commonly used boundary condition to calculate the surface Reynolds stress [35]. It includes the logarithmic law-of-the-wall and assumes constant turbulent fluxes in wall normal direction of the surface layer, which can "loosely estimated to be $\approx 10\%$ of the boundary-layer depth" [35]. One method to apply the MOST was proposed by [36] and improved by [37] (in the following denoted as Schumann-Grötzbach (SG) wall function). Due to the constant flux condition, using the first grid point as in the SG wall function is no requirement of MOST and according to [38], yields to an overestimation of the wind shear near the surface. Following [38] any height inside the surface layer can be used. Therefore [35] proposed a modified version of the SG wall function, implemented as

$$\nu_{t,w} = \frac{|\overline{\mathbf{U}}_e|^2\ \kappa^2}{\frac{\partial|\widetilde{\mathbf{U}}_1|}{\partial z}\left[\ln\left(\frac{z_e+z_0}{z_0}\right)\right]^2}\frac{|\widetilde{\mathbf{U}}_1|}{|\overline{\mathbf{U}}_1|} - \nu, \tag{10}$$

for the turbulent viscosity at the wall, where $|\overline{\mathbf{U}}_e|$ is the magnitude value of the horizontal averaged filtered velocity at the elevated height z_e and $|\overline{\mathbf{U}}_1|$ and $|\widetilde{\mathbf{U}}_1|$ are magnitude values of the horizontal averaged and the instantaneous filtered velocities in the first cell, z_0 is the surface roughness coefficient and ν is the fluid viscosity. Consistently, using the first grid cell in (10) yields to the formulation SG. In [38] a continuous reduction of the positive log-layer mismatch by setting the used cell from the first to the fifth cell was found, at which a convergence was achieved with the third grid point. Whereas [39] also got good results for the velocity profile over smooth walls with the third cell, Maronga et al. (2020) used the 7'th cell for their simulation of ABL flow over rough ground with the static Deardorff SGS model in their Parallelized Large-Eddy Simulation Model (PALM). In an preliminary investigation the influence of the elevated height was analyzed. The use of the SG wall function leads to high underestimations of the velocity in the near ground region. By taking the third grid cell, improved velocity profiles could achieved, whereas higher elevation heights have been found to yield to reoccurring under-predicted velocities.

2.2.4 Remaining boundary conditions

Periodic boundary conditions are employed on the lateral boundaries. At the top zero normal velocity and zero gradient tangential velocity as well as zero-gradient condition for all other variables is set. At the outlet a fixed value is given for the pressure whereas for the remaining variables zero-gradient boundary condition is used.

2.3 NUMERICAL SETTINGS

The described setup shall be used for the investigation of the propagation of neutral and dense gases inside a build-up area. Therefore we considered, for uniform comparison reasons, the filtered form of the general continuity equation (11), as well as the compressible Navier-Stokes equation (12) in the following form,

$$\frac{\partial\rho}{\partial t} + \boldsymbol{\nabla}\cdot\left(\rho\widetilde{\mathbf{U}}\right) = 0, \tag{11}$$

$$\frac{\partial\rho\widetilde{\mathbf{U}}}{\partial t} + \boldsymbol{\nabla}\cdot\left(\rho\widetilde{\mathbf{U}}\widetilde{\mathbf{U}}\right) = \boldsymbol{\nabla}p + \mu\nabla^2\widetilde{\mathbf{U}} - \boldsymbol{\nabla}\cdot\boldsymbol{\tau}_{\mathrm{SGS}} + \rho\mathbf{g}, \tag{12}$$

where ρ is the density, t is the time, p is the pressure, μ is the viscosity, $\mathbf{g}$ is the gravitational force vector. The energy equation are solved but not further considered here. The density and the viscosity of air are assumed to be constant. The subgrid-scale (SGS) stress tensor $\boldsymbol{\tau}_{\mathrm{SGS}} = \widetilde{\mathbf{U}\mathbf{U}} - \widetilde{\mathbf{U}}\widetilde{\mathbf{U}}$ is modeled with the one equation eddy-viscosity model proposed by [40],

$$\frac{\partial\rho k_{\mathrm{SGS}}}{\partial t} + \boldsymbol{\nabla}\cdot\left(\rho k_{\mathrm{SGS}}\widetilde{\mathbf{U}}\right) = \boldsymbol{\nabla}\cdot(\mu_{\mathrm{SGS}}\boldsymbol{\nabla}k_{\mathrm{SGS}}) + 2\mu_{\mathrm{SGS}}\widetilde{\mathbf{S}} - \frac{2}{3}\rho k_{\mathrm{SGS}}\mathbf{I} - \rho\epsilon, \tag{13}$$

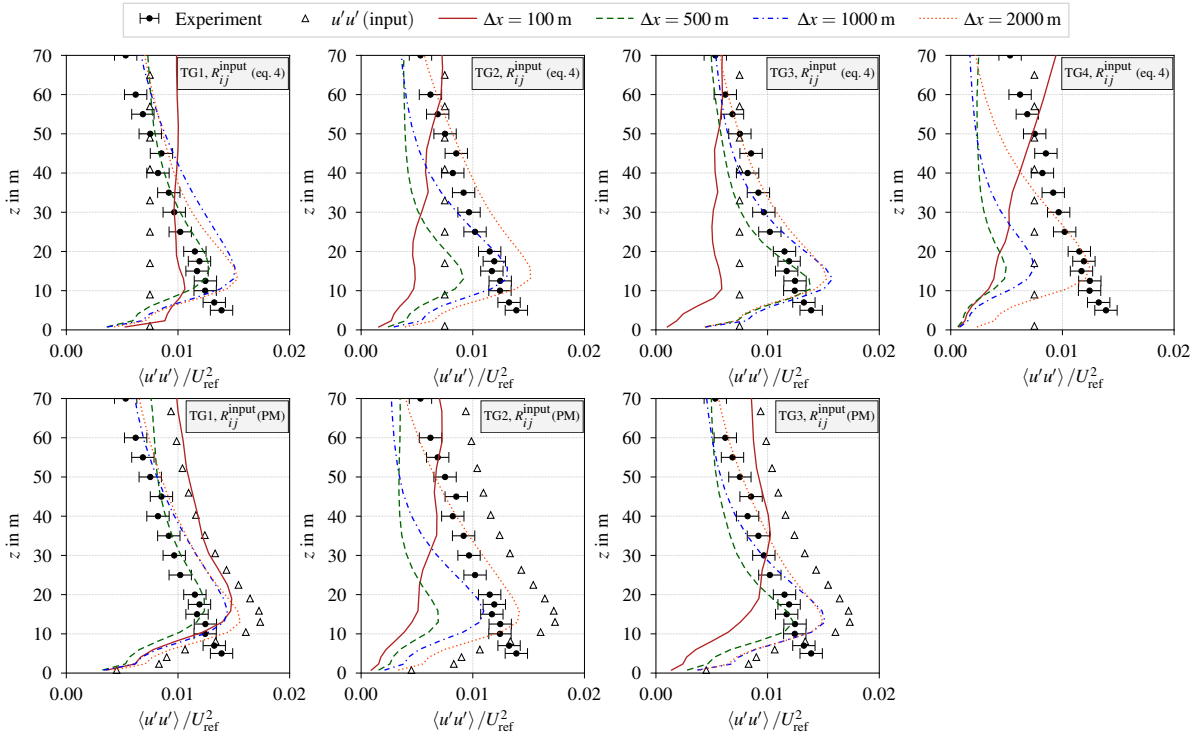

Fig. 3 Normalized normal stress in stream-wise direction of described inflow generators for MR and two methods of providing input Reynolds stress tensor, input is generated with RANS (left) and LES (right).

where $\epsilon = C_\epsilon k_{\mathrm{SGS}}^{2/3}/\Delta$ is the dissipation, $\mu_{\mathrm{SGS}} = C_k k_{\mathrm{SGS}}^{1/2}\Delta$ is the SGS eddy-viscosity and $\widetilde{\mathbf{S}}$ is strain rate tensor. The model constants are defined with $C_\epsilon = 1.048$ and $C_k = 0.094$.
For the pressure-velocity coupling, the PISO algorithm [41] with two pressure correction steps and a time step of 0.25 s is used. All cases are initialized with a velocity field of a previous LES of ABL with coarser grid resolution. The initialization time of every simulation is about 10 flow through times ($10H/U_{\mathrm{m}}$, where U_{m} is the mean velocity over the height) to ensure a developed turbulent boundary layer before starting the averaging. For statistical convergence a sampling of 104 flow through times is applied. Second order implicit backward differences scheme is used for temporal integration, while convection terms are discretized using second order scheme. For the divergence term a fixed blending of 90% second order linear and 10% second order upwind scheme is used for the velocity to avoid checker boarding, whereas the second order linear scheme is imposed for remaining variables.

3 RESULTS

The use of TG at the inlet of LES is often driven by the wish to decrease the numerical costs, which emerges from the decreased grid size upstream the investigated field, with simultaneously reproduce naturally developed turbulence as good as possible. Since none method of synthetic inflow generation can truly imitate the chaotic structure of a natural velocity field, a run-in phase is always needed. Besides the computational effort for calculating the velocity field, this additional length determines about the gain resulting from the use of TG.

3.1 COMPARISON OF INPUT REYNOLDS STRESS

As mentioned in section 2.2.2 two methods of generating the input Reynolds-stresses are applied and analyzed in this study. Regarding the velocity field the disagreement between the both methods is negligible. The influence on the distribution of the resolved normal stress $\langle u'u' \rangle$ and the resolved vertical momentum flux $\langle u'w' \rangle$ of TG1-TG3 in medium roughness conditions is shown in Fig. 3 and Fig. 4, respectively. Therefor vertical profiles are compared with measurement data and the particular input profiles (using Boussinesq approximation on the upper row and using a former LES with periodic BC on the lower row) for various distances to the inlet patch ($\Delta x = 100\,\mathrm{m}, 500\,\mathrm{m}, 1000\,\mathrm{m}$ and $2000\,\mathrm{m}$). The Δx depending

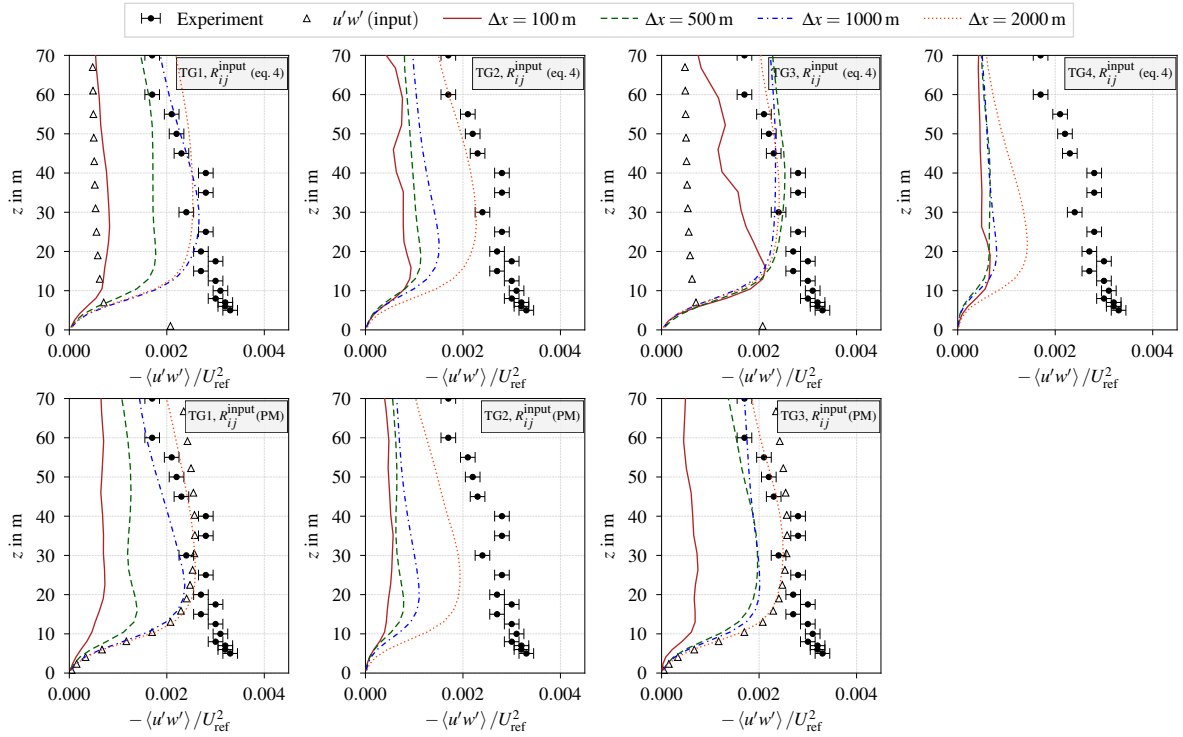

Fig. 4 Normalized vertical momentum flux described inflow generators for MR and two methods of providing input Reynolds stress tensor, input is generated with RANS (left) and LES (right) simulations.

distribution of the random inflow generator (TG4) is shown as well, at which no distinction is made due to the simple input method described in section 2.2.1. Generally, due to additional damping caused by nonphysical synthetic turbulence, $u'u'$ initially decreases downstream the inlet before it increases towards the profile of periodic boundary conditions, when the stresses of a prior LES is taken as input parameter. This damping varies depending on the synthetic method. Whereas only minor changes can be seen for TG1 and TG3, a major decrease occurs for TG2. For TG2 and TG3, this initial change towards lower values also takes place when (4) is used. It should be noted, that for all TG already 100 m downstream the inlet only minor differences exist between both input methods (eq. (4) or LES). In case of TG1 and TG3 the increase of $u'u'$ towards the cyclic profile takes place earlier and the profile at $\Delta x = 1000\,\mathrm{m}$ nearly matches the final one at $\Delta x = 2000\,\mathrm{m}$. It should be noted, that slightly underestimation compared to the profile of the PM remains even after 4000 m. Due to the random perturbations with no physical correlation to each other, the longest run-in length is found for TG4. Similar behavior can be observed with the lateral and vertical normal stresses.
The corresponding vertical momentum flux is shown in Fig. 4, where profiles for the input values are only presented for TG1, since the other two only use the normal stresses for the generation of the turbulent velocity field. It can be observed, that the input R_{ij} has only minor influence on the development of the vertical flux. In any case $u'w'$ collapses behind the inlet, though again TG1 and TG3 recover most quickly and nearly reach the values of PM after 1000 m. Remarkably is, that the profiles reaching a constant distribution faster when using R_{ij} values generated with the simple Boussinesq approximation as input parameter.
For $z_0 = 0.29\,\mathrm{m}$ the adaption towards a constant profile takes generally longer, though it is faster with using (4) then employing a prior LES with cyclic BC as input for the synthetic turbulence generators. Due to the much simpler approach and comparable results in the Reynolds stresses for both roughness lengths, eq. (4) is used in all following investigations.

3.2 VELOCITY PROFILE

In Fig. 5 the time averaged stream-wise velocity component $\langle U_x \rangle$ is shown for all used inflow generation techniques at various distances ($\Delta x = 100\,\mathrm{m}, 500\,\mathrm{m} and 2000\,\mathrm{m}$) from the inlet patch. The experimental

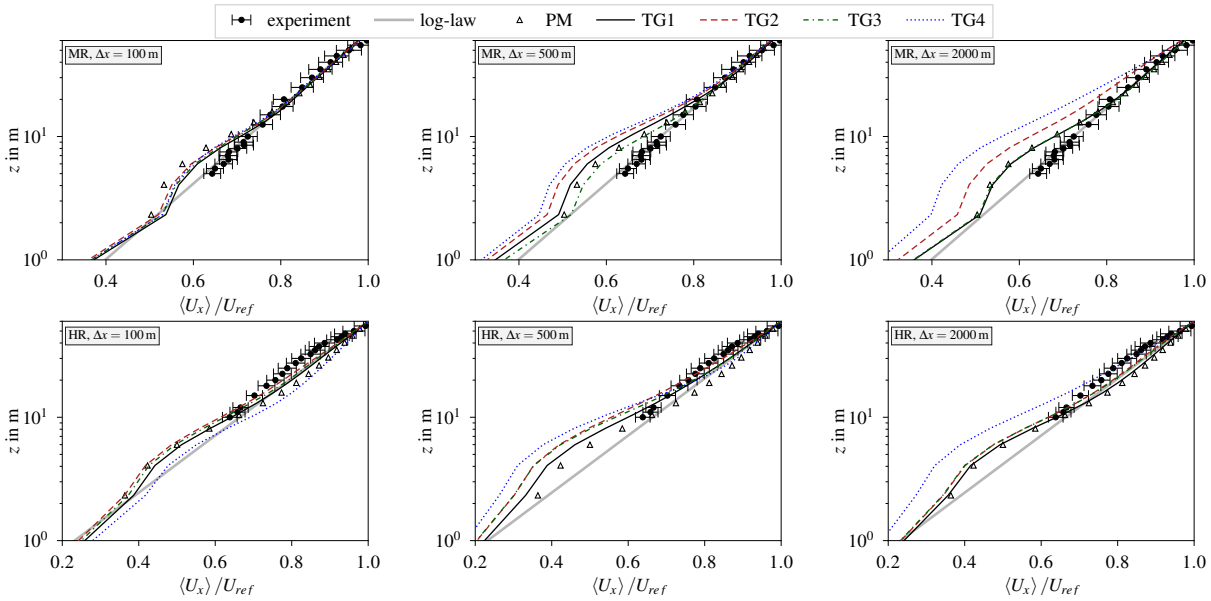

Fig. 5 Mean stream-wise velocity profile for 4 synthetic inflow methods and two roughness length (top: MR and bottom: HR) for four distances to the inlet ($\Delta x = 100\,\text{m}, 500\,\text{m}, 2000\,\text{m}$).

values, the theoretical logarithmic law of the wall and the profiles received with periodic boundary conditions (PM) are presented as well. First it should be noted, that the velocity profile of cyclic boundary conditions differs, especially in the ground region, from the logarithmic law. After the second grid point in wall normal direction $\langle U_x \rangle$ collapses for both shown roughness lengths and recovers not before the height reaches about 10 m to 20 m. This velocity distribution can also be seen in other publications using OpenFOAM such as [42]. With reducing the grading in vertical direction (coarser vertical resolution) this velocity break down is reduced, whereat instead $\langle U_x \rangle$ of the wall adjacent cell is highly underestimated. But by studying various vertical and horizontal resolutions as well as different elevation heights for (10) for both roughness lengths, we determined the here used setup as best compromise.
Nevertheless the ideal logarithmic profile is set at the inlet patch when using TG. A change in stream-wise direction to the profile of PM can therefore be expected. A quick change to lower velocities can be already seen after $\Delta x = 100\,\text{m}$. For the medium rough case the alteration of TG1 and TG3 to cyclic condition profile is nearly completed after 500 m, whereas TG2 and TG4 tend to further underestimate the velocities with increasing distance from the inlet up to a height of $z = 40\,\text{m}$. At the end of the domain ($\Delta x = 4000\,\text{m}$) a change towards the profile of periodic boundary conditions can be observed for all inflow methods (not shown here). It should be noted, that the order of reaching the converged state can be estimated with the sub-figure at $\Delta x = 2000\,\text{m}$. With higher roughness lengths the induced friction and therefor the influence on the velocity field increases. This can also be seen at the change of the velocity profiles. After $\Delta x = 500\,\text{m}$ the velocities of TG2-TG4 are significantly below the profile of cyclic boundary conditions and the profile of TG1 is close to the final one, but not yet converged, as in the case of medium roughness. As seen for medium roughness, TG4 massively underestimates the wind speed near the ground.At the end of the domain all profiles match the one of PM whereas the order of convergence is the same as with MR. One main fact identified with Fig. 5 is, that the alternation of the velocity profile strongly depends on the roughness length. For both studied roughness lengths TG1 needs the least and TG4 have the longest run-in length.

3.3 TURBULENCE SPECTRA

In Fig. 6 the spectra of the stream-wise velocity of the PM and all TG is shown for two heights in medium rough condition. The spectra is calculated with the stream-wise velocity component at one point over a time series of 115000 s with a time step of 0.25 s, which was divided in 20 parts and afterwards averaged to smooth the curves. The Energy spectra of PM follows the Kolmogorov $-5/3$ slope for about one order of magnitude. It can be seen, that with increasing distance to the ground ($z = 100\,\text{m}$) the energy

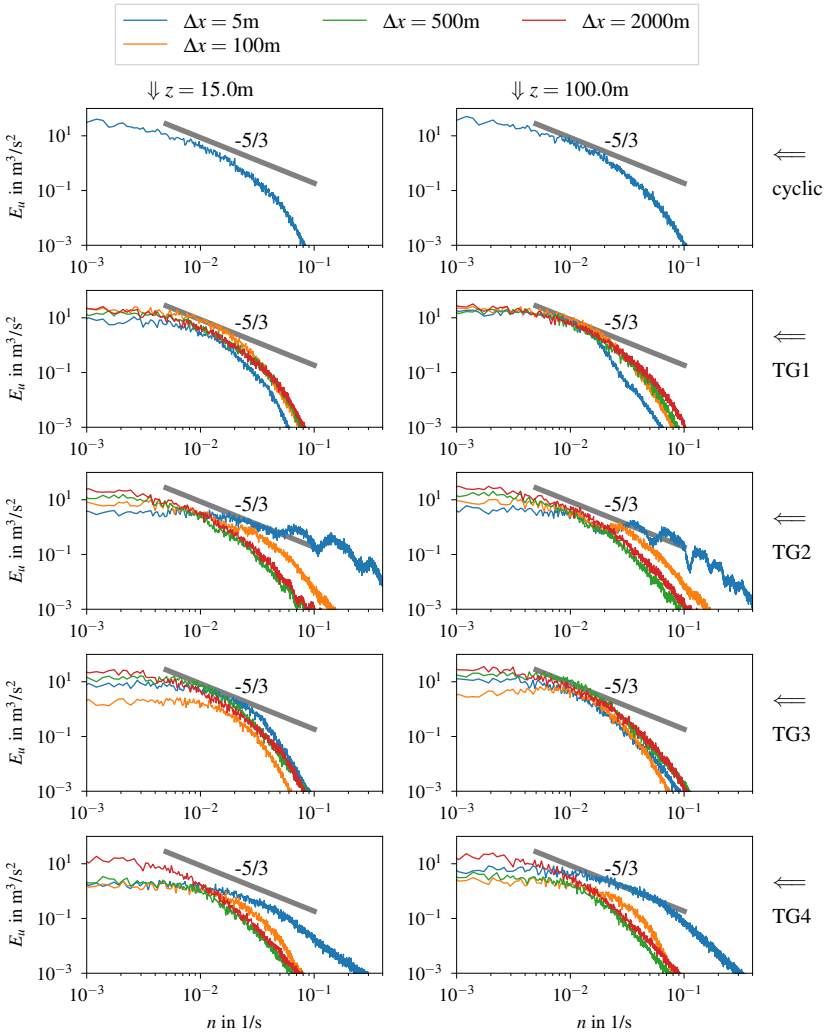

Fig. 6 Spectra of streamwise velocity.

content of the flow is slightly higher. With TG1 and TG3 the curves generated at the inlet ($\Delta x = 5$ m) are already close to spectra of the PM, which leads to a quick adaption in stream-wise direction. Whereas for TG3 a decrease of energy for low frequencies can be observed at $\Delta x = 100$ m, a minor increase is seen for TG1 at that position. After 500 m nearly the final energy progression is achieved. The spectra of TG2 shows periodical reduction for specific frequencies directly behind the inlet and overestimates the energy for high frequencies, which can also be seen for TG4. In both cases the energy quickly decreases (to be seen after $\Delta x = 500$ m). It should be noted that even after 2000 m the energy content of TG2 and TG4, especially at lower frequencies, is not converged to the final one, represented by the cyclic method. Corresponding to the profiles of $\langle U_x \rangle$ and the second order moments, the least variation of the spectra between inlet ($\Delta x = 5$ m) and further upstream positions is found for TG1 and TG3. Both TG produce a reasonable turbulent velocity field.

3.4 INTEGRAL LENGTH SCALES

Fig. 7 shows the lateral integral length scales L_{xx} in the first cell behind the inlet for TG1-TG4 as well as the respective input data. As described in section 2.2.2 the input length scales for the TG1 is given for one certain height (15 m), whereas for TG2 and TG3 a height dependent L_{xx} is used. It can be seen, that L_{xx} of TG1 is somewhat underestimated in the near ground region and matches the input values above 100 m. TG3 follows the specified curve reasonably well over the complete height, whereas TG2 shows increasing L_{xx} with height, whereat the values are considerably under-predicted. In case of the simple random generator (TG4) L_{xx} is almost constant over height, with values significantly below the other three TG. It should be recalled here, that the prescribed input length scales are approximations

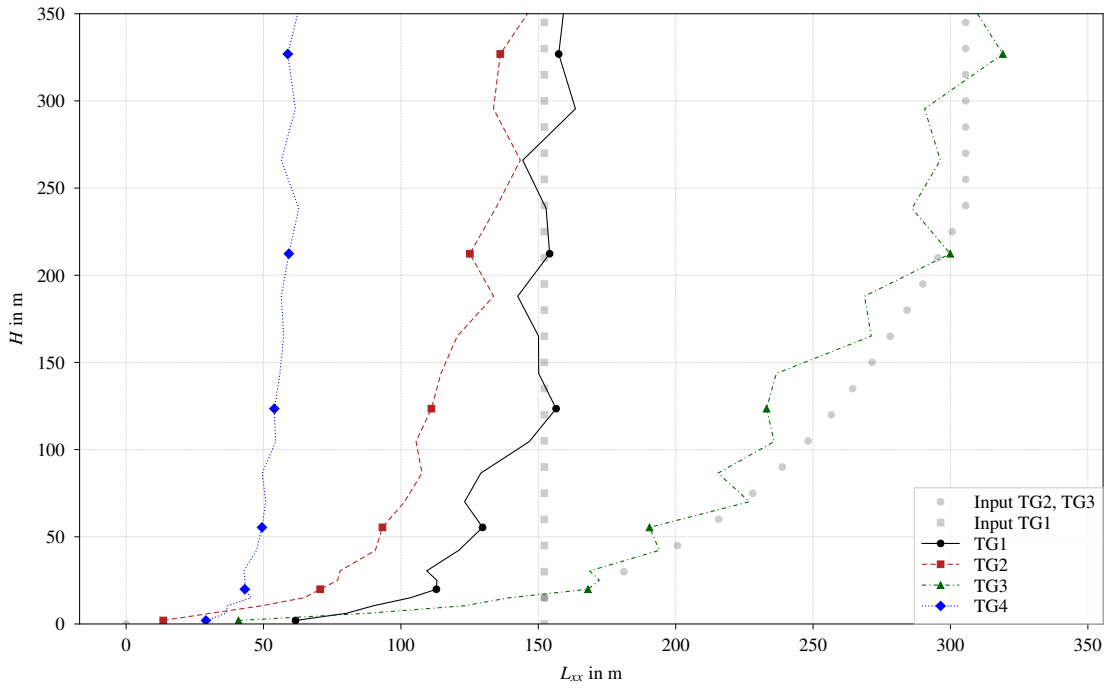

Fig. 7 Length scale L_{xx} at $\Delta x = 5$ m behind the inlet.

and are not in balance with the numerical solution. Thereby, similar to the shown velocity and second order moments profiles, L_{xx} is not constant in lateral direction. For both roughness lengths it initially decreases in case of TG1 and TG3, whereas the profile remains approximately constant for TG2 and TG3. The final profile is reached after

4 CONCLUSION

The simulation of rough atmospheric boundary layer flow was performed with periodic boundary conditions as well as four synthetic inflow generation techniques and compared to wind tunnel measurement data. Two variants of providing the input Reynolds stresses for the turbulence generators have been compared, where the results of the simple Boussinesq approach after 500 m in stream-wise direction were comparable with them of an LES with periodic boundaries for all TG. The run-in length of the synthetic methods have been analyzed with the alteration of the velocity profile, the stream-wise normal stress and the vertical momentum flux. Reasonable distinctions can be seen in the adaption speed between the TG as well as between the roughness lengths. Generally TG1 and TG3 reach the the final profiles of the periodic boundary condition first. Similar can be observed for the lateral velocity spectra, where the inlet spectra of TG1 and TG3 is already in good comparison with the naturally one of cyclic boundaries and therefore a quick adaption to the final curse can be observed. The lateral length scales at the inlet of TG1 and TG3 are in good comparison with the input profiles, whereas TG2 noticeably underestimates the prescribed L_{xx}.
In summery it can be said, that with using synthetic generated turbulence at the inlet, the inflow length of simulations examining e.g. the gas dispersion in an urban boundary layer can be significantly reduced without introducing major errors into the solution.

ACKNOWLEDGEMENTS

The IGF-Project No.: 20719 BG of the Research Association Society for Chemical Engineering and Biotechnology (DECHEMA), Theodor-Heuss-Allee 25, 60486 Frankfurt am Main, was encouraged via the German Federation of Industrial Research Associations (AiF) within the framework of the Industrial Collective Research (IGF) support program by the Federal Ministry for Economic Affairs and Energy

due to a decision of the German Bundestag.

REFERENCES

[1] Rob Stoll, Jeremy A Gibbs, Scott T Salesky, William Anderson, and Marc Calaf. Large-eddy simulation of the atmospheric boundary layer. *Boundary-Layer Meteorology*, 177(2):541–581, 2020.

[2] Nitin S Dhamankar, Gregory A Blaisdell, and Anastasios S Lyrintzis. Overview of turbulent inflow boundary conditions for large-eddy simulations. *Aiaa Journal*, 56(4):1317–1334, 2018.

[3] Xiaohua Wu. Inflow turbulence generation methods. *Annual Review of Fluid Mechanics*, 49:23–49, 2017.

[4] Henry G Weller, Gavin Tabor, Hrvoje Jasak, and Christer Fureby. A tensorial approach to computational continuum mechanics using object-oriented techniques. *Computers in physics*, 12(6):620–631, 1998.

[5] Andreas Bechmann and Niels N Sørensen. Hybrid rans/les applied to complex terrain. *Wind Energy*, 14(2):225–237, 2011.

[6] Ashvinkumar Chaudhari, Ville Vuorinen, Jari Hämäläinen, and Antti Hellsten. Large-eddy simulations for hill terrains: validation with wind-tunnel and field measurements. *Computational and Applied Mathematics*, 37(2):2017–2038, 2018.

[7] Markus Klein, Amsini Sadiki, and Johannes Janicka. A digital filter based generation of inflow data for spatially developing direct numerical or large eddy simulations. *Journal of computational Physics*, 186(2):652–665, 2003.

[8] L Di Mari, M Klein, WP Jones, and J Janicka. Synthetic turbulence inflow conditions for large eddy simulation. *Physics of Fluids*, 18(2):doi:10.1063/1.2130744., 2006.

[9] T Lund, X Wu, and D Squires. Generation of turbulent inflow data for spatially-developing boundary layer simulations. *Journal Computational Physics*, 140:233–258, 1998.

[10] Nicolas Jarrin, Sofiane Benhamadouche, Dominique Laurence, and Robert Prosser. A synthetic-eddy-method for generating inflow conditions for large-eddy simulations. *International Journal of Heat and Fluid Flow*, 27(4):585–593, 2006.

[11] Hannes Kröger and Nikolai Kornev. Generation of divergence free synthetic inflow turbulence with arbitrary anisotropy. *Computers & Fluids*, 165:78–88, 2018.

[12] N Kornev and E Hassel. A new method for generation of artificial turbulent inflow data with prescribed statistic properties for les and dns simulations. *Schiffbauforschung*, 42(4):35–44, 2003.

[13] AA Townsend. On the fine-scale structure of turbulence. *Proc. R. Soc. London*, Ser A(208):534, 1951.

[14] TS Lundgren. Strained spiral vortex model for turbulent fine structure. *Physics of Fluids*, 25:2193, 1982.

[15] DI Pullin and PG Saffman. Reynolds stresses and one-dimensional spectra for a vortex model of homogeneous anisotropic turbulence. *Physics of Fluids*, 6:1787–1796, 1994.

[16] ME Sergent. *Vers une methodologie de couplage entre la simulation des grande echelles et les modeles statistiques*. Ecole Central de Lyon, 2002. Ph.D. thesis.

[17] N Kornev and E Hassel. Method of random spots for generation of synthetic inhomogeneous turbulent fields with prescribed autocorrelation functions. *Communications in numerical methods in engineering*, 23(1):35–43, 2007.

[18] N Kornev, H Kroeger, and E Hassel. Synthesis of homogeneous anisotropic turbulent felds with prescribed second-order statistics by the random spots method. *Communications in numerical methods in engineering*, 24(0):875–877, 2008.

[19] Nikolai Kornev and Egon Hassel. Synthesis of homogeneous anisotropic divergence-free turbulent fields with prescribed second-order statistics by vortex dipoles. *Physics of Fluids*, 19(6):068101, 2007.

[20] P Saffman. Vortex interactions and coherent structures in turbulence. In *Proc. Symp. Transition and Turbulence in Fluids*. N. Y., Academic Press, 1981.

[21] R Poletto, T Craft, and A Revell. A new divergence free synthetic eddy method for the reproduction of inlet flow conditions for les. *Flow, turbulence and combustion*, 91(3):519–539, 2013.

[22] Zheng-Tong Xie and Ian P Castro. Efficient generation of inflow conditions for large eddy simulation of street-scale flows. *Flow, turbulence and combustion*, 81(3):449–470, 2008.

[23] Jian Zhong, Xiaoming Cai, and Zheng-Tong Xie. Implementation of a synthetic inflow turbulence generator in idealised wrf v3. 6.1 large eddy simulations under neutral atmospheric conditions. *Geoscientific Model Development*, 14(1):323–336, 2021.

[24] PJ Richards and RP Hoxey. Appropriate boundary conditions for computational wind engineering models using the k-ϵ turbulence model. *Journal of wind engineering and industrial aerodynamics*, 46:145–153, 1993.

[25] PJ Richards and SE Norris. Appropriate boundary conditions for computational wind engineering models revisited. *Journal of Wind Engineering and Industrial Aerodynamics*, 99(4):257–266, 2011.

[26] DM Hargreaves and Nigel G Wright. On the use of the k–ε model in commercial cfd software to model the neutral atmospheric boundary layer. *Journal of wind engineering and industrial aerodynamics*, 95(5):355–369, 2007.

[27] B En et al. Eurocode 1: Actions on structures-part 1–4: General actions-wind actions. *NA to BS EN, Brussels, Belgium*, 1991.

[28] Claës Dyrbye and Svend Ole Hansen. *Wind loads on structures*. 1997.

[29] Roland B. Stull. *An introduction to boundary layer meteorology*, volume 13. Springer Science & Business Media, 1988.

[30] JO Counihan. Adiabatic atmospheric boundary layers: a review and analysis of data from the period 1880–1972. *Atmospheric Environment (1967)*, 9(10):871–905, 1975.

[31] Marija Bervida, Luca Patruno, Samo Stanič, and Stefano de Miranda. Synthetic generation of the atmospheric boundary layer for wind loading assessment using spectral methods. *Journal of Wind Engineering and Industrial Aerodynamics*, 196:104040, 2020.

[32] Bao-Shi Shiau. Velocity spectra and turbulence statistics at the northeastern coast of taiwan under high-wind conditions. *Journal of Wind Engineering and Industrial Aerodynamics*, 88(2):139–151, 2000. International Conference on wind Engineering.

[33] R.G.J. Flay and D.C. Stevenson. Integral length scales in strong winds below 20 m. *Journal of Wind Engineering and Industrial Aerodynamics*, 28(1):21–30, 1988.

[34] AS Monin and AM Obukhov. Basic laws of turbulent mixing in the atmosphere near the ground. *Tr. Geofiz. Inst., Akad. Nauk SSSR*, 24(151):163–187, 1954.

[35] Björn Maronga, Christoph Knigge, and Siegfried Raasch. An improved surface boundary condition for large-eddy simulations based on monin–obukhov similarity theory: evaluation and consequences for grid convergence in neutral and stable conditions. *Boundary-Layer Meteorology*, 174(2):297–325, 2020.

[36] Ulrich Schumann. Subgrid scale model for finite difference simulations of turbulent flows in plane channels and annuli. *Journal of computational physics*, 18(4):376–404, 1975.

[37] Günther Grötzbach. Direct numerical and large eddy simulation of turbulent channel flows. *Encyclopedia of fluid mechanics*, 6:1337–1391, 1987.

[38] Soshi Kawai and Johan Larsson. Wall-modeling in large eddy simulation: Length scales, grid resolution, and accuracy. *Physics of Fluids*, 24(1):015105, 2012.

[39] Timofey Mukha, Mattias Johansson, and Mattias Liefvendahl. Effect of wall-stress model and mesh-cell topology on the predictive accuracy of les of turbulent boundary layer flows. In *7th European Conference on Computational Fluid Dynamics (ECFD 7), Glasgow, UK*, pages 323–334, 2018.

[40] Akira Yoshizawa. Statistical theory for compressible turbulent shear flows, with the application to subgrid modeling. *The Physics of fluids*, 29(7):2152–2164, 1986.

[41] Raad I Issa. Solution of the implicitly discretised fluid flow equations by operator-splitting. *Journal of computational physics*, 62(1):40–65, 1986.

[42] Beatrice Giacomini and Marco G Giometto. On the suitability of second-order accurate finite-volume solvers for the simulation of atmospheric boundary layer flow. *Geoscientific Model Development*, 14(3):1409–1426, 2021.

Identification and Analysis of vortical structures over an airliner's wing-fuselage junction

Stylianos Adamidis[1, 2], Nicholas C. Markatos[1, *]

[1]*National Technical University of Athens, Athens, Greece*
[2]*Hellenic Air Force, Athens, Greece*
** Corresponding Author: n.markatos@ntua.gr*

Turbulence and flow disturbances occurring at the wing-fuselage junction of aircraft cause a drop in its aerodynamic performance and an increase in the aircraft's drag force. The main objective of this work is to study the junction flow's characteristics and the vortices, which dominate such flows. The flow condition corresponds to 5 degrees angle of attack with freestream Mach number of 0.189 and a Reynolds number based on the root chord of 2.43 million. The study is carried out using LES computational modeling and various sub-grid models. Specifically, this research study proposes a new junction flow parameter employed, in combination with the existing ones, in order aircraft designers to be able to assess more efficiently the horseshoe vortex behavior on the junction designs; and it is focused on the junction flow's and its vortices' characteristics, under the prism of vortices' structure formation and the flow patterns.

It is a fact that the majority of the junction flow studies focus on the horseshoe vortex considering it as the dominant vortex structures and many modern studies investigate the corner separation formation. The current study verifies the former vortices domination on these flows, but it also gives a more extended view, showing that all the vortex structures interact among themselves and form the junction flow regime.

Vortex Dynamics Effects on the Development of a Confined Wake and a Channel Flow in a Rectangular Duct Under Identical Inlet Flow Conditions

Ioannis Kalogirou*

Laboratory of Heating-Cooling & Refrigeration Dept of Mechanical Engineering Univ. of Peloponnese, Patras, Greece
** Corresponding Author: kalogirou@uop.gr*

A circular cylinder turbulent wake developing in a confined flow environment, corresponding to a blockage ratio of 14%, has been studied experimentally in a wind tunnel comprising a parallel section followed by a constant area distorting duct. Near field measurements indicate that the confined wake exhibits to a certain extent similarity to the unbounded case with some differences, the most important being the modification of the Kármán Street topology. Further downstream, the confined wake velocity distributions demonstrate resemblance to channel flow behavior. Comparison of bounded wake and channel flow measurements, (taken in the absence of the cylinder), both obtained in the same apparatus under identical inlet flow conditions, has been also carried out. This procedure serves to elucidate the influence of near field formation dynamics on the far field structure with and without the presence of a bluff-body.

Wake measurements covered the Reynolds number range, (based on the cylinder diameter d), of $1.9x10^3 \leq Re_d \leq 1.5x10^4$. Some additional measurements were taken in the absence of the cylinder, (channel flow), at Re_h=15630, h=21 mm being the channel half height. Here three-dimensional quantitative wake and channel flow data for Re_d=4300 and Re_h=15630 respectively, both obtained with the same free-stream centreline velocity U_r=11.25 ms^{-1}, are presented. Additionally, qualitative results (flow visualisation) for the confined wake at Re_d=760 are presented.

Fig. 1: Visualization of the near vortex street in the region x_1/d=0-26.

A general view of the near wake region is shown in Fig. 1. A characteristic of the confined wake is the observed transposition of vortices. An upward movement of counterclockwise vortices with positive circulation to the upper midplane of the flow occurs. Simultaneously, countermotion of eddies with negative vorticity across the symmetry axis towards the lower half of the street takes place.

The vortex street reversal described above controls the evolution of the confined wake flow. The obtained near field mean profiles, shown in Fig. 2, exhibit "velocity deficit" distributions do not persist indefinitely. For x_1/d>60 the mean velocity distributions differ markedly from those attained in the near wake region. Figure 3 compares a distant confined wake mean velocity profile with a corresponding channel flow one, under identical inlet flow conditions. Figure 4 shows autocorrelation functions for bounded wake and channel flow as well. The changes observed in the two latter figures are attributed to basic differences in the vortex dynamics prevailing in the respective flow cases.

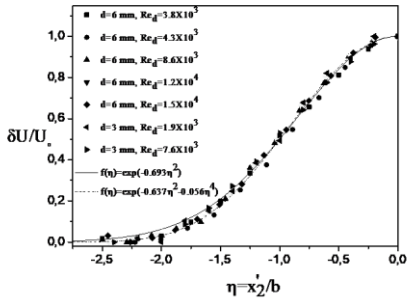

Fig. 2: Near wake similarity.

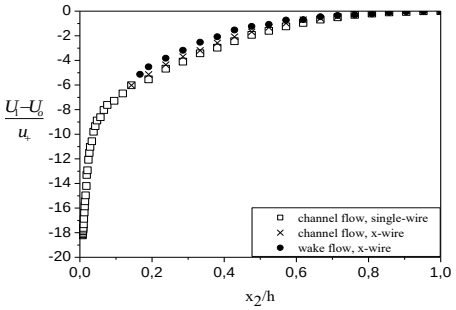

Fig. 3: Mean streamwise velocity distributions for confined wake and channel flow close to the end of the parallel section, (x_1/d=119.3), in channel coordinates.

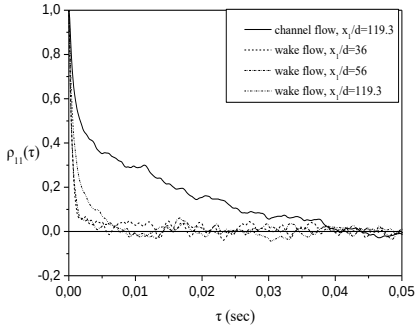

Fig. 4: Off-axis, (x_2/h=0.71), autocorrelation functions of the streamwise velocity fluctuations for confined wake and channel flow along the parallel section.

References

[1] Taniguchi, S. and Miyakoshi, K. Fluctuating fluid forces acting on a circular cylinder and interference with a plane wall. Experiments in Fluids, 1990, 9:197-204.

Article S7.4

The Numerical Simulation of the Vortex Shedding Flow from Two Circular Cylinders of the Parallel Arrangement in the Lock-in State in the Different Mode

Yoshifumi Yokoi[1*]

[1]*National Defense Academy of Japan, 1-10-20 Hashirimizu, Yokosuka, Japan*
** Corresponding Author:yokoi@nda.ac.jp*

ABSTRACT

This study carries out the numerical simulation of the interference vortex flow when varying the interval of two circular cylinders in a natural lock-in state (Karman vortex shedding) and two kinds artificial lock-in state (alternate vortex shedding and simultaneous vortex shedding) using a vortex method. The purpose of this research is to investigate the mutual interference flow characteristic from the circular cylinder in mutually different lock-in mode. It is the enjoyment of this study to investigate how the artificial lock-in state influences the natural lock-in state (Karman's vortex discharge). It is very interesting to know how the vortex flow in which it interfered will change. It was found that the alternate vortex shedding type lock-in receives interference by cylinder arrangement. In the case of such a complex state, it became clear to completely differ from the result obtained when the aspect and fluid force of the flow are single.

KEYWORDS: Vortex, Numerical Simulation, Lock-in, Two Circular Cylinders, Parallel Arrangement

1. INTRODUCTION

If a circular cylinder is placed into a steady flow without a time change, vortices will be discharged alternately. And a Karman vortex street is formed behind the circular cylinder. The Karman vortex is a very stable vortex street, and the vortex corresponding to the flow velocity is formed. That can also be said to be a natural synchronous phenomenon. Many of flows which exist really are what are called unsteady flow to which velocity is changed in time. When unsteady, it is thinkable that the characteristics of the phenomenon differ compared with the case of being steady. It is industrially important to grasp the fluid force characteristic and the vortex shedding characteristic of the object put on the unsteady flow field. However, in order to realize an unsteady flow with sufficient accuracy, serious troubles are required in a laboratory. In order to experiment simple, in the laboratory, the object which exercises in the direction of the flow was installed into the steady flow, so the relative unsteady flow is made. If the circular cylinder which is oscillating in the flow is placed, the vortex shedding which synchronized with circular cylinder oscillating frequency will be observed. This phenomenon was called "lock-in phenomenon" and, as for this "interference of the flow velocity change", research has been done by many researchers [1 - 4]. The flow pattern in the lock-in state is divided roughly into the "alternate vortex shedding type" and the "simultaneous vortex shedding type". On the other hand, when a structure is in the flow independently, it is rare, and it consists of two or more objects in many cases. Therefore, it is also important to investigate "interference by arrangement". As fundamental research, there are many research of interference of two circular cylinders and many presented results [5 - 9].

In recent years, by an author's research consortium, research which combined "interference of the flow velocity change" and "interference by arrangement" is done, and "interference by arrangement" has reported obtaining the result which changes with influences of "interference of the flow velocity change" [10 - 12]. However, there are many strange portions. Not all the structural rigidity of the structure is same and differing separately is common. That is, even if it is in the same cross-sectional

form, structural rigidity differs, and character frequency also differs. Even if this is placed under the same flow velocity, it can consider causing the lock-in where each differs. It is one of the most interesting things in related research. The purpose of this research is to investigate the mutual interference flow characteristic from the circular cylinder in mutually different lock-in mode. It is the enjoyment of this study to investigate how the artificial lock-in state influences the natural lock-in state (Karman's vortex discharge). It is very interesting to know how the vortex flow in which it interfered will change. The research was carried out by numerical simulation by use of vortex method.

2. NUMERICAL CALCULATION

2.1 CALCULATION APPARATUS AND METHOD

The numerical experiment apparatus was consisted of simulation software and a notebook type computer (NEC; LaVie LC958/T) as calculation hardware which are on the market. The software which named 'UzuCrise 2D ver.1.1.3 rev.H (College Master Hands Inc., 2006)' is used. This software used the vortex method which is based on the Lagrangian analysis. Since the vortex method is the grid-less method, it is suitable for the unsteady problem of such moving boundary. The vortex method is a direct viscid-inviscid interaction scheme, and the emanation of velocity shear layers due to boundary layer separation is represented by introduction of discrete vortices with viscous core step by step of time. In the present study, the flow was assumed incompressible and two-dimensional flow field. The configuration of circular cylinder was represented 40 vortex panels using a boundary element method. The separating shear layers were represented the discreet vortices, which were introduced at the separation points. The details of calculation technique of vortex method and accuracy of calculation are shown in Kamemoto [13, 14]. As example computation, the aspect of the vortex shedding flow from a stationary circular cylinder and the aspect of the vortex shedding flow from an in-line oscillating circular cylinder are shown in reference [15, 16].

2.2 CALCULATION CONDITIONS AND PARAMETERS

In the present study, the calculations were performed at the two-dimensional flow field for incompressible and viscous flow. Two circular cylinders have been arranged right-angled to the flow. Here, the circular cylinder located in left-hand side toward the flow was called the 1st circular cylinder, and the circular cylinder located in right-hand side toward the flow was called the 2nd circular cylinder. The arrangement of circular cylinders is shown in Fig. 1. The cylinder diameter d and the main flow velocity U were determined as 16 mm and 0.04 m/s so that it could compare with the previous experimental result [10]. Here, the diameter of two circular cylinders is the same. Since water is assumed as for test fluid, Reynolds number Re becomes 500. Every calculation continued to until non-dimensional time $T = 200$.

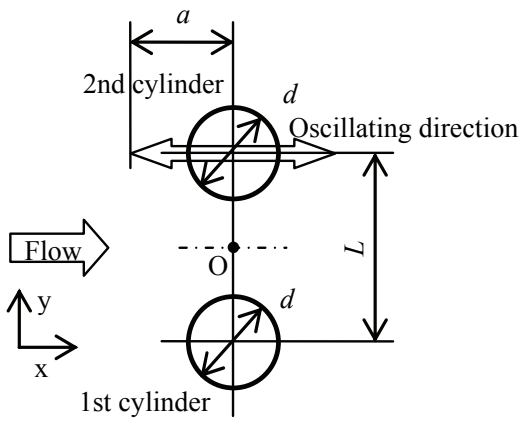

Fig. 1 Coordinate system and definition of symbols (O: the coordinate origin)

The main parameters of numerical experiment were the existence of oscillation, the oscillation frequency ratio f/f_K, the oscillation amplitude ratio $2a/d$ and the distance ratio L/d. Existence of the oscillation is 2 kinds and they are in the states of cylinder stationary and cylinder oscillation. The oscillation is given only to the 2nd circular cylinder and the 1st circular cylinder is in a fixed state. The oscillating frequency ratio f/f_K is 2 kinds and they are in two typical lock-in states of the single oscillating circular cylinder obtained from the previous experimental result. As for the oscillating frequency ratio, f/f_K = 1.4 and f/f_K = 2.4 were used. (Here, as for the natural Karman vortex shedding frequency, previous calculation result f_K = 0.6489 Hz [15, 16] was used.) The oscillation amplitude ratio $2a/d$ is 2 kinds, and they are 0.25 and 0.50, respectively. The distance ratio L/d is 5 kinds and they are 1.5, 2.5, 5.5, 10.0 and 20.0.

3. CALCULATION RESULTS

3.1 STATIONARY CASE

In order to investigate the influence of circular cylinder installation interval, the interval of stationary two circular cylinders was varied and calculations were performed. It is known that mutual interference will become large and the aspect of the flow will change as the distance ratio becomes small. Although well known about the variation of vortex shedding, it is scarcely known about the variation of fluid force which acts on the body at the time. So, it is very interesting to investigate the variation of the aspect of the flow and the variation of fluid force. The calculation result carried out for every distance ratio is shown in Fig. 2. Here, since the variation was not seen when the distance was separated enough, in the case of L/d = 20, it has omitted. The flow pattern, the time history of drag coefficient, and the time history of lift coefficient are shown in the figure, respectively. All flow patterns show the instantaneously aspect at the time of non-dimensional time T = 200. In those figures, a lower side circular cylinder is "the 1st circular cylinder", and an upper side circular cylinder is "the 2nd circular cylinder." The time histories of those fluid force are shown from the non-dimensional time T = 100 to the non-dimensional time T = 200. An abscissa is the non-dimensional time. The ordinate is drag coefficient C_D and lift coefficient C_L. It can be seen that the flow is changing as the distance ratio L/d becomes smaller. When the distance ratio L/d is comparatively large (L/d = 10 and L/d = 5.5), the vortex shedding from each circular cylinder has been independent, and the Karman vortex is respectively formed in the wake. The relationship of the oscillating period of the drag coefficient and the lift coefficient is drag 2 period to lift 1 period, and is the same as the case of the single circular cylinder. The magnitude of each waveform amplitude was also the same. This has brought a calculation result which expresses the experimental result of a previous report well. It is known that a biased gap flow appears at the distance ratio of L/d = 2.5. However, if the flow pattern shown in Fig. 2 (c) is seen, the vortex is discharged in the direction of down-stream from each circular cylinder, and the biased gap flow which is seen in the experiment is not seen. However, the direction of the flow changes due to the interference between the vortices emitted from about $5d$ behind the cylinder, and it seems that the biased gap flow is formed. In the waveform of fluid force, the same tendency is seen and the amplitude is also comparable. However, offset is seen have occurred in the lift fluctuation waveform of both of circular cylinders. Here, the "offset" is the difference of the waveform average value (C_{DAVE} = 1.0757 and C_{LAVE} = 0.0018) of the single circular cylinder, and the waveform average value of each circular cylinder at the time of two cylinder arrangement. The 1st circular cylinder is offset to the minus side, and the 2nd circular cylinder is offset to the plus side. It is considered that the influence of the interference between the vortices is fed back to the pressure on the surface of the cylinder, causing the offset in the lift fluctuation waveform of each cylinder. It is thought that the presence of the offset disrupts the balance of lift between the two cylinders and causes the biased gap flow. In this calculation, the lift amplitude and offset amount were similar in both cylinders, so it is probable that no biased gap flow occurred in the vicinity of the cylinders. Moreover, when the flow pattern was investigated for every progress of time, the interference position of vortexes seemed to approach circular cylinders gradually. From this, it can be inferred that additional calculation time is required for the biased gap flow to occur immediately after the two cylinders. At the distance ratio L/d = 1.5, both the flow pattern and the fluid force waveform show complicated aspects. Before the separating shear layer discharged from two circular cylinders,

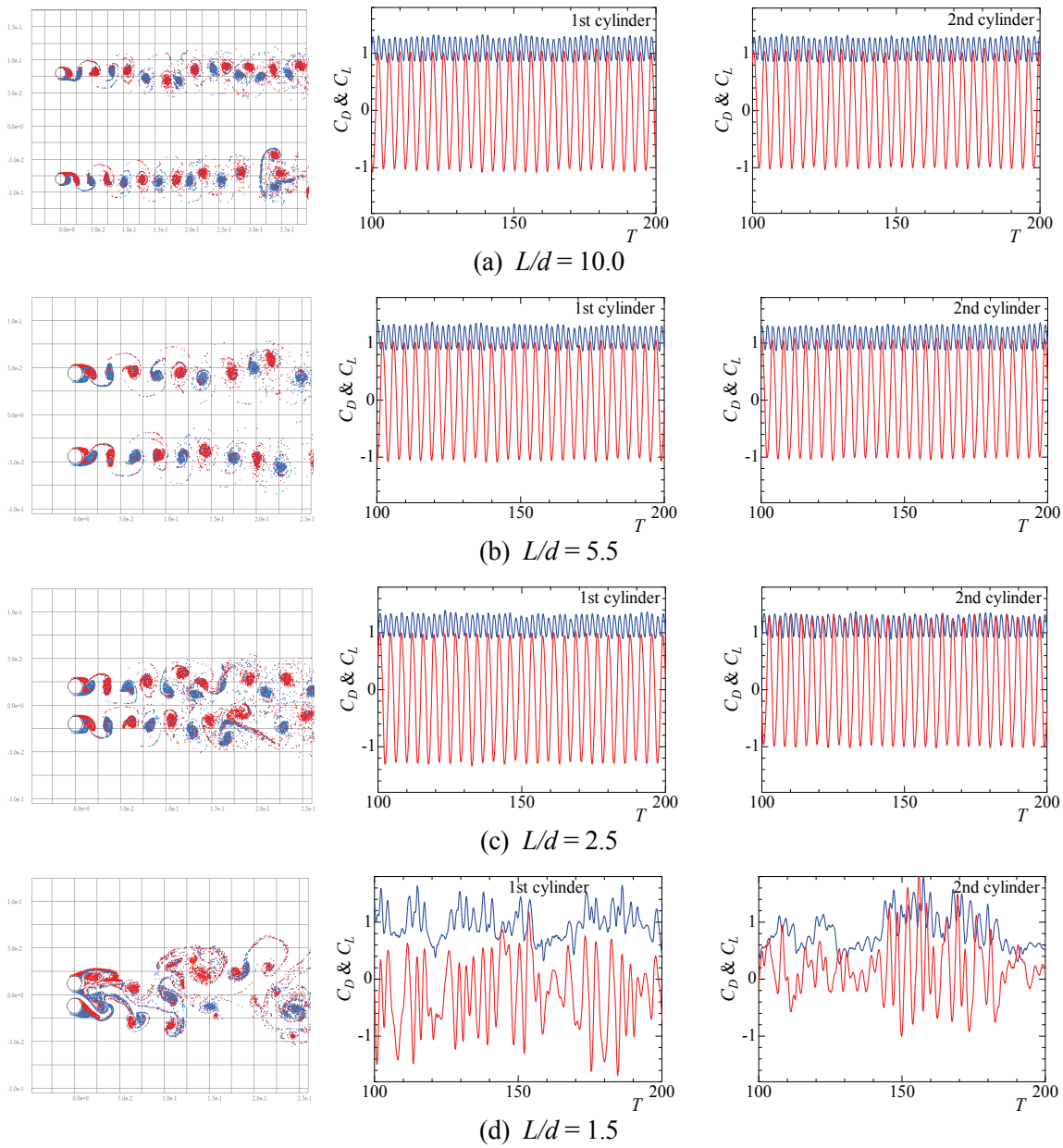

Fig. 2 Instantaneous flow feature at the time T = 200 and time histories of drag and lift coefficients

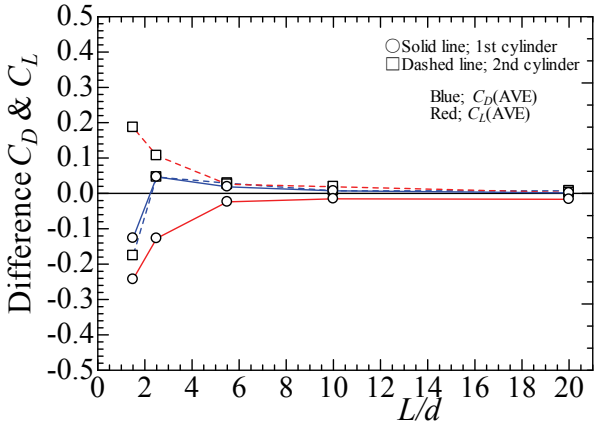

Fig. 3 The variation of the amount of offset for every distance ratio; combination of stationary 1st circular cylinder and stationary 2nd circular cylinder

respectively constitutes a vortex, it is unified, and it forms the large-scale oscillating flow. When the neighborhood of two circular cylinders is seen carefully, it seems that the biased gap flow has occurred. A discrete vortex group in which the negative circulation is dominant is formed at a position about 5*d* behind the cylinder, and a discrete vortex group in which the positive circulation is dominant is formed at a position about 9*d* behind the cylinder. In the waveform of fluid force, the periodicity of oscillation can be seen lost. It can be seen that the amplitude is not constant. Here, it is an interesting discovery that the times when the period of the waveform is uneven and the amplitude is large or small are different between the cylinders. Since the biased gap flow is near the two circular cylinders, it is imagined that the waveform of each fluid force of the 1st circular cylinder and the 2nd circular cylinder has remarkable offset, and both magnitude differs. In the waveform of the lift coefficient, the offset can imagine producing in the minus side with the 1st circular cylinder, and producing it in the plus side with the 2nd circular cylinder.

Figure 3 shows the amount of offset between the average drag coefficient (blue color in the figure) and the average lift coefficient (red color in the figure) for each distance ratio. An abscissa is a distance ratio and an ordinate is each amount of offset. The circle solid line in the figure shows the data of the 1st circular cylinder, and the square mark dashed line shows the data of the 2nd circular cylinder. Here, the value of the zero in the ordinate means the value of the single circular cylinder. About the drag coefficient, the amount of offset can be seen increasing as the distance ratio becomes small. When the distance ratio is L/d = 1.5, it shifts to the minus side, and the offset amount differs between the 1st circular cylinder and 2nd circular cylinder. It means that thrust has produced the drag of minus. It is very interesting that interference of the vortex leads to drag reduction. On the other hand, about a lift coefficient, the amount of offset can be seen increasing gradually as the distance ratio becomes small, but a variation rapid in the amount of offset is seen from distance ratio L/d = 2.5. Although distance ratio L/d = 5.5 have symmetry in the amount of offset, they can read that the symmetry has also collapsed in L/d = 2.5. It was found that the amount of offset of the 1st circular cylinder is larger than the amount of offset of the 2nd circular cylinder.

3.2 ALTERNATE VORTEX SHEDDING MODE OSCILLATION CASE

It is one of the most interesting matters of this study to investigate the mutual interference of the vortex shedding from two circular cylinders in different lock-in mode. The mutual interference flow was investigated with the 1st circular cylinder in stationary state and the 2nd circular cylinder oscillating in the flow direction. The aspect of flow when the 2nd circular cylinder oscillates in alternate vortex shedding lock-in mode (f/f_K = 1.4, $2a/d$ = 0.5), and the time history of each circular cylinder are shown in Fig. 4. When the distance between circular cylinders is large (L/d = 20.0 and L/d = 10.0), the mutual interference is considered to be very little like the case of two stationary circular cylinders. At the distance ratio of L/d = 5.5, it is shown that the natural Karman vortex shedding is performed from the 1st circular cylinder and the alternating vortex shedding type lock-in vortex shedding is performed from the 2nd circular cylinder without interfering with each other. Moreover, it is recognized in each cylinder that there is no change in the period of lift fluctuation due to vortex shedding, as in the case of large distance ratio. Mutual interference occurs in distance ratio L/d = 2.5, and the flow shows the complicated aspect. Since it is expected that offset has occurred in the minus side to the lift coefficient waveform of the 1st circular cylinder, it is imagined between two circular cylinders that the biased gap flow has occurred in the direction of the 1st circular cylinder. It is an interesting occurrence that the biased gap flow occurs also in the combination of the oscillating circular cylinder and stationary circular cylinder. From the time history of the fluid force, there is no change in the lift fluctuation cycle of the oscillating 2nd circular cylinder, but there is a change in the lift fluctuation cycle of the stationary 1st circular cylinder. This shows that an assailant is the 2nd circular cylinder and a victim is the 1st circular cylinder. In distance ratio L/d = 1.5, the aspect of a compound single vortex street that the vortex is discharged from one circular cylinder is seen. Since the vortex shedding is interference of lock-ins carried out alternately, it is expected that those fusion is carried out easily and the clear wake vortex is made. In the lift fluctuation waveforms of both cylinders, the offset can be seen on the minus side in the 1st circular cylinder, and the offset can be seen on the plus side in the 2nd circular cylinder. There is no surge in the lift fluctuation waveform of

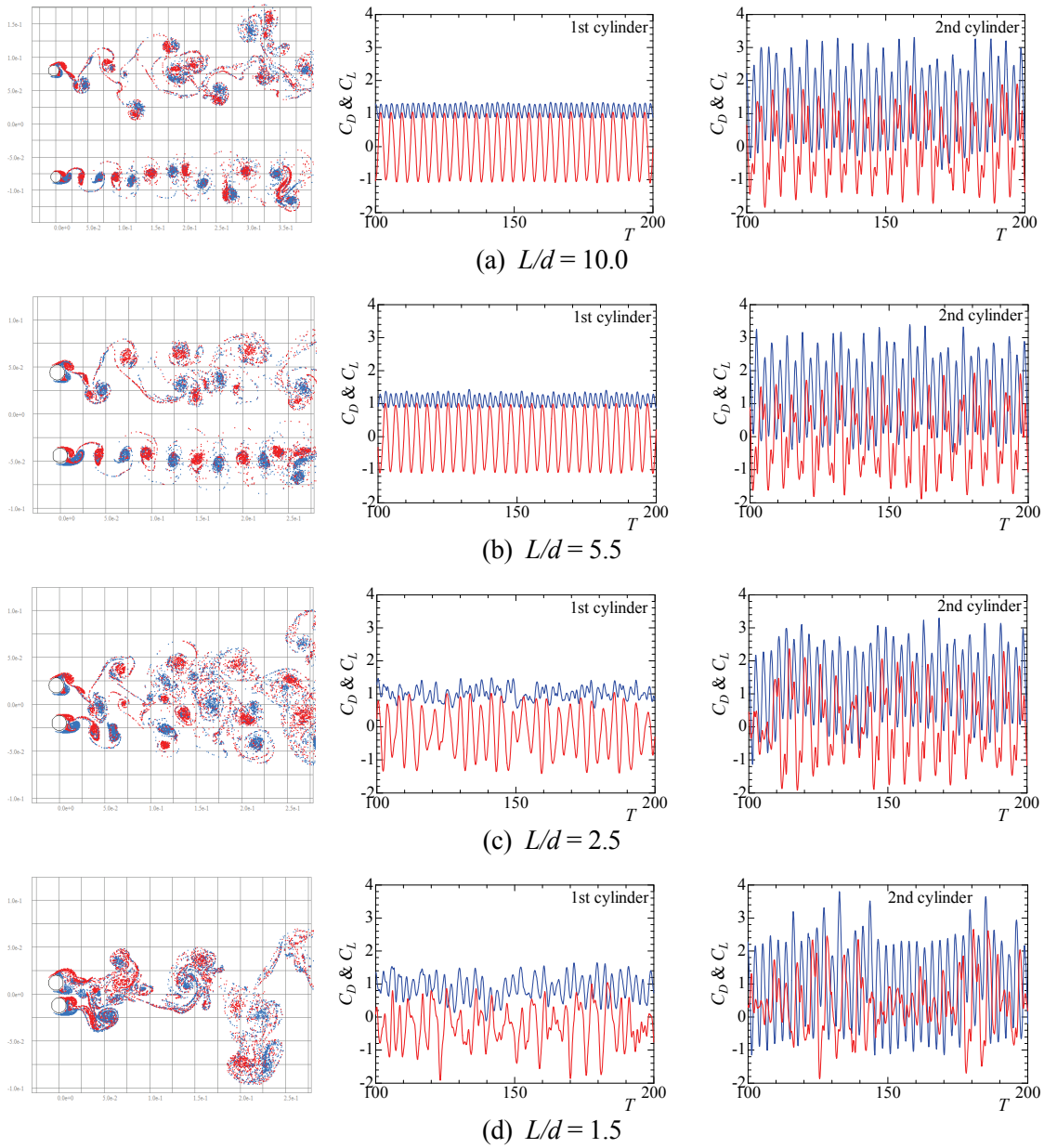

Fig. 4 Instantaneous flow feature at the time T = 200 and time histories of drag and lift coefficients

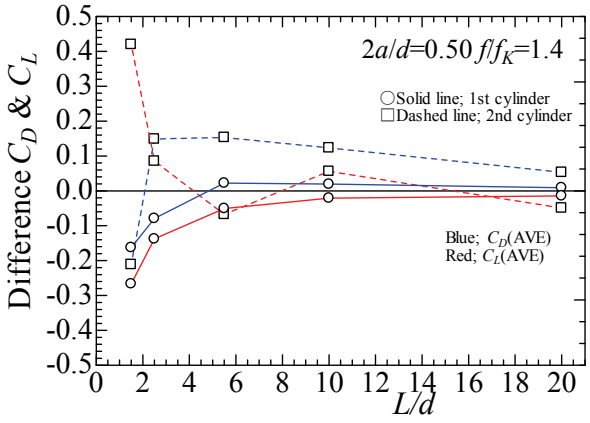

Fig. 5 The variation of the amount of offset for every distance ratio; combination of the stationary 1st circular cylinder and the 2nd circular cylinder of alternate vortex shedding lock-in oscillation

the 1st stationary circular cylinder so much. On the other hand, the surge has occurred in the lift fluctuation waveform of the 2nd oscillating circular cylinder. It is interesting that the influence is rebounding upon the affecting side.

Figure 5 shows the amount of offset of the average drag coefficient (blue color in the figure) and an average lift coefficient (red color in the figure) for every distance ratio. The abscissa is the distance ratio and the ordinate is each amount of offset. Here, the reference value of the oscillating 2nd circular cylinder is the average value of the waveforms of the single vibrating cylinder (C_{DAVE} = 1.1751 and C_{LAVE} = 0.0278). The amount of offset of the lift coefficient of the 1st circular cylinder can be seen increasing to the minus side with reduction of distance ratio L/d. On the other hand, with the 2nd circular cylinder, although there is no clear regularity, the amount of offset can be seen increasing to the plus side distance ratio L/d = 2.5 and L/d = 1.5.

3.3 SIMULTANEOUS VORTEX SHEDDING MODE OSCILLATION CASE

The calculation result at the time of oscillating 2nd circular cylinder in the direction of the flow in simultaneous vortex shedding lock-in mode (f/f_K = 2.4, $2a/d$ = 0.5) is shown in Fig. 6 and Fig. 7. Figure 6 shows the instantaneous flow pattern at the non-dimensional time T = 200, and the time histories (from T = 100 to 200) of the fluid force. Figure 7 shows the amount of offset of the average drag coefficient (blue color in the figure) for every distance ratio, and an average lift coefficient (red color in the figure). When the distance ratio L/d is large, as shown in Fig. 6 (a), the vortex shedding flows from both cylinders do not interfere with each other, and the 1st circular cylinder is the natural Karman vortex shedding. In the 2nd circular cylinder, simultaneous vortex shedding was performed to form a symmetric vortex street, and then the oscillation flow was observed in the wake. The time history of the fluid force was the same as that of each individual state. At the distance ratio L/d = 5.5, it can be seen that the position where the oscillating flow occurs in the 2nd circular cylinder goes back to the upstream side, but it does not interfere with the wake vortex street of the 1st circular cylinder. There is no notable change in the time history of fluid force. In distance ratio L/d = 2.5, they are an alternate vortex shedding and simultaneous vortex shedding near each circular cylinder. The aspect of the flow was changed by interference of these vortex streets. In the wake of the 1st circular cylinder, it became the vortex flow which is not regarded as the Karman vortex. The large-scale oscillating flow is formed in the wake of the 2nd circular cylinder. In the time history of fluid force, since the vortex shedding was carried out alternately, the relationship between the oscillating period of the lift coefficient and the oscillating period of the drag coefficient of the near wake of the 1st circular cylinder was the same as that of the case of being single. On the other hand, since the vortex shedding is carried out simultaneously as for the near wake of the 2nd circular cylinder, the amplitude of the drag coefficient is large far from the amplitude of the lift coefficient. About oscillation of the drag coefficient, it was the same as the case of being single. In distance ratio L/d = 1.5, the aspect of the flow was the same as that of alternate vortex shedding lock-in mode oscillation. The compound single vortex street was formed there. Under the influence in which the 2nd circular cylinder is carrying out the vortex shedding simultaneously, it was found that the vortex shedding from the 1st circular cylinder also grows into simultaneous discharge. This is clearly shown in the time history of fluid force. In the time history of the fluid force of the 1st circular cylinder, it can be seen that the oscillation cycle of the lift coefficient is different from the past and is synchronized with the oscillation cycle of the drag coefficient. On the other hand, in the time history of the fluid force of the 2nd circular cylinder, except that the surge increased to the time history of the lift coefficient, variation is not seen. Accordingly, it became clear on the 2nd circular cylinder that influence by interference was not received.

Figure 7 shows the offset amount of the average drag coefficient (blue color in the figure) and the average lift coefficient (red color in the figure) for each distance ratio. The abscissa is the distance ratio and the ordinate is each amount of offset. Here, the reference value of the oscillating 2nd circular cylinder is the average value of the waveforms of the single vibrating cylinder (C_{DAVE} = 0.8500 and C_{LAVE} = 0.0045). With the 1st circular cylinder, the lift coefficient tends to decrease and the drag coefficient tends to increase as distance ratio L/d becomes small, but it decreases suddenly by distance

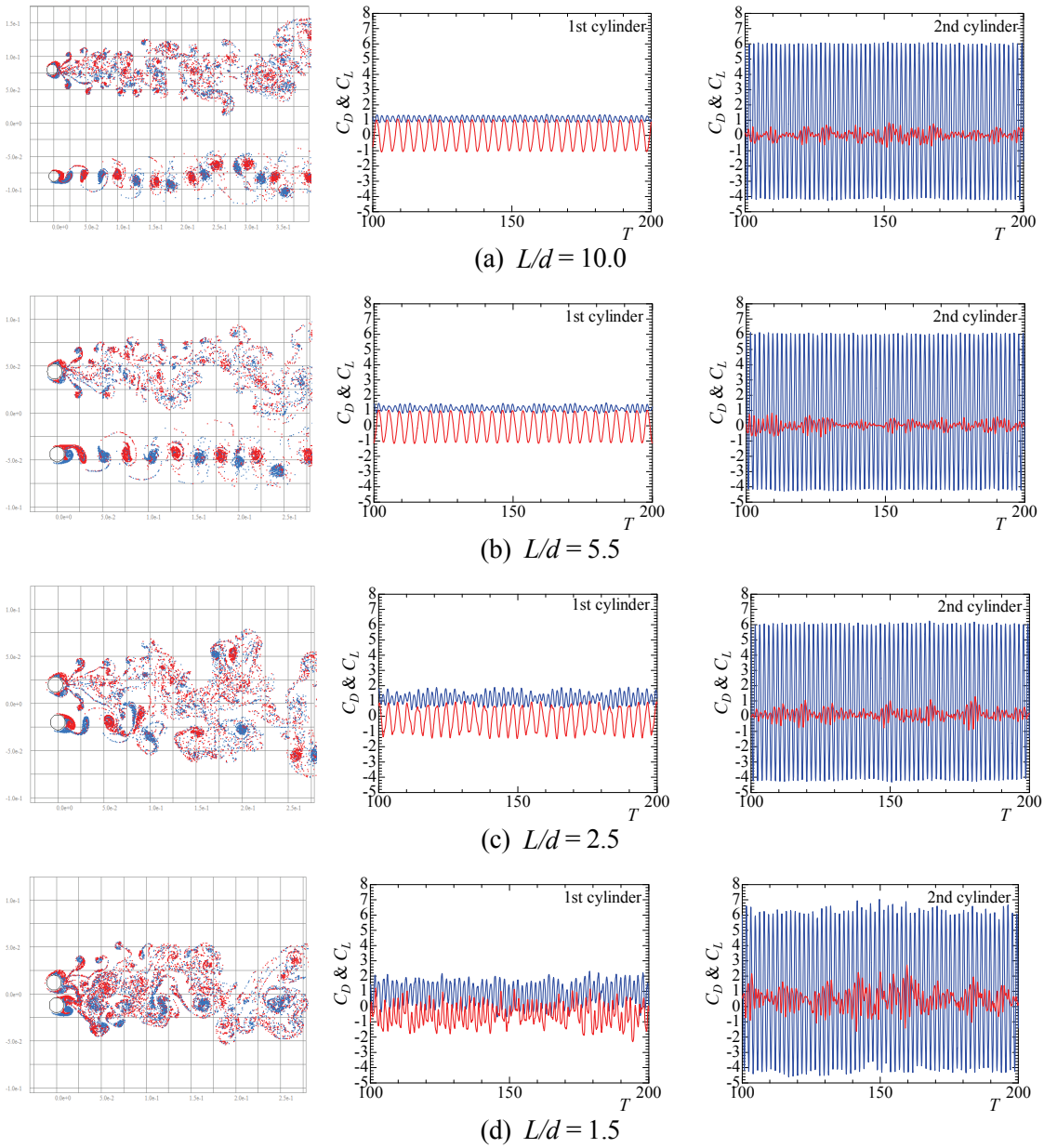

Fig. 6 Instantaneous flow feature at the time $T = 200$ and time histories of drag and lift coefficients

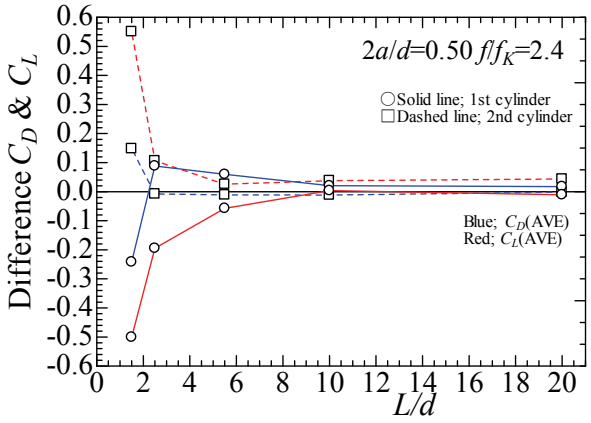

Fig. 7 The variation of the amount of offset for every distance ratio; combination of stationary 1st circular cylinder and the 2nd circular cylinder of simultaneous vortex shedding lock-in oscillation

ratio L/d = 1.5. It is shown that there is no remarkable change in the 2nd circular cylinder except for a sudden increase at the distance ratio of L/d = 1.5.

4. CONCLUSIONS

Numerical interference experiments about the vortex flow from two circular cylinders which are having the different lock-in modes were performed by using the vortex method. The following conclusions were obtained.

1. In the case of stationary two circular cylinder, the aspect of three characteristic flows based on the value of the distance ratio L/d was obtained in numerical computation, and the aspect of the variation of the fluid force by the variation of the distance ratio was found.

2. When the interval of two circular cylinders is wide, there is no interference of mutual lock-in modes.

3. The interference vortex flow from an oscillating circular cylinder and a stationary circular cylinder turns into the complicated flow from distance ratio L/d = 2.5, and the offset is included in the oscillatory wave form of fluid force.

4. The alternate vortex shedding type lock-in receives interference by cylinder arrangement.

5. The biased gap flow was produced also in the combination of an oscillating circular cylinder and a stationary circular cylinder.

REFERENCE

[1] Lebon B, Perret G, Coëtmellec S, et al. A digital holography set-up for 3D vortex flow dynamics[J]. Experiments in Fluids, 2016, 57(6):1-11
[1] Griffin O. M, Hall, M. S. Review-Vortex Shedding Lock-on and Flow Control in Bluff Body Wakes. Transactions of the ASME, 1991, 113: 526-537
[2] King, R. A Review of Vortex Shedding Research and its Application. Ocean Engineers, 1997, 4: 141-171
[3] Okajima, A. Flow-Induced Vibration of a Bluff Body. Transaction of the Japan Society of Mechanical Engineers Series B, 1999, 65(635): 2190-2195
[4] Okajima, A. Vortical Flow and Fluiddynamic Characteristics of an Oscillating Bluff Body. Transaction of the Japan Society of Mechanical Engineers Series B, 2000, 66(644): 948-953
[5] Sarpkaya, T, Cinar, M. Hydrodynamic Interference of Two Cylinders in Harmonic Flow. In Proceeding of Annual Offshore Technology Conference, 1980, 12(2): 333-340
[6] Chen, S. S. A Review of Flow-Induced Vibration for Two Circular Cylinders in Crossflow. Transactions of the ASME J Pressure Vessel Technology, 1986, 108(4): 382-393
[7] Sumner, D, Price, S. J, Paidoussis, M. P. Flow-Pattern Identficantion for Two Staggered Circular Cylinder. Journal of Fluid Mechanics, 2000, 411: 263-303
[8] Zdravkovich, M. M. Flow Around Circular Cylinder Vol. 2 Applications. Oxford University Press, 2003, ISBN 0-19-856561-5
[9] Kim, S, Sakamoto, H. A Study on Characteristics of Flow-Induced Vibrations of Two Circular Cylinders in Staggered Arrangement. Transactions of Japan Society of Mechanical Engineers Series B, 2007, 73(725): 139-146
[10] Yokoi, Y, Hirao, K. Vortex Flow Around an In-Line Forced Oscillating Circular Cylinder. Transactions of Japan Society of Mechanical Engineers Series B, 2008, 74(746): 2099-2108
[11] Yokoi, Y, Hirao, K. The Appearance of Two Lock-in States in the Vortex Flow Around an In-Line Forced Oscillating Circular Cylinder. EPJ Web Conferences, 2014, 67: 02131-1--02131-8
[12] Yokoi, Y, Hirao, K. The Mutual Interference Vortex Flow from a Pair of In-Line Forced Oscillating Staggered Arranged Circular Cylinders. Bulletin on the JSME Journal of Fluid Science and Technology, 2014, 9(3): JFTS0057-1--JFTS0057-11
[13] Kamemoto, K. The expandability of the vortex method as a turbulent flow model (the first part: to think a basic of vortex method). Japan Society of Computational Fluid Dynamics, 1993, 2(1): 20-29
[14] Kamemoto, K. The expandability of the vortex method as a turbulent flow model (the second part: to grasp the flow by vortex method). Japan Society of Computational Fluid Dynamics, 1994, 2(2): 28-39
[15] Yokoi, Y. Numerical experiment of the vortex shedding from an oscillating circular cylinder in a uniform flow by the vortex method. Proc. 4th International Conference on Particle-Based Methods. Fundamental and Applications (PARTICLES2019), 2019, 590-597
[16] Yokoi, Y. The numerical simulation of the changes of lock-in phenomenon produced from an in-line oscillating circular cylinder by the vortex method. IOP Conf. Series: Materials and Engineering, 2020, 904: 012009-1-012009-7

Turbulent channel flow past a wall-mounted cuboid

Ariane N. R. Vieira[1*], Hendrik C. Kuhlmann[1], Johann Waringer[3], Carina Zittra[3], Jan Martini[3], Simon Vitecek[4], Stephan Handschuh[5]

[1]*Institute of Fluid Mechanics and Heat Transfer, TU Wien, Tower BA/E322, Getreidemarkt 9, A-1060 Vienna, Austria*
[2]*Department of Functional and Evolutionary Ecology, Division Limnology, University of Vienna, Althanstrasse 14, A-1090 Vienna, Austria*
[3]*WasserCluster Lunz, Dr. Carl Kupelwieser Promenade 5, A-3293 Lunz am See, Austria*
[4]*VetCore Facility for Research, Imaging Unit, University of Veterinary Medicine, Veterinärplatz 1, A-1210 Vienna, Austria*
[*]*Corresponding Author: ariane.vieira@tuwien.ac.at*

We investigate the incompressible turbulent flow past a wall-mounted square cuboid placed in a channel. Large Eddy Simulation (LES) is used in combination with the divergence-free synthetic eddy method (DFSEM) [1] to generate the turbulent inflow conditions. The geometry of the computational domain is shown in Fig. 1. To close the problem, we impose convective boundary conditions at the outlet, periodic boundary conditions in span direction, and no-slip conditions at the top wall, bottom wall, and all faces of the cuboid.

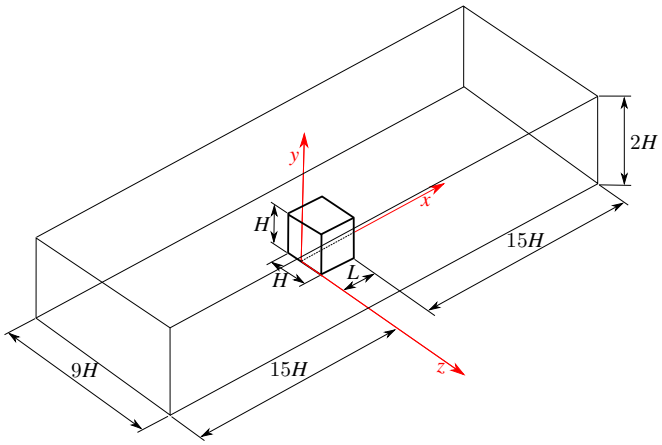

Fig. 1: Sketch of the geometry of the computational domain and coordinate system.

We validate the procedure by comparing with experimental data for a wall-mounted cube ($L = H$) and bulk Reynolds number $\mathrm{Re}_H = HU_b/\nu = 4\times10^4$ [2] (U_b: bulk velocity). Simulations are performed for bulk Reynolds number $\mathrm{Re}_H = 2\times10^4$, and for different length-to-height aspect ratios Γ of the cuboid in the range $0.25 \le \Gamma \le 6$. We compute the mean flow structures and the different separated regions.

A horseshoe vortex is formed in front and aside of the cuboid, as seen in Fig. 2. For $0.25 \le \Gamma < 1.5$, its vorticity feeds, along with the shear layer from the top, the arch vortex in the wake. For $\Gamma > 1.5$, we observe a reattachment point on the sides of the cuboid and an alteration of some topological points: the two hyperbolic points, one beneath the cuboid and one in the wake, present when $\Gamma < 1.5$, merge into one. In addition, the separation point on the rear wall of the cuboid moves to the sidewall of the cuboid. Those alterations modify the footprint of the arch vortex from an almost circular shape to one elongated in the streamwise direction.

For small Γ the streamwise length of the mean wake recirculation bubble L_w decreases with Γ, reaching a minimum at $\Gamma \approx 2$. The length of the sidewall separation bubble L_s exhibits the opposite trend and reaches a maximum at $\Gamma \approx 2$. For $\Gamma \gtrsim 2$ the vortices shed from the sidewalls cause an increase of L_w, while L_s saturates. An increase of the channel height from $2H$ to $4H$ reduces the size of the recirculation region at the top of the cuboid (not shown). Other than that, the flow structures remain almost the same.

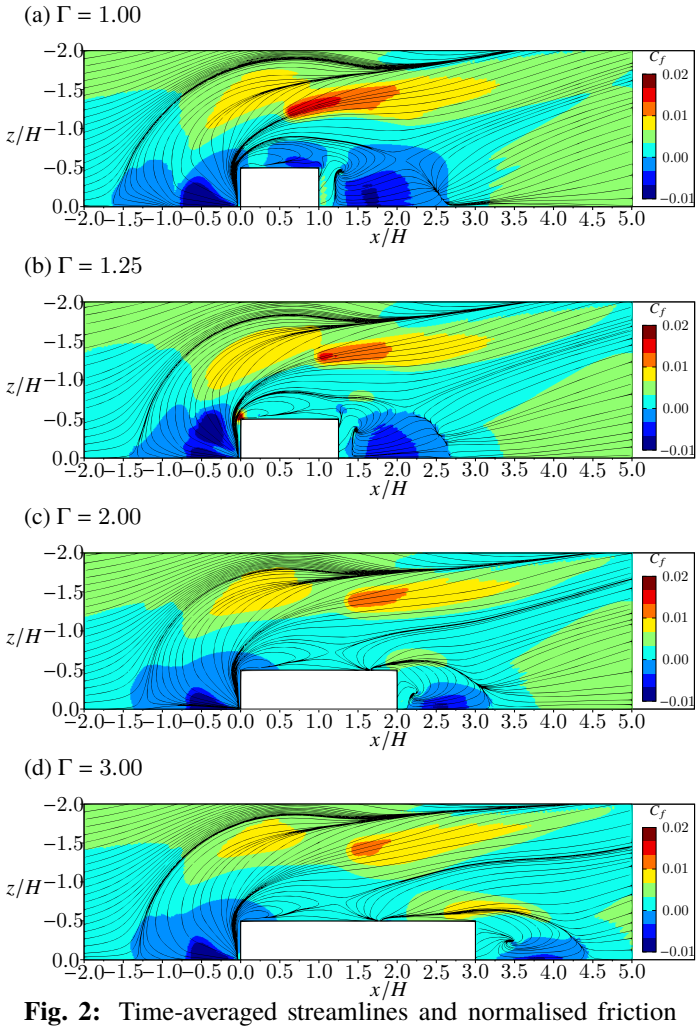

Fig. 2: Time-averaged streamlines and normalised friction coefficient (color) in the plane $y/H = 0.003$ from the bottom for different aspect ratios Γ.

Summarising, the dependence of the characteristic mean flow structures on the aspect ratio Γ of the cuboid have been established. The most sensitive vortical structure is the main recirculation bubble in the wake of the cuboid.

References

[1] Poletto R, Revell A, Craft T, A new divergence free synthetic eddy method for LES inflow boundary conditions, Flow Turbul. Combust. **91** (2013) 519-539.

[2] Martinuzzi R, Tropea C, The flow around surface-mounted, prismatic obstacles placed in a fully developed channel flow (Data Bank Contribution), J. Fluids Eng. **115** (1993) 85-92.

Numerical Investigation of a Backward Facing Step Flow Controlled by a Synthetic Jet

Dionysia Voultsou[1], Alexandros Romeos[2,1*], Alexandros Kalarakis[1], Athanasios Giannadakis[2,1]

[1]Mechanical Engineering Dept., University of the Peloponnese, Patra, Greece
[2]Mechanical Engineering & Aeronautics Dept., University of Patras, Patra, Greece
** Corresponding Author: romaios@upatras.gr*

In the present work, the flow over a backward-facing step with the presence of a synthetic jet is studied using a 2D CFD model. The geometry under investigation can be found in numerous engineering applications in aeronautics and industry such as heat exchangers, nuclear reactors, diffusers, air conditioning systems. This study focus on recirculating flows detaching and reattaching to the main flow. Knowledge of the conditions under which these phenomena are observed helps in the development of flow control technologies and thus minimize flow disturbance, and kinetic energy losses.

Separation of the flow over the Backward Facing Step is created by a 2-D channel configuration (Fig. 1), resulting in the creation of evolving recirculation zones that reattach to the main flow. An active synthetic jet is situated, after the back face of step to control the evolution of the recirculation zones.

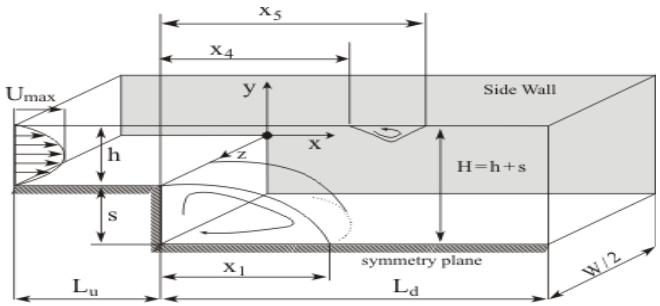

Fig. 1: Backward Facing Step

The operation of the synthetic jet is based on the periodic alternation between the suction and injection phases so that the mass supply to the main flow balance remains zero per period The motion of jet flow is caused by a diaphragm that moves periodically inside a cavity (Fig. 2).

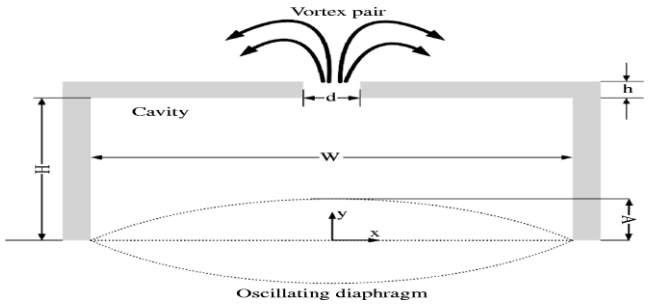

Fig. 2: Synthetic jet

Simulation the flow field, is realized via a K-ω SST turbulence model implemented on a tetrahedral structured mesh. The operating frequency of the synthetic jet is 90 Hz with a Strouhal number, St = 0.03. Typical images of synthetic jet flow evolution are presented in figure 3.

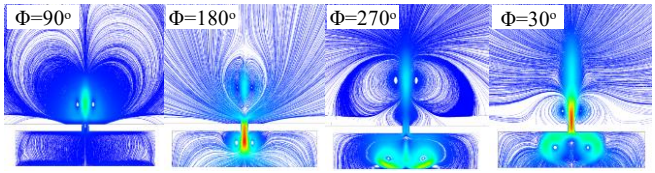

Fig. 3: Typical synthetic jet flow evolution at different pulse phases

At first, the numerical simulation study, is performed without the presence of the synthetic jet for several Reynolds number (Re=350-10000). Then, the influence of the synthetic jet on flow control is investigated. Characteristic velocity contours for the case of U=1 m/s bulk inlet velocity and Re=10000 are presented in figure 4.

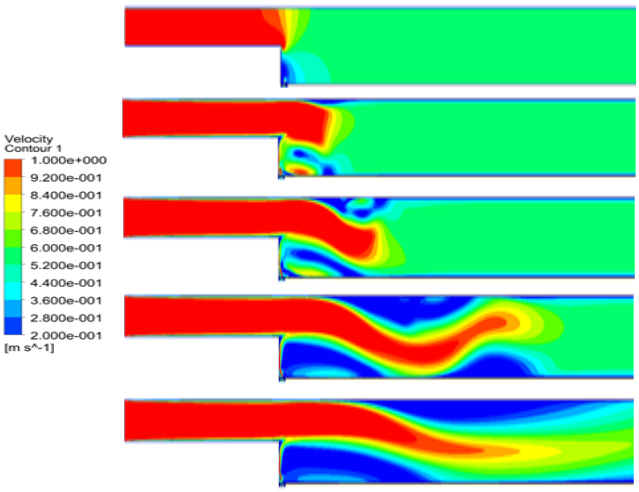

Fig. 4: Mainstream mean velocity contours at different time steps (t=0.01, 0.5, 1, 2, 4 sec)

References

[1] Strzelczyk P., Gil P., Properties of velocity in the vicinity of synthetic jet generator, Journal of Physics, 2016, (760).

[2] Li Z., Zhang D., Liu Y., Wu C., Gao N., Effect of periodic perturbations on the turbulence statistics in a backward-facing step flow, Physics of fluids, 2020, 32(7).

[3] Biwas G., Breuer M., Durst F., Backward-Facing Step Flows for Various Expansion Ratios at Low and Moderate Reynolds Numbers, J. Fluids Eng., 2004 (126(3).

An experimental study on the wake of a sphere having a uniaxial through-hole

Hayato Kato[1*], Kotaro Takamure[2],Tomomi Uchiyama[2]

[1]Graduate School of Informatics, Nagoya University, Nagoya, Japan
2Institute of Materials and Systems for Sustainability, Nagoya University, Nagoya, Japan
** Corresponding Author: kato.hayato@a.mbox.nagoya-u.ac.jp*

We refer flows arise from bodies moving in stationary fluids or them placed in uniform flow to wake. Flows involving wake are frequently observed in our life exposed to various fluid environments and have big effects on circumstances surrounding us. So, it is very important to understand these characteristics. Many experiments about wake of a sphere [1] or a circular cylinder [2-3] were carried out so far. Effects of a bluff body shape on the wake were investigated. Igarashi [2-3] placed a circular cylinder having a slit within a uniform flow to investigate the effect of the slit angle on the wake of the circular cylinder. When the slit was parallel to the streamwise direction, the slit angle β equals to 0°. For 0° ≦ β ≦ 40°, the self-injection jet from the slit into the wake was observed, and the resulting vortex formation region move downstream. For, 60° ≦ β ≦ 90°, the boundary layer suction was observed periodically with the period of the vortex shedding. These results indicate the possibility to control the wake by modifying the body shape

This study placed a sphere having a through-hole within a uniform flow and explored the effects of the angle between the through-hole and the uniform flow direction on the wake of the sphere.

Fig.1 (a) shows an overview of the experimental setup. This experiment was performed using a wind tunnel. The dimension is 500 mm × 180 mm × 180 mm. A sphere was placed 125 mm away from the exit of the wind tunnel. The coordinate origin was the center of a sphere. *X*, *Y*, and *Z* represent the streamwise, spanwise, and vertical directions, respectively. Fig.1 (b) shows the definition of the angle of through-hole and the dimensions of the sphere. The sphere diameter *d* was 25.4 mm, and the through-hole diameter was 6mm. The angle α was 0° when the through-hole was set to be along the *X* axis. The flow velocity in the wake of the sphere was measured by a hot-wire anemometer (KANOMAX 7000ser.). In this experiment, a uniform flow velocity U_0 was 7 m/s and the Reynolds number based on *d* and U_0 was almost 12,000.

Fig.2 shows the spanwise distributions of the streamwise mean velocity normalized by *d* at *X*/*d* = 1. When α = 0°, a jet from the through-hole was observed, and accordingly the velocity defect was the smallest. When α = 45°, the velocity distribution was left-right asymmetry and the velocity defect was smaller locally near the edge of the through-hole. When α = 90°, the velocity distribution was similar to that of a sphere without a through-hole, but the velocity defect was smaller. As stated above, the effect of a through-hole on the wake changes as a function of *α*.

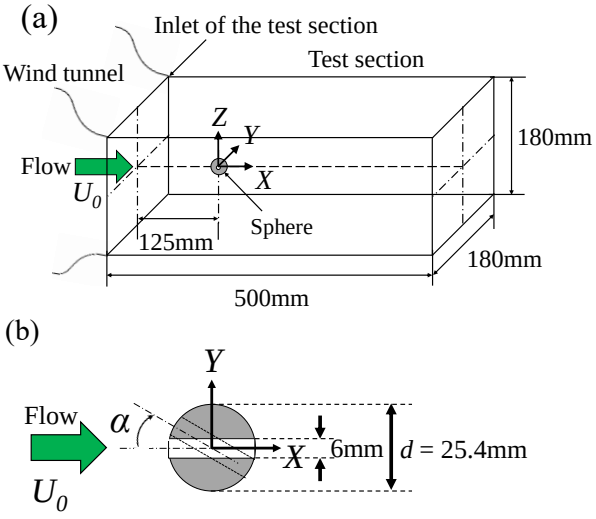

Fig.1: Schematic of the test section. (a) Overview of the experimental setup, (b) details of angle and dimension s of sphere and through-hole

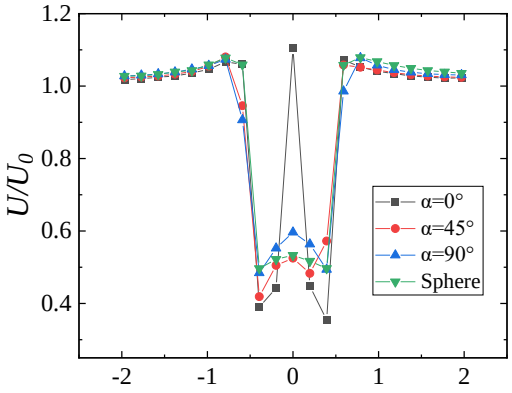

Fig.2: Spanwise distributions of streamwise mean velocity at *X*/*d* = 1

Acknowledgment

This work was supported by the TOYOAKI SCHOLARSHIP FOUNDATION, Japan.

References

[1] E. Achenbach, “Vortex shedding from spheres.” J. Fluid Mech., vol.62 (2), pp209–221(1974).

[2] T. Igarashi, ”Flow Characteristics around a Circular Cylinder with a slit (1st Report, Flow Control and Flow Patterns) ,”Bulletin of the JSME, vol.21, No.154, pp154-16 (1978).

[3] T. Igarashi, ”Flow Characteristics around a Circular Cylinder with a slit (2nd Report, effect of Boundary Layer Suction),” Bulletin of the JSME, vol.25, No.207, pp207-8 (1978).

Article S8.4

Vortical systems, generated by Darrieus and Savonius Rotors

Dmytro Redchyts[1], Svitlana Moiseienko[2], Yevhenii Shkvar[3*], Shiju E[3]

[1]*Institute of Transport Systems and Technologies of the NASU, Pysarzhevskoho str., 5, Dnipro, Ukraine*
[2]*Kherson National Technical University, Beryslavske highway, 24, Kherson, Ukraine*
[3]*College of Engineering, Zhejiang Normal University, 688 Yingbin Road, Jinhua, China*
** Corresponding author: redchits_da@ua.fm*

ABSTRACT

Numerical modeling of unsteady turbulent separated flows of incompressible fluid around vertical axis wind turbines (VAWT) with Darrieus and Savonius rotors was performed on the basis of the Reynolds-averaged Navier-Stokes equations, closed by the Spalart-Allmaras turbulence model. The numerical solution was obtained using original homemade program code that implements an implicit finite volume algorithm based on the artificial compressibility method. Overlapping structured grids were applied in multi-domain areas. Verification of developed CFD code has been carried out by simulation of several typical testing problems, namely: laminar and turbulent flow around steady and unsteady cylinder, subcritical and supercritical flow around steady and oscillating NACA 4412, NACA 0015 airfoils, aerodynamics of the turbulent flow around a 30P30N multi-element airfoil in cruise, takeoff and landing configurations, turbulent flow around tractor-trailer. The results of Darrieus and Savonius rotors simulation, physical and computational experiments with different number and geometry of blades are presented in the form of detailed flow visualization and reconstruction for two- and three-blade Darrieus rotor. The analysis of flow field near rotors was carried out and the main stages of vortex development were identified and analyzed. The results of three series of computational experiments on aerodynamic of two and three-bucket Savonius rotor were obtained, presented and discussed.

KEYWORDS: Vortical systems, Wind Turbine, Darrieus, Savonius Rotor, Navier-Stokes Equations

1. INTRODUCTION

Aerodynamics plays a major role in the operation of wind turbine. Final efficiency of wind turbine depends on optimization of a rotor form, aerodynamic qualities of rotating surfaces of the wind turbine itself. The simplicity and reliability of the VAWT, the ability to work under of conditions of moderate wind allows them to be installed in hard-to-reach areas of significant social importance [1].
It is well known that Darrieus rotors have superior power factors, which are still inferior to horizontal-axis wind turbines in terms of aerodynamic efficiency [2]. Insufficient level of understanding of the aerodynamic processes of the VAWT plays a major role in such state of affairs [3]. Another reason is the outdated methodology for development of industrial samples of high-power wind turbines which are based on empirical assumptions on the flow pattern around the VAWT rotors and discards adequate calculations of the blade aerodynamics for the case of dynamic stall [4].
This paper aims to study the vortical structure of unsteady flow around of VAWT Darrieus and Savonius rotors based on the numerical solution of the dynamic's equations of a viscous incompressible fluid.

2. MATHEMATICAL MODEL

This research considers the orthogonal Darrieus and Savonius rotors (see Fig. 1). The typical blades are much longer than the chord that allows to neglect end effects on blades and to take advantage of a hypothesis about plane-parallel structure of flow. Thus, the problem supposes two-dimensional statement in a plane which is perpendicular to the axis of rotor rotation. Darrieus and Savonius rotors are assumed to be absolutely rigid. Wind turbine aerodynamic processes are described by

incompressible RANS equations closed by Spalart-Allmaras (SA) eddy viscosity turbulence model as quite simple, reliable and appropriate for a wide range of external flows.

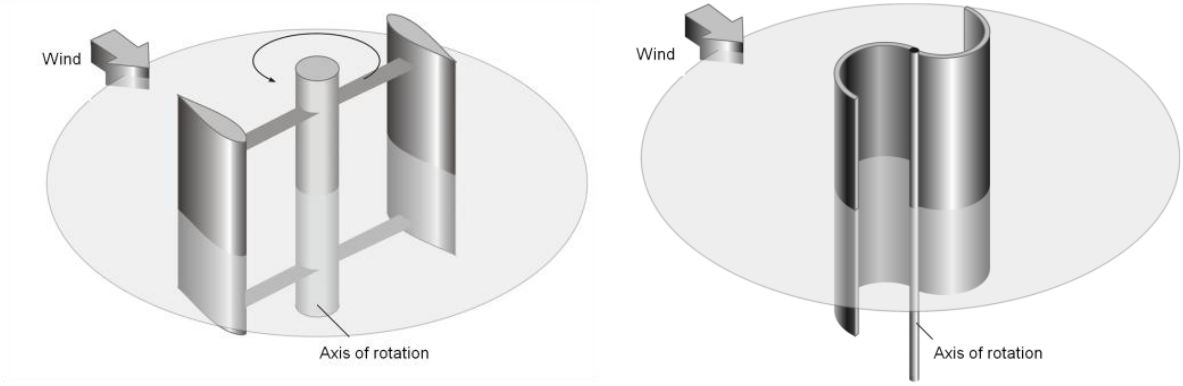

a) b)

Fig. 1 Computational schemes of Darrieus (a) and Savonius (b) rotors

2.1 GOVERNING EQUATIONS

The paper examines the low-speed air movement at small Mach numbers (M<0.3). In this case, the effects of air compressibility can be neglected, so the RANS equations for a viscous incompressible flow [5] have been applied for the studied kind of turbulent flow modeling

$$\frac{\partial u_j}{\partial x_j} = 0\,, \tag{1}$$

$$\frac{\partial u_i}{\partial t} + \frac{\partial \left(u_j u_i\right)}{\partial x_j} = -\frac{1}{\rho}\frac{\partial p}{\partial x_i} + \frac{\partial}{\partial x_j}\left[\left(\nu + \nu_t\right)\left(\frac{\partial u_i}{\partial x_j} + \frac{\partial u_j}{\partial x_i}\right)\right], \tag{2}$$

where x_i, $i = 1, 2$ are the Cartesian coordinates; t – time; u_i are the Cartesian components of the velocity vector; p – pressure; ρ – density; ν and ν_t are the kinematic coefficients of molecular and turbulent viscosity.

2.2 SIMULATION OF TURBULENCE

The differential single-parametric SA turbulence model is used to close the RANS equations [6]. The standard SA model is intended to determine the kinematic coefficient of turbulent viscosity

$$\nu_t = \tilde{\nu}_t \cdot f_{v1}, \qquad f_{v1} = \chi^3 \Big/ \left(\chi^3 + c_{v1}^3\right), \tag{3}$$

where f_{v1} is a damping function of kinematic viscosities χ. Here $\tilde{\nu}_t$ is the working variable. The equation to determine $\tilde{\nu}_t$ in the SA model takes the form [6]

$$\frac{D\tilde{\nu}_t}{Dt} = c_{b1}\tilde{S}\tilde{\nu}_t + \frac{1}{\sigma}\frac{\partial}{\partial x_k}\left[\left(\nu + \tilde{\nu}_t\right)\frac{\partial \tilde{\nu}_t}{\partial x_k}\right] + \frac{c_{b2}}{\sigma}\frac{\partial \tilde{\nu}_t}{\partial x_k}\frac{\partial \tilde{\nu}_t}{\partial x_k} - f_w\left(\frac{c_{b1}}{k^2} + \frac{1+c_{b2}}{\sigma}\right)\left(\frac{\tilde{\nu}_t}{d}\right)^2. \tag{4}$$

The values for other constants can be found in paper [6].

2.3 BOUNDARY CONDITIONS

On the solid body surface, no-slip condition is used. The pressure is obtained by specifying a zero pressure gradient normal to the wall. The boundary conditions used for inflow and outflow regions are based on the method of characteristics [7], [8].

3. SPECIALIZED CFD PACKAGE

The specialized CFD package, developed by Redchyts [9], has been applied by the authors team in frames of this study. This software allows to effectively and flexibly achieve a necessary level of compromise between the required computational resources and the results quality. The developed

basis of computational methodology provides a complete CFD approach, based on the Navier-Stokes equations, including RANS approach and several differential turbulence models, as well as multi-block approach for the flows in multiply connected domains. Designed CFD package allows to solve the problem of dynamics and aerodynamics, including electrodynamics processes, electrochemistry, multiphase fluids, combustion processes and plasma kinetics [10], [11].
Modern requirements to reliability of received numerical results and CFD reliability demand careful testing and verification of the developed programs. In order to verify developed numerical method the test problems such as laminar and turbulent flow around immovable and rotating cylinder [9], subcritical and supercritical flow around steady and oscillating NACA 4412, NACA 0015 airfoils, aerodynamics of the turbulent flow around a 30P30N multi-element airfoil in cruse configuration and in takeoff and landing configuration [12], turbulent flow around tractor-trailer [13] were solved.

4. RESULTS AND DISCUSSION

4.1 DARRIEUS ROTOR

4.1.1 Two-blade Darrieus rotor.

Most experimental and theoretical studies [4], [14], [15], [16] devoted to the study of the Darieus rotor VAWT aerodynamics and power coefficient consider only symmetric airfoils of NACA 00XX family. It is common that solidity varies through adding blades. These studies were conducted for VAWT equipped with blades of symmetric airfoil NACA0018 only and under zero angle of pitch [17], [18]. Flow visualization and reconstruction were performed for two-blade Darrieus rotor on the basis of physical [4] and computational experiments (see Fig. 2). For greater clarity, only the vortices of maximum intensity are left. The stages of origin, development and stall of vortices are allocated at various positions of the blade along the trajectory. At the beginning of a leeward side of a trajectory and before angular position of a rotor two hundred and forty degrees the flow around the blade has the attached character.

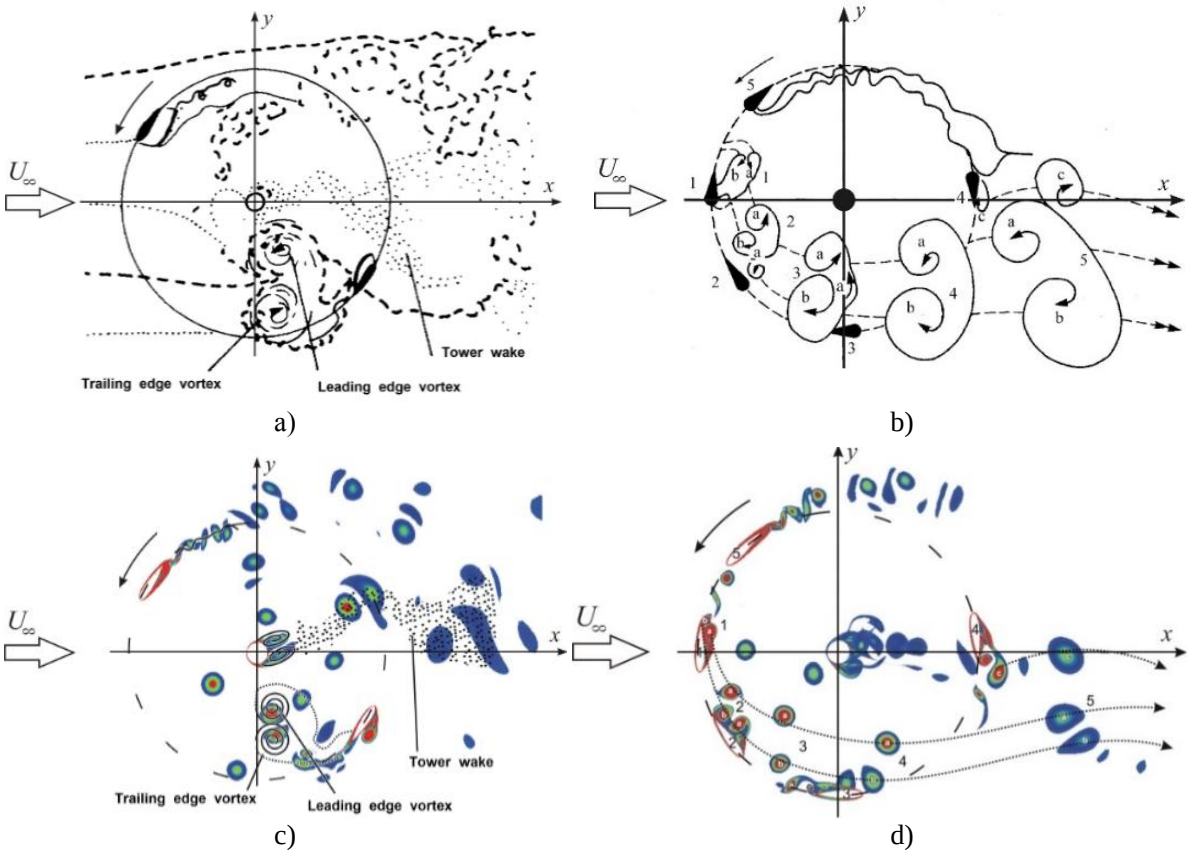

Fig. 2 Visualization (a, c) and reconstruction (b, d) of the flow field at operation of two-blade Darrieus rotor, based on physical [4] (a, c) and computational (b, d) experiments

Separated flow appears at mentioned rotor angle (240º). As well as in case of dynamic stall on the inner surface, vortices separate from a leading edge of the blade and begin movement along a surface. Calculations were carried out in two stages. At the first stage free stream in all area was set in, which suddenly initiated Darrieus rotor. At the second stage the structure was investigated at the fixed tip-speed-ratio and main parameters were defined at unsteady flow around Darrieus rotor.
For the considered parameters, the flow picture is characterized by essential unsteady phenomena such as: dynamic stall, generation of complex system of vortices, interaction of vortices of different sizes, speeds and intensities with the rotor surface.

4.1.2 Three-blade Darrieus rotor.

The experimental study [19] provides the flow pattern around three-blade Darrieus rotor. They illustrate the trailing edge vortices shedding at the different blade angular positions and tip-speed-ratio $\lambda = 3$ (Fig. 3 a, b). The instantaneous flow structure comprises a system of large counter rotating vortices. There is an asymmetry between different parts of the blade trajectory. The most of shed vortices moving toward the flow exceed the vortices moving along the flow in intensity. This is due to the fact that the relative flow velocity at this section of the blade trajectory is higher than at the opposite. In the front part of the Darrieus rotor there is a crowding of vortices, which were originated by the first blade. Downstream there is a crowding of vortices originated by previous blade.

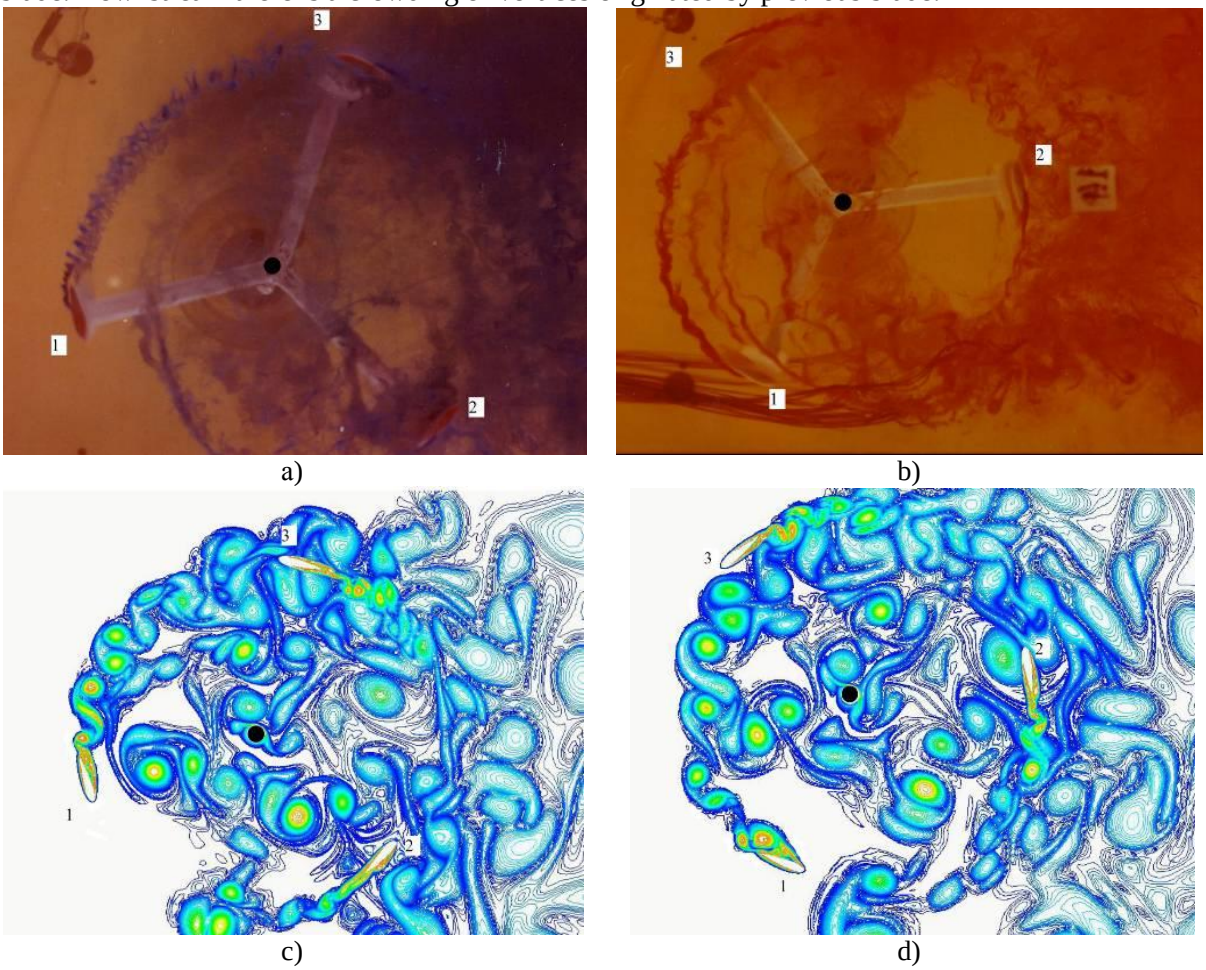

Fig. 3 Visualization of the flow field at operation of three-blade Darrieus rotor, based on physical [19] (a, b) and computational (c, d) experiments for different angles of rotation

4.2 SAVONIUS ROTOR

This study gives the results of three series of computational experiments on aerodynamic and power characteristics of two and three-bucket Savonius rotor.
The first set of computational experiments was conducted for steady Savonius rotor which was fixed at various angles of attack. For the majority of angular positions the two-bucket Savonius rotor

time-averaged torque coefficients are positive, but for angles 55-80º they are negative. For three-bucket configurations torque coefficients are always positive.
The second set of computational experiments was conducted for fixed tip-speed-ratio of Savonius rotor (see Fig. 4). The maximum value of the torque coefficient is 0.4 for two-bucket and it is 0.35 for three-bucket Savonius rotor. They correspond to the tip-speed-ratio of 0.4. The maximum value of power coefficient is 0.23 for two-bucket and 0.19 for three-bucket Savonius rotor. The obtained results agree well with experimental data [20], the maximum discrepancy is observed in the wake region and does not exceed 15%.

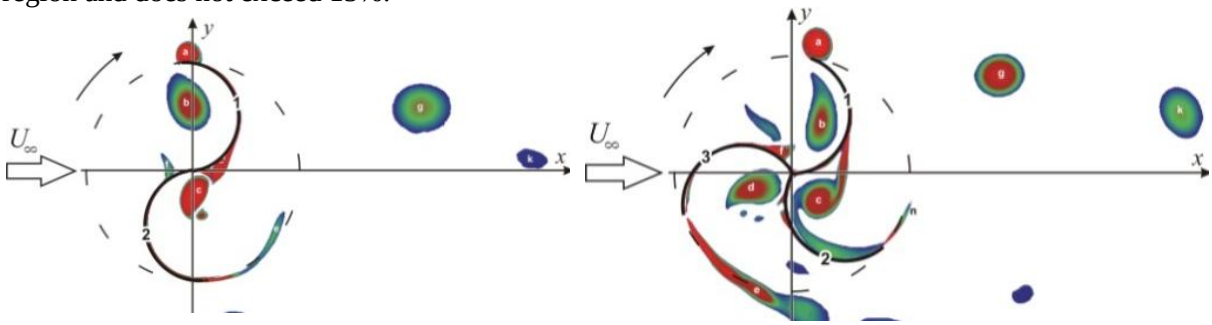

a) b)

Fig. 4. Visualization of the flow field at operation of two-bucket (a) and three-bucket (b) Savonius rotor on the base of computational experiments

The third set of computational experiments corresponds to the coupled problem solution including dynamics and aerodynamics of three-bucket Savonius rotor. Calculations were carried out in three stages. The purpose of the first stage was to determine a periodic flow with a structure similar to the Karman vortex street. At the second and third stages, the coupled equations describing Savonius rotor aerodynamics and rotation were solved. After unlocking the rotor begins to rotate under effect of incoming wind flow that intensifies the vortex formation. The frequency of vortex detachment depends on incoming flow velocity, characteristic dimensions and rotor rotation speed. At the third stage the torque of load is applied to the Savonius rotor that results in stabilization of rotor angular speed and near to cyclic variations of drag, lift and torque coefficients.

5. CONCLUSIONS

New solutions describing unsteady flow around vertical-axis wind turbine rotors are obtained on the basis of RANS equations and Spalart-Allmaras turbulence model. The system of governing equations was integrated numerically using the control volume method. The Rogers-Kwak counter-flow approximation of third-order accuracy was effectively applied for convective terms. In the turbulence model, a TVD scheme with a third-order ISNAS flow limiter was used to approximate the convective terms. The properties of two types of Darrieus and Savonius rotors differing in the number of blades and their geometry, were calculated and studied. The analysis of development of unsteady turbulent incompressible flows was performed for the flows around VAWT Darrieus and Savonius rotors. The instantaneous flow structure comprises a system of large counter rotating vortices. There is an asymmetry between different parts of the blade trajectory. It was found that at the beginning of a leeward side of a trajectory and before angular position of two-blade Darrieus rotor 240º the flow around the blade has the attached character. Separated flow appears at mentioned above rotor angle (240º). Vortices separate from a leading edge of the blade and begin movement along a surface. For the considered parameters, the flow picture is characterized by essential unsteady phenomena. The instantaneous flow structure comprises a system of large counter rotating vortices. There is an asymmetry between different parts of the blade trajectory. The most of shed vortices moving toward the flow exceed the vortices moving along the flow in intensity. The vortices affect the flow structure around Darrieus rotor blades. Vortices, originated by the forward blade, intensify the level of turbulence of the incoming flow for the following blade. The obtained results are in good agreement with experimental data, the maximum discrepancy is observed in the wake region and does not exceed 15%.

REFERENCE

[1] Paraschivoiu I. Wind Turbine Design with Emphasis on Darrieus Concept [B]. Polytechnic International Press: Montreal, QC, Canada, 2002.
[2] Strickland J. A vortex model of the Darrieus turbine: an analytical and experimental study [J]. SAND79-7058 report. Sandia, 1980.
[3] Biadgo A, Simonovic A, Komarov D, et al. Numerical and Analytical Investigation of Vertical Axis Wind Turbine [J]. FME Transactions, 2013, 1(41):132-150.
[4] Brochier G, Fraunie P, Beguier C, et al. Water channel experiments of dynamic stall on Darrieus wind turbine blades [J]. Propulsion, 1986, 5(2):445-449.
[5] Anderson J. Computational Fluid Dynamics [J]. McGraw-Hill Education, New York, 1995.
[6] Spalart P, Allmaras P. A one-equation turbulence model for aerodynamic flow [J]. AIAA, 1992, 12(1): 439-478.
[7] Rogers S, Kwak D. Upwind differencing scheme for the time-accurate incompressible Navier-Stokes equations [J]. AIAA, 1990, 28 (2):253-262.
[8] Rogers S, Kwak D. An upwind differencing scheme for the incompressible Navier-Strokes equations [J]. Applied Numerical Mathematics, 1991, 8 (1):43-64.
[9] Prikhod'ko A, Redtchits D. Numerical modeling of a viscous incompressible unsteady separated flow past a rotating cylinder [J]. Fluid Dynamics, 2009, 6 (44):823-829.
[10] Redchyts D, Shkvar E, Moiseienko S. Control of Karman Vortex Street by using Plasma Actuators [J]. Fluid Dynamics and Materials Processing, 2019, 15(5):509-525.
[11] Redchyts D, Moiseienko S. Numerical simulation of unsteady flows of cold plasma during plasma actuator operation [J]. Space Sci. & Technol, 2021, 27(1):85-96.
[12] Redchyts D, Gourjii A, Moiseienko S, et al. Aerodynamics of the turbulent flow around a multi-element airfoil in cruse configuration and in takeoff and landing configuration [J]. Eastern-European Journal of Enterprise Technologies, 2019, 9(5):36-41.
[13] Redchyts D, Shkvar E, Moiseienko S. Computational Simulation of Turbulent Flow Around Tractor-Trailers [J]. Fluid Dynamics and Materials Processing, 2020, 1(16): 91-103.
[14] Longhuan D, Grant I, Robert D. A review of H-Darrieus wind turbine aerodynamic research [J]. Journal of mechanical engineering science, 2019, 233(23-24):7590-7616.
[15] Hu Y, Wang T, Jin H, et al. Experimental study on aerodynamic characteristics of vertical-axis wind turbine [J]. Smart Grid and Clean Energy, 2017, 2(6):104-113.
[16] Miller M, Duvvuri S, Brownstein I, et al. Vertical-axis wind turbine experiments at full dynamic similarity [J]. Fluid Mech, 2018, 844:707-720.
[17] Yi M, Jianjun Q, Yan L. Airfoil Design for Vertical Axis Wind Turbine Operating at Variable Tip Speed Ratios [J]. The Open Mechanical Engineering Journal, 2015, 9:1007-1016.
[18] Rezaeiha A, Montazeri H, Blocken B. Towards optimal aerodynamic design of vertical axis wind turbines [J]. Impact of solidity and number of blades Energy, 2018, 165:1129-1148.
[19] Dzenzerskiy V, Tarasov S, Kostyukov I, et al. Flow field around H-rotor Darrieus [B]. Naukova Dumka, 2013, 95.
[20] Blackwell B, Sheldahl R, Feltz L. Wind tunnel performance data for two- and three-bucket Savonius Rotors [J]. SAND76-0131. Sandia National Laboratories Albuquerque, 1976.

Article S8.5

The Assessment of the Impact of Turbulence Generated by Wind Turbines Planned for Construction in Close Proximity of High Voltage Power Transmission Lines on the Wind Farm Location Problems

Waldemar Kamrat

Gdansk University of Technology, Faculty of Electrical and Control Engineering,
Power Engineering Department, 11/12 Narutowicza Street, 80-233 Gdansk, Poland
** Corresponding Author: waldemar.kamrat@pg.edu.pl*

ABSTRACT

This paper presents selected aspects of network construction related to the location of wind turbines due to their aerodynamic impact on power lines of high and highest voltage. The technical context has been described in the light of the applicable formal and legal conditions. Based on the source data concerning the aerodynamic impact of a wind farm consisting of eight turbines on a 400 kV transmission power line, an analysis of the possibility of wind farm locating in the immediate vicinity of the line was carried out. There are very serious problems with locating higher capacity wind farms in the context of their connection to the transmission grid. One of the most important issues in the design/construction of wind farms is the rationalization of the typology of distribution of individual generating units due to the turbulence they generate . An example of a report on the assessment of the aerodynamic impact of wind turbines on a high-voltage power transmission line in the case of planning their location in the vicinity of the line is presented. Ways of solving the wind farm location problems have been proposed, which allow the wind farm to be located in the vicinity of an overhead high-voltage power transmission line.

KEYWORDS: Electric power engineering, Wind turbines, Turbulent vortex, Wind farm location

1. INTRODUCTION

The advantages of onshore wind energy are obvious. Onshore wind energy is a relatively cheap technology for generating electricity. Currently, the latest generation wind farms installed onshore in Germany, Sweden, Finland, and Ukraine, with rotors from 150 m, tower heights from 160 m and generator power from 4 MW, show a sustainable efficiency factor regardless of the location of the wind turbine in a given country. Important problems that hinder the development of wind energy, which undoubtedly have a negative impact, i.e. the stochastic nature of energy generation, e.g. are an increase in demand for flexible power in the system, potential social problems and the impact on network problems (greater susceptibility to failures, the need for grid development, the aerodynamic impact of wind turbines on high and highest voltage power lines caused by the generation of turbulent vortices by them. There are many models (physical and mathematical methods) and the methods used to calculate the impact of turbulence on the efficiency of a wind farm. Their excellent characteristics are included in the works[1],[2],where the currently used models and programs for numerical calculations are described. Reference [2] shows frequently used computational programs include: WAsP, WindPro, WindFarmer, WindFarm, WindSim, where respectively Jensen models [3] and the linearized CFD model are used, a module with WAsP; while the WindFarmer program uses the following models: Ainslie, RANS and CFD. On the other hand, the following models were used in the WindFarm software: Jensen, Ainslie and Larsen, and the models: Larsen [3],[4] and Ishikara [5] in the WindSim program, which give a relatively short computation time. Finite element methods are also used for modelling/calculating turbulence [6],[8],[9].
It should be noted that turbulence/disturbance of the even flow of air streams can reach considerable values, even up to 20%. The main source of turbulence is the terrain, the influence of electromagnetic

radiation of the sun and obstacles, e.g. trees, neighboring wind turbines, weather masts and other obstacles in the field. In the case of wind farms (both off-shore and on-shore), the value of wind velocity turbulence is considered to be the main cause of a decrease in generated power, which in turn affects the stability of the electricity network. This is of paramount importance when planning the location of a wind farm near power lines, understood as distances up to 5 diameters (**5d**) of the turbine rotor. Assuming a kind of "obstacle" in the form of a power line occurring on the path of airflow from the turbine to the line (in the most unfavorable case perpendicular to the axis of the section/span route), it is absolutely necessary to take into account the aerodynamic impact of the turbine on the line, which practically means - when testing wind turbine location - analysis of the distance between its foundation and the power line. These issues are the subject of this article, in which the author shows a case study set in a real decision-making situation.

2. GENERAL FORMAL AND LEGAL CONDITIONS

The public debate on the development of renewable energy sources often generalizes the issue of the adequacy of the transmission/distribution infrastructure, ignoring or trivializing the limitations resulting from it. As a result, from the point of view of network development planning and the concept of managing it, it creates a permanent state in which there is a very large surplus of projects, ideas and concepts, most of which will naturally not be implemented. Wind power plants require the existence of sources that will balance them in the period of the lack of primary energy. Currently, the "firm capacity" level for onshore wind farms is ca.10-15%,and offshore- ca. 20%. This creates challenges for the centralization organization in the electricity wholesale market, as it should create a business space for balancing sources. At present, it seems that the market is not correctly evaluating the balancing value. It is indirectly done by the capacity market, but it is not treated as an opportunity to solve the problem - only as support for coal-based energy. Intensive introduction of renewable energy sources (with their specific grid operation characteristics) causes an increasing number of grid operation different problems (failure frequency, source disconnection, a necessity to modernize and change grid automation). In summary, it is impossible to introduce all sources into the current networks in any way and the process of connecting (and obtaining permits) will become more and more complicated. This may be a factor that significantly limits, and certainly slows down, the possibility of introducing zero-emission energy - a factor that is not currently included in optimistic development plans. Additionally , developing renewable energy, in particular wind farms, creates, inter alia, essential requirements for the location of wind turbines with a horizontal axis of rotation. One of the main obstacles in the development of renewable energy is the principle that determines the distance at which wind farms can be located and built. The permissible distance of the wind turbine from the residential buildings is to be equal to or greater than ten times the height of the wind turbine measured from the ground level to the highest point of the windmill, including the rotor with blades (**10 h** rule). The **10h** rule, according to many experts, slowed down / expired construction of new wind farms and hindered spatial planning processes in the field of residential construction in communes where farms were previously located [10]. The rigidly defined distance from buildings does not reflect the conditions of an individual location, as it may turn out to be too large or too small for a specific place. Since the often used onshore turbines have a total height of no more than approx. 220 m, it is difficult/impossible to develop further projects, because the existing wind farm sites will not be able to be used for more modern and more efficient machines due to the lack of areas for their development. Changing the **10h** rule seems to be necessary to avoid an investment gap in wind farms. There is a risk of such stagnation in investments in a few years, after the completion of investments in the recently concluded auctions. The change would unblock the development of wind energy and planning difficulties in land development. In addition, it is advisable to introduce the principle of reliable forecasting of noise emissions, in particular, the impact of a turbine as a source of turbulence, at the stage of investment preparation and preparation of planning documents, and then appropriate measurements after the completion [10]. One can then check whether the assumed acoustic standards are met and whether any problems can be remedied, which in practice happens occasionally due to the technical conditions of the devices. In the opinion of the author of this paper, the existing rules for the location of wind turbines

should be clarified, while maintaining the safety requirements for the construction of the wind turbine foundation in the event of resignation from the rigid 10 h distance criterion, as the postulates to introduce transitional regulations or attempts to ease the distance criterion do not solve the location problems.

3. TECHNICAL CONTEXT

In general, the assumption of a rational reduction in air velocity as it passes through the turbine, where the air velocity behind the rotor is 1/3 of the velocity in front of the rotor, leads to Betz's law (the power of the wind varies proportionally to the third power of its speed), by which the theoretical maximum useful power taken from the flowing air stream is calculated according to the formula [11]:

$$\boldsymbol{P_{u,max} = \frac{8}{27} p A_1 V_0^3} \quad (1)$$

where:
$P_{u,max}$- theoretical maximum useful power taken from the air stream,
V_0 - wind speed in front of the wind turbine set rotor,
ρ - air density,
A_1 - surface "swept" with the rotor of the wind turbine set.,

Betz's law determines the maximum theoretical efficiency of converting the power of the wind flowing to the wind turbine set into mechanical power used by this turbine set (this efficiency is approximately 59.3%). The occurrence of wind is stochastic. The wind speed, on the other hand, depends largely on the topography (roughness) and the height above the ground. There are various definitions of ground roughness depending on its topography. According to the study [11], three types of terrain roughness are most often distinguished:
• open (with few obstacles of low height),
• rural (with low buildings or wooded area),
• urban (with high buildings).

A four-level scale of terrain roughness dominates in Europe, taking into account the height of obstacles, their cross-sections, and areas of horizontal projections. For the purposes of the development of domestic wind energy, a more detailed, i.e. a six-level roughness scale [11] has been proposed, presented (while retaining the original markings) in Table 1.

Table 1 Terrain roughness classes

Roughness class	**Gradient wind height HG [m]**	**Roughness factor K**	**Exponent α**	**Description of the area**
0	300	0,005	0,150	Flat open area where the height of unevenness is less than 0.5 m
1	330	0,007	0,165	Flat, open, or slightly undulating terrain. There may be individual buildings or trees at large distances from each other
2	360	0,010	0,190	Flat or undulating terrain with large open spaces. There may be groups of trees or low buildings at a considerable distance from each other

3	400	0,015	0,220	Areas with obstacles, wooded areas, suburbs of larger cities and small towns, industrial areas with built-up areas
4	440	0,025	0,270	Areas with numerous obstacles in close proximity to each other, i.e. clusters of trees, buildings, at a minimum distance of 300 m from the observation site
5	500	0,035	0,035	Areas with numerous large obstacles located close to each other, forest areas, centres of large cities

The current standard technical specification of the transmission system operator (PSE) specifies the requirements for the distance between wind turbines and overhead high voltage power lines as a minimum of **3d** , counting from the tip of the turbine blade to the axis of the line route, and the condition for using active anti-vibration protection in the case of locations less than **5d** [14]. This is basically in line with the previously applicable PSE standard, where the distance is **3.5d**, but from the axis of the turbine foundation to the axis of the line route. Interesting considerations are presented in [2], where, based on the standards [12], [13]; in addition to a brief description of the models and methods used to calculate the impact of turbulence on the farm efficiency, examples of sectors/areas in which the operation of the turbine are significantly influenced by various obstacles are given (creating an aerodynamic footprint) in the air/wind path (see Figure 1).

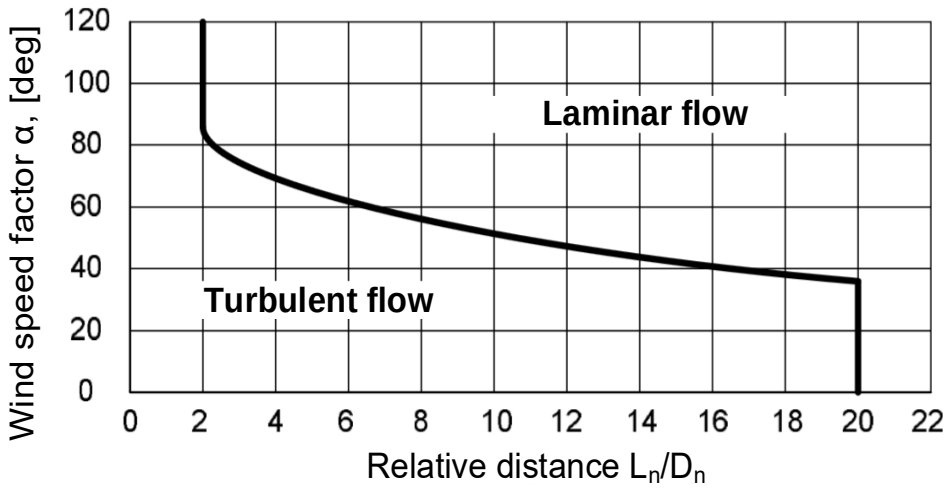

Fig.1 Air flows dependency on the relative distance Ln / Dn

The study of the impact of obstacles on the efficiency of wind farms, and more specifically the impact of an obstacle on the value of wind speed, is illustrated by the coefficient α, which determines the rate of changes in wind speed as a function of distance and is calculated from the formula:

$$\alpha = \frac{0,5}{\ln\frac{z}{z_0}} \tag{2}$$

where:

z - distance between the ground surface level and the turbine hub generating the disturbances,
z_0 - roughness coefficient of the terrain between the turbines (a kind of equivalent of the K coefficient from Table 1).
As is known, the value of **α** depends on the intensity of turbulence. Table 2 presents the relative values of wind velocity turbulence and the corresponding values of the change factor.

Table 2 The relationship between the value of turbulence and the coefficient of changes in wind speed

No.	Turbulence. intensity [%]	Change factor α
1	8	0,040
2	10	0,052
3	13	0,063
4	15	0,075
5	16	0,083
6	18	0,092
7	20	0,099
8	21	0,100
9	24	0,108
10	29	0,117

As the power of individual generating units increases, the rotor diameter grows. Therefore, the influence of turbines as a source of wind flow turbulence increases. According to the authors of the work [2], optimization of wind farm topology can be performed, based on TOPFARM programming, where one can model various structures of wind farms use various models of wind speed distribution, considering turbulence components, analyze technical and economic aspects and carry out multi-criteria optimization.
Assuming the shape of a turbulent vortex as a truncated cone (with a slightly irregular shape) lying on its side, with a smaller circular base with a diameter equal to the diameter of the turbine rotor, and a larger one with a diameter equal to (d + 2ltgα, where for small values of the angle up to approx. 15 degrees - its tangent is equal to the angle of the arc measure), where l is the distance between the turbine and the line element (column, line segment, span, etc.), i.e. the height of our cone, and α - the cone/vortex forming angle with the base (in the longitudinal section of a trapezium[14] - for example, see Fig. 2 , using the formulas of analytical geometry and planimetric relationships and having source data, it is possible to analyze and study possible cases of penetration of a turbulent vortex body with a line chain curve for each case of foundation of a specific turbine in the planned location.

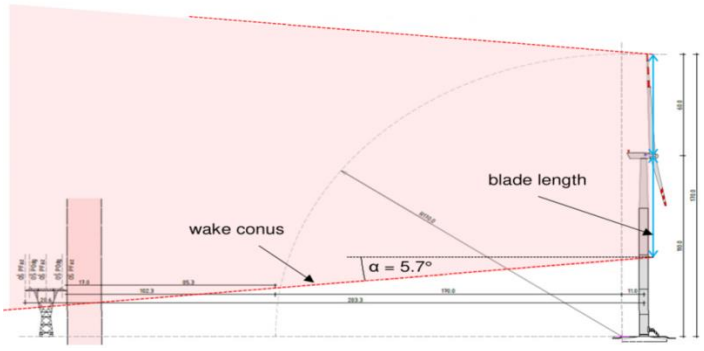

Fig.2. An example of a longitudinal section of a turbulent vortex for a specific designed wind farm (original designations have been retained-adopted from [15])

4. REPORT FOR THE ASSESMENT OF THE IMPACT OF TURBULENCE GENERATED BY WIND TURBINES ON THE HIGHEST VOLTAGE POWER LINE-CASE STUDY

4.1 GENERAL REMARKS

In an exemplary preliminary evaluation report, the results of the author's rough formal analysis are presented and the author's calculations and an illustration of a trial application of the numerical analysis of turbulent eddies generated by the considered turbines in the planned places of their foundation are presented. The location of the planned wind farm is shown in Fig. 3.

Fig.3 Wind turbines location

As shown in this site plan, wind turbines are planned in close proximity to the highest voltage transmission power line.

4.2 PRELIMINARY RESULTS OF THE ANALYSIS

Lightning protection wires (P_{og}) are the highest situated elements of the power transmission line excluding from the height of their suspension on a specific pole in relation to the ground surface. Using the equation of the chaining curve for their, at the point of intersection of the perpendicular line as the shortest distance to the longitudinal profile of power transmission line , the suspension heights Hpog for each turbine were calculated. The value of the "vortex spread angle" specified in the study by Aero Dynamic Consult [6] for a specifically planned turbine at 5.7 degrees was positively verified by two existing models of turbulent vortex propagation, as the author of this paper calculated it 5 to 6 degrees, depending on the model used [15]. It should be noted that the calculation of the height of the "excess" includes the tangent of the angle, which with these slightly different values is within the error resulting from rounding. Thanks to this, it can be assessed whether the phase conductors, as suspended lower than the lightning protection, may be located below the lower ribbon of turbulent eddies, which will flow above the line at the appropriate H_{wir} elevation (calculated from the ground surface). It is shown in Table 3, which presents a preliminary analysis of the phenomenon of "overshoot" of turbulent eddies while maintaining the original numbering of the power plant (EW-X) according to the order of location along the route of the transmission power line [14].

Table 3 Results summary of the phenomenon of "surpassing" turbulent eddies analysis

No. wind power plant	Distance L from the line [m]	Suspension H_{Pog} [m]	Elevation Hwir [m]	Reserve[m]	Remarks
EW-3	260,2	22,17	24,14	+1,97	the vortex will not "catch" on the line
EW-1	283,3	29,79	21,84	-7,95	the vortex will "catch" the line
EW-2	258,2	23,25	24,34	+1,09	the vortex will not "catch" on the line
EW-4	237,9	22,73	26,35	+3,62	the vortex will not "catch" on the line
EW-5	263,7	18,46	23,79	+5,33	the vortex will not "catch" on the line
EW-8	287,2	28,65	21,45	-7,20	the vortex will "catch" the line
EW-6	209,9	26,25	29,14	+2,89	the vortex will not "catch" on the line
EW-9	233,1	22,45	23,78	+1,33	the vortex will not "catch" on the line

The results presented in Table 3 are rough calculation results. The author of this paper recommends detailed calculations and numerical analysis by the finite element method (in the past and currently used by many experts) of turbulent vortex propagation for 8 turbines (for 3 wind speeds: 10.8; 20.0; 25.0 [m / s]) and for the following four variants (W-1, W-2, W-3, W-4):
W-1 Basic: turbine type 2.75 / 120, hub height 110 m and location - no changes;
W-2 Corrected A - turbine type 2.75 / 120, for EW-1, EW-8 hub height change from 110 m, for example 139 m, without changing the location of all eight power plants;
W-3 Corrected B - turbine type 2.50 / 120, for EW-1, EW-8 hub height change from 110m, for example 120m, without changing the location of all eight power plants;
W-4 Corrected C - turbine type 2.75 / 120, hub height unchanged, and for EW-1, EW-8 change of location (approaching the line at a distance allowing to obtain the effect of "surpassing" the turbulent vortex, which will not catch on the line.
This will require, after detailed calculations and in-depth numerical analysis of turbulent vortices using the above-mentioned methods and models, the presentation of turbulent vortices originating from individual eight turbines on 96 drawings, and calculations and illustrations of "summary" vortices - resulting from the interaction of "adjacent" turbines together. To illustrate the scope of research and analyzes, for illustrative purposes, below - examples of illustrations of a turbulent vortex (see Fig. 4-6) are attached below made at the Gdansk University of Technology [15], which were obtained for the object with the assumption that the wind blows from the left side to the right, the turbine stands on the X axis in position 0, and the 400 kV transmission power line pole on the X axis at 250 meters (it is hardly visible because it is low compared to the turbine itself).

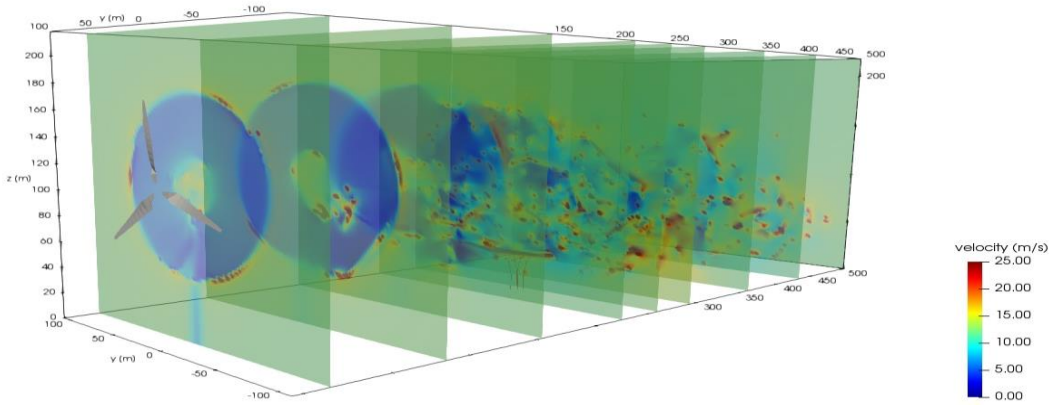

Fig. 4 View of a turbulent whirl (adopted from[16])

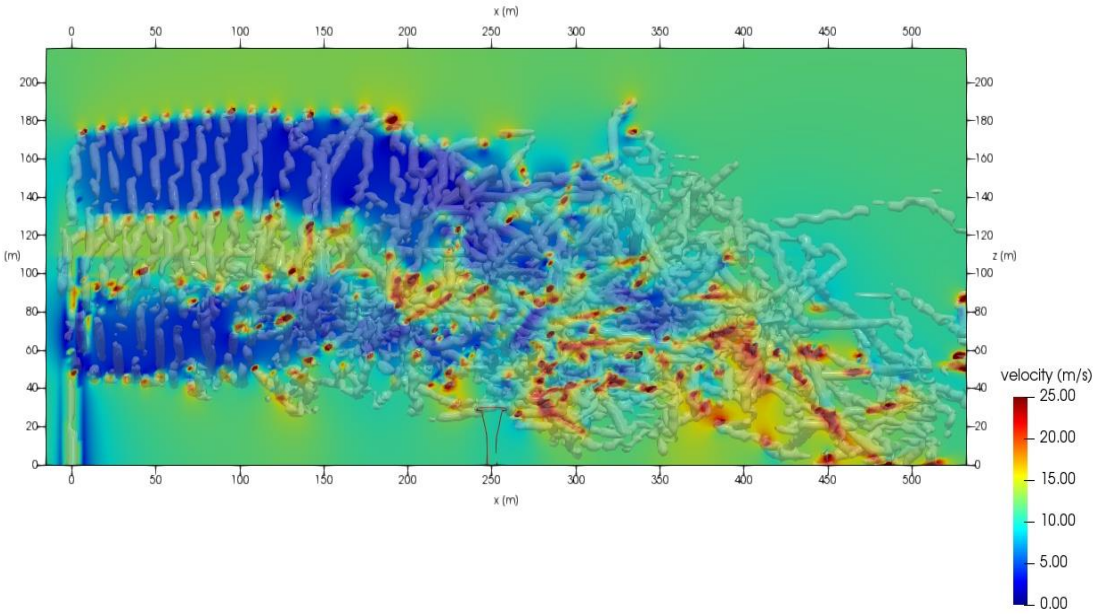

Fig. 5 Longitudinal section of a turbulent vortex (adopted from [16])

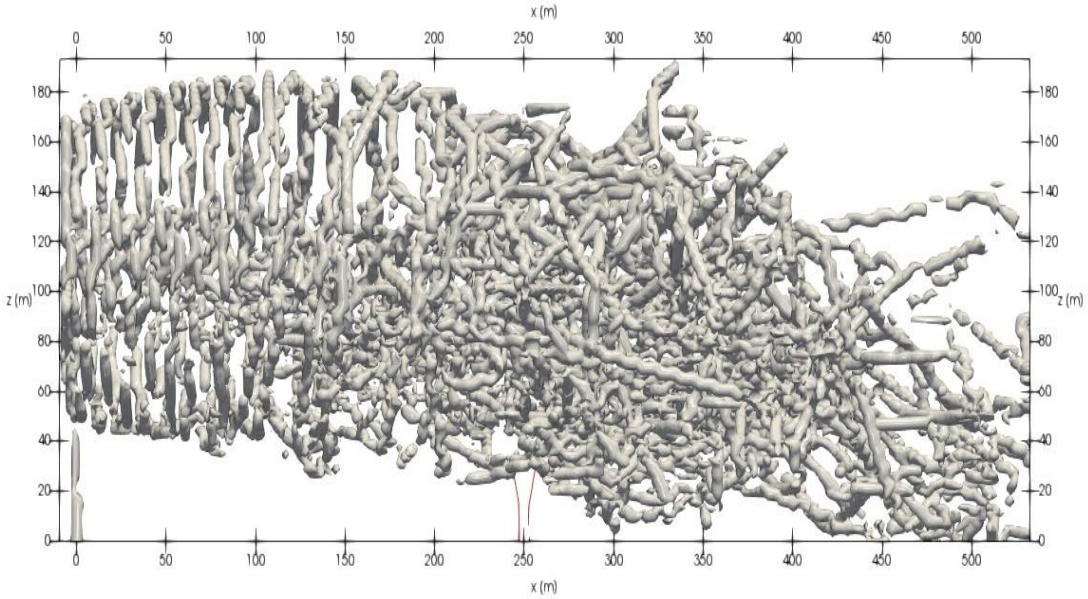

Fig. 6 Projection of the turbulent vortex (adopted from [16])

As can be seen from the above illustrations, the lower ribbon of the turbulent vortex has a chance to flow above the power transmission line, if it is possible to bring the turbine closer to the line to a distance of L_{min}. In this case maintain 10% buffer zone of construction safety related to the risk of the structure falling towards the line, which gives an obvious condition distances $L_{min} = z + d / 2 + 0.1 (z + d / 2)$, where **z** - distance between the ground surface level and the noise generating turbine hub, **d**- turbine rotor diameter.

4.3 INFERENCES OF THE ANALYSIS

With the use of source materials [14], original calculations were made and a trial application of numerical analysis of turbulent eddies was made. On this basis, it can be concluded that out of the eight considered - six turbines can probably be located in the planned places of foundation. Turbines: EW-1, EW-8, located respectively at real distances: 283.3 m; 287.2 m from the 400 kV transmission power line will probably require additional procedures in order to be installed, which should be documented in the planned study based on in-depth research and numerical analyzes. This analyzes should include a number of calculations and tests to convince the owner/operator of the transmission power line to the advisability of changing the standards for locating wind farms due to the possibility of turbulent vortices that could threaten the safety of the power line structure.

5. CONCLUSIONS

Until 2030, with the gradual departure from carbon fuels caused by environmental pressure, renewable technologies will play a significant role for energy power development. They can partially replace the shrinking coal fuel base. In addition, they can find employment/use of the constructed electricity transmission and distribution system infrastructure . Current development constraints for RES is among others lack of an adequate transmission/distribution network.
The place in the network is generally reserved at the stage of connection conditions establishment. This creates the famous case/possibility of "sitting" on the grid at an early stage of projects, blocking the development of others. Transmission operators calls for actions in this area:

- introduction of master plans (Energy Policy, Climate Policy, etc.) - at least partially, specifically setting priorities in terms of the number, pace and location of connected sources,
- in the case of sources benefiting from support - the introduction of a promising system, which would become connection conditions only after the received support,
- in the case of sources not benefiting from support - introducing a declaration of investment implementation without support along with a system of security and guarantees enabling "reservation" of a place in the network,
- unification of the law so that at the stage of applying for conditions, energy banks, like other sources, pay an advance on the connection fee.

The power grid should be planned and implemented in a sustainable manner, meeting the goals and directions for the development of the energy sector indicated in the country's energy policy, including e.g. diversification of electricity generation technology. In particular, the development of the transmission system must ensure the creation of technical conditions to cover the growing demand for power and electricity in individual areas of the country, power evacuation from the planned new generation sources and improvement of conditions for the integration of the Pan-European energy market. In view of the rather irreversible direction of the transformation of the power sector (Green Deal), it will be necessary to invest in RES, which in real conditions will result in investing mainly in wind farms and photovoltaic farms. The current formal and legal conditions are rather not accommodating to such investments. Therefore, it seems necessary to change the law to avoid an investment gap in wind farms. Changes in the law could unblock the development of wind energy and planning difficulties on the part of municipalities. It is advisable to introduce the principles of reliably conducted noise emission forecasts, in particular, the impact of the turbine as a source of turbulence already at the stage of investment preparation and preparation of planning documents, and then taking appropriate measurements after the construction is completed. For example, it will require detailed calculations and in-depth numerical analyzes of turbulent eddies with the use of effective methods and models, studying the processes of generating turbulent vortices from turbines included in the wind farm, and calculations and illustrations of "summary" eddies - originating from the interaction with each other of "adjacent" turbines in the form of a compact report on the assessment of the aerodynamic impact of wind turbines on high and extra-voltage power lines. In the opinion of the author of this study, the existing rules for the location of wind turbines should be clarified, while maintaining the safety requirements for the construction of wind turbine foundation, in particular in the event of abandoning/resigning from the existing rigid distance criterion, which would allow for the acquisition of rational locations for the wind turbine foundation.

REFERENCES

[1] Crasto G., et al., Wind turbines wake calculations. Comparins of actuator disc against analitycal models, AWEA 2011. Wind Power Proceedings, Anaheim, California, 2011
[2] Drozdowicz A., et al., Badanie wpływu przeszkód na sprawność farm wiatrowych na modelach, Poznan University of Technology Academic Journals - Electrical Engineering 2016 no. 87 (in Polish), Poznan Poland 2016
[3] Jensen N. O., A note on wind generator interaction, Technical Report Riso-M-2411, Roksikte, Denmark, November 1983
[4] Choi J., Shan M., Advancement of Jensen (Park) wake model, Proceedings of the EWEA Annual Meeting, Vienna, 2013
[5] Ishihara T.,Yamaguchi A., Fujino Y., Development of a new wake model based on a wind tunnel experiment, Global Wind Power, 2004
[6] Kleinstahl S.,Schwenk J., Effect of turbulence on high-voltage line, ADC Report 2020-10, Rev.2.2. Feb.2020, Dynamik Consult, Neuhausen, Germany, 2020
[7] Micaleff C., et al., The origins of wind turbine tip vortex, Journal of Physics: Conference Series 555012074, 2014
[8] Tesch K., Metody numeryczne. Podstawy modelowania turbulencji, Zakład Mechaniki Płynów, Politechnika Gdanska (in Polish), Gdansk, Poland 2020
[9] Kubica-Żach K., Hałas, a nie odległość, powinien decydować o lokalizacji wiatraka , Prawo.pl, 01.2020https://www.prawo.pl/samorzad/ustawa-wiatrakowa-resort-rozwoju-zapowiada-nowelizacje-w-2020,497249.html (in Polish)
[10]Gumuła S., et al., Energetyka wiatrowa, Uczelniane Wydawnictwa Naukowo-Dydaktyczne AGH (in Polish), Kraków, Poland in Polish),2006
[11]Technical standard, PSE-SF.ODLTW.NNPL/2019 ed.1. Odległości turbin wiatrowych od linii NN, PSE Konstancin-Jeziorna (in Polish), 2019
[12] Technical standard, PN-EN 61400-12-2:2006.Turbozespoły wiatrowe.Cz.12:Badania energetyczne (in Polish), Warsaw, Poland, 2006
[13]Technical standard, PN-EN 61400-1-:2005. Turbozespoły wiatrowe.Cz.1:Badania dotyczące bezpieczeństwa (in Polish), Warsaw, Poland, 2005
[14]Source materials, Mashav Management Sp.z o.o. (in Polish -unpublished),Warsaw, Poland, 2020.
[15]Kamrat W., *Own studies (2015-2020),* Katedra Elektroenergetyki (in Polish -unpublished). Politechnika Gdańska, Gdansk, Poland 2020
[16]Kamrat W., Selected problems of wind turbines location under wake conditions due to power transmission lines, Elektroenergetyka, Vol. 1, No. 22, 2020

Vortical flows in the wake of bluff bodies and their role in flame anchoring.

Georgios Paterakis, Konstantinos Souflas, Evangelos Panagiotis Mitsopoulos, Eleni Manouskou, Panagiotis Koutmos

Laboratory of Applied Thermodynamics, Department of Mechanical Engineering and Aeronautics, University of Patras.
University of Patras, 26504, Patras Greece.
** Corresponding Author: epmitsopoulos@gmail.com*

The time averaged and fluctuating flow field characteristics of vortical flows established downstream of a variety of axisymmetric baffles, have been investigated for a double-cavity fuel-air premixer/stabilizer arrangement, for isothermal and reacting conditions. The work aims to broaden knowledge regarding the impact of different bluff body shapes, leading and trailing edge contours, blockage ratios and incoming flow profiles, on the development of the downstream bluff body formed wake–vortex structures. Particle Image Velocimetry (PIV) measurements have been applied to obtain the mean and turbulent velocity fields throughout the afterbody near wake zone.

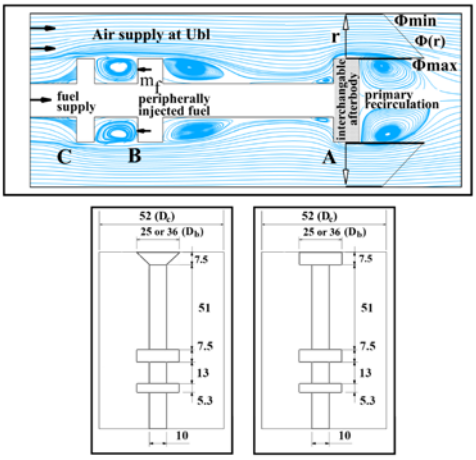

Fig. 1: Bluff body/burner configurations

The experimental facility is shown in Fig. 1 and has been described in detail in [1,2]. Three axisymmetric baffles (A, B, C) connected along their axis with a 10mm hollow tube comprise the premixer/burner arrangement. Two bluff body shapes and blockage ratios have been studied for both isothermal and reacting conditions. The stabilizing afterbody "A" is either a disk- (D) or cone- (C) shaped body, with a diameter of 25 or 36mm (D_b) and a rim thickness of 7.5mm, as shown in Fig. 1.

Measurements of the velocity fields have been conducted with a two-dimensional Particle Image Velocimetry configuration (2DPIV, LaVision® FlowMaster 2D) and described in detail in [3].

The results highlighted the importance of the velocity characteristics at the wake inlet zone as predisposed by the interaction of the trailing edge geometry with the upstream double cavity premixer, and the difference between geometric and aerodynamic bluffness for each bluff body.

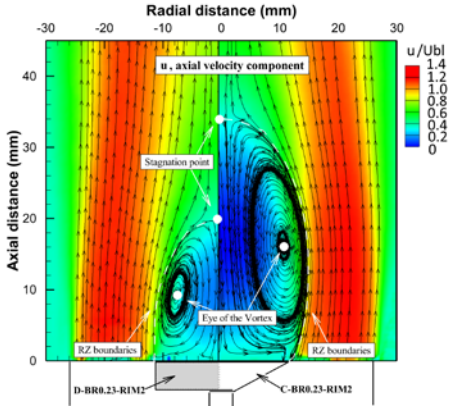

Fig. 2: Bluff body/burner configurations

Downstream of the cone shaped bluff bodies, larger recirculation zones have been encountered, For the same basic bluff body shapes, an increase in blockage ratio had a minor effect on the width of the RZ. Also, shifting from a cone to a disk shaped baffle, resulted in a reduction of the RZ length of about 29-35%. Finally, cone shaped bluff bodies produced, in general, total strain rate values of about 1.7 times greater that the disk shaped ones, for the same blockage ratios. The above information combined with the inlet fuel-air mixture topologies that emanate from the investigated premixer/burner set ups can provide important information on the interaction of fuel-air mixture disposition and the vortical flows established in the near wake zone. Such knowledge is crucial for the promotion of flame stabilization under operation with a variable range of fuel types.

References

[1] Karagiannaki C, Dogkas E, Paterakis G, Souflas K, Psarakis EZ, Vasiliou P, et al. A comparison of the characteristics of disk stabilized lean propane flames operated under premixed or stratified inlet mixture conditions. Exp Therm Fluid Sci 2014;59. doi:10.1016/j.expthermflusci.2014.04.002.

[2] Paterakis G, Politi E, Koutmos P. Experimental investigation of isothermal scalar mixing fields downstream of axisymmetric baffles under fully premixed or stratified inlet mixture conditions. Exp Therm Fluid Sci 2019;108:1–15. doi:10.1016/j.expthermflusci.2019.05.018.

[3] Banyon C, Rodriguez-Henriquez JJ, Paterakis G, Malliotakis Z, Souflas K, Keramiotis C, et al. A comparative study of the effect of varied reaction environments on a swirl stabilized flame geometry via optical measurements. Fuel 2018;216. doi:10.1016/j.fuel.2017.09.105.